Slag-based alkali-activated concrete: from material properties to structural shear behaviour.

Experimental Study

Robin Straathof

Delft University of Technology

TU Delft

Slag-based alkali-activated concrete: from material properties to structural shear behaviour.

Experimental Study

by

Robin Straathof

Author:	Robin Straathof	
Student number:	4846877	
Thesis committee:	Dr. ir. Mladena Luković	Chair
	Ir. Jelle Bezemer	Daily supervisor
	Prof.dr.ir. Jan Rots	Secondary supervisor
Project Duration:	September 2024 - March 2025	
Faculty:	Civil engineering - Structural engineering, TU Delft	

TU Delft

Preface

This thesis marks the final stage of my master's degree in civil engineering at Delft University of Technology.

My interest in this research topic stems from my passion for structural design and calculations, combined with a strong focus on sustainability. Over the past few years, I have come to appreciate the growing importance of sustainability in engineering. I often ask myself how I can merge my interest in structures with sustainable practices and how civil engineers can contribute to a more sustainable future. I hope that in the near future, more sustainable building materials will be safely integrated and become the industry standard. Through this research, I aim to contribute to the safe implementation of AAC in structural applications.

Readers interested in material tests on AAC and PCC can find relevant information in Section 3.4, while details on shrinkage are provided in Section 3.5. For information on structural shear tests on AAC and PCC concrete, please refer to Section 3.6.

I am deeply grateful to all those who supported me throughout this period.

First, I would like to thank the members of my thesis committee: Dr. Mladena Luković, Ir. Jelle Bezemer, and Prof. Dr. Ir. Jan Rots. I am especially grateful to Dr.ir. Mladena Luković, the chair, for suggesting this topic and for dedicating her time to answering my questions, offering valuable suggestions and guiding me in the right direction. I also extend my sincere thanks to Ir. Jelle Bezemer, my daily supervisor, for assisting me with the planning and execution of experiments in the Stevin II lab, encouraging me to critically assess my results and sharing his insights on the findings. Lastly, I would like to thank Prof. Dr. Ir. Jan Rots for his role as my secondary supervisor, providing critical feedback, helping me refine how I communicate my findings and sharing his enthusiasm for the topic.

Furthermore, I would like to express my appreciation to the technicians of the Stevin II lab, especially Ton Blom, Ake Blom, Fred Schilperoort, Giorgos Stamoulis and Oscar Straathof. Ton played a crucial role in the casting process, preparing the materials and ensuring that everything ran smoothly and efficiently. Ake and Fred provided invaluable support in executing the tests with precision, while Giorgos assisted with the DIC measurements. Finally, a special thanks to Oscar, who was always ready to lend a hand with shrinkage measurements, UPV and preparations for the numerous tests. I could not have completed this work without them.

Lastly, I would like to thank my family and friends for their support and encouragement throughout this journey, especially Timo, who patiently endured my stress and was always there to support and help me. Finally, I would like to give a special thank you to my dad, who saved me when my laptop shut down completely.

Robin Straathof
Delft, March 2025

Abstract

The cement industry has set a goal of reducing CO_2 emissions by 80% by 2050 (European Environment Agency, 2024, Wang et al., 2023). One approach that can contribute to this reduction is the complete replacement of cement with industrial by-products, such as Granulated Blast Furnace Slag (GGBFS) obtained from the steel industry. GGBFS can become a binding substance when activated with an alkali-metal solution, creating a new type of concrete known as slag-based alkali-activated concrete (AAC).

Studies on slag-based AAC have shown promising results, but they have primarily focused on material behaviour tests, with testing typically limited to 28 days (Bendapudi et al., 2017, Lu et al., 2023). Research investigating the long-term behaviour of AAC beyond 28 days has reported a reduction in mechanical properties over time (Prinsse, 2017, Bezemer et al., 2023). Despite these findings, there is a significant gap in understanding the long-term material behaviour of AAC. To the best of the author's knowledge, no studies have examined shear strength development beyond 28 days. Considering the long-term material properties of AAC and their influence on shear transfer mechanisms, differences in shear behaviour between AAC and Ordinary Portland Cement Concrete (OPCC) can be anticipated.

This study aims to evaluate the long-term flexural shear failure of AAC. To better understand long-term shear behaviour, the research also examines the compressive strength, tensile strength, elastic modulus, autogenous shrinkage and drying shrinkage of slag-based AACs at 28 days and 6 months. The study focuses on two GGBFS-based AAC mixtures of strength classes C30 and C50 (S-AAC-C30 and S-AAC-C50), comparing them with Portland Cement Concrete (PCC) of similar strength classes (S-PCC-C30 and S-PCC-C50).

The main research question is: ***"What is the difference in shear behaviour of reinforced beams made of slag-based alkali-activated concrete versus Portland cement concrete, including the influence of age, shrinkage and strength class?"***

To answer this question, the following sub-questions are addressed:

1. What are the differences in material properties influencing shear behaviour, namely tensile strength, elastic modulus and shrinkage, between slag-based alkali-activated concrete and Portland cement concrete mixtures?
2. What is the effect of age on the material properties and structural behaviour of slag-based alkali-activated concrete?
3. What is the effect of concrete strength class on the shear behaviour of slag-based alkali-activated concrete?

Firstly, the results from the material behaviour tests indicate similarities in tensile strength and elastic modulus for C30 mixtures of AAC and PCC at both 28 days and 6 months. At 28 days, the tensile strengths were 3.5 MPa and 3.3 MPa, while the elastic modulus values were 38 GPa and 39 GPa, respectively. By 6 months, the tensile strengths had decreased to 2.6 MPa and 2.7 MPa, and the elastic modulus had declined to 37 GPa for both mixtures. This represents a 26% reduction in tensile strength and a 4% reduction in elastic modulus over six months.

However, differences were observed in the C50 mixtures. Although AAC exhibited the same compressive strength as traditional PCC concrete, it showed lower tensile strength and elastic modulus at 28 days, with even greater differences at 6 months. At 28 days, the tensile strengths were 2.9 MPa and 3.9 MPa for the S-AAC-C50 and S-PCC-C50 mixtures, respectively. Additionally, the measured elastic modulus values were 38 GPa and 41 GPa, respectively. By 6 months, the tensile strength of the S-AAC-C50 mixture had further decreased by 14% to 2.5 MPa, while the tensile strength of the S-PCC-C50 mixture remained constant. Furthermore, the elastic modulus of the S-AAC-C50 mixture declined by 24% to 29 GPa, whereas the elastic modulus of the S-PCC-C50 mixture remained unchanged.

Secondly, the AAC mixture exhibited greater shrinkage compared to the PCC mixture over 6 months. The S-AAC-C30 and S-AAC-C50 mixtures experienced autogenous shrinkage that was 45% and 145% higher, respectively, and drying shrinkage that was 47% and 38% higher, respectively, compared to PCC mixtures of the same strength class.

It is important to note that the material behaviour tests were conducted on unreinforced specimens, which were free to shrink. Therefore, the high levels of shrinkage observed did not influence the test results.

Thirdly, the structural behaviour was tested on reinforced concrete (RC) beams that were not free to shrink. As a result, over 6 months of testing, the effects of shrinkage became evident. When specimens are restrained from shrinking, internal stresses develop in the material. If these stresses exceed the tensile resistance of the concrete, micro-cracks form, leading to a loss of strength and stiffness. Ultrasonic pulse velocity (UPV) testing confirmed the presence of these micro-cracks in the AAC beams.

Shear behaviour test results indicated that AAC mixtures had lower tensile strength and elastic modulus at both 28 days and 6 months compared to the values measured in the material behaviour tests. At 28 days, the elastic modulus of AAC mixtures was reduced by 30%, while the tensile strength decreased by 20%. By 6 months, the elastic modulus had further declined by 50%. Additionally, AAC mixtures exhibited a different crack pattern than PCC mixtures, displaying more bending cracks of shorter lengths, a characteristic effect of shrinkage.

Despite higher shrinkage and lower stiffness and tensile strength, AAC mixtures achieved similar or higher ultimate shear capacity compared to PCC mixtures, by 0-14%, likely due to the increased influence of equilibrium crack mechanisms (dowel action, aggregate interlock, and residual tensile stress) over time. However, the exact contribution of these mechanisms to the overall shear failure process remains uncertain. Therefore, the long-term influence of shrinkage on the equilibrium crack stage cannot yet be fully predicted.

In conclusion, while material tests at 28 days indicate promising results for AAC, it is crucial to evaluate its performance over a longer period. Shrinkage is a significant factor that must be considered when applying AAC concrete. Furthermore, the relationship between compressive strength and other material properties does not necessarily apply to new types of concrete and should be reassessed before implementation.

Contents

Nomenclature

Abbreviations

Abbreviation	Definition
AAB	Alkali-Activated Binder
AAC	Alkali-Activated Concrete
AAS	Alkali-Activated Slag
CO_2	Carbon Dioxide
CEMBUREAU	European Cement Association
DIC	Digital Image Correlation
EN	European Standard
FA	Fly Ash
GGBFS	Ground Granulated Blast Furnace Slag
GSDM	General shear design method
ISO	International Organization for Standardization
ITZ	Interface Transition Zone
LVDT	Linear Variable Displacement Transducer
OPC	Ordinary Portland Cement (CEMI 100% clinker)
OPCC	Ordinary Portland Cement Concrete
PCC	Portland Cement Concrete (CEMIII/B 30% clinker and 70% GGBFS)
RC	Reinforced Concrete
$NaOH$	Sodium Hydroxide
Na_2CO_3	Sodium Carbonate
Na_2SiO_3	Sodium Silicate
SF	Silica Fume
UPV	Ultrasonic Pulse Velocity

1

Introduction

1.1. Background and motivation

Climate change is one of the biggest challenges of our century. Due to human activity, significant amounts of additional carbon dioxide (CO_2) have been released into the atmosphere, causing global temperatures to rise and climates to change (European Environment Agency, 2024, Wang et al., 2023). The cement industry contributes approximately 4% to 8% of global CO_2 emissions (Olivier and Peters, 2020). To address this issue, CEMBUREAU has set a goal of reducing CO_2 emission in the cement industry by 80 % by 2050 (Cembureau, 2024).

Concrete production requires several ingredients: aggregates, cement and water. Cement is an essential component in achieving the desired strength and durability of the concrete. The cement industry has a high contribution to climate change due to several factors: cement is one of the most widely used building materials in the world (Soomro et al., 2023); cement production is a highly energy-intensive process (Nasir et al., 2024); and the availability of raw materials to produce cement, such as limestone and clay, is decreasing (Soomro et al., 2023). Strategies to reduce these impacts are using energy-efficient systems, renewable energy sources and lowering the clinker-to-cement ratio (Nasir et al., 2024).

One way to reduce carbon emissions in the building industry is to replace cement with an alternative Alkali-Activated Binder made from industrial by-products. Using this new binder could reduce the carbon footprint by 20 to 80% (Nasir et al., 2024). However, studies are needed to understand the material fully before introducing this binder in the industry. Studies at 28 days show promising results: the study of Bendapudi et al., 2017 and A. Shah and C. Shah, 2017 concluded that the flexural strength at 28 days is similar to those of Ordinary Portland Cement Concrete (OPCC) and the study of Liu et al., 2023 and Wu et al., 2020 concluded that also the shear strength 28 days is similar to those of OPCC. Although this new type of binder seems promising, there is limited research on its long-term behaviour. Studies that have investigated long-term properties, beyond 28 days, reported a decrease in mechanical properties over time (Prinsse et al., 2020). This behaviour is different than found in OPCC, there the properties show an increase over time (Bezemer et al., 2023). This difference suggests that standard testing procedures at 28 days may be inappropriate for Alkali-Activated Concrete (AAC) because 28 days value does not present a safe reference for design. For example, the compressive strength of concrete at 28 days is used to predict the long-term behaviour of concrete structures. This is founded on the assumption that the strength of the concrete increases further or remains similar over time.

Only a limited number of studies have investigated the shear strength of AACs. To the author's knowledge, none have examined the shear strength beyond the standard testing age of 28 days. Nevertheless, considering the mechanisms of shear transfer, it can be hypothesized that the long-term shear strength of AACs might also decrease over time. This is because the shear transfer mechanisms strongly depend on compressive strength, tensile strength, matrix strength and bond strength. Therefore, key properties to investigate include the tensile properties and bond strength of AACs.

1.2. Objective of the research

This study aims to investigate the long-term structural behaviour of AAC under shear. To better understand the long-term shear behaviour, this study will also examine the long-term behaviour of compressive strength, shrinkage, tensile strength and elastic modulus in AACs. Tensile strength is expected to play a governing role in the first stage of shear behaviour, such as the formation of initial cracks, affecting the fracture pattern in beams and influencing the load-displacement curves at lower load levels. Furthermore, it is expected that shrinkage plays a vital role in the long-term shear behaviour, affecting the material properties because RC beams are restrained from shrinking. This is an exploration study investigating if the long-term behaviour should be further investigated before AAC can be safely applied.

1.3. Scope of the research

Although there are multiple possibilities to formulate an alkaline-activated concrete, the current research is limited to two Ground Granulated Blast Furnace Slag (GGBFS)-based alkaline activated concretes, in strength class C30 and C50. In this study, the AAC is compared to Portland Cement Concrete (PCC) of a similar strength class.

1.4. Research question

The main research question is ***"What is the difference in shear behaviour of reinforced beams made of slag-based alkali-activated concrete versus Portland cement concrete, including the influence of age, shrinkage and strength class?"***

To provide an answer to the main research question, the following sub-questions will be addressed:

1. What are the differences in material properties influencing shear behaviour, namely tensile strength, elastic modulus and shrinkage, between slag-based alkali-activated concrete and Portland cement concrete mixtures?
2. What is the effect of age on the material properties and structural behaviour of slag-based alkali-activated concrete?
3. What is the effect of concrete strength class on the shear behaviour of slag-based alkali-activated concrete?

These questions will be answered by conducting a literature review, performing experimental tests and data analysis.

1.5. Outline of master thesis

The structure of this report is as follows: Chapter 2 presents the findings of the literature review, first focusing on material behaviour and then on structural behaviour. Chapter 3 describes the methodology, including the mixtures, casting process, and types of experiments included in the study. Chapter 4 discusses the experimental results. Chapter 5 provides an interpretation of the shear results, delving deeper into the different stages of shear failure, followed by comparing the material properties obtained from the shear behaviour experiments. Chapter 6 discusses the experimental results by first combining findings from the material and shear behaviour test, followed by comparing the results with literature and finally by providing the limitations of the study. Finally, Chapter 7 presents the conclusions and recommendations for further research and application of AAC in practice. Appendix A provides graphs verifying the DIC measurements against the LVDT measurements for the shear tests of all tested beams. Appendix B includes images of the tested dogbone specimens. Appendix C presents all the shear results, followed by load paths of all tested beams. Finally, Appendix D contains a comparison of the experimental shear results with existing methods, including the NEN-EN 1992-1-1, 2015 and the GSDM.

2

Literature review

2.1. What is alkali-activated concrete?

AAC is a sustainable alternative to traditional concrete, made using a binder created from industrial by-products combined with an alkaline solution. This binder can fully replace cement in the concrete mixture, making it a more environmentally friendly option.

The selection of raw materials plays a crucial role in the sustainability of AAC. To understand how AAC is produced, it is first essential to grasp the basic composition of concrete. Traditional PCC consists of two main components: aggregates and a binder. In conventional concrete, cement mixed with water acts as a binder, hardening through hydration. In contrast, AAC uses a binder composed of alkali-metal solutions, known as activators, and aluminosilicate-rich material, known as precursor (Provis, 2014).

Various activators can be used in AAC, with some of the most common being sodium hydroxide ($NaOH$), sodium carbonate (Na_2CO_3), sodium silicate (Na_2SiO_3) and aluminosilicate-rich compounds ($(AlO_4)^{5-}$) (Provis, 2014). The precursor materials are often industrial by-products, including fly ash (FA) from coal-powered plants, ground granulated blast furnace slag (GGBFS) from the steel industry, silica fume (SF) from silicon production and agricultural by-products (Nasir et al., 2024).

With a wide range of raw materials available for AAC production, the formulation significantly impacts the mechanical properties of the material. As a result, caution is necessary when comparing results from different studies. This report will specifically focus on GGBFS-based alkali-activated concretes, as GGBFS is a readily available by-product in the Netherlands from the steel industry.

2.1.1. Geopolymers

The term ”geopolymers” is often broadly used in the industry to refer to a large family of alkali-activated binders. However, geopolymers are actually a subset of alkali-activated materials that undergo polymerization, forming a rigid aluminosilicate network (Djobo, 2016, Prinsse, 2017). They primarily use low-calcium aluminosilicate precursors, such as fly ash (FA) or metakaolin, activated with alkaline solutions like sodium hydroxide and sodium silicate. This reaction produces N-A-S-H gel (sodium-aluminosilicate-hydrate).

Alkali-activated concrete (AAC), on the other hand, is a broader category that includes both geopolymers and other alkali-activated systems that may also form calcium-silicate-hydrate (C-S-H) gels, similar to traditional cement-based concrete. AAC can be made from both high-calcium (slag-based) and low-calcium (fly ash-based) materials, meaning that some AACs behave like geopolymers, while others rely on C-S-H formation(Djobo, 2016, Prinsse, 2017).

In conclusion, while all geopolymers fall under the AAC category, not all AACs are geopolymers. The key difference lies in the reaction mechanism: geopolymers rely on polymerization, while slag-based AACs behave more like traditional cementitious materials due to C-S-H formation.

2.2. Material behaviour

2.2.1. Compressive strength

When working with PCC, knowing the 28-day compressive strength is important because it forms the basis of all codes. Most material properties are correlated to 28 days compressive strength and can be determined based on it (Prinsse, 2017). However, whether a similar correlation exists between the compressive strength of AAC, and whether 28 days strength presents a safe reference for the design of AAC, is still unknown.

The compressive strength of AAC depends on the strength development, which is influenced by factors such as the quality of the precursor and activator used, the mix proportions and the curing process. When examining the strength development of slag-based AAC, it shows relatively high early strength and rapid strength development. This is due to two factors. Firstly, the fast rate of the chemical reaction at elevated pH levels contributes to higher early strength. Secondly, the dense and homogeneous interface transition zone (ITZ) results in a small strength difference between the interface transition zone and the binders, resulting in stronger material (Ding et al., 2016).

2.2.2. Tensile strength

When studying PCCs and AACs, their tensile strength is found to be very low compared to their compressive strength. As a result, concrete is not used to resist direct tensile loads. However, understanding the tensile strength is important for determining the load at which cracks will develop (Prinsse, 2017). The tensile strength of PCC can be measured through a tensile splitting test or estimated using compressive strength in combination with empirical relations. Whether a similar correlation exists for AAC is still unknown (Ding et al., 2016).

The tensile strength is the maximum stress a material can withstand well being pulled before breaking (Ouyang et al., 2024). The relationship between the characteristic compressive cylinder strength f_{ck} and the mean tensile strength f_{ctm}, as suggested by Eurocode 2 (NEN-EN 1992-1-1, 2015) is shown in equation 2.1 & 2.2.

$$f_{ctm} = 0.30 \cdot (f_{ck})^{\frac{2}{3}}, f_{ck} \leq \text{C40/60} \tag{2.1}$$

$$f_{ctm} = 2.12 \cdot \ln\left(1 + \frac{f_{cm}}{10}\right), f_{ck} > \text{C50/60} \tag{2.2}$$

The splitting tensile strength is the maximum splitting force. To obtain the tensile splitting strength a specimen is subjected to a diametrical compression. The splitting tensile strength test is mostly used for concrete, masonry and asphalt to assess their resistance to cracking and splitting forces (Shen et al., 2019). Research has shown that splitting tensile strength tests can be influenced by the factors of loading conditions and specimen size (Shen et al., 2019). The relationship between tensile splitting strength $f_{ct,sp}$ and the mean tensile strength, as suggested by Eurocode 2 (NEN-EN 1992-1-1, 2015) is shown in equation 2.3.

$$f_{ctm} = 0.9 \cdot f_{ct,sp} \tag{2.3}$$

Studies into the splitting tensile strength of AAC have been done. The study of Prinsse, 2017, Bezemer et al., 2023 and Wardhono et al., 2017 reported a decrease in tensile strength over time for AAC based on GGBFs. This is different than found for OPCC. The study of Bezemer et al., 2023 reported an increase in tensile splitting strength over time for OPCC. To the author's knowledge, no publication of a direct tensile test of AAC based on GGBFS has been made so far.

The study of Prinsse, 2017 tested the tensile splitting strength over time for slag-based (100%) alkali-activated concrete. To determine the splitting tensile strength, cubes of 100 mm^3 were tested. The tests were executed at 28, 49, 72 and 91 days. The precursor used is Blast Furnace Slag and the activator used is sodium hydroxide with deionised water and sodium silicate solution. This study reported a decrease in the tensile splitting strength of 11% at 91 days compared to the 28-day strength.

An additional study by Bezemer et al., 2023 added OPCC mixtures of similar strength as the slag-based alkali-activated concrete mixtures of the study from Prinsse, 2017. This was to compare the results of the BFS mixtures with the long-term results of OPCC mixtures. The results show that the OPCCs exhibit an increase in their tensile strengths until the tested age of 3.5 years. However, the BFS concrete shows a significant decrease of 21% in tensile splitting strength between 2 years and 5 years, while its tensile splitting strength remained relatively constant for the first 2 years.

The study of Wardhono et al., 2017 reported the tensile strength of alkali-activated slag concrete for up to 540 days. To determine the tensile strength, a splitting tensile test was executed. The precursor used is GGBFS (100%) and the activator used is sodium silicate with sodium hydroxide solution. The splitting tensile strength remained constant during the testing time.

2.2.3. Elastic modulus

The elastic modulus, or Young's modulus, is an important material property for PCC concrete, reflecting its stiffness. Typical values for the elastic modulus of PCC range from 20 GPa to 40 GPa, depending on factors like mix proportions, aggregate type and curing conditions. A higher elastic modulus indicates that the material is stiffer and will deform less under applied loads.

The relationship between the characteristic compressive cylinder strength f_{ck} and the secant modulus of elasticity of concrete E_{cm}, as suggested by Eurocode 2 (NEN-EN 1992-1-1, 2015) is show in equation 2.4.

$$E_{cm} = 22 \cdot \left(\frac{f_{cm}}{10} \right)^{0.3} \tag{2.4}$$

Studies into the elastic modulus of AAC have been done. The study of Collins and Sanjayan, 1999, reported that the elastic modulus of AAC was lower than those of OPCC. Resulting in a less stiffer material, deforming more when loads are applied. The study of Bezemer et al., 2023 and Prinsse, 2017 reported a reduction in the elastic modulus of the AAC mixtures over 695 days. This behaviour is different than fount in OPCC. The study of Bezemer et al., 2023 reported an increase in elastic modulus over time for OPCC. However, the study reported that the increase is not consistent with previously reported reductions in the elastic modulus of OPCCs under drying.

In the study of Collins and Sanjayan, 1999, the elastic modulus of cylinders with a diameter of 100 mm and a height of 200 mm was tested. The precursor used was GBFS (100%). Four different activators were included in the experimental program, namely powdered and liquid sodium silicate, hydrated lime, liquid sodium hydroxide and sodium carbonate. The results show a lower elastic modulus for AAC than for OPCC. The study suggests that the lower elastic modulus may help reduce the risk of cracking due to drying shrinkage under restrained conditions.

The study of Bezemer et al., 2023 tested prisms of 100 x 100 x 400 mm^3 at a loading rate of 0.65 MPa/s, following the method B of EN 12390-13. The precursor used is GGBFS (100%) and the activator used is sodium hydroxide solution with a sodium silicate solution. The study reported a higher elastic modulus for GGBFS-AAC compared to the elastic modulus of OPCC at 28 days. However, the elastic modulus of the AAC mixtures shows a reduction of 20% in the first 193 days. After the first 193 days, the elastic modulus remains constant up to the tested age of 5 years. This behaviour is different than found for OPCC mixtures which show an increase in elastic modulus. However, the study reported that the increase is not consistent with previously reported reductions in the elastic modulus of OPCCs under drying.

These results were in line with the study of Prinsse, 2017. This study also tested prisms of 100 x 100 x 400 mm^3 of similar AAC mixtures as the study of Bezemer et al., 2023. The results also reported a decrease over time of 13% for the AAC mixtures up to 91 days.

2.3. Shrinkage

One of the limiting factors for the application of GGBFS-based AACs is its durability (Ridtirud et al., 2011, Cartwright et al., 2015). For example, GGBFS-based AACs are characterized by significant shrinkage,

which can result in cracks. This can lead to a reduction in material performance and an increased risk of penetration of harmful substances. When investigating shrinkage in AAC, a distinction is made between autogenous shrinkage and drying shrinkage.

2.3.1. Autogenous shrinkage

Autogenous shrinkage is a reduction in the volume of concrete caused by a combination of chemical shrinkage and self-desiccation, occurring without any moisture exchange with the environment (Tang et al., 2021, van Breugel, 2023). To understand chemical shrinkage, one needs to know that there is a difference in volume between unreacted and reacted materials. As the unreacted material continues to react, its volume decreases. To keep hydrating, the material will need water. Due to diffusion, water in the capillary pores is drawn into the particles. The hydration of the cement continues. Furthermore, when concrete hardens, the outer layer of a particle will relatively quickly hydrate and form a shell. Therefore, the concrete appears solid and has stiffness and strength. The inside of the particles will continue hydrating. As the pores empty, they tend to shrink and with the resistance of the concrete, capillary stresses will build up. This process is also called self-desiccation or autogenous shrinkage. These processes take place in the cement paste uniformly across the cross-section, see figure 2.1. Autogenous shrinkages mostly take place in mixtures with a low w/c-ratio.

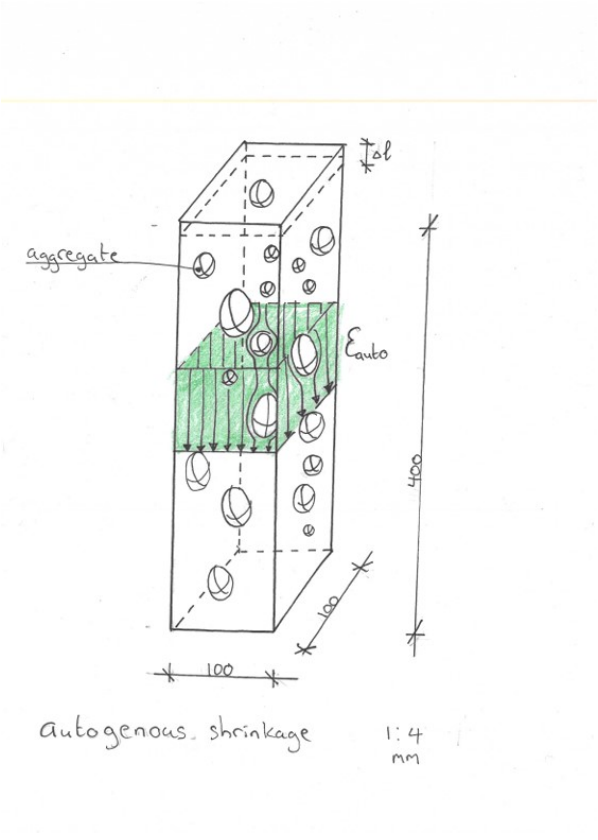

Figure 2.1: Autogenous shrinkage, concrete strains

The study of Li et al., 2020 investigates the cracking potential of AAC exposed to restrained autogenous shrinkage. In this study, the autogenous shrinkage was measured with an autogenous deformation testing machine for up to 21 days. This machine consists of a prismatic mould made from thin steel plates with external insulating materials. The size of the specimens was 1000 x 150 x 100 mm^3. The precursor used was slag (100%) and the activator used was a mixture of sodium hydroxide and sodium silicate solution in a ratio of 0.334. The results show a rapid development of autogenous shrinkage in the first 2 days. At 21 days the autogenous shrinkage of AAC based on slag reached 609 $\mu m/m$. Furthermore, a higher autogenous shrinkage was observed for AAC based on slag compared to the literature-found results for OPCC. The results also report a decrease in elastic modulus, suggesting

that this can be due to the development of microcracks resulting from the autogenous shrinkage.

2.3.2. Drying shrinkage

Drying shrinkage is the reduction in volume or contraction of hardened concrete caused by the loss of capillary moisture, which generates capillary tension within the pore structure of the cement matrix (Awoyera et al., 2022). The principle of self-desiccation is the same as described for autogenous shrinkage. The difference is that for drying shrinkage, moisture loss occurs because of exposure to the environment. Drying shrinkage is therefore higher at the surface, exposed to the environment and less in the centre, as shown in figure 2.2.

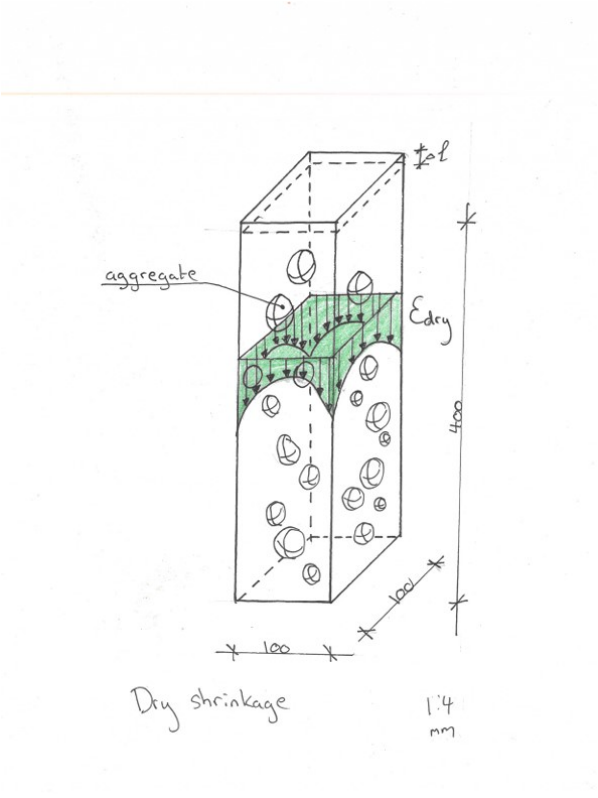

Figure 2.2: drying shrinkage, concrete strains

In the study of Cartwright et al., 2015, volumetric instability is investigated focusing on autogenous, chemical and drying shrinkage. Variable parameters in the test are four different alkali-activated mixtures, time of setting and compressive strength. The precursor used is GGBFS (100%) and the activator used is sodium hydroxide and sodium silicate. The four different mixtures consist of a different ratio of water, sodium hydroxide and sodium silicate. The elastic modulus for their GGBFS-based AAC varied from 13-21 GPA, compared to 20 GPa for OPCC. The results show that the alkali-activated slag mixtures show a higher autogenous and drying shrinkage compared to the OPCC mixture, see figure 2.3. The results show a lower elastic stiffness over time, suggesting that this can be due to the development of microcracks resulting from the shrinkage.

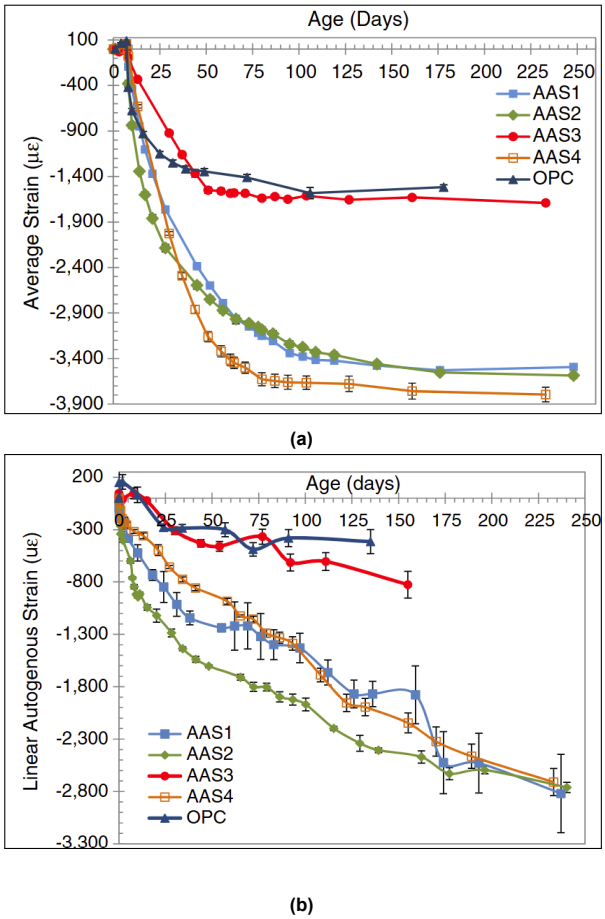

Figure 2.3: Test results obtained from the study of Cartwright et al., 2015. a) development of drying shrinkage and b) development of autogenous shrinkage

2.4. Flexural behaviour of RC beams

Although the development of the mechanical properties of AACs is becoming better understood, there is also interest in understanding the long-term structural behaviour. At the moment, limited research has been done on its long-term structural behaviour, beyond 28 days.

There are some studies that investigated at 28 days the flexural behaviour of reinforced slag-based AAC. The study of Bendapudi et al., 2017 and the study of A. Shah and C. Shah, 2017, reported that the flexural capacity of AAC, at 28 days, is higher than those of OPCC of similar strength classes.

The study by Bendapudi et al., 2017 conducts experiments, at 28 days, on twelve beams of 150 x 150 x 700 mm^3, tested on flexural behaviour with varying combinations of GGBS and Metakaolin. The beams were tested in a four-point bending test. The precursors used were GGBS (70%) and Metakaolin (30%). The activator used was a combination of sodium hydroxide solution and sodium silicate solution. The results indicate that the load-deflection behaviour of OPCC beams, containing up to 70% GGBS and 30% Metakaolin, are almost similar. However, the cracking moment was lower for AAC beams containing more than 30% GGBS. The ultimate moment capacity of the AAC beams was found to be greater than that of the OPCC beams because of higher compressive strength.

The study of A. Shah and C. Shah, 2017, focuses on understanding the structural behaviour and crack development pattern of geopolymer concrete beams. Beams (150 x 150 x 600 mm^3) were reinforced with either flexural and shear reinforcement or only flexural reinforcement. The experimental test executed is a four-point bending test until the ultimate failure load. The precursors used are GGBS (30%) and fly ash (70%) and the activator used is sodium hydroxide and sodium silicate. The results show that the beams from geopolymer concrete, cured at ambient temperature, carried 15% more load than

those of OPCC at 28 days. The displacements of the OPCC beams measured before failure were lower than those of geopolymer concrete beams.

Recently, some studies started to focus on long-term behaviour. Prinsse, 2017, investigated the development of the flexural behaviour of reinforced beams, 150 x 200 x 1900 mm^3, up to 151 days. The beams were tested in a four-point bending test. The precursor used is BFS (100%). The activators used in this study are sodium hydroxide and sodium silicate. The results indicate that the decrease in the elastic modulus and tensile splitting strength, as discussed in Section 2.2, did not significantly affect the load-carrying capacity of the reinforced AAC beams. The structural behaviour of the reinforced beams of AAC shows no effect of the change in material properties over time. The papers suggested that the observed decrease in material properties over time might be temporary due to eigen stresses caused by moisture losses, but further research is necessary.

In continuation of Prinsse, 2017, Bezemer et al., 2023 investigated results from previous experiments of the flexural strength of AAC up to 151, adding results on crack widths, crack load and bending stiffness. From this analysis, differences between the AAC based on slag and OPCC are observed. The reinforced GGBFS-based AAC beams showed larger crack widths than those of OPCC at the age of 34 days. Furthermore, the bending stiffness of the studied flexural test of AACs showed a decrease over time.

2.5. Shear behaviour of RC beams

Furthermore, the structural shear behaviour of AAC is investigated, as it can be a critical factor in the design of bridges and slabs. This study aims to enhance the understanding of the shear behaviour of slag-based AAC. To provide a solid foundation, this section will first offer a more detailed overview of shear behaviour in general.

It is important to note that shear behaviour remains a topic of ongoing discussion. One of the key debates revolves around the mechanisms of shear force transfer in cracked concrete beams and their interactions. Experimentally isolating each mechanism poses significant challenges, making it a complex area of research.

2.5.1. Failure mechanism

A reinforced concrete beam without shear reinforcement can fail in three types of failure modes: shear-tension failure, shear-flexure failure and shear-compression failure (Y. Yang, 2014; Sarkhosh, 2014).

Shear-tension failure

Shear-tension failure is common in members with thin webs, such as prestressed hollow-core slabs or T-beams (Sarkhosh, 2014). The final failure in the beam will be due to the anchorage failure of the tension reinforcement. The shear cracks typically develop in the web of the beam, while the top and bottom portions may remain uncracked. Figure 2.4 shows a typical cracking pattern for a beam in shear-tension failure.

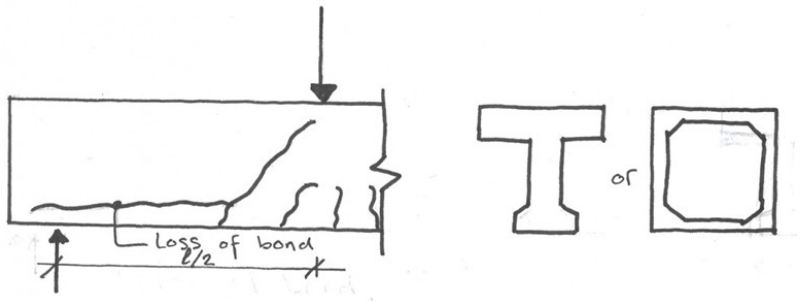

Figure 2.4: Cracking pattern of a beam with shear-tension failure (Samad et al., 2016)

Shear-compression failure

Shear-compression failure occurs when the concrete strut is crushed due to excessive shear forces in the compression zone. This can lead to a diagonal compression failure, often resulting in a sudden and brittle failure, particularly near the support region. Figure 2.5 illustrates a typical cracking pattern for a beam experiencing shear-compression failure.

This type of failure is common in beams with a low span-to-beam-depth ratio (l/d < 2.5) and is often referred to as arch action. In such cases, shear force transfer occurs through a changing lever arm while internal forces remain constant. This mechanism is frequently modelled using the strut-and-tie method (Sarkhosh, 2014; Y. Yang, 2014).

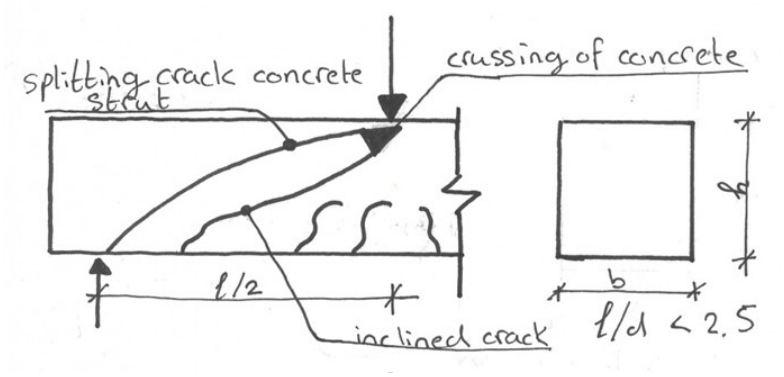

Figure 2.5: Cracking pattern of a beam with shear-compression failure (Y. Yang, 2014)

Shear-flexural failure

Shear-flexural failure mode involves a combination of bending (flexural) and shear stresses. It usually occurs in the region between the support and mid-span, where both bending and shear forces are significant. Flexural cracks can propagate and when shear cracks intersect them, the beam fails (Y. Yang, 2014). Figure 2.6 shows a typical cracking pattern for a shear-flexural failure. Flexural-shear failure is a common failure mode in normal reinforced concrete members (Y. Yang, 2014). The mechanism of this failure occurs when the shear force is distributed over a constant distance (lever arm), while the internal forces vary along the beam's length. This is typically observed in beams with a l/d ratio $\geq$ 2.5.(Sarkhosh, 2014; Y. Yang, 2014).

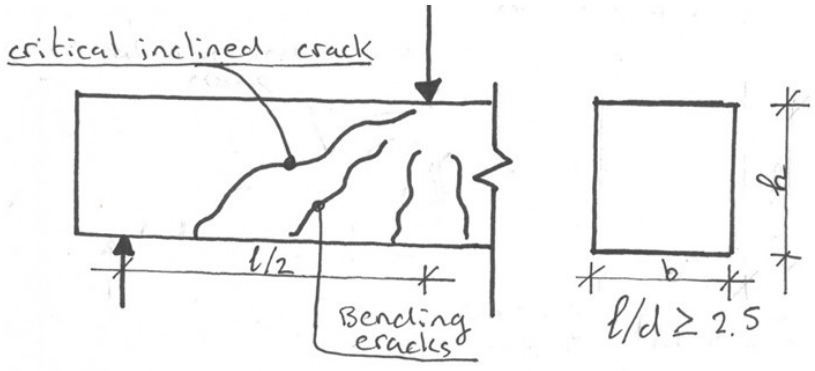

Figure 2.6: Cracking pattern of a beam with shear-flexural failure (Y. Yang, 2014)

From now on this report will mainly focus on shear-flexural failure.

2.5.2. Mechanisms of shear transfer

Y. Yang, 2014 and ASCE-ACI Committee 445, 1998 report that, while the failure mechanism in beams with flexural cracks remains a topic of discussion, it is widely accepted that four distinct mechanisms can transfer shear force in a cracked concrete beam: shear transfer in uncracked concrete, aggregate

interlock, dowel action and residual tensile stresses in cracks. The different mechanisms of shear transfer are shown in Figure 2.7. Nevertheless, there is no agreement yet on how those components influence the overall shear failure process and which one is the governing mechanism in the failure process.

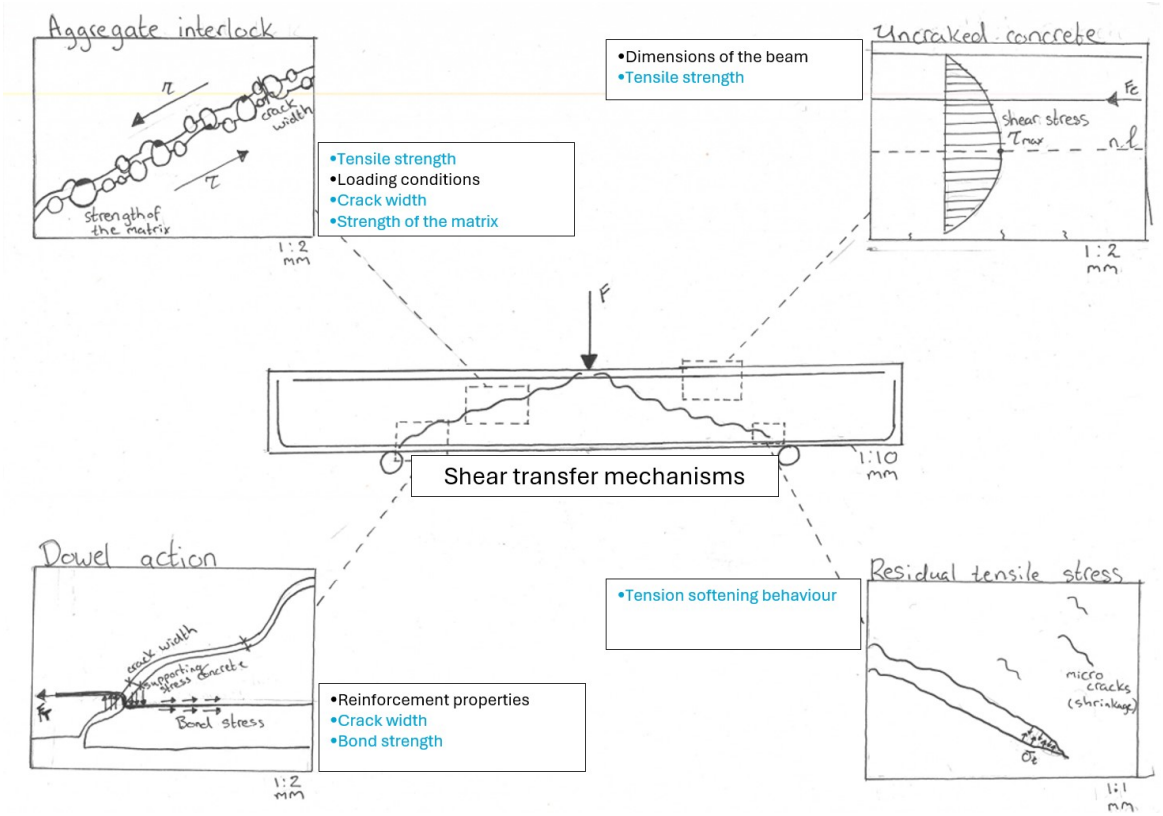

Figure 2.7: Mechanisms of shear transfer with influencing properties listed. Properties highlighted in blue can be influenced when applying AAC concrete.

Uncracked concrete

Firstly, the failure mechanism of uncracked concrete strongly depends on the uncracked portion of the beam, specifically the top section known as the compression zone (Fenwick and Paulay, 1968). In this region, the stress distribution follows a parabolic curve, with the highest shear stress occurring near the neutral axis (see Figure 2.8).

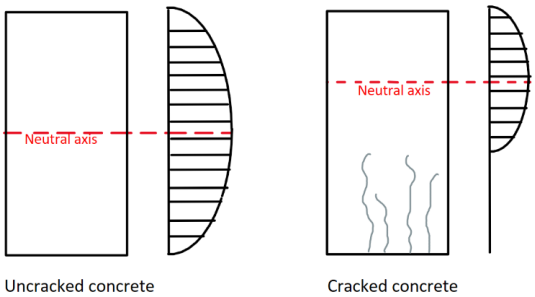

Figure 2.8: The stress distribution in the uncracked concrete.

The concrete's compression zone resists shear forces through compressive stresses, which are distributed according to the parabolic or similar elastic curve described by Mörsch in 1909 (Mörsch, 1909).

The Mörsch shear formula, Equation 2.5, is an empirical equation making certain assumptions about the distribution of shear stress derived from observations and experimental data (Fenwick and Paulay, 1968).

$$V_c = \frac{f_{ck} \cdot b \cdot d}{\gamma_c} \tag{2.5}$$

Where V_c is the shear resistance of the concrete in N, f_{ck} is the characteristic compressive strength of the concrete in MPa, b is the width of the beam in mm, d is the effective depth of the beam in mm and γ_c is the partial safety factor for concrete.

Aggregate interlock

Second, the failure mechanism of aggregate interlock involves the surfaces of broken aggregate particles. These surfaces are typically rough and irregular in shape. This roughness generates frictional resistance along the crack faces, helping to transfer shear forces across the crack and providing some shear capacity even after cracking has occurred. Aggregate interlock depends on factors such as the size and shape of the aggregate, the width of the crack, the strength of the matrix between the particles, and the overall loading condition (Huber et al., 2019).

The general shear resistance due to aggregate interlock can be approximated using Equation 2.6.

$$V_{ai} = \tau_c \cdot A_s \tag{2.6}$$

Where V_{ai} is the shear resistance provided by aggregate interlock in N, τ_c shear stress at the crack (based on concrete strength and crack width) in MPa and A_s is the surface area of the crack that contributes to shear transfer in mm^2.

The factor τ_c in the formula is calculated by multiplying the concrete compressive strength by a factor k, which is derived from empirical data. This factor accounts for crack width, loading conditions, and concrete properties. In this study, crack width is particularly important, as an increase in crack width reduces aggregate interlock. This occurs because a wider crack creates more space between the aggregates, limiting their ability to interlock. Additionally, the strength of the matrix plays a crucial role when investigating shear behaviour in AAC. A stronger matrix enhances bonding between the aggregate and particles (Huber et al., 2019). If the bonding between the aggregate and cement paste exceeds the strength of the aggregate, the crack will propagate through the aggregates, creating a smoother surface and ultimately leading to a loss of aggregate interlock.

Dowel action

Firstly, the failure mechanism of dowel action is the mechanism by which longitudinal reinforcement will resist the slipping and opening of cracks across the reinforcement. This resistance results in a combination of bending and shear forces on the longitudinal reinforcement (Jeli et al., 1999).

The general shear resistance due to dowel action can be approximated by equation 2.7.

$$V_d = A_s \cdot f_y \cdot d \cdot s \tag{2.7}$$

Where V_d is the shear resistance due to dowel action in N, A_s area of the longitudinal reinforcement crossing the crack in mm^2, d is the effective depth of the member in mm and s is the spacing of the reinforcement bars in mm.

The influencing factors on dowel action are crack width, concrete properties and steel properties. A wider crack may reduce the engagement of the reinforcement with the surrounding concrete, thereby decreasing the effectiveness of dowel action. Also, the bond strength between the concrete and the rebar is important, to resist the tendency for the steel to slip (Jeli et al., 1999).

Residual tensile stress

Finally, the failure mechanism of residual tensile stress in cracks refers to the remaining tensile stress that exists across a crack in concrete after the material has cracked. This phenomenon is possible in cracks between 0.1 mm - 0.6 mm. Influencing factors concrete tensile strength and softening behaviour (Y. Yang, 2014).

2.5.3. Development of flexural-shear cracks

Initial flexural cracks

Initially, a crack will appear on the tension face of the beam due to the bending moment causing tensile stress in the outer fibres of the beam, see Figure 2.9.

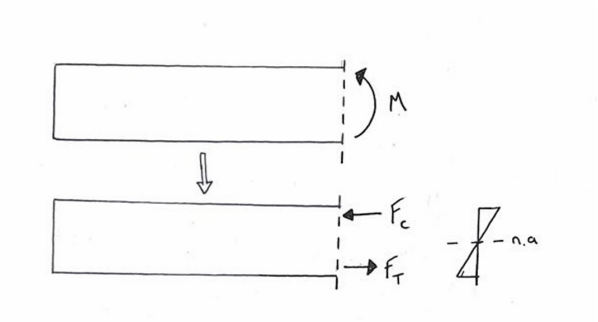

Figure 2.9: Bending moment resulting in a tensile and compression force on the cross-section

When the bending moment causes the tensile stress to exceed the tensile strength of the concrete, vertical cracks will form around the mid-span of the beam. Cracking of the beam results in upward movement of the neutral axis (Y. Yang, 2014). See Figure 2.10.

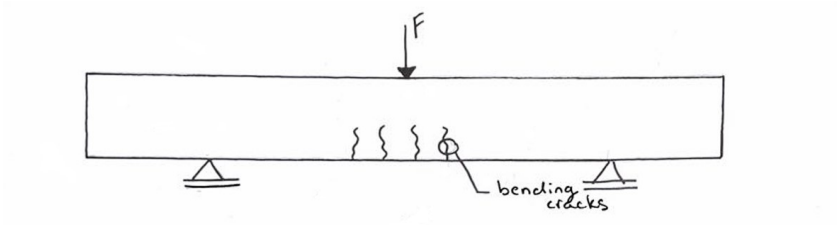

Figure 2.10: Development of initial flexural cracks

Inclination of the flexural crack under shear

As the load increases, shear forces near the supports generate diagonal stresses around the neutral axis. These stress paths are inclined at an angle. Cracks develop along these principal stress paths, leading to inclined cracks that are characteristic of combined shear and bending failure, see figure 2.11

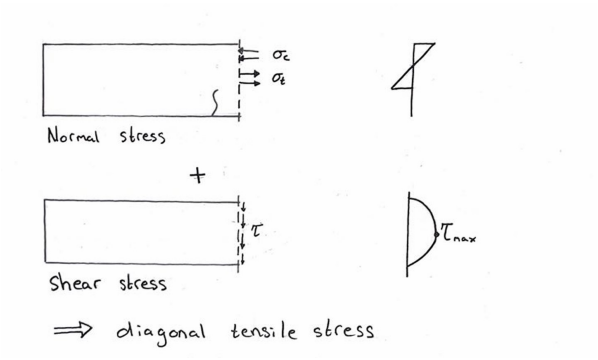

Figure 2.11: Inclined cracks are characteristic of combined shear and bending failure.

The crack patterns follow the principal stress paths (Y. Yang, 2014).See Figure 2.12.

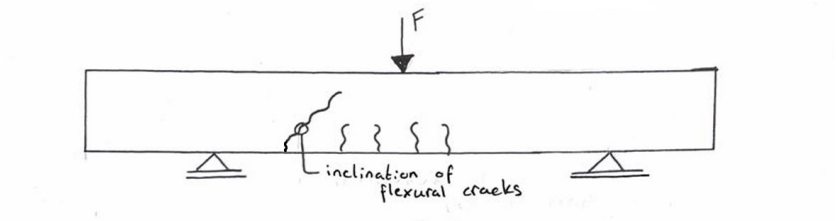

Figure 2.12: Inclination of the flexural cracks under shear.

crack stabilization stage

After shear cracks are formed, the beam still can increase the load capacity. This extra capacity is formed by the concrete in the compressive zone, dowel action, aggregate interlock and residual stresses. See Figure 2.13.

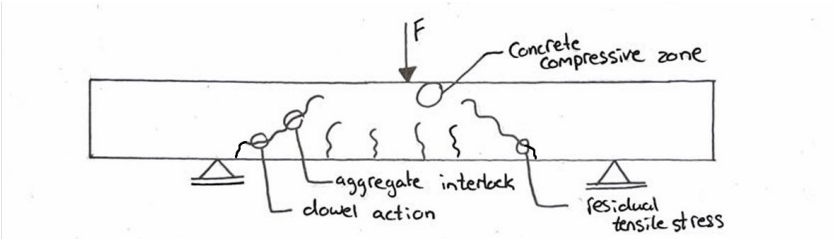

Figure 2.13: Development of crack stabilization stage.

Failure mechanisms

As the load continued to increase, two things happened: 1) the crack openings around the tips of the shear crack continued to grow and 2) the shear cracks expanded vertically. When these cracks extend into the compression zone, it results in a loss of concrete capacity. Additionally, when these cracks extend onto the longitudinal reinforcement, dowel cracking may occur due to dowel forces. Vertical crack expansion leads to a loss of aggregate interlock. Resulting in the beam failing. See Figure 2.14.

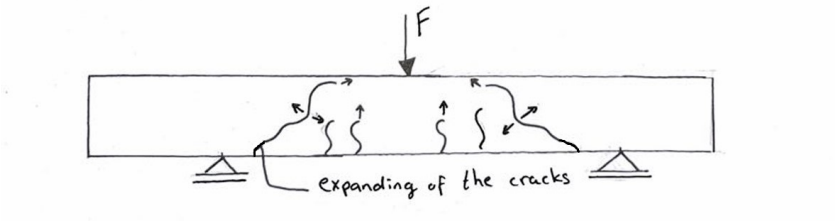

Figure 2.14: Failure of the beam due to opening and widening of the cracks.

Residual capacity

After failure, the load does not increase, but the beam's load-carrying capacity is not entirely lost. A possible explanation for this can be found in the theories presented by Kani, 1964. According to this theory, once the concrete's resistance to cracking is overcome, a tied arch structure remains. As the cracks widen and lengthen, the compressive zone diminishes. The formation of flexural cracks transforms the reinforced concrete beam into a comb-like structure, where the compressive zone acts as the backbone of the comb, and the concrete in the tensile zone represents the comb's teeth. As this process continues, the stress in the compressive zone increases, primarily due to the reduction in the compressive zone's area caused by the cracks. See Figure 2.15.

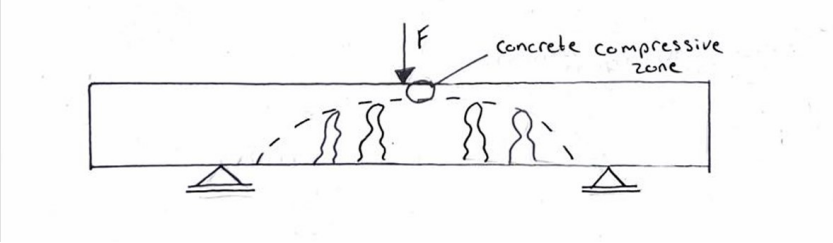

Figure 2.15: Residual capacity, arch structure.

2.5.4. Shear in AAC beams

Studies have been conducted on the shear behaviour of AAC. These studies indicate that the shear strength of AAC, at 28 days, is similar to those OPCC (Liu et al., 2023, Wu et al., 2020, Visintin et al., 2017).

In the study of Liu et al., 2023, the shear transfer behaviour of AAC was investigated by executing push-off tests. 32 Z-shaped specimens were tested, with varying strength class (C30, C50 and C70), shear reinforcement ratio (0.84%, 1.31% and 1.88%) and shear plane size (120 x 100 mm^2, 120 x 200 mm^2 and 120 x 300 mm^2). The precursors used are slag (70%) and Fly ash (30%) and the activators used are sodium hydroxide and sodium carbonate. The shear strength of the reinforced AAC plane was similar to that of PCC. However, AAC planes cracked earlier due to their higher presence of micro-cracks. The shear strength in the reinforced AAC plane increased with the increase in concrete strength. The increase of shear plane width and depth would lead to a decrease in shear strength.

In the study of Wu et al., 2020, the shear behaviour is investigated by testing 18 reinforced slag-based geopolymer concrete beams and 3 OPCC beams of 200 x 300 x 2250 mm^3. Variable parameters in the test were concrete strength (40, 60 and 80 [MPa]), longitudinal reinforcement ratio (1.50, 1.82 and 2.72%), shear span-to-depth ratio (1.5, 2.5 and 4) and beam depth (300 and 400mm). The precursor used is slag (100%, 0%, 70%) and fly ash (0%, 100%, 30%) and the activator used is sodium hydroxide and sodium carbonate. The shear strength of the geopolymer specimens where 94.3% - 99.1% of the tested OPCC beams. The crack distribution and failure mode were comparable.

Furthermore, up to the author's knowledge, no study investigated the shear strength beyond its standard testing age, 28 days.

2.6. Reasearch gap

From the literature review executed the following conclusions are obtained:

- The strength development of slag-based AAC shows relatively high early strength and rapid strength development, due to the fast polymerisation reaction. Furthermore, AAC shows a dense and homogeneous ITZ resulting in a strong material.
- The 28-day compressive strength forms nowadays the basis of all codes. Other material properties can be estimated using this 28-day strength. If existing relationships and codes can be used for AAC is questionable, because AAC shows a difference in material properties compared to OPCC.
- Studies reported a decrease in tensile strength over time for slag-based AAC. This behaviour is different than found in OPCC. OPCC shows an increase in tensile splitting strength over time. There are no studies found on the direct tensile strength development of AAC.
- Studies reported a lower elastic modulus for AAC concrete compared to OPCC, at 28 days. Furthermore, studies reported a reduction in the elastic modulus of slag-based AAC over 695 days.
- Studies have reported an increase in drying and autogenous shrinkage for slag-based AAC. Higher shrinkage can result in de development of microcracks, due to internal stresses.
- Studies that did investigate the flexural behaviour of slag-based AAC reported a higher flexural capacity of AAC, at 28 days, compared to OPCC. The study of Prinsse, 2017 that investigated the long-term flexural capacity of AAC over 91 days reported some loss of flexural capacity over

time. Also, AAC beams showed larger crack widths when tested at later ages, tested up to 33 days, and the bending stiffness of the studied AACs showed a decrease over time, reported in the study of Bezemer et al., 2023.

- Some studies investigating the long-term properties, beyond the 28 days, of AAC. Those studies reported a decrease in mechanical properties over time (Bezemer et al., 2023; Prinsse et al., 2020). This behaviour is different than found in OPCC, there the properties show an increase over time (Bezemer et al., 2023). These studies included compressive strength, flexural strength, tensile splitting strength and elastic modulus.
- When investigating the shear mechanisms, differences in behaviour for AAC can be expected due to literature results on shrinkage behaviour and crack width, as well as uncertainties regarding tensile strength, matrix strength and bond strength.

This report focuses on the long-term shear behaviour of slag-based AAC. Table 2.1 provides an overview of the material properties associated with different shear failure mechanisms. For each influencing factor, the table indicates whether similarities or differences are expected between AAC and PCC. The boundary conditions beam geometry, loading conditions, and reinforcement properties are kept consistent for all tested RC beams.

Table 2.1: Summary of the comparison of shear transfer mechanisms in AAC and PCC

Mechanism of shear transfer	Influencing factors	PCC vs AAC
Shear stress in uncracked concrete	• Tensile strength	Differences hypothesised
Aggregate interlock	• Crack width	Differences hypothesised
	• Tensile strength	Differences hypothesised
	• Strenght of the matrix	Differences hypothesised
Dowel action	• Crack width	Differences hypothesised
	• Bond strength	Differences hypothesised
Residual tensile stress	• Shrinkage	Differences hypothesised
	• Tension softening behaviour	Differences hypothesised

Comparing the mechanism of shear transfer in AAC beams and PCC beams:

- Shear stress in uncracked concrete depends on the beam dimensions and tensile strength. The beam dimensions are expected to be similar for both types of concrete. According to the literature, the tensile strength of concrete decreases over time, which can reduce the capacity of uncracked concrete to handle shear stress. Concrete with higher tensile strength is better able to resist tensile stresses, resulting in fewer or delayed cracks.
- Aggregate interlock relies on tensile strength, crack width, the strength of the matrix and loading conditions. While the loading conditions are similar for both types of concrete, crack width and the strength of the matrix are interesting factors to investigate. Based on material properties found in the literature, a higher matrix strength is expected, leading to a stronger ITZ. This can result in smoother cracks and, consequently, a loss of aggregate interlock. Additionally, the literature indicates that AAC exhibits wider cracks, which could further contribute to a reduction in aggregate interlock.
- Dowel action is influenced by the properties of the reinforcement, bond strength and crack width. The properties of the reinforcement are expected to remain similar for both types of concrete. However, based on the literature, the bond strength of AAC is expected to be higher than that of PCC, while the crack widths in AAC are anticipated to be larger than those found in PCC. Higher bond strength can enhance dowel action, but wider cracks may reduce its capacity.
- Residual tensile stress depends on shrinkage and the tension-softening behaviour of the beams. According to the literature, AAC exhibits increased autogenous and drying shrinkage. This increase in shrinkage can lead to the formation of microcracks caused by internal stresses, particularly when the concrete is restrained.

From the literature review, it can be concluded that only a limited number of studies have investigated the shear strength of AAC and, to the best of the author's knowledge, none have examined its shear

strength beyond the standard testing age of 28 days. However, when considering the long-term material properties of AAC and their influence on the mechanisms of shear transfer, differences in the shear behaviour of AAC compared to OPCC can be anticipated.

Studies on the long-term material properties of AAC have primarily focused on compressive strength, tensile splitting strength and elastic modulus. These studies report a decrease in tensile strength and elastic modulus over time. Additionally, they highlight higher autogenous and drying shrinkage, which can lead to increased internal stresses due to the longitudinal reinforcement in shear beams. Furthermore, a stronger bond in the interfacial transition zone (ITZ) of AAC is reported, which can result in reduced aggregate interlock. From flexural failure tests larger crack widths have been reported at later testing ages, which can negatively affect both aggregate interlock and dowel action.

Considering the mechanisms of shear transfer, it can be assumed that the long-term shear strength of AAC will decrease over time. This is because tensile properties and bond strength are critical factors that significantly influence shear transfer in AAC.

3

Methodology

3.1. Experimental overview

The experimental study focuses on understanding the material behaviour of AAC. The tests include measurements of compressive strength, splitting tensile strength, direct tensile strength and the elastic modulus. Additionally, to explore the structural shear behaviour of AAC, shear beams will be tested both with and without stirrups. To assess the long-term development of the material and structural behaviour, tests will be conducted at 28 days and 6 months (183 days). Table 3.1 provides an overview of the experimental program. It is important to note that some tests were conducted by Guanzhi Liu and Jelle Bezemer, who shared their experimental results for this report.

Table 3.1: Overview of experimental programme. Tested by: Guanzhi Liu, Jelle Bezemer

Type of test		Testing age	S-AAC-C30	S-AAC-C50	S-PCC-C30	S-PCC-C50
Compressive strenght		28 days	12 Cubes	14 Cubes	6 Cubes	6 Cubes
		183 days	6 Cubes	6 Cubes	3 Cubes	3 Cubes
Tensile strenght	Splitting tensile	28 days	6 Cubes	3 Cubes	2 Cubes	3 Cubes
	Direct tensile	28 days	4 specimens	4 specimens	4 specimens	4 specimens
		183 days	4 specimens	4 specimens	4 specimens	4 specimens
Elastic modulus		28 days	6 Prisms	6 Prisms	3 Prisms	3 Prisms
		183 days	3 Prisms	3 Prisms	3 Prisms	3 Prisms
Shrinkage	Autogenous shrinkage	1 - 183 days	3 specimens	3 specimens	3 specimens	3 specimens
	Drying shrinkage	28 - 183 days	3 specimens	3 specimens	3 specimens	3 specimens
Shear test	Stirrups	28 days	1 beam	1 beam	1 beam	1 beam
	Without stirrups	28 days	2 beams	2 beams	2 beams	2 beams
	Without stirrups	183 days	1 beam	1 beam	1 beam	1 beam

3.2. Mixture designs

The study includes two AAC mixtures with different strength classes, namely S-AAC-C30 and S-AAC-C50. The precursor for both mixtures is GGBFS, for the chemical composition of the precursor, see Table 3.3. The activator used for both mixtures is an alkaline solution consisting of a hydroxide solution mixed with a sodium silicate solution. The resulting solutions had a silica modulus of 0.5 for C30 and 0.95 for C50, respectively. Both solutions had 4.5 wt.% NaO. The solutions were prepared 24 hours in advance. For comparison, two PCCs with similar strength classes are included in the study, namely S-PCC-C30 and S-PCC-C50. The mixture designs for the AACs and PCCs mixtures are presented in Table 3.2.

Table 3.2: Mix designs for the studied AACs and PCCs

Ingredients	**S-AAC-C30** $[kg/m^3]$	**S-AAC-C50** $[kg/m^3]$	**S-PCC-C30** $[kg/m^3]$	**S-PCC-C50** $[kg/m^3]$
CEMIII/B 42.4N	-	-	381	426
GGBFS	400	400	-	-
liquid	200	200	183	165
Sand (0.125-0.25 mm)	130	130	130	130
Sand (0.25-0.50 mm)	346	346	346	346
Sand (0.5-1 mm)	102	102	102	103
Sand (1-2 mm)	71	71	71	71
Sand (2-4 mm)	63	63	63	63
Sand (4-8 mm)	75	75	75	75
Gravel (4-16 mm)	947	947	947	947
Absorbed liquid	11.8	12.2	10.4	10.4

Table 3.3: Chemical composition of GBFS and CEMIII/B, defined by X-ray fluorescence results by Nedeljković et al., 2019

	SiO_2	Al_2O_3	CaO	MgO	Fe_2O_3	S	Na_2O	K_2O	TiO_2	P_2O_5	LOI
GGBFS	35.5	13.5	39.8	8.0	0.6	1.0	0.4	0.5	1.0	0.0	-1.3
CEMIII/B	30.0	11.0	45.0	7.0	1.3	1.9	0.4	0.5	0.9	0.6	0.1

3.3. Casting process

Important safety measures that have been taken during the concrete casting process are as follows:

- Dust and fine particles are generated during dry mixing. Protective masks are worn to prevent inhalation of these particles. A ventilator tube is positioned near the mixer opening during the dry mixing process.
- Alkaline activators (and wet concrete in general) may cause skin burns. To protect against this, rubber gloves, lab coats, facial masks, and plastic face shields are worn when handling the activator or casting concrete.

Firstly, in the preparation phase, all materials must be prepared and placed by hand before the casting can take place. This ensures that the casting process runs smoothly and quickly. The activator is prepared 24 hours before the casting begins and is placed in a room with controlled laboratory conditions, maintaining a temperature of 20°C. Additionally, the moulds required for the cast are cleaned, and it is important to lubricate the parts. For OPCC moulds, oil is used, whereas for AAC moulds, Vaseline is applied.

Secondly, for the casting process, the first step is to gather all the necessary equipment for the cast, including the mixer, shovels, scoops, and wheelbarrows. Next, the mixing process begins by adding all the dry materials, sand, and gravel, into the mixer. Mixing continues until a homogeneous distribution is achieved. Once the dry materials are thoroughly mixed, the liquid is added gradually in small increments, and the mixing continues until a consistent mixture is obtained. For OPCC mixtures, the liquid used is water, while for AAC mixtures, the liquid used is the activator. The mix is then poured into the wheelbarrows, from which the moulds are filled. After filling the moulds halfway, vibration begins. The moulds are then filled completely, and the vibration continues until no more air can be removed. After finishing filling the moulds, they are covered with plastic film and left for 24 hours.

Since concrete hardens quickly, with the initial set occurring within 45 minutes, the casting process must be completed quickly. Equipment must be cleaned immediately after casting.

Finally, after 24 hours, all specimens are demoulded and placed into the fog room for 28 days. The temperature of the fog room is 20°C, and the relative humidity is >95%. After 28 days, half of the specimens are tested, while the other half is placed in a room with laboratory conditions, a temperature of 20°C, and a relative humidity of 55%.

3.4. Material behaviour

3.4.1. Compressive strength

The compressive strength of the studied concretes is determined from a triplicate of 150 mm cubes (Figure 3.1), using a loading rate of 13.5 kN/s, following NEN-EN 12390-3, 2019.

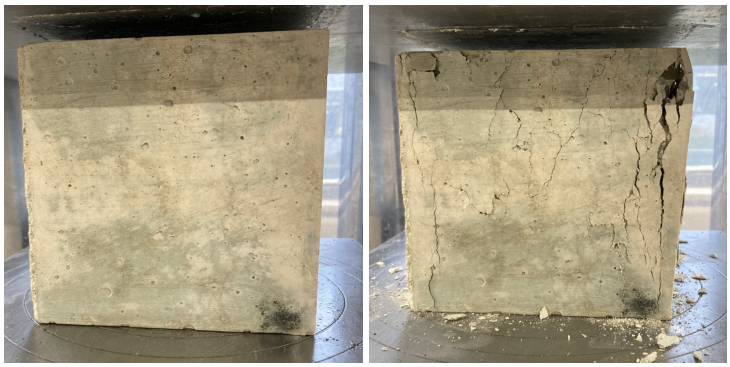

(a) (b)

Figure 3.1: Testing the compressive strength where a) before testing and b) after testing.

The compression strength will be determined at 28 days and 6 months. The compressive strength can be calculated using the formula 3.1.

$$f_c = \frac{F}{A_c} \tag{3.1}$$

Where f_c is the compressive strength in MPa, F is the maximum load at failure in N and A_c is the cross-sectional area on which the compressive force acts in mm^2.

3.4.2. Tensile strength

Splitting tensile strength

To determine the splitting tensile strength of the mixtures a triplicate of 150 mm cubes was loaded using packing strips made of hardboard of 3 x 10 x 194 mm^3 (h x w x l), see Figure 3.2. The test was executed with a constant loading rate of 2.1 kN/s, according to the standard NEN-EN 12390-6, 2023.

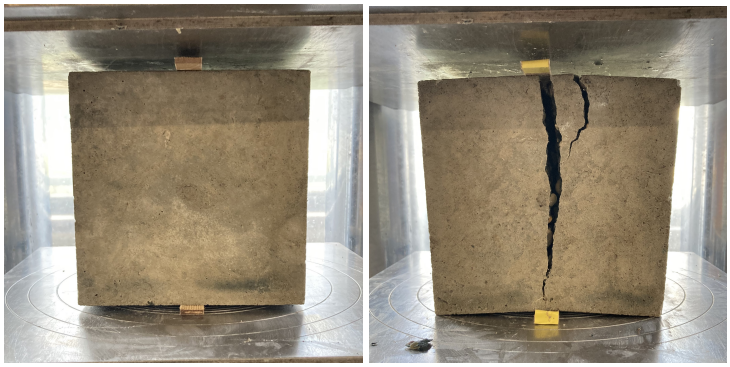

(a) (b)

Figure 3.2: Testing the tensile splitting strength where a) before testing and b) after testing.

The splitting tensile strength will be determined at 28 days and 6 months. The splitting tensile strength can be calculated using the formula 3.2.

$$f_{ct} = \frac{2 \cdot F}{\pi \cdot L \cdot d} \tag{3.2}$$

Where f_{ct} is the tensile splitting strength in MPa, F is the maximum load at failure in N, L is the length of the specimen in mm and d is the designated cross-sectional dimension in mm.

Direct tensile strength

For the tensile test, dogbone-shaped specimens were tested directly under tension (Figure 3.3). The test was conducted using the Hordijk setup, a specially designed testing rig for evaluating glued dogbone-shaped specimens under uniaxial tension. This setup features a guiding system on top and four load cells at the bottom, to ensure non-rotating loading platens. A loading rate of 3.7 µm/s was applied. Each test round consists of 4 specimens. The first specimen is tested until failure, while the remaining three are subjected to loading cycles at 10% to 33% of their expected capacity, using a loading rate of 0.6 kN/s. After this, the specimens are unloaded and then tested under strain control until failure. Data is collected through jack and with Linear Variable Data Transformers (LVDTs).

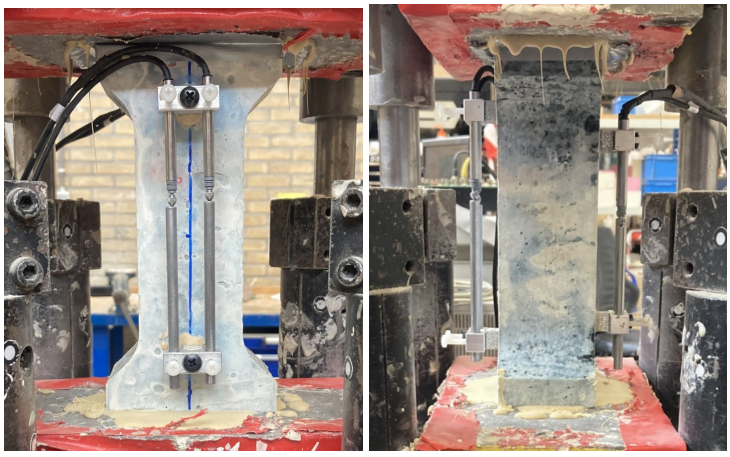

(a) (b)

Figure 3.3: Tensile test with dogbones-shaped specimens. a) front view and b) side view.

In total 16 tensile test specimens are cast, 8 specimens of mixture S-PCC-C30 and 8 specimens of mixture S-AAC-C30. The dimensions of the concrete dogbones are 210 x 100 x 60 $[mm^3]$, see figure 3.4. In total, 4 specimens for the mixtures S-PCC-C30 and S-AAC-C30 are tested at 28 days and 4 specimens at 6 months. For the mixtures S-PCC-C50 and S-AAC-C50 also 4 specimens are tested at 28 days and 6 months by Jelle Bezemer. For an overview of the experimental program see table 3.1.

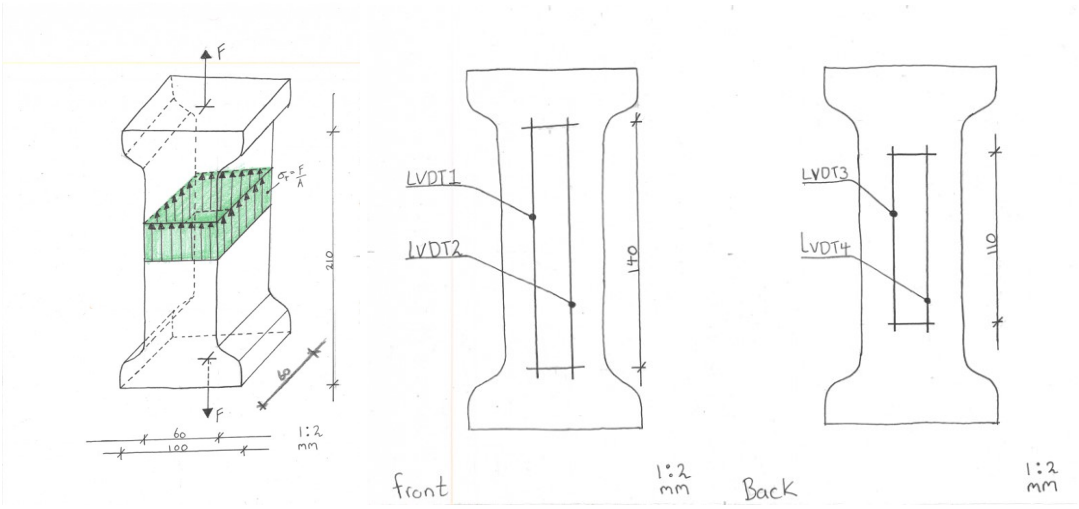

(a) (b)

Figure 3.4: Drawings of the specimens for the direct tensile test. a) 3D anticipated concrete strains before reaching peak load in direct tensile test and b) front and back drawings

3.4.3. Elastic modulus

To determine the elastic modulus of the mixtures, prisms measuring 100 $\times$ 100 $\times$ 400 mm^3 are tested in compression. A load-controlled test is conducted using a loading rate of 1 kN/s. The prisms are tested in cycles: three cycles at $5\% - 10\% f_{cm,\text{prisms}}$ and three cycles at $10\% - 33\% f_{cm,\text{prisms}}$. After the cycles are completed, the loading rate is reduced to 3.7 $\mu m/s$ and the prism is tested until failure. Following method B of NEN-EN 12390-13, 2021. The compressive strength of the prism is calculated using the formula 3.3.

$$f_{cm,\text{prisms}} = \frac{\alpha \cdot f_{cm,\text{cube,150mm}}}{\beta} \tag{3.3}$$

Where α is the conversion factor for slenderness ($h/b = 4$) and β is the conversion factor for size effect. For AAC, $\alpha_{s-\text{aac}} = 0.74$ and $\beta_{s-\text{aac}} = 0.87$ are used and for PCC, $\alpha_{s-\text{pcc}} = 0.78$ and $\beta_{s-\text{pcc}} = 0.87$ are used. These factors have been experimentally established by Jelle Bezemer.

3.5. Shrinkage

3.5.1. Autogenous shrinkage

Autogenous shrinkage is determined from a triplicate of sealed prismatic specimens. These prisms (100 x 100 x 400 mm³) were sealed 24 hours after casting and instrumented with two measurement clocks (Figure 3.5 and Figure 3.6). The seal was made out of 3 layers of plastic film and 2 layers of aluminium bitumen tape and aluminium tape. Measurement clocks are used to report the elongation or shrinkage of the specimens in mm. Additionally, the weight of the samples was reported. Furthermore, 4 prisms (2 of AAC and 2 of PCC) had a thermocouple embedded to track the development of the heat evolution of the concrete in the first 28 days.

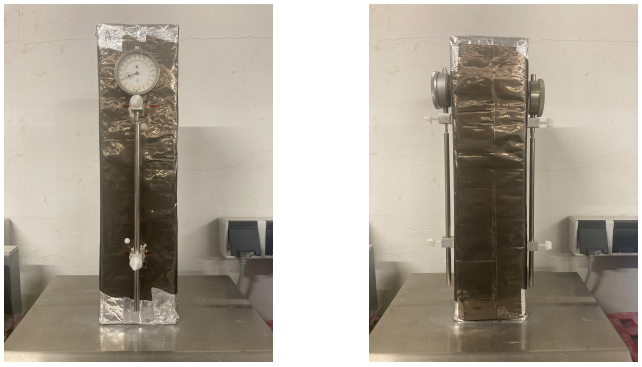

(a) (b)

Figure 3.5: Autogenous shrinkage, sealed specimens. a) front view and b) side view.

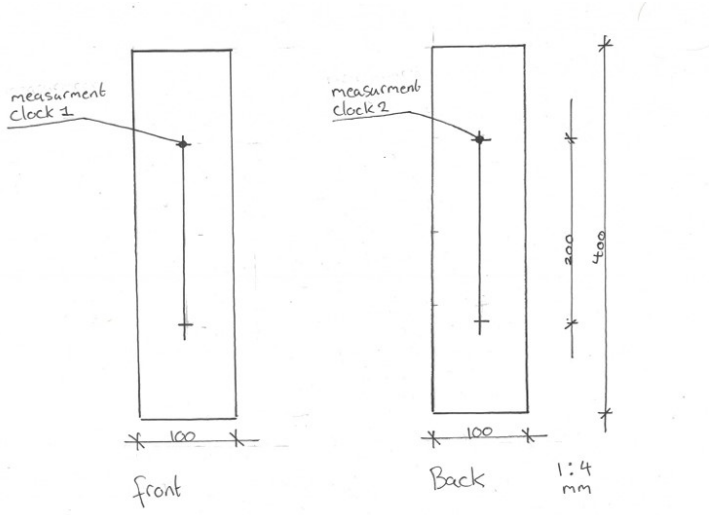

Figure 3.6: Dimensions of the shrinkage specimens and placement of the measurement clocks.

In total 6 specimens are tested for autogenous shrinkage. 3 of the mixture S-PCC-C30 and 3 of the mixture S-AAC-C30. The test is also done for 3 specimens of mixture S-PCC-C50 and 3 specimens of mixture S-AAC-C50 by Jelle Bezemer. The measurements start 1 day after casting and continue for up to 6 months.

Autogenous shrinkage was determined by eliminating the temperature changes from the measurement data (See equation 3.4).

$$\varepsilon_{autogenous} = \varepsilon_{measured\ data} - \varepsilon_{thermal} \tag{3.4}$$

Where $\varepsilon_{thermal}$ was obtained by using equation 3.5.

$$\varepsilon_{thermal} = \text{CTE} \cdot \Delta T \tag{3.5}$$

The coefficient of thermal expansion (CTE) is assumed to be constant at $10 \cdot 10^{-6}$ as described by Eurocode 2 (NEN-EN 1992-1-1, 2015).

3.5.2. Drying shrinkage

Drying shrinkage is determined from a triplicate of prismatic specimens. These prisms (100 x 100 x 400 mm³) are fog-cured for 28 days (20 ^{o}C and RH = > 95%), afterwards, the specimens are exposed to air (20 ^{o}C and RH = > 55%), then instrumented with two measurement clocks (Figure 3.7 and Figure 3.6). Measurement clocks are used to measure the elongation or shrinkage of the specimens in mm. Additionally, the weight of the samples was measured.

(a) (b)

Figure 3.7: Drying shrinkage, unsealed specimens. a) front view and b) side view.

In total 6 specimens are tested for drying shrinkage. 3 of the mixture S-PCC-C30 and 3 of the mixture S-AAC-C30. The test is also done for 3 specimens of mixture S-PCC-C50 and 3 specimens of mixture S-AAC-C50 by Jelle Bezemer. The measurements start 28 day after casting and continue for up to 6 months.

Drying shrinkage was determined by eliminating the autogenous shrinkage from the measurements (See equation 3.6). Nevertheless, also the measured data consisting of the drying shrinkage and autogenous shrinkage are presented in the results.

$$\varepsilon_{drying} = \varepsilon_{measured\ data} - \varepsilon_{autogenous} \tag{3.6}$$

3.6. Structural behaviour of RC beams

3.6.1. Shear behaviour

To determine the shear resistance, a 3-point bending test was conducted. The effective span used was 1000 mm, with both supporting conditions provided by sliding hinges. A point load was applied at the centre of the beam, and the test was executed in displacement-control at a speed of 0.01 mm/s. Data was collected using jack measurements, Digital Image Correlation (DIC), and LVDTs.

A total of 16 beams will be cast: 3 beams without stirrups and 1 beam with stirrups for each mixture. The dimensions of the beams are 1600 mm x 200 mm x 150 mm (length x height x width). Each beam will contain two Ø25 mm B500 steel longitudinal tensile reinforcements and two Ø20 mm B500 steel longitudinal compressive reinforcements, as shown in Figure 3.8. For the beam with stirrups, four strips of Ø8 mm B500 steel will be added. At 28 days, 2 beams without stirrups and 1 beam with stirrups will be tested for each mixture. At 182 days, an additional 1 beam without stirrups will be tested for each mixture.

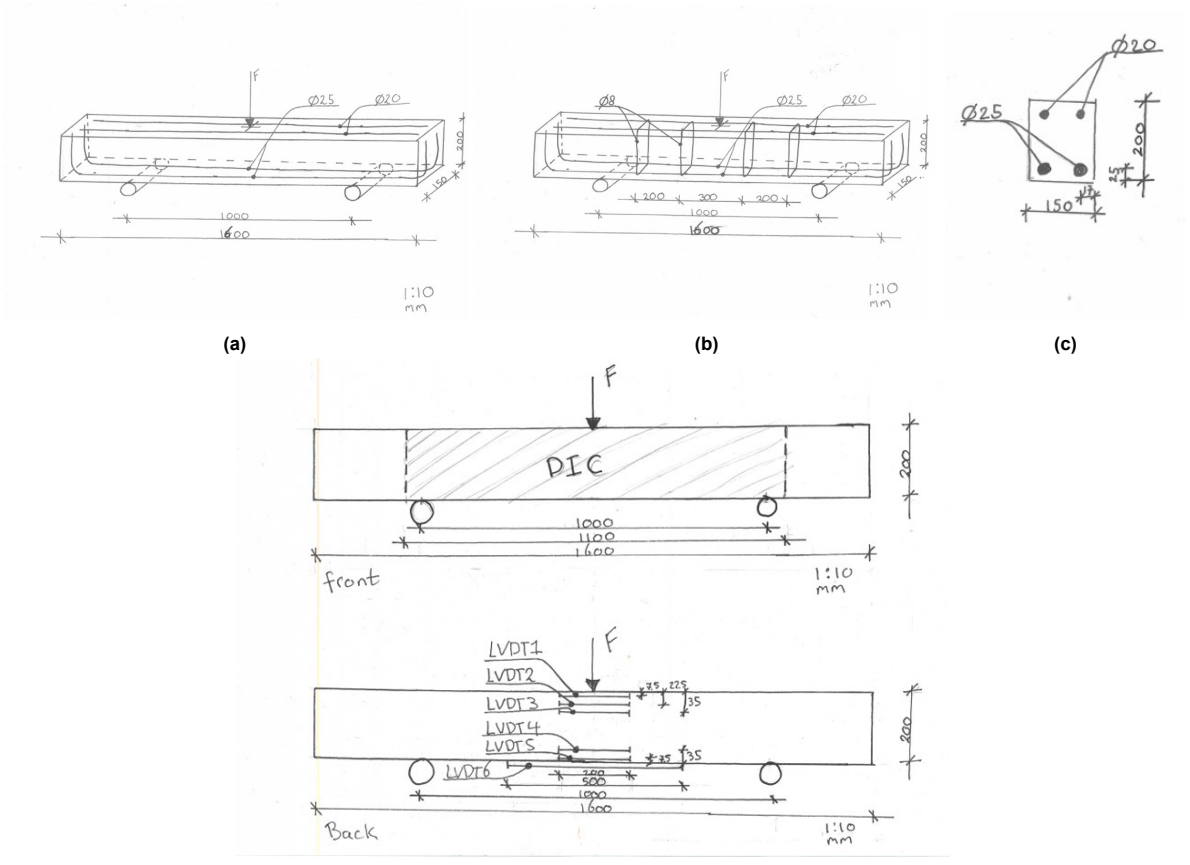

Figure 3.8: Drawings of the specimens for the shear test. a) Shear beam without stirrups, b) shear beam with stirrups, c) cross-section of the beam and d) front and back of the specimens with measurement techniques, DIC, and LVDT layout.

On top of the supports, two plates were placed to facilitate sliding. The plates measured $57 \times 6 \times 200$ mm^3 (w × h × l). Furthermore, beneath the load cell: a felt pad, a plate, and a round cell were placed. The felt pad measured $98 \times 8 \times 360$ mm^3 (w × h × l), the plate measured $50 \times 22 \times 300$ mm^3 (w × h × l), and the round cell had a inner diameter of 60 mm and a outer diameter of 140 mm and a height of 37 mm. See figure 3.9.

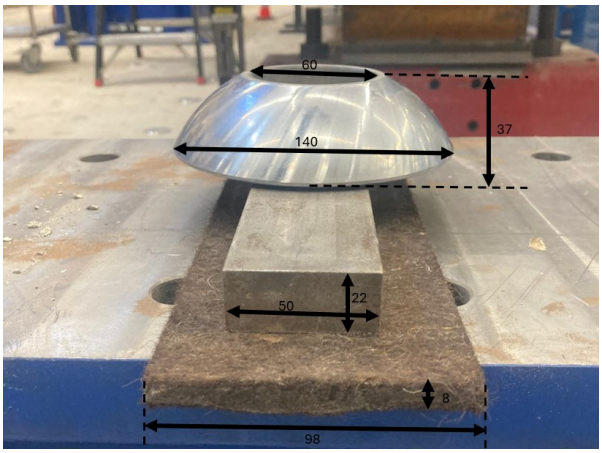

Figure 3.9: Felt pad, plate and round cell with dimensions that have been placed underneath the load cell.

3.7. Measuring Techniques

3.7.1. Digital image correlation (DIC)

Digital Image Correlation (DIC) is a technique developed for measuring displacements and relative displacements. From this displacement mechanical properties of materials at the micro and nano scale can be calculated. Image registration is used to obtain accurate 2D and 3D measurements of changes in images. The comparison is performed by overlapping the images. During this process, an image is divided into sets of pixels, referred to as sub-images. Each sub-image is assigned specific coordinates. The displacement of a sub-image within an image is determined by correlating it with the corresponding sub-image in the reference image. This method provides finer and more detailed information about deformation, strain, and displacement. The advantages of this method include providing sub-pixel accuracy, capturing full-field displacement information, visual documentation of the results, as well as the ability to capture complex deformation patterns (R. Yang et al., 2016).

The preparation for this method involves applying a speckle pattern of random black and white spots to the surface of the test material. The pattern was applied to the front side of the shear beams, in the middle of the beam, from -550 to +550 mm. The application process began by cleaning the surface with ethanol. Then, two thin layers of white paint were applied. Finally, a black speckle pattern was applied using a spray gun, prepared by the technicians, to ensure the pattern had an appropriate grain size.

This pattern then acts as a reference for tracking changes. During the test, images are captured using a 50 MP Canon 5DSR II camera with a 35 mm lens, set to ISO 100, aperture f/6.3, and shutter speed 1/125. Additionally, a flash was used. Finally, DIC software is used to compare the pattern at different loading stages, capturing 2D measurements of displacement, strain, and deformation.

See Figure 3.10 for the DIC set-up of the shear test.

Figure 3.10: DIC set up used at the shear behaviour tests

The DIC data was analysed using the software GOM Correlate. A facet size of 25 pixels and a point distance of 12 pixels were used. In this software, the quality of the pattern can be checked. The colour green indicates that the pattern has a good correlation and is suitable for use. Red or yellow indicates that the pattern has a weak correlation and needs to be adjusted. The pattern used for the shear beams showed a green pattern and was accepted (see Figure 3.11).

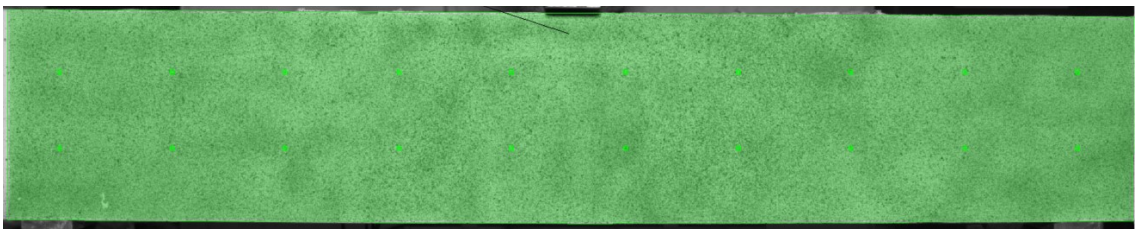

Figure 3.11: Quality check of the pattern, using GOM Correlate.

Furthermore, a noise analysis can be performed by taking two images before the test starts. The maximum x-displacement between the images will be determined to assess the noise. The maximum found displacement is below 0.015 mm, no red parts, and therefore the camera setup will be accepted (see Figure 3.12).

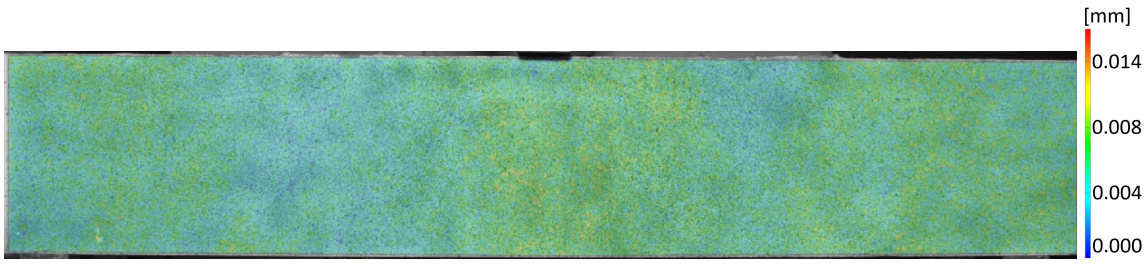

Figure 3.12: Noise analysis, using GOM Correlate.

3.7.2. Linear Variable Data Transformer (LVDT)

Linear Variable Differential Transformers (LVDTs) are contactless sensors used to measure linear displacement, which is the movement of an object along a straight line. LVDTs determine the displacement by measuring the difference in position between two predefined points. The sensor contains a movable core that adjusts the position of a spring. As the core moves, the resistance in the electrical circuit changes. This change in resistance is then measured and converted into a displacement value (ST sentech, 2023).

The preparation for this method involves positioning holders for the bars and LVDTs as required. First, the correct position and distance are marked on the specimens. The specimen and holders are then cleaned with ethanol. After cleaning, the holders can be glued in place using a two-component Permacol epoxy glue. Once the specimen is placed into the test setup, the bars holding the LVDT holders can be slowly removed from one side. The LVDT is then positioned in the holder, making contact with the bar still placed in the other LVDT holder. The LVDT should be placed in compression if elongation is expected, or in tension if contraction is expected. It is important to always use the same LVDT configuration when testing, this helps when analyzing the data.

See Figure 3.13 for the LVDT set-up at the shear test.

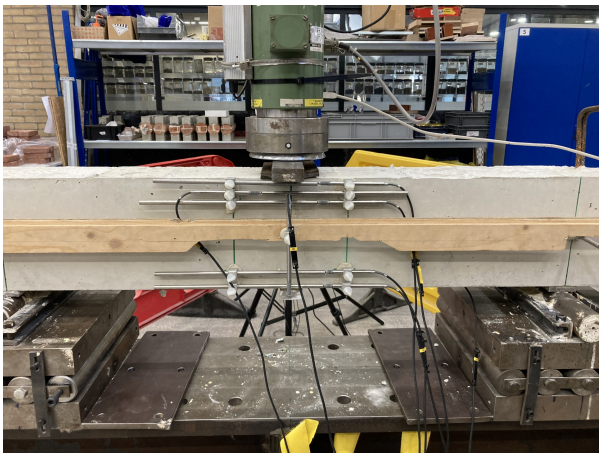

Figure 3.13: LVDT set up used at the shear behaviour tests

3.7.3. Verification of the DIC measurements with the LVDT measurements

For all beams, the DIC measurements were verified against the LVDT measurements. This verification was performed by simulating virtual LVDTs in the DIC software and plotting the displacement-force curves of the actual LVDTs versus those obtained through DIC. The placement of the virtual LVDTs in the DIC software is shown in Figure 3.14a and the placement of the LVDTs on the test specimen is shown in Figure 3.14b.

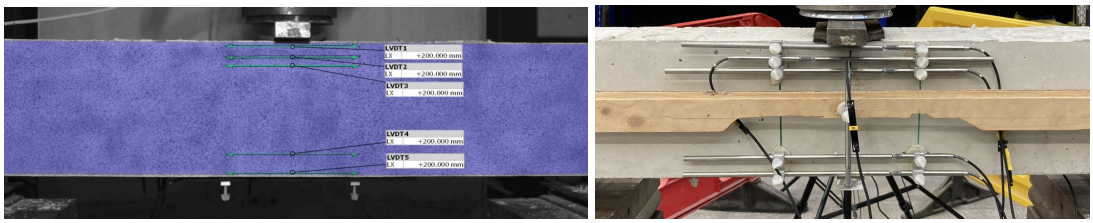

(a) **(b)**

Figure 3.14: Placement of LVDTs. a) Virtual LVDTs in the DIC software, and b) LVDTs on the test specimen.

The displacement-force curves for the LVDTs of beam S-AAC-C30-3 are shown in Figure 3.15. The results demonstrate that the virtual LVDTs from DIC are consistent with the physical LVDTs used in the experimental setup. This conclusion is supported by the fact that the LVDT and DIC measurements initially follow a similar displacement trend. This behaviour was observed in all shear beams tested. For the displacement-force curves of all tested shear beams, refer to Appendix A.

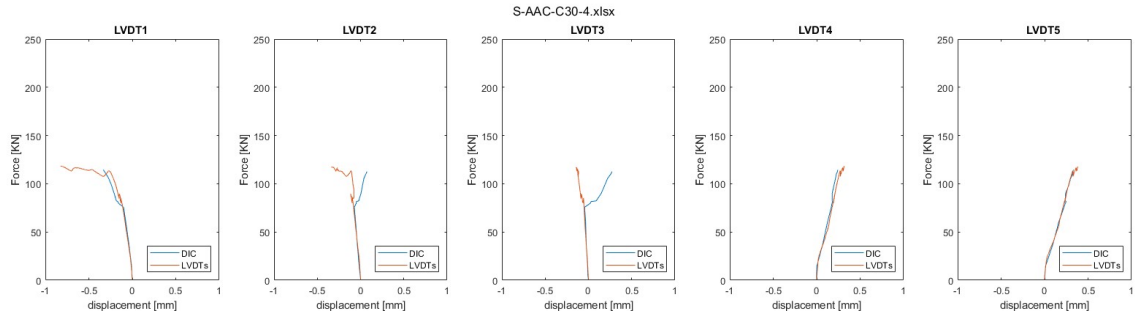

Figure 3.15: Verification of the DIC measurements with the LVDT measurements for beam S-AAC-C30-3.

3.7.4. Ultrasonic pulse velocity (UPV)

The Ultrasonic Pulse Velocity (UPV) test is a non-destructive method used to determine the quality of concrete. During this test, the time it takes for an ultrasonic pulse to pass through a concrete element is measured, see Figure 3.16. This information is used to detect flaws such as voids and cracks in the concrete. Cracks cause a significant decrease in the ultrasonic pulse velocity because they disrupt the continuity of the concrete matrix. When the pulse encounters cracks it either travels around the crack, depending on the crack's orientation, or encounters a discontinuity that slows down the pulse. Therefore, a higher UPV indicates good-quality concrete with minimal internal damage, cracks, or voids, while a lower UPV suggests the presence of cracks, voids, or other internal flaws (Kalyan and Kishen, 2016).

(a) **(b)**

Figure 3.16: Pictures showing the execution of a UPV test: a) side view and b) top view.

In Table 3.4, the different pulse velocities obtained from the UPV test are listed, along with their corresponding interpretations regarding the quality of the concrete (Farhan et al., 2019).

Table 3.4: Quality classification of concrete using UPV

Pulse velocity [km/s]	Quality of the concrete
>4.5	excellent
3.5 - 4.5	good
3.0 - 3.5	medium
2.0 - 3.0	poor
< 2.0	very poor

The UPV test has been executed on the C50 beams and corresponding cubes, for mixtures S-AAC-C50 and S-PCC-C50. The places where the measurements are taken are shown in Figure 3.17.

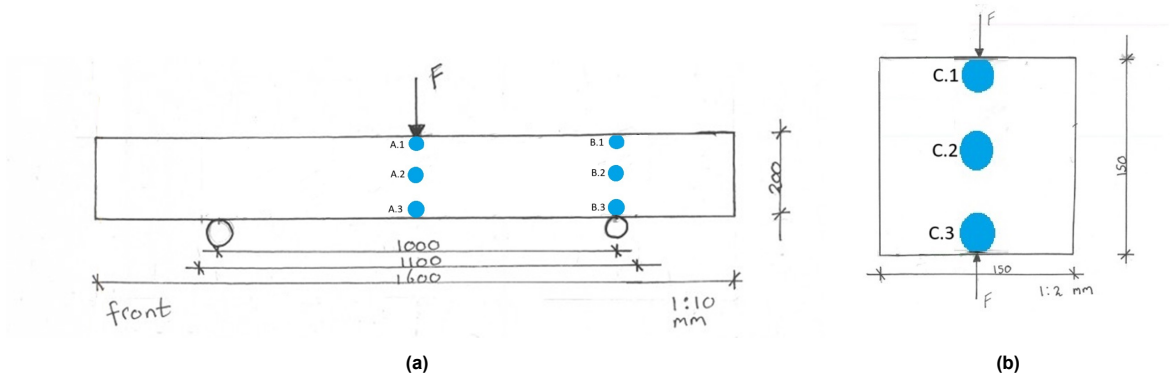

Figure 3.17: Pictures showing the positioning of the UPV test: a) on the beams, and b) on the cubes.

3.7.5. Crack opening and slip measurements

The shear resistance of concrete beams comes from friction at the crack surface, which is connected to the main normal stresses at the shear plane. When the shear strength is exceeded, shear failure happens, which is seen as the crack surfaces separating and the load decreases. Crack slip and crack opening happen together during this separation (Huang et al., 2023).

To determine the crack opening and crack slip of the shear crack, a method introduced by Huang et al., 2023 is applied. This method uses DIC analysis to obtain the crack opening and slip by generating a two-dimensional displacement field for multiple load steps. A 4-point reference system is used, as shown 3.18. The reference points are split into kinematic points (A and B) and rotation points (C and D). When a load is applied, the specimen deforms and rotates, causing the points to shift to new positions, labelled A′, B′, C′, and D′. From the selected points, the x-displacement and y-displacement can be obtained for different load steps. The obtained displacements can be used to calculate the crack opening (Equation 3.9) and crack sliding (Equation 3.10), taking into account and correcting for rotations of the specimen itself (Equation 3.7).

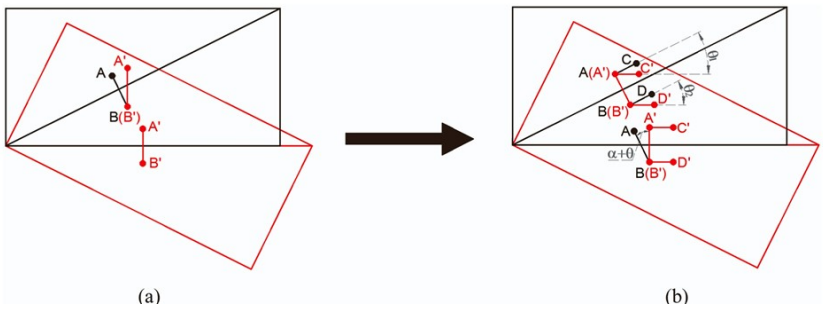

Figure 3.18: Crack displacement calculation: a) 2-point reference system and b) 4-point reference system (Huang et al., 2023).

The rigid rotation angle θ is the change in angle between the original and new positions.

$$\theta = \frac{1}{2}\left(\arccos\frac{\overrightarrow{AC}\cdot\overrightarrow{A'C'}}{||\overrightarrow{AC}||\cdot||\overrightarrow{A'C'}||} + \arccos\frac{\overrightarrow{BD}\cdot\overrightarrow{B'D'}}{||\overrightarrow{BD}||\cdot||\overrightarrow{B'D'}||}\right) \tag{3.7}$$

The angle change due to applied load α is calculated.

$$\alpha = \arccos\frac{\overrightarrow{AB}\cdot\overrightarrow{A'B'}}{||\overrightarrow{AB}||\cdot||\overrightarrow{A'B'}||} - \theta \tag{3.8}$$

Finally, the crack opening and crack sliding can be obtained.

$$Crackopening = ||\overrightarrow{A'B'}|| \cdot \cos\alpha - ||\overrightarrow{AB}|| \tag{3.9}$$

$$Cracksliding = ||\overrightarrow{A'B'}|| \cdot \sin\alpha \tag{3.10}$$

4

Experimental results

4.1. Material behaviour

4.1.1. Compressive strength

The results for the compressive strength test at 28 days and 6 months are presented in Figure 4.1.

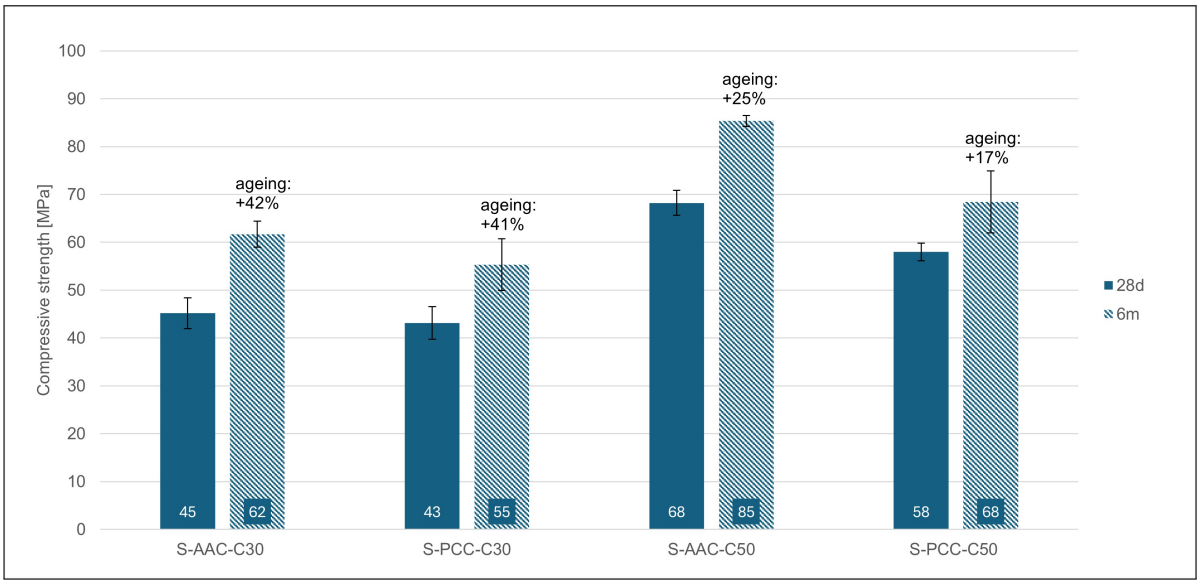

Figure 4.1: Comparison of the compressive strength of mixtures S-AAC-C30, S-PCC-C30, S-AAC-C50, and S-PCC-C50 at 28 days and 6 months.

At 28 days, all mixtures exceed their designed compressive strengths. The C30 mixtures achieve strengths above the minimum requirement of 37 MPa, and the C50 mixtures are close to 60 MPa. Additionally, the AAC concrete mixtures exhibit higher compressive strength, by 5% and 17%, compared to the PCC mixtures at 28 days. At 6 months, all mixtures show a significant increase in compressive strength, with the AAC mixtures maintaining higher compressive strengths, exceeding those of the PCC mixtures by 13% and 25%. This indicates that the increase in compressive strength over 6 months is greater for the AAC mixtures compared to the PCC mixtures.

An overview of the compressive strength development over time, 28 days and 6 months, is given in figure 4.2. The trend show that the compressive strength in all materials improves over time, with AAC-C50 showing the best performance. The AAC mixtures appear to gain strength at a faster rate over time than PCC mixtures.

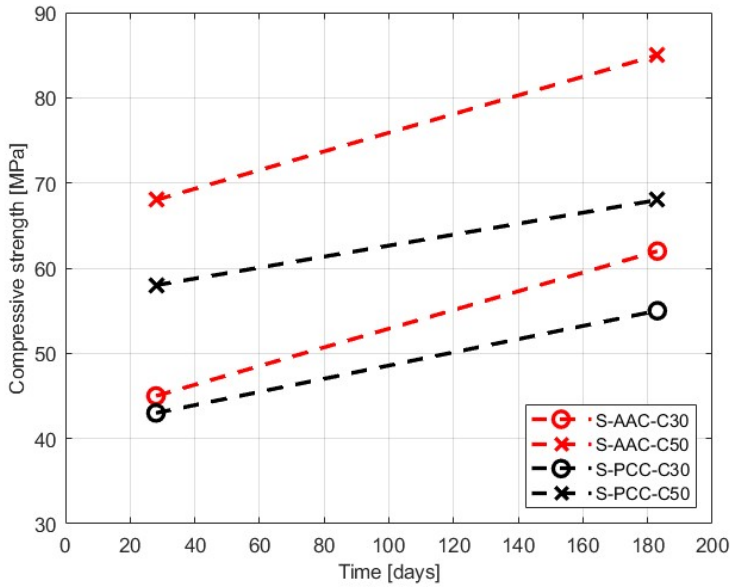

Figure 4.2: The compressive strength versus time at 28 days and 6 months for the mixtures S-AAC-C30, S-PCC-C30, S-AAC-C50, and S-PCC-C50.

4.1.2. Tensile strength

The results of the splitting tensile strength at 28 days and the results of the direct tensile strength test at 28 days and 6 months are presented in Figure 4.3.

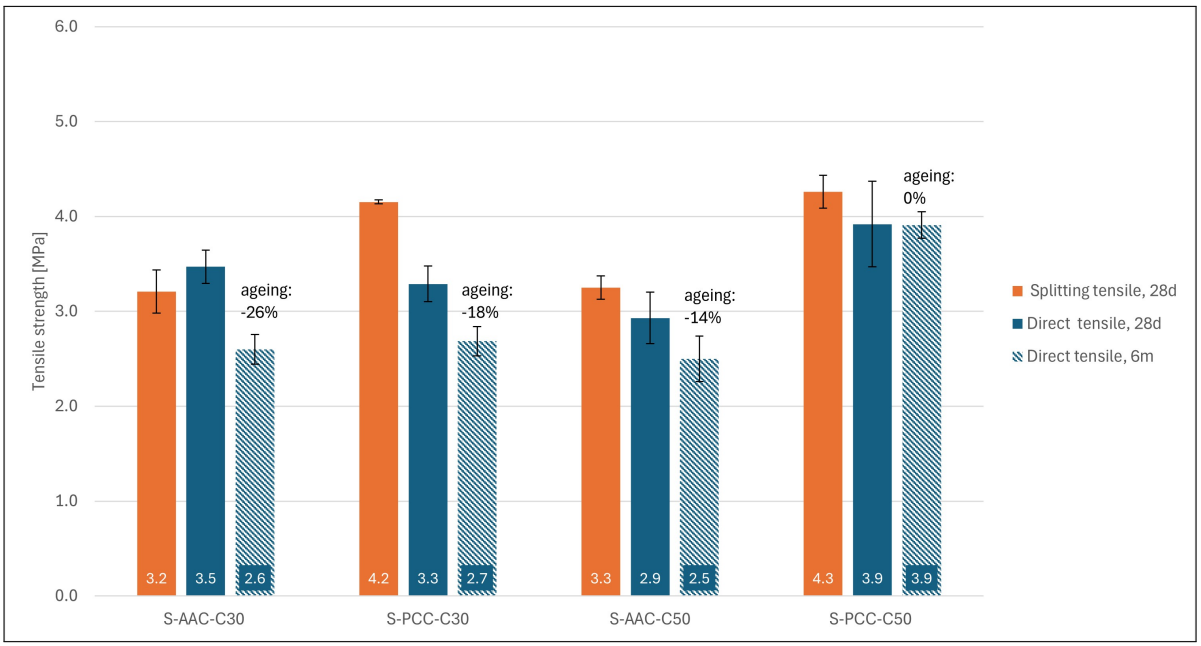

Figure 4.3: The 90% splitting tensile strength at 28 days and the direct tensile strength at 28 days and 6 months for the mixtures S-AAC-C30, S-PCC-C30, S-AAC-C50, and S-PCC-C50.

First, when examining the 90 % splitting tensile test results, the PCC mixtures show a higher splitting tensile strength, by 28% and 31% compared to the AAC concrete mixtures. Splitting tensile test results are higher for the mixtures S-PCC-C30, S-AAC-C50 and S-PCC-C50 mixture compared to the direct tensile strength test results. For the S-AAC-C30 mixture, this is not the case, the tensile splitting strength is 9% lower compared to the 28-day direct tensile strength.

Moreover, when comparing the direct tensile strength at 28 days, the C30 mixtures exhibit comparable results, with the S-AAC-C30 and S-PCC-C30 mixtures achieving 3.5 MPa and 3.3 MPa, respectively. For the C50 mixtures, the S-AAC-C50 mixture shows a lower direct tensile strength, 35% lower than the S-PCC-C50 mixture, namely at 2.9 MPa compared to 3.9 MPa. The stress deformation curves at 28 days for the C30 mixtures are shown in figure 4.6a and for the C50 mixtures in figure 4.6b.

Furthermore, when comparing the direct tensile strength at 6 months to the 28-day results, the strength differences are -26%, -18%, -14%, and 0% for the S-AAC-C30, S-PCC-C30, S-AAC-C50, and S-PCC-C50 mixtures, respectively. The results indicate that the AAC mixtures experience a greater reduction in tensile strength compared to the PCC mixtures of corresponding strength. Despite this reduction, the final tensile strengths of the C30 mixtures are still comparable at 6 months, measuring 2.6 MPa and 2.7 MPa, respectively. However, for the C50 mixtures, the tensile strength of the S-AAC-C50 mixture is even lower at 2.5 MPa, compared to 3.9 MPa for the S-PCC-C50 mixture. The stress deformation curves at 6 months for the C30 mixtures are show in figure 4.8a and for the C50 mixtures in figure 4.8b.

An overview of the direct tensile strength development over time, 28 days and 6 months, is given in figure 4.4. The results show that for the different mixtures, different trends can be observed. The S-AAC-C30 mixture shows the most rapid decrease over 6 months. The decline in tensile strength is more pronounced in AAC than in PCC mixtures. This trend is in contrast with those observed for compressive strength.

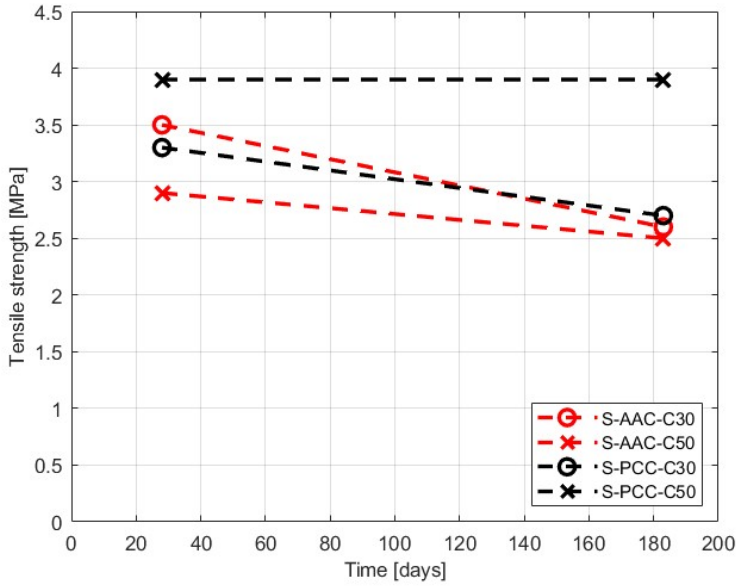

Figure 4.4: The direct tensile strength versus time at 28 days and 6 months for the mixtures S-AAC-C30, S-PCC-C30, S-AAC-C50, and S-PCC-C50.

This reduction over time can be the effect of self-induced stresses. If a specimen is completely free to shrink, self-induced stresses will assumed to be minimal or non-existent. However, in some cases initial stresses may still develop due to: 1) heterogenous hydration, different parts of the specimen may hydrate at different rates, leading to localized stresses. 2) Pore structure effects, the difference in porosity can cause uneven shrinkage, even without external restraint. 3) temperature effects, if heat is generated unevenly during hydration, parts of the specimen may expand and contract at different rates, leading to thermal self-induced stresses.

Hordijk, 1991 observed that specimens experience a noticeable decrease in strength when allowed to dry. However, if drying continues for extended periods, this reduction diminishes and can eventually transform into a strength gain. The study attributes this initial drop in strength to differential shrinkage in the drying specimens, which induces eigen-stresses. It is also suggested that this effect varies with the dimensions of the specimens. The study used CEM I with a high water-to-cement ratio. therefore,

the observed increase in tensile strength over time can likely be explained by the presence of sufficient water and unhydrated cement particles, allowing continued hydration. Moreover, autogenous shrinkage is less significant in these mixtures.

The study of Awasthy et al., 2023 examines the impact of eigen-stresses on the behaviour of NSC, HSC, and UHSC. After 28 days of moist curing, drying temporarily lowers direct tensile strength in both NSC and HSC, especially at early ages. This is due to hygral gradients a variation in moisture content, where the outer layers of the specimen dry faster than the inner core, creating internal moisture differences. These gradients cause differential shrinkage, generating additional tensile stresses at the surface, which combine with mechanical loading and reduce failure load. As drying progresses and moisture equilibrium is reached, these stresses decrease, gradually restoring tensile strength.

Deformation-Stress curves

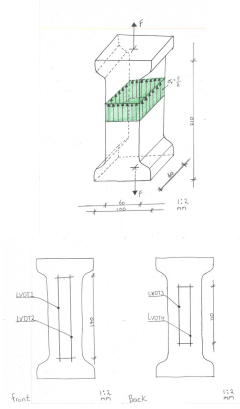

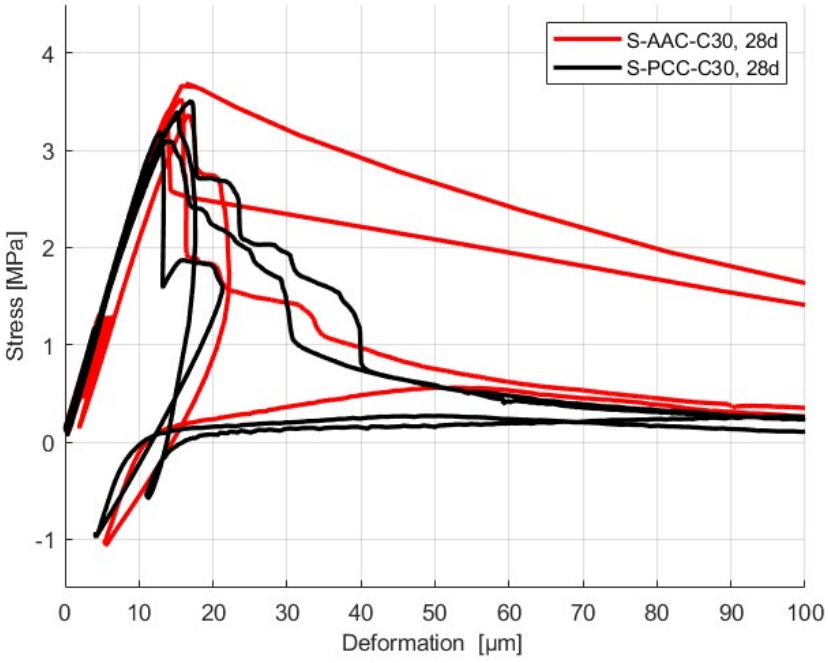

(a)

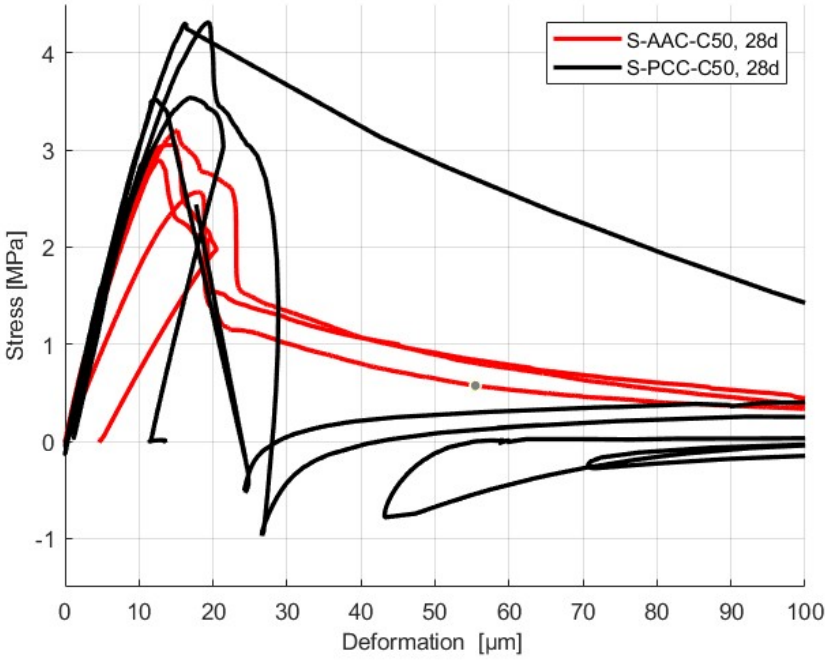

(b)

Figure 4.6: Deformation-stress relations obtained from the direct tensile test, where the stress is in MPa and the deformation are in $\mu m/m$, where the deformation is determined over the length of the LVDTs and the stress is calculated by force / smallest area: a) C30 mixtures and b) C50 mixtures.

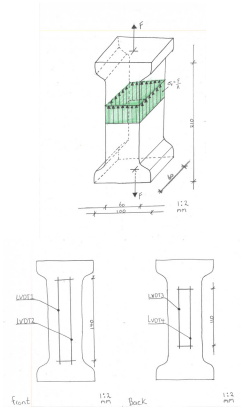

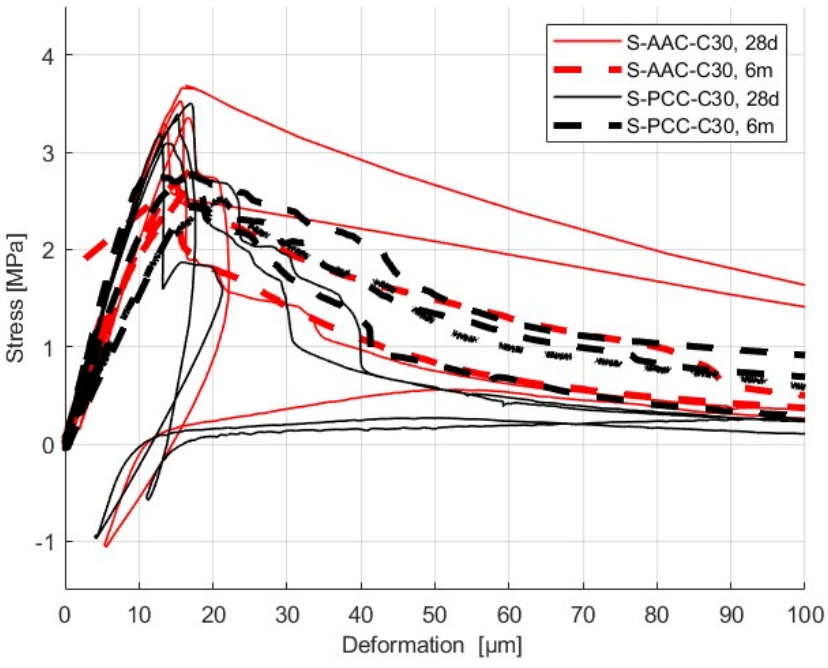

(a)

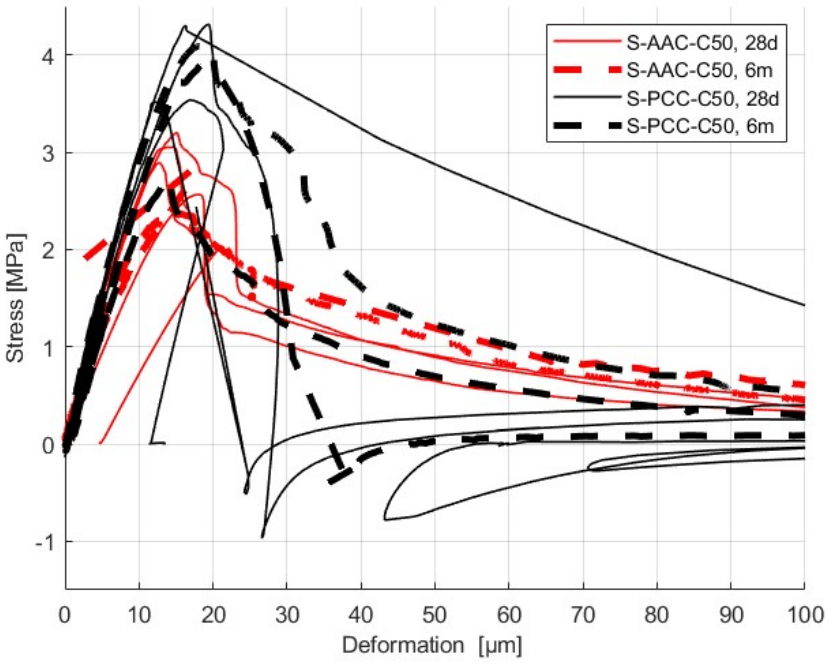

(b)

Figure 4.8: Deformation-stress relations obtained from the direct tensile test, where the deformation is determined over the length of the LVDTs and the stress is calculated by force / smallest area: a) C30 mixtures and b) C50 mixtures.

Fracture energy

Fracture energy refers to a material's ability to absorb energy after cracking, representing the total energy dissipated during failure. In simpler terms, it is the energy required to create and propagate a crack over a unit area. This property is crucial for understanding the post-peak behaviour of concrete,

as it determines how the material responds after reaching its maximum load capacity (Faraj et al., 2022).

A higher fracture energy signifies greater toughness, meaning the material can endure more stress and deformation before breaking, reducing its brittleness. This is particularly important when analyzing shear beam performance, as materials with high fracture energy can dissipate more energy through mechanisms like micro-cracking, ultimately enhancing their resistance to sudden failure.

In this study, fracture energy was calculated by determining the area under the stress-strain curve. The calculation was based on a deformation range from 0 to 200 μm. To exclude the effects of initial loading cycles, a linear approximation was applied from 0 up to the maximum stress. Additionally, tests where the samples were not well controlled after the max stress was reached were excluded from the calculation.

The fracture energy values for the direct tensile test are shown in Figure 4.9. The results indicate that over a 6-month period, the fracture energy of the specimens either increased (for S-AAC-C30, S-PCC-C30, S-AAC-C50) or remained similar (for S-PCC-C50). This suggests that the material becomes more resistant to higher levels of stress, deformation, and micro-cracking before failure as time progresses.

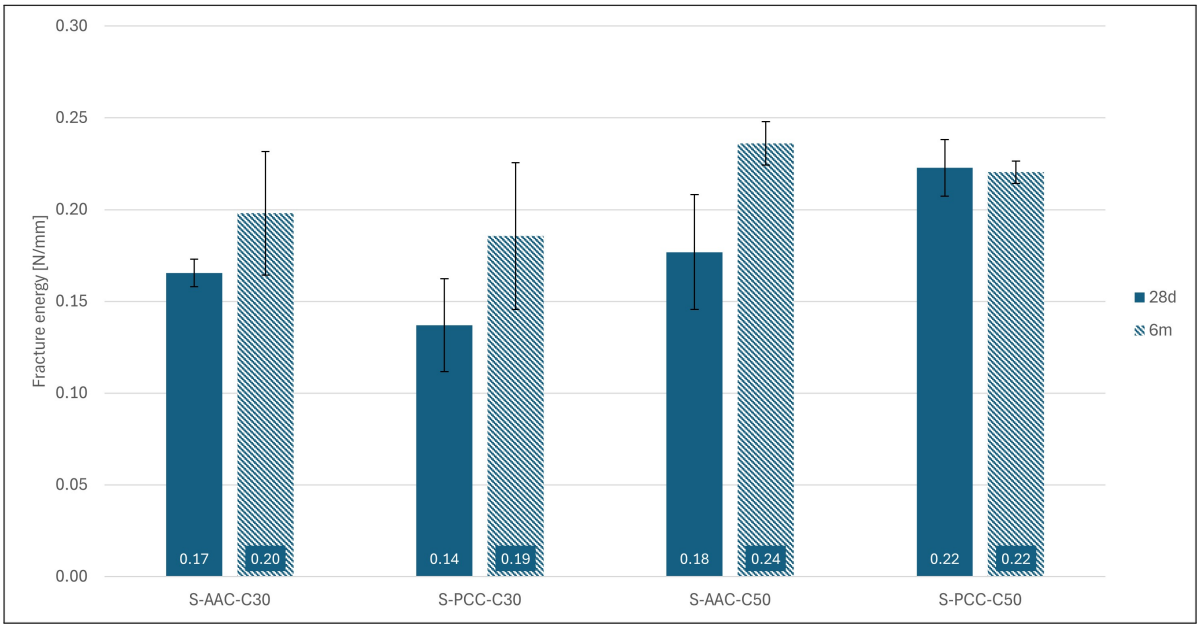

Figure 4.9: Fracture energy from the direct tensile test.

Strain-stress curves

Figures 4.11 and 4.13 present the strain-stress relationships. These curves are valuable for numerical models used to predict the behaviour of AAC concrete. Figure 4.11 shows the strain-stress relationships categorized by strength class, while Figure 4.13 presents them based on mixture type.

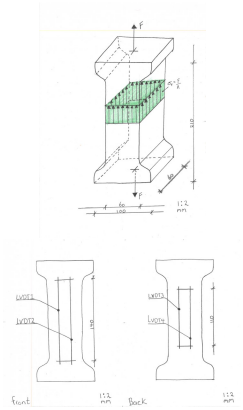

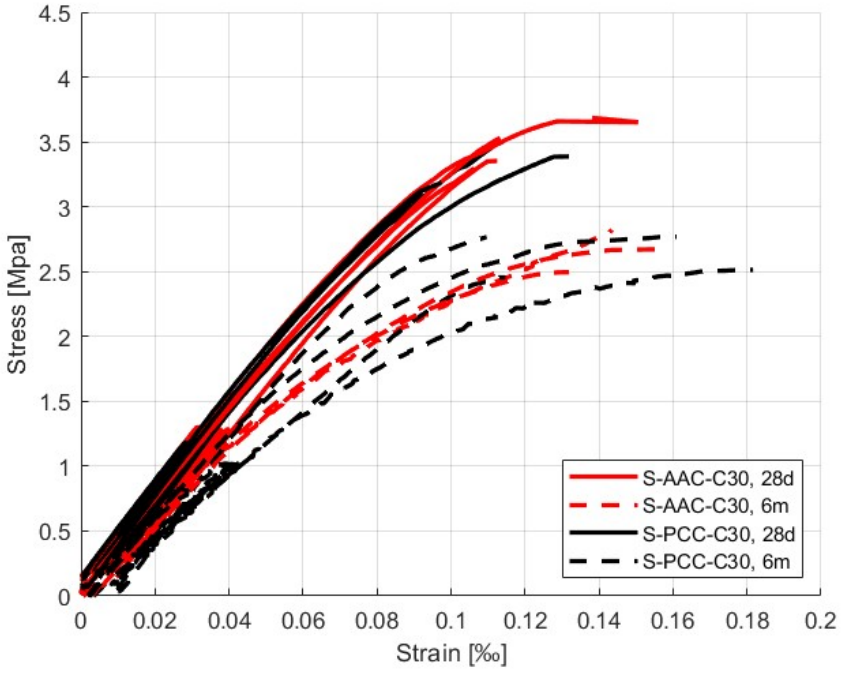

(a)

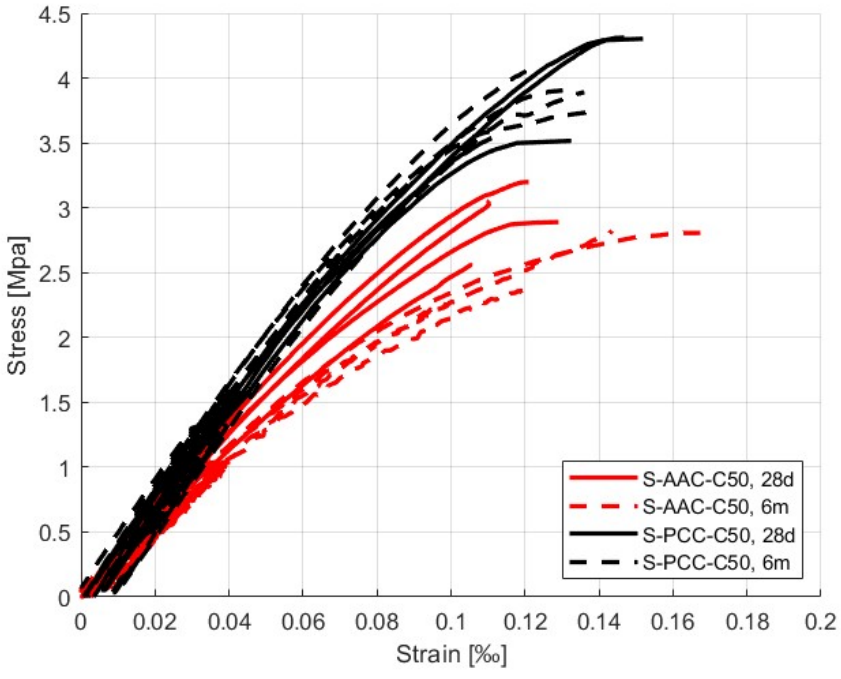

(b)

Figure 4.11: Strain-stress relations obtained from the direct tensile test, where the strain is determined by the displacement of the LVDTs / length of the LVDT measurements and the stress is calculated by force / smallest area: a) C30 mixtures and b) C50 mixtures.

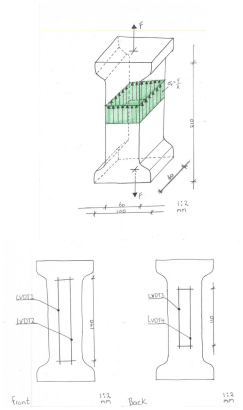

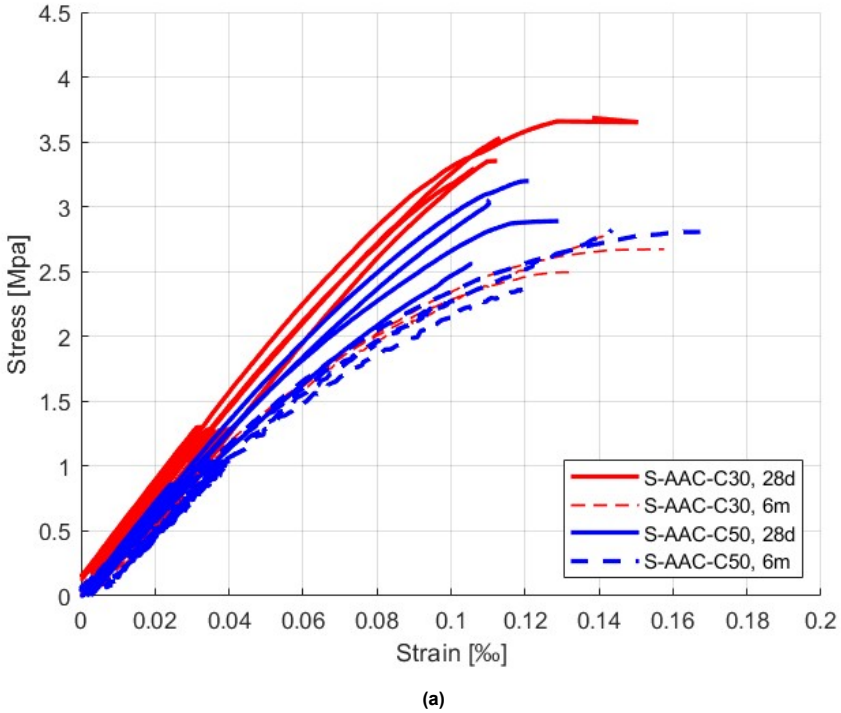

(a)

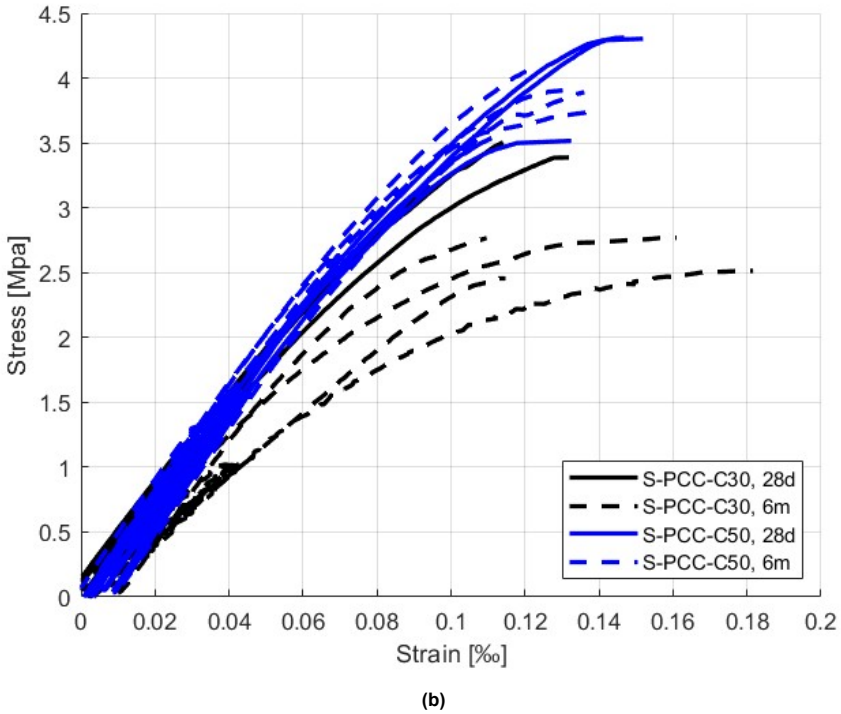

(b)

Figure 4.13: Strain-stress relations obtained from the direct tensile test, where the strain is determined by the displacement of the LVDTs / length of the LVDT measurements and the stress is calculated by force / smallest area: a) AAC mixtures and b) PCC mixtures.

Pictures of the cross-sections after testing

After performing the direct tensile strength test, the cross-sections of S-PCC-C30 and S-AAC-C30 mixtures were examined. Figure 4.14 shows pictures taken from specimens of the S-PCC-C30 mixture. These pictures reveal that the crack formed goes around most of the aggregates in the mixture. Figure

4.15 shows pictures taken from specimens of the S-AAC-C30 mixture. These pictures indicate that the crack passes through many of the aggregates in the mixture. From this, it can be concluded that the initial transition zone (ITZ) in the AAC mixtures is stronger than in the PCC mixtures. Pictures of all al the dogbones are added in Appendix B.

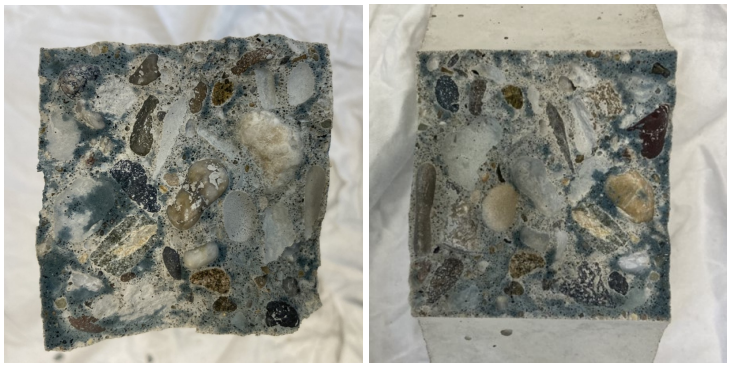

(a) (b)

Figure 4.14: Cross-section after the direct tensile test of the S-PCC-C30 mixture, with aggregate sizes ranging from 0.125 mm to 16 mm: a) bottom section and b) top section.

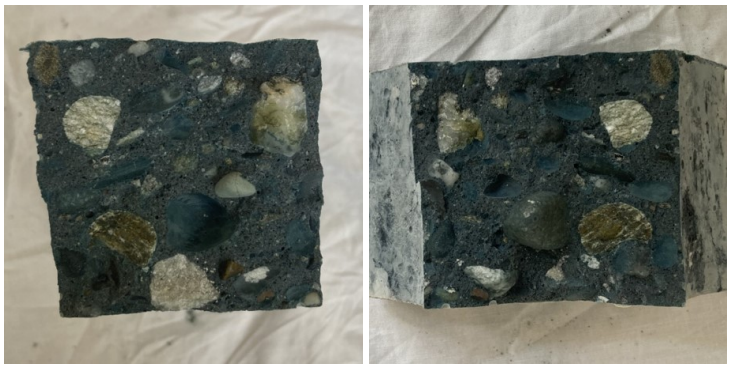

(a) (b)

Figure 4.15: Cross-section after the direct tensile test of the S-AAC-C30 mixture, with aggregate sizes ranging from 0.125 mm to 16 mm: a) bottom section and b) top section.

4.1.3. Elastic modulus

The results for the elastic modulus at 28 days and 6 months are presented in Figure 4.16.

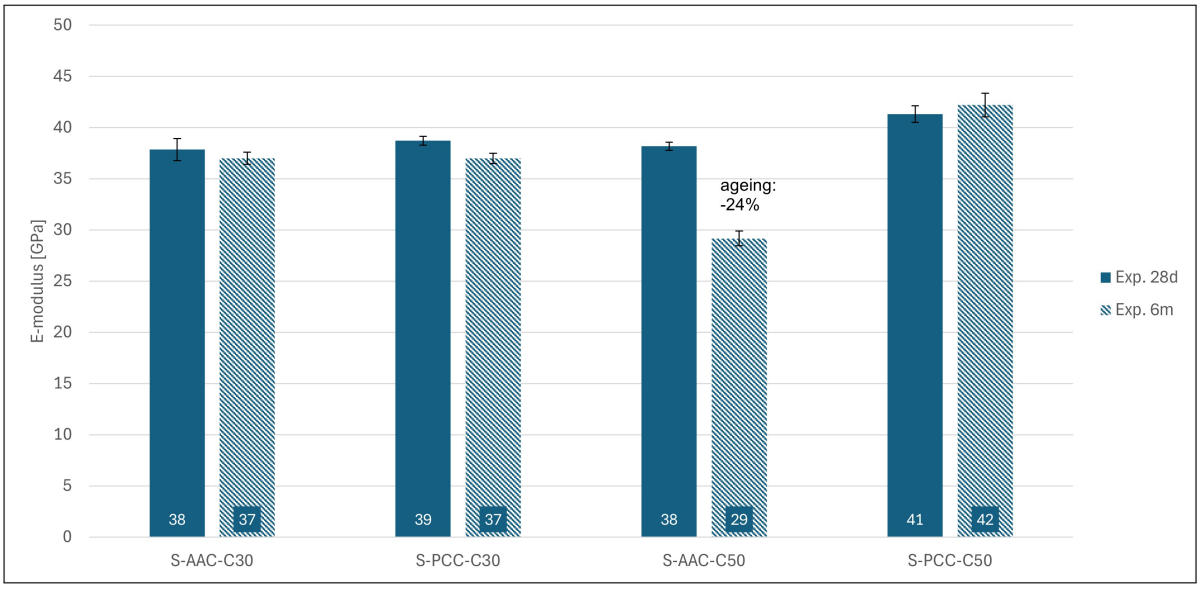

Figure 4.16: The elastic modulus at 28 days and 6 months for the mixtures S-AAC-C30, S-PCC-C30, S-AAC-C50, and S-PCC-C50.

Firstly, when looking at the 28-day results, the C30 mixtures, S-AAC-C30 and S-PCC-C30, show a similar elastic modulus of 38 GPa and 39 GPa, respectively. Comparing the C50 mixtures, S-AAC-C50 and S-PCC-C50, the AAC mixture exhibits a lower elastic modulus of 38 GPa compared to 41 GPa for PCC. Secondly, when examining the 6-month results, a 24% reduction in the elastic modulus for the AAC-C50 mixture is observed.

An overview of the elastic modulus development over time, 28 days and 6 months, is given in figure 4.17. The results show that for the different mixtures, different trends can be observed. The S-AAC-C50 mixture shows the most rapid decrease over 6 months, while the S-AAC-C30 mixture shows only a minor reduction over time. This trend is in contrast with those observed for compressive strength.

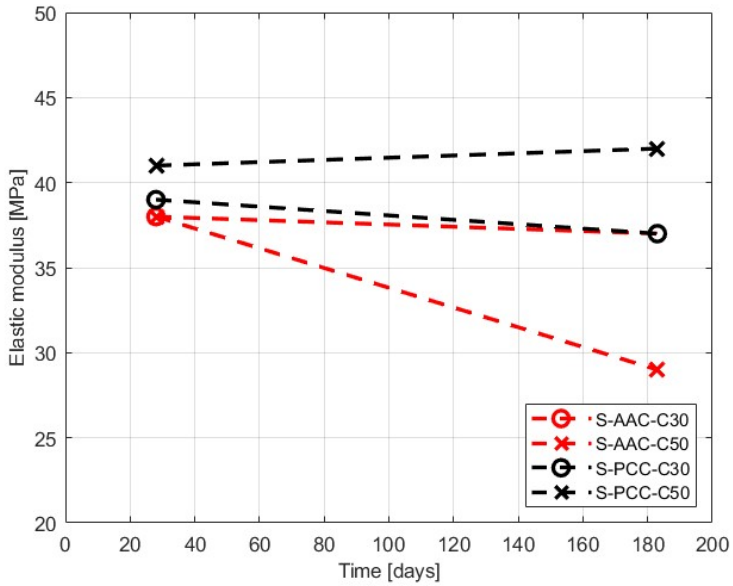

Figure 4.17: Elastic modulus versus time at 28 days and 6 months for the mixtures S-AAC-C30, S-PCC-C30, S-AAC-C50, and S-PCC-C50.

The explanation for this reduction is similar to that provided for the decrease in tensile stress over time. It can be attributed to self-induced stresses that arise from factors such as heterogeneous hydration, the effects of pore structure, and temperature variations. These factors contribute to changes in the material's internal structure, which can lead to a reduction in its overall performance over time.

4.2. Shrinkage

4.2.1. Temperature

The temperature mensuration from the embedded thermocouples for the mixtures S-AAC-C30 and S-PCC-C30 mixtures are presented in Figure 4.18 from 0 to 28 days.

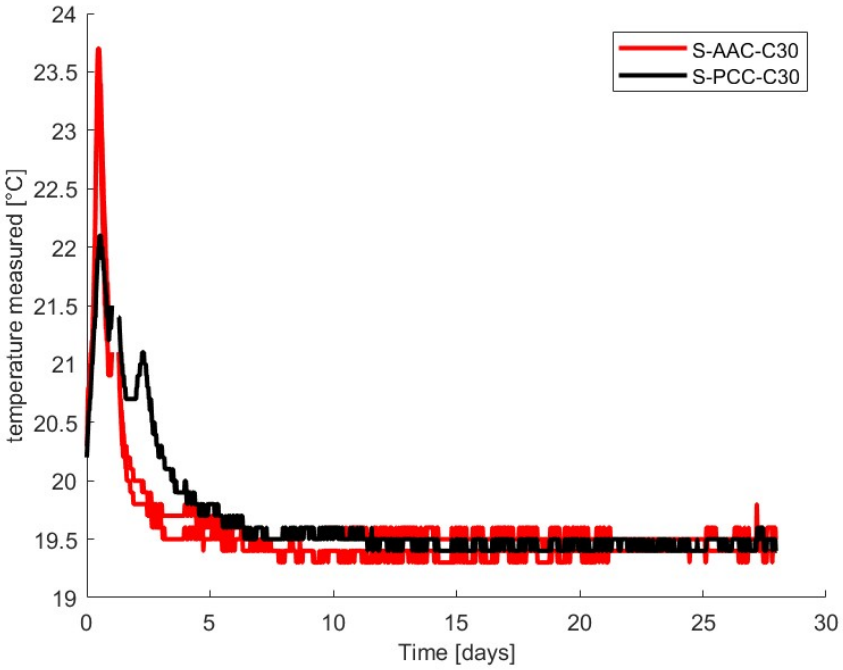

Figure 4.18: Comparison of internal temperatures in ^{o}C measured with thermocouple embedded in the prisms over time, from 0 to 28 days.

The results show an increase in internal temperature for both types of concrete directly after casting at 0.5 days (12 hours). The highest increase in internal temperature is shown by the S-AAC-C30 mixture, up to 24 ^{o}C compared to an increase of 22^{o}C for the S-PCC-C30 mixture. Eventually, both mixtures reach a stable temperature of 19.5^{o}C over time. The S-AAC-C30 mixture shows a steeper decrease in temperature after 0.5 days than the S-PCC-C30 mixture.

4.2.2. Autogenous shrinkage

The results for autogenous shrinkage over time are presented in Figure 4.20.

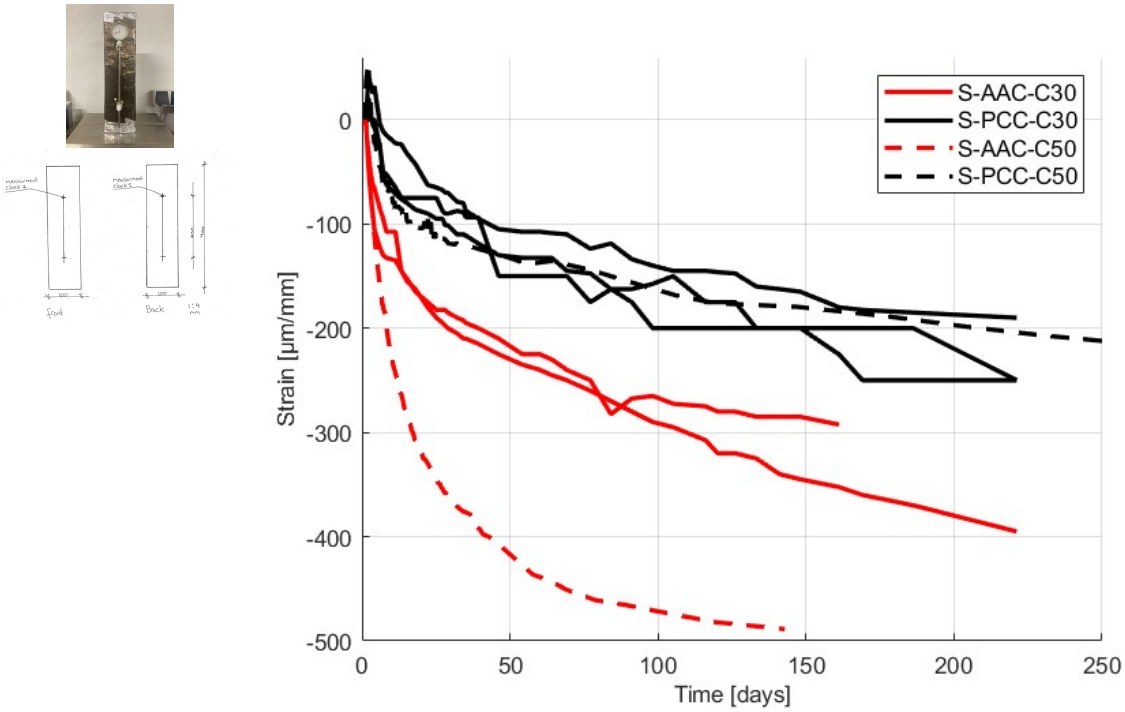

Figure 4.20: Autogenous shrinkage in µm/mm over time, from 0 to 222 days.

These results indicate that the AAC mixtures, S-AAC-C30 and S-AAC-C50, exhibit greater autogenous shrinkage compared to the PCC mixtures. Notably, the autogenous shrinkage of the S-AAC-C50 mixture is significantly higher than that of the S-PCC-C50 mixture. Additionally, both PCC mixtures demonstrate an initial expansion on the first day due to the internal temperature increase. In contrast, both AAC mixtures begin to shrink on day 1, the shrinkage in the AAC mixtures exceeds the expansion caused by the internal temperature increase.

Afterwards, the results obtained for the PCC mixtures are compared with the findings from the literature. The studies by Liang et al., 2023 and Mors, 2011 reported autogenous shrinkage for different w/c ratios of PCC mixtures (using CEMIII/B). The w/c ratio of the S-PCC-C30 mixture in this study is 0.5, while for the S-PCC-C50 mixture, it is 0.4.

The study by Liang et al., 2023 reported an autogenous shrinkage of -600 µm/mm for a w/c ratio of 0.5 and -650 µm/mm for a w/c ratio of 0.42 at 28 days under room temperature conditions of 20°C. These values are higher than those observed in our study. Furthermore, the study suggested that the S-PCC-C50 mixture should exhibit more significant autogenous shrinkage than the S-PCC-C30 mixture, which is not the case in our findings.

However, the study by Mors, 2011 reported an autogenous shrinkage of -220 µm/mm at 91 days for mixtures with w/c ratios of 0.5 and 0.44 under a room temperature of 20°C. These results align with the findings obtained in this study. This behaviour is different than found for mixtures based on OPCC (CEMI), for this type of mixtures, a lower w/c-ratio resulted in higher autogenous shrinkage.

Figure 4.21 presents the weight measurements of the autogenous shrinkage specimens for the C30 mixtures only. The results indicate that there are only minor changes in weight over time. Therefore, it can be concluded that the seals made were effective.

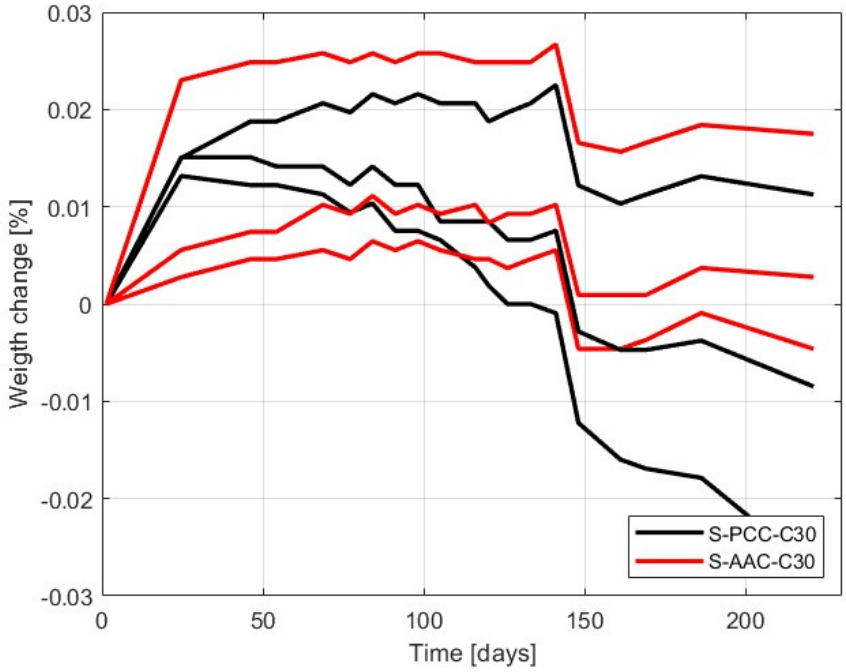

Figure 4.21: The weight from the autogenous shrinkage samples over time, from 1 to 222 days.

4.2.3. Drying shrinkage

Figure 4.23 presents the results for drying shrinkage including the autogenous shrinkage over time.

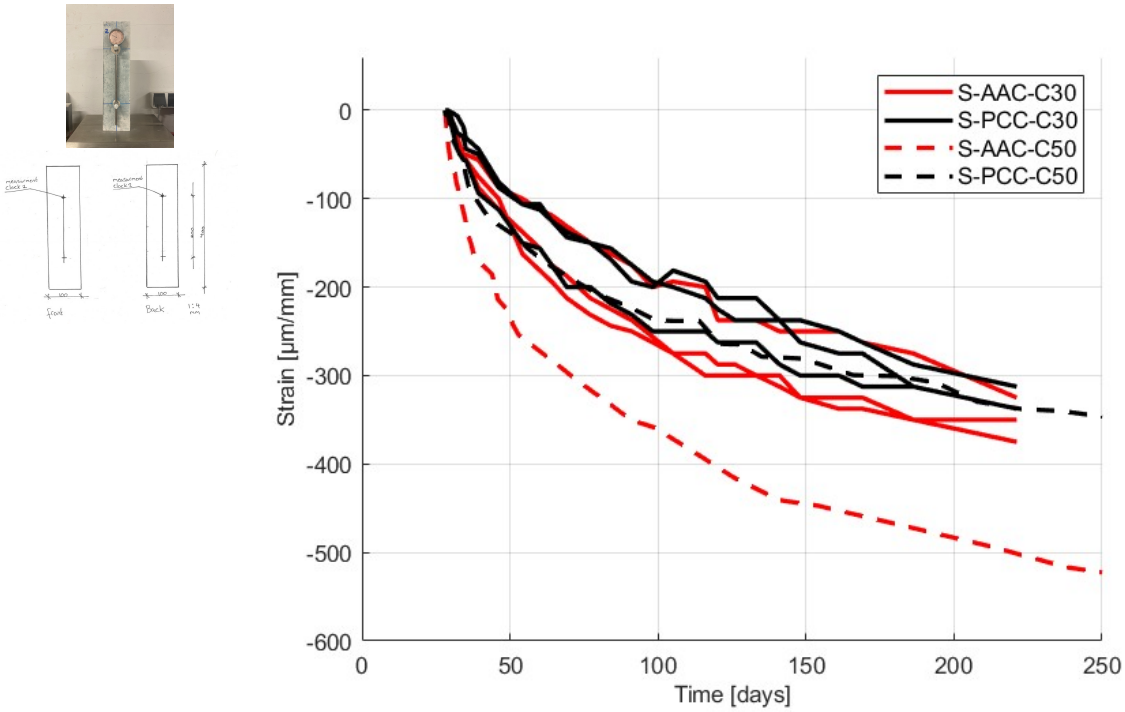

Figure 4.23: Drying shrinkage including autogenous shrinkage over time, from 28 to 222 days.

Figure 4.25 presents the results for drying shrinkage without autogenous shrinkage over time.

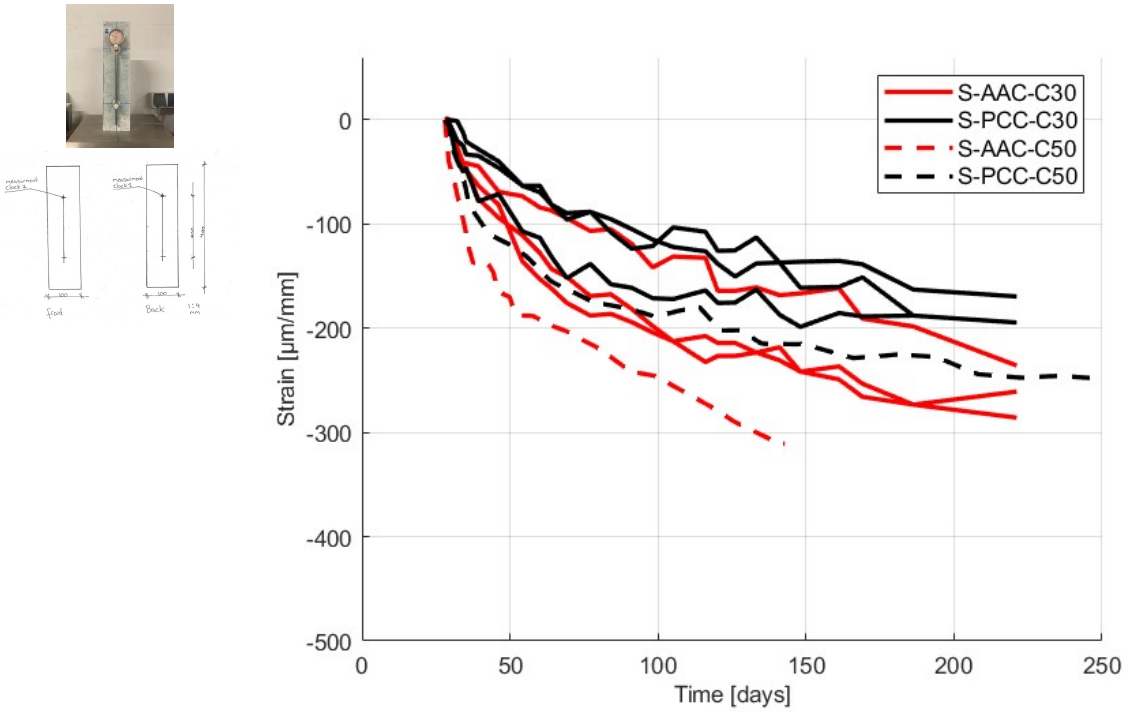

Figure 4.25: Drying shrinkage without autogenous shrinkage over time, from 28 to 222 days.

The results indicate that drying shrinkage is larger in the C50 mixtures than in the C30 mixtures. Additionally, the AAC mixtures, S-AAC-C30 and S-AAC-C50, exhibit greater drying shrinkage than the PCC mixtures of similar strength classes, S-PCC-C30 and S-PCC-C50.

Figure 4.26 presents the weight measurements of the drying shrinkage specimens for the C30 mixtures only. The results indicate that the S-AAC-C30 specimens exhibit less weight loss compared to the S-PCC-C30 specimens. Interesting, because the S-AAC-C30 mixtures display more drying shrinkage. These results show that using existing analytical models using weight loss to predict drying shrinkage will not provide accurate results for the S-AAC-C30 mixture.

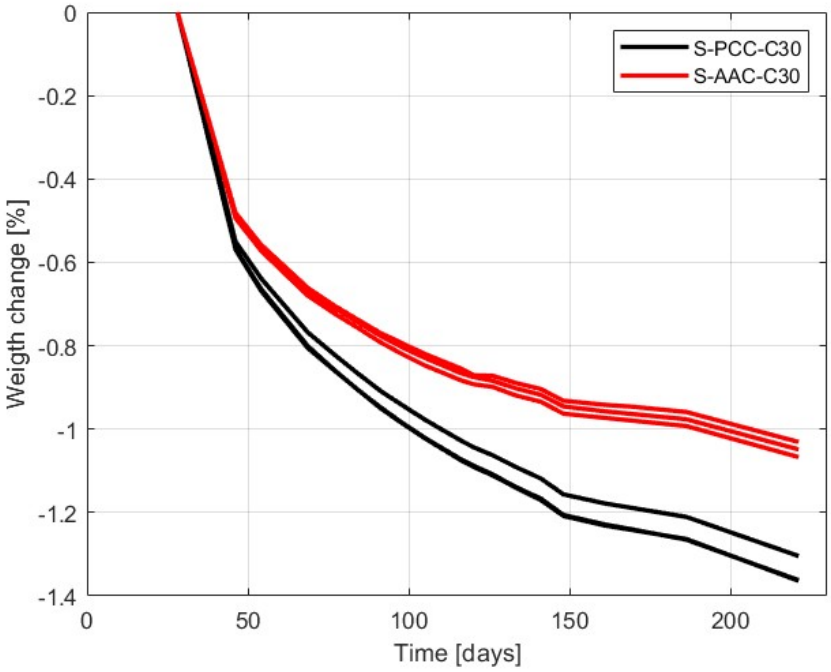

Figure 4.26: The weight from the drying shrinkage samples over time, from 28 to 222 days.

4.2.4. Shrinkage-Induced Cracks

Surface Imaging

When the specimens are restrained and not free to shrink, shrinkage induces high stresses within the specimens. Due to the higher drying and autogenous shrinkage in the S-AAC-C50 mixture, microcracks were observed on the surface at 6 months. See Figure 4.27.

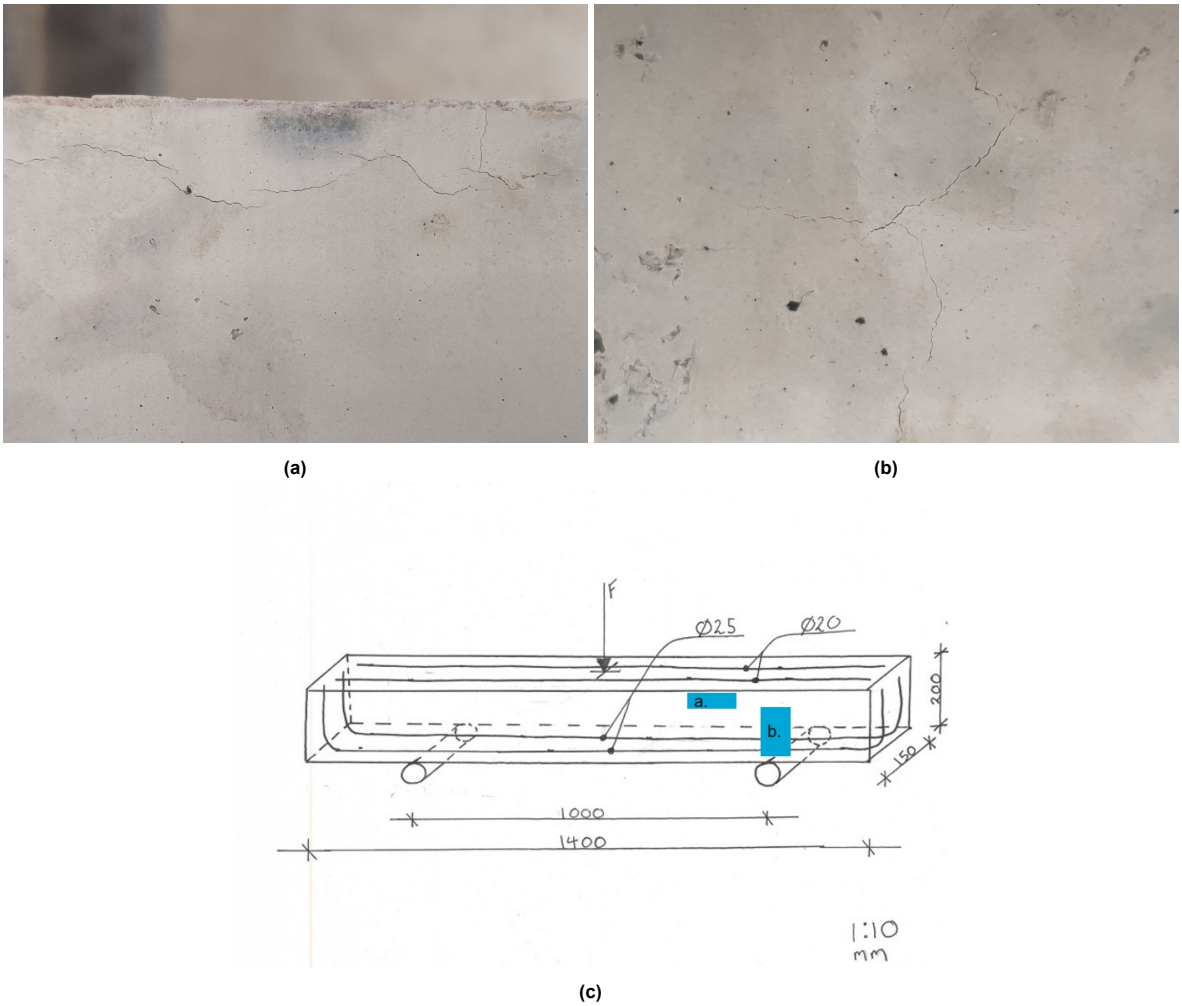

Figure 4.27: Cracks observed on the surface of the shear beam of the S-AAC-C50 mixture at 6 months: a) cracks at the edge of the beam, b) cracks above the support, c) locations on the beam where the pictures were taken.

Ultrasonic pulse velocity (UPV)

The results of the UPV test are presented in Figure 4.30, with the vertical mean values shown in Figure 4.30a. The UPV results prove the presence of micro-cracks in the S-AAC-C50 mixture compared to the S-PCC-C50 mixture.

The results reveal lower UPV values for the S-AAC-C50 beam, measuring 4.7 km/s at the middle of the beam and 4.6 km/s above the support. In contrast, the cubes of the same mixture display a higher UPV of 5.0 km/s. These findings suggest that in the S-AAC-C50 beam, the longitudinal reinforcement restricts shrinkage, leading to higher internal stresses due to shrinkage (See figure 4.28). When these internal stresses exceed the tensile resistance, micro-cracking occurs.

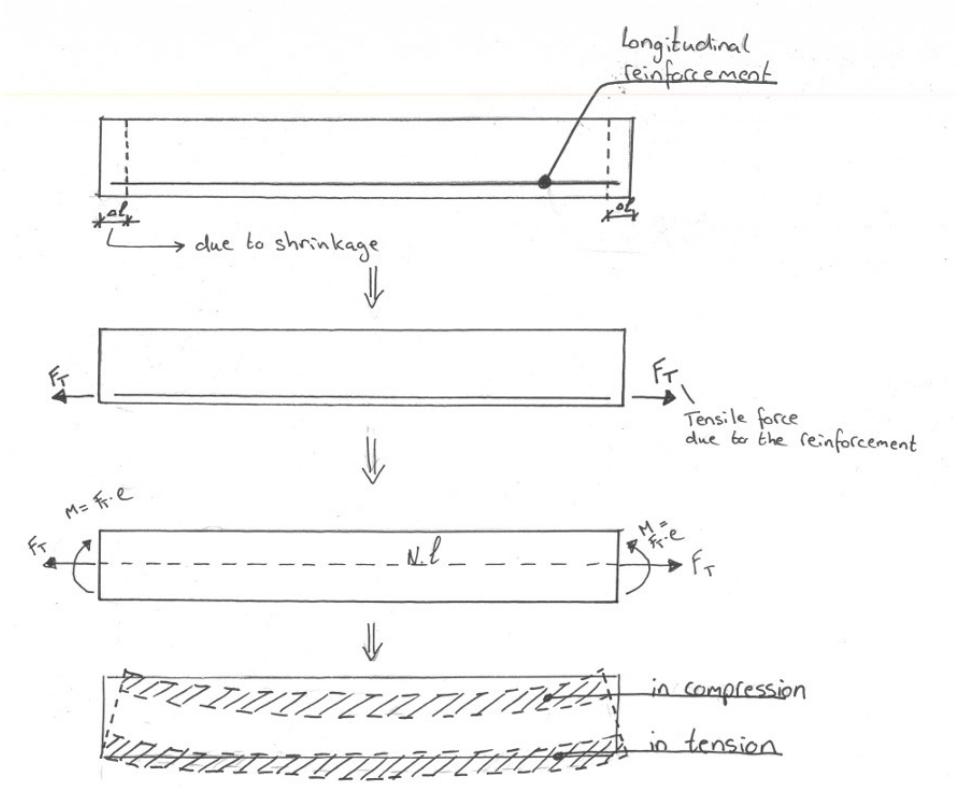

Figure 4.28: Drawings illustrating how shrinkage in a simplified reinforced beam results in higher internal stresses.

The horizontal mean values are shown in Figure 4.30b. These results show a lower UPV of 4.5 km/s for the S-AAC-C50 beams at the top (casting surface) of the specimens' height and a higher UPV of 4.8 km/s at the bottom of the specimens' height. This suggests that more micro-cracks are present at the top (casting surface) of the beam. Possible reasons for this can be increased exposure to air/wind on the top surface, making the top of the specimen more sensitive to drying shrinkage than the bottom.

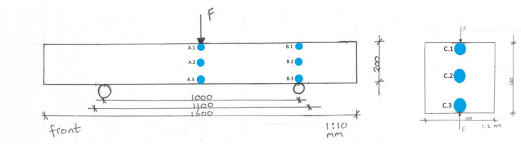

(a) (b)

Figure 4.29: Pictures showing the positioning of the UPV test: a) on the beams and b) on the cubes.

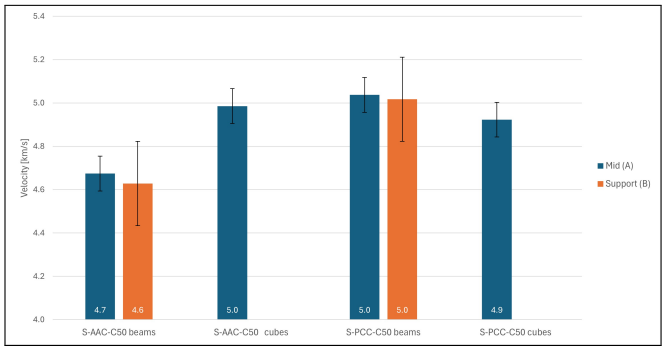

(a)

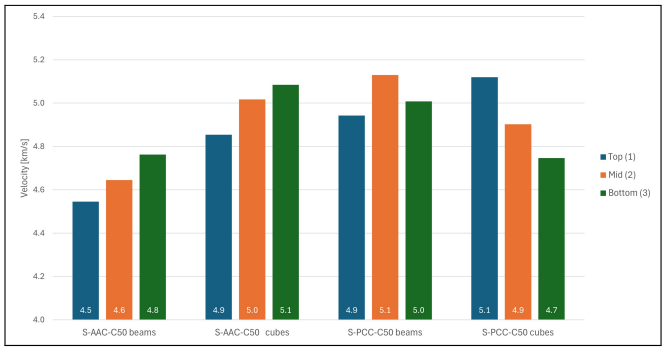

(b)

Figure 4.30: UPV measurements on S-AAC-C50 and S-PCC-C50 beams and cubes. a) Vertical results (mean of 1,2,3) b) Horizontal results of the RC beam (mean of A & B).

4.3. Structural behaviour of RC beams

4.3.1. Shear behaviour

28-day results without stirrups

The results for beams without stirrups tested at 28 days are presented in Figure 4.32. For the C30 mixtures, the results are shown in Figure 4.32a, while for the C50 mixtures, the results are presented in Figure 4.32b. The ultimate load capacities for the 28-day results are 117 kN, 114 kN, 145 kN, and 113 kN for the mixtures S-AAC-C30, S-PCC-C30, S-AAC-C50, and S-PCC-C50, respectively. These results are discussed in more detail in Chapter 5. Furthermore, the load paths for strain development for all the beams are provided in Appendix C.2.

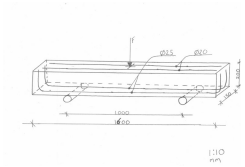

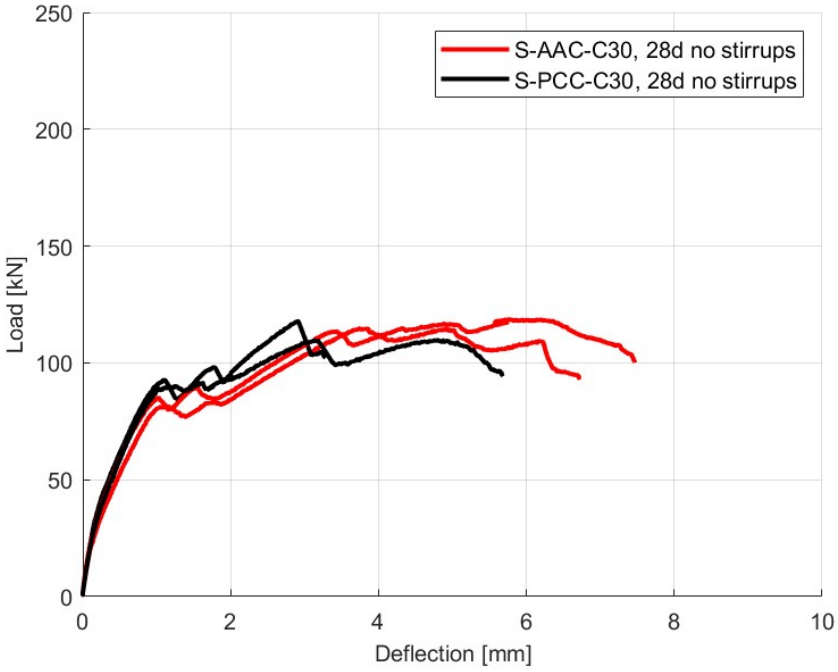

(a)

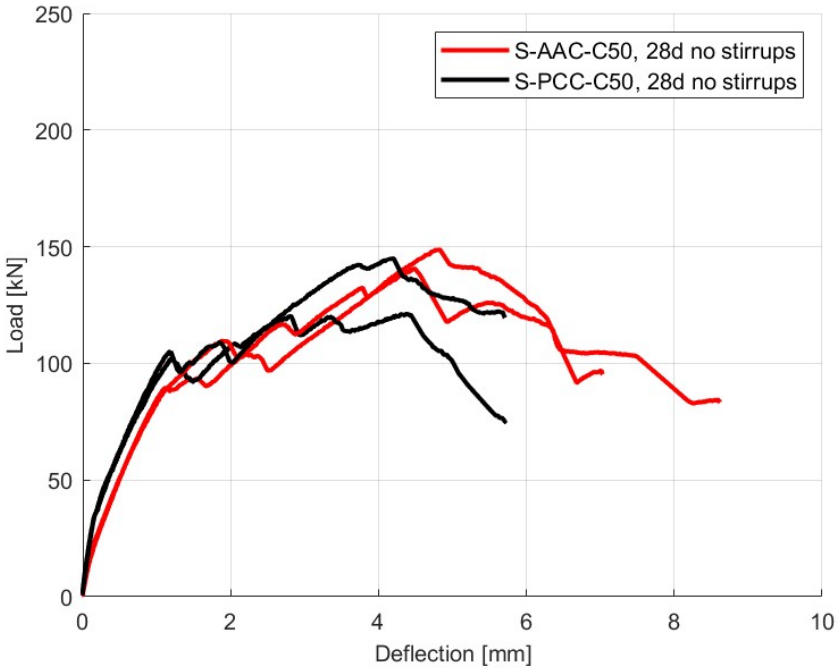

(b)

Figure 4.32: Load-displacement graphs of shear beams without stirrups tested at 28 days. (a) beams from mixtures C30, and (b) beams from mixtures C50.

28-day results with stirrups

The results for beams with stirrups tested at 28 days are presented in Figure 4.34. For the C30 mixtures, the results are shown in Figure 4.34a, while for the C50 mixtures, the results are displayed in Figure 4.34b. The ultimate load capacities for the 28-day results with stirrups are 214 kN, 198 kN, 224 kN, and 216 kN for the mixtures S-AAC-C30, S-PCC-C30, S-AAC-C50, and S-PCC-C50, respectively.

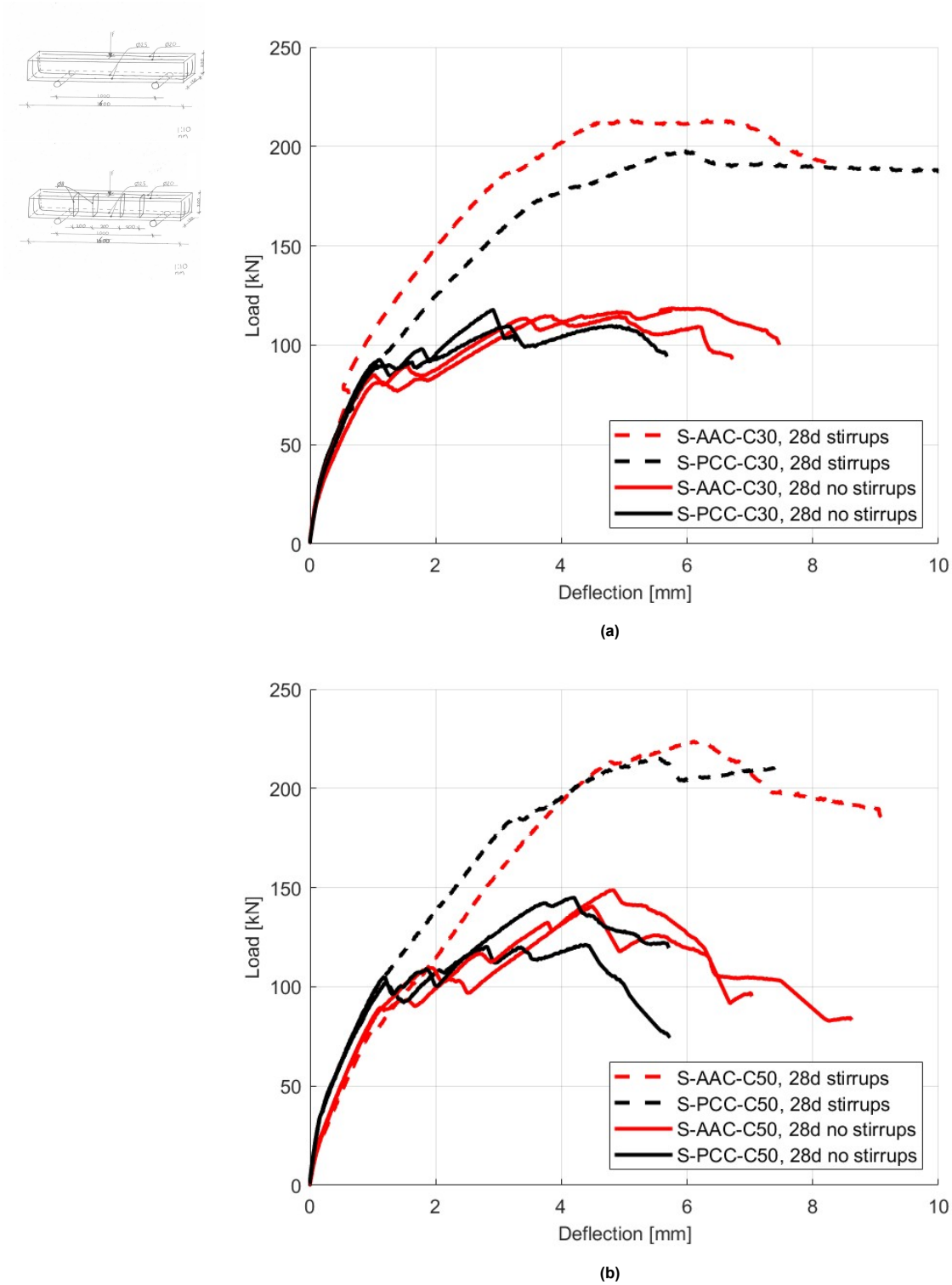

Figure 4.34: Load-displacement graphs of shear beams with and without stirrups tested at 28 days: (a) beams from C30 mixtures, and (b) beams from C50 mixtures.

6-months results without stirrups

The results for beams without stirrups tested at 6 months are presented in Figure 4.36. For the C30 mixtures, the results are shown in Figure 4.36a, while for the C50 mixtures, the results are presented in Figure 4.36b. The ultimate load capacities for the 6-month results are 146 kN, 146 kN, 156 kN, and 134 kN for the mixtures S-AAC-C30, S-PCC-C30, S-AAC-C50, and S-PCC-C50, respectively. These

results are discussed in more detail in Chapter 5.

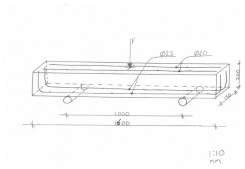

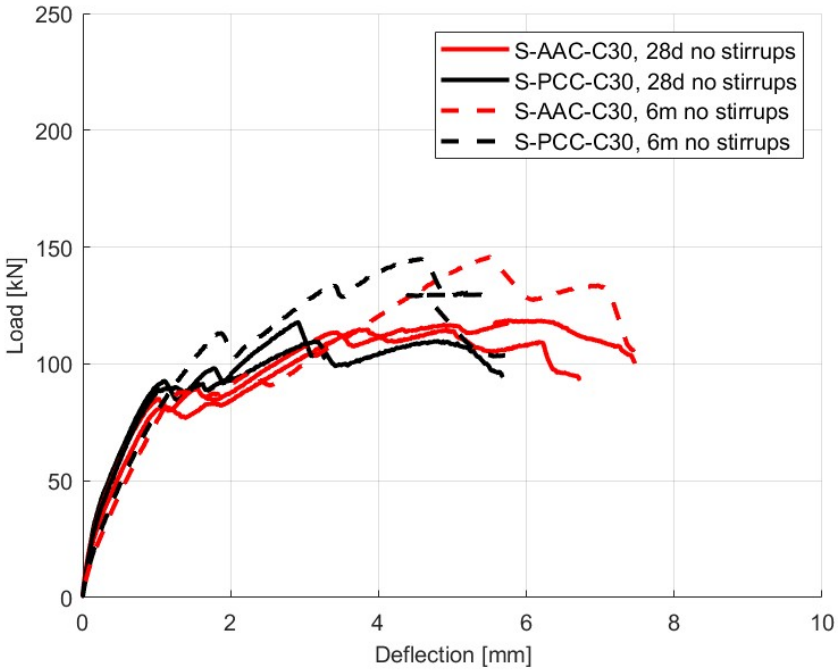

(a)

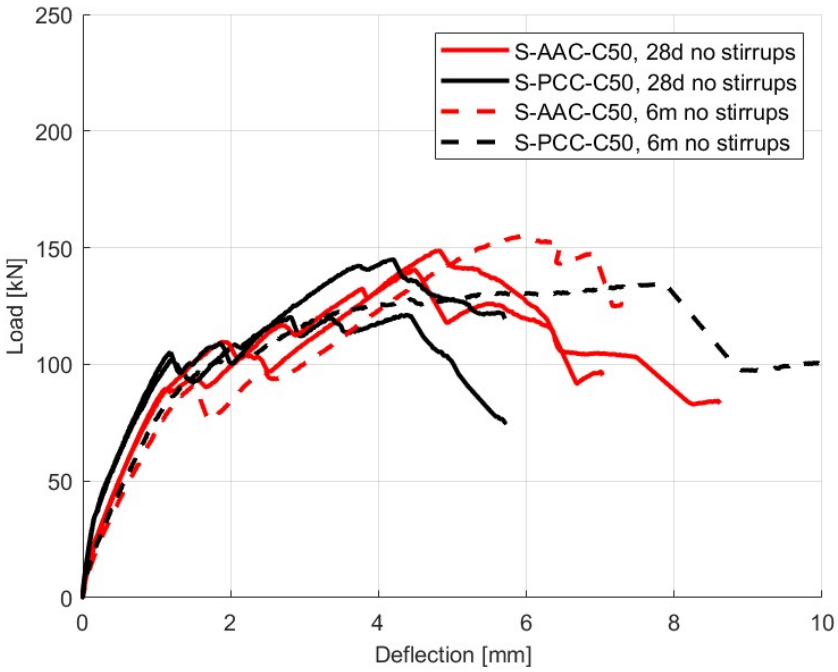

(b)

Figure 4.36: Load-displacement graphs of shear beams without stirrups tested at 28 days and 6 months: (a) beams from C30 mixtures, and (b) beams from C50 mixtures.

An overview of the ultimate shear capacity over time, 28 days and 6 months, is given in Figure 4.37. The results show similarity or an increase in ultimate shear capacity for all mixtures over 6 months. The biggest increase in ultimate shear capacity is shown in the C30 mixtures. The S-AAC-C50 also showed

a bigger increase over time compared to the S-PCC-C50 mixture.

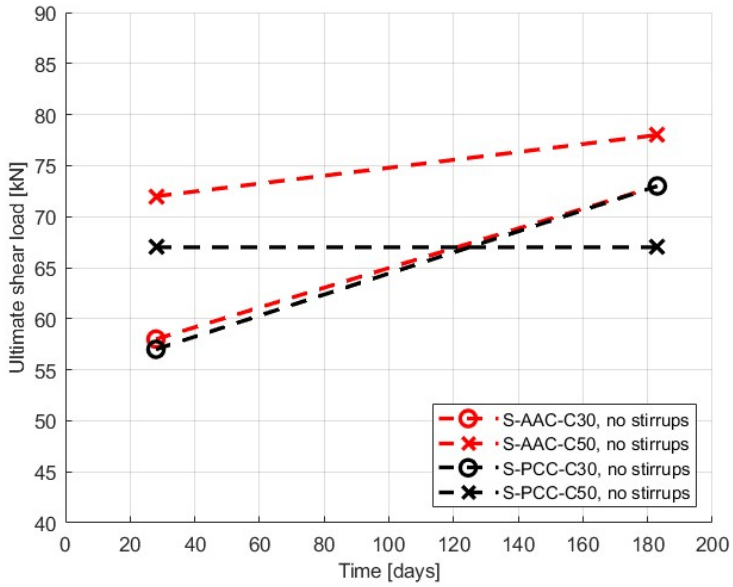

Figure 4.37: The mean ultimate shear load of the beam without stirrups versus time at 28 days and 6 months for the mixtures S-AAC-C30, S-PCC-C30, S-AAC-C50, and S-PCC-C50.

Normalized stress ratio

Furthermore, the shear results for beams without stirrups have been plotted as a normalized stress ratio using Equation 4.1 in Figure 4.39, and as a normalized stress including compressive strength using Equation 4.2 in Figure 4.41 and in Figure 4.43. The compressive strength f_c used is the mean experimental compressive strength 45, 43, 68 and 68 MPa at 28 days and 62, 55, 85 and 68 MPa at 6 months for the mixtures S-AAC-C30, S-PCC-C30, S-AAC-C50 and S-PCC-C50, respectively.

$$v = \frac{V}{b \cdot d} \tag{4.1}$$

$$v = \frac{V}{b \cdot d \cdot f_c^{1/3}} \tag{4.2}$$

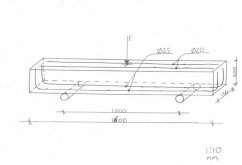

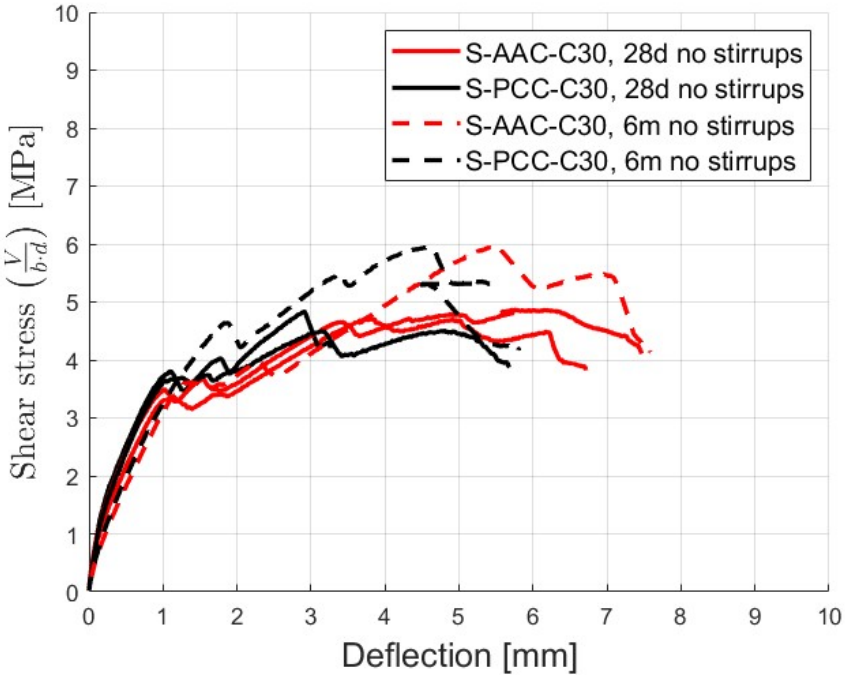

(a)

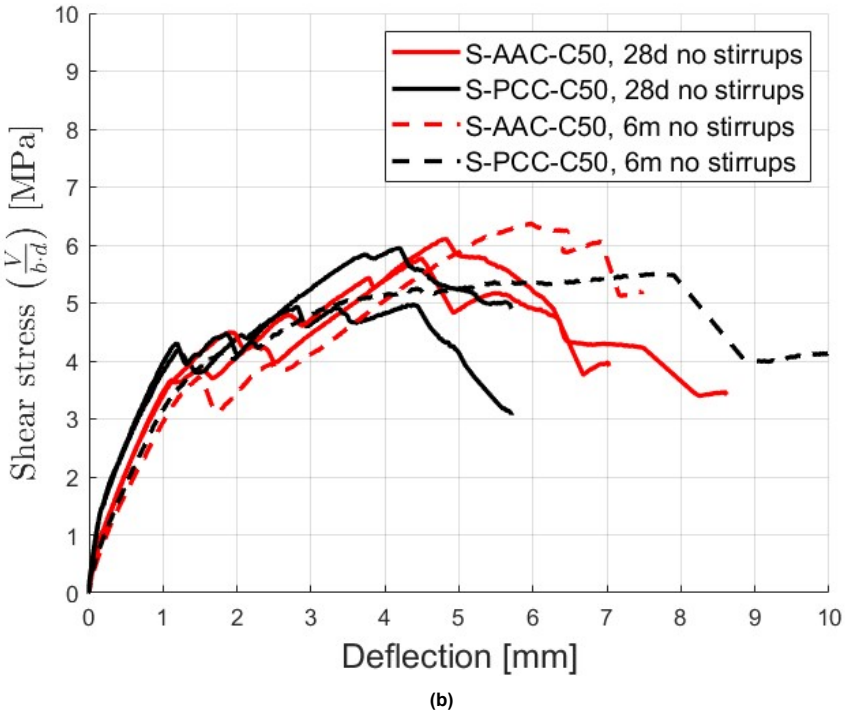

(b)

Figure 4.39: Normalized stress ratio $v = \frac{V}{b \cdot d}$ of shear beams without stirrups tested at 28 days and 6 months: (a) beams from C30 mixtures, and (b) beams from C50 mixtures.

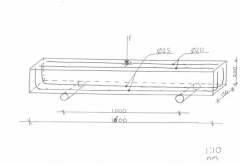

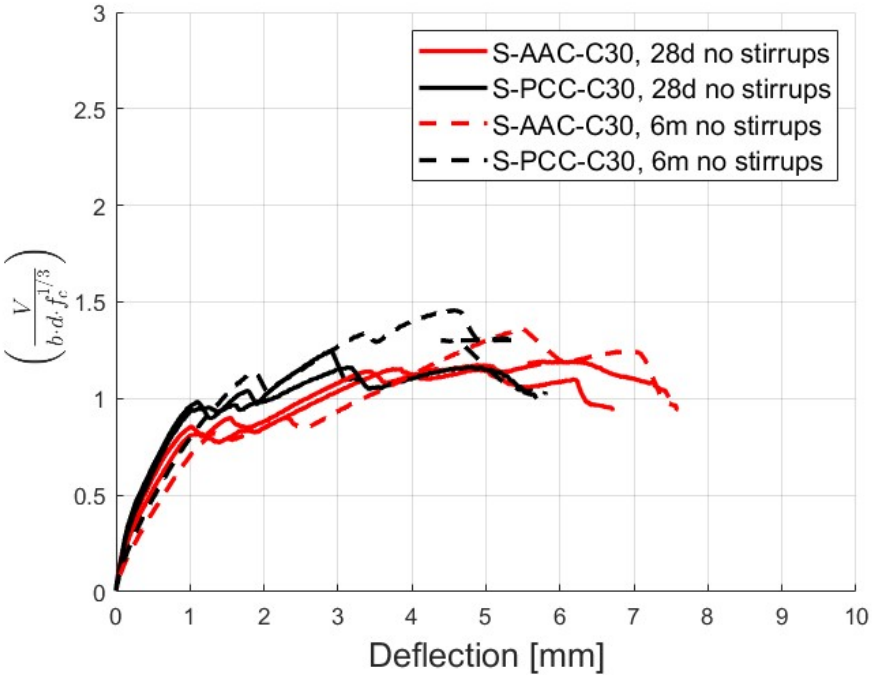

(a)

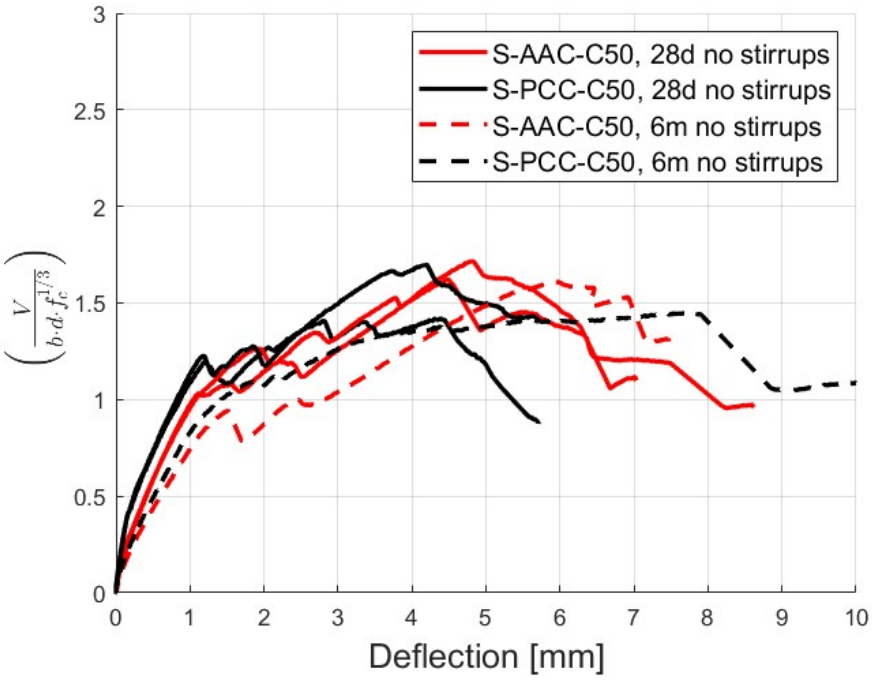

(b)

Figure 4.41: Normalized stress ratio including compressive force $v = \frac{V}{b \cdot d \cdot f_c^{1/3}}$ of shear beams without stirrups tested at 28 days and 6 months: (a) beams from C30 mixtures, and (b) beams from C50 mixtures.

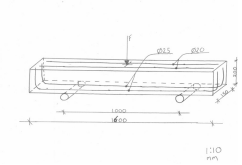

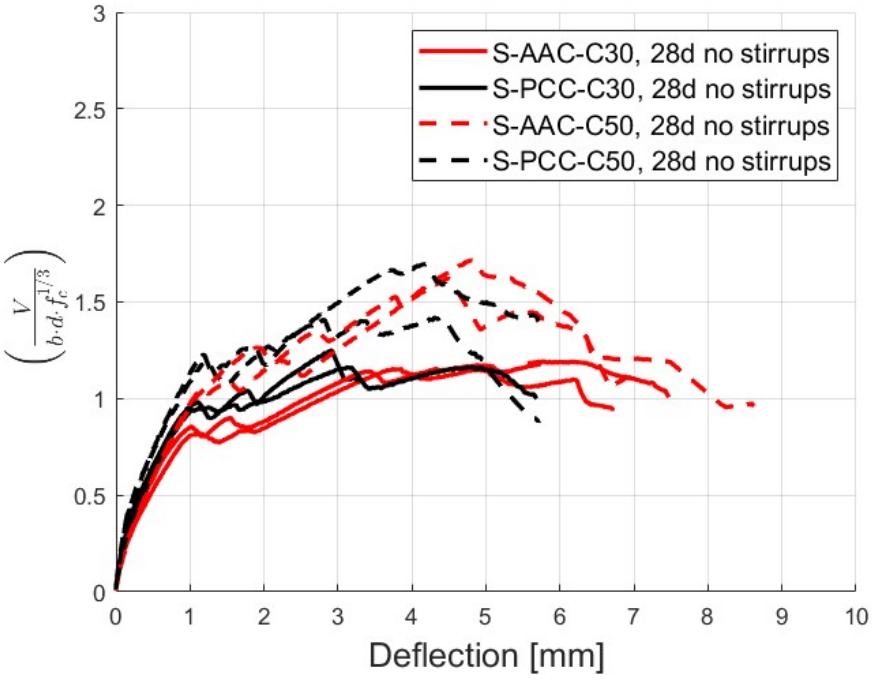

(a)

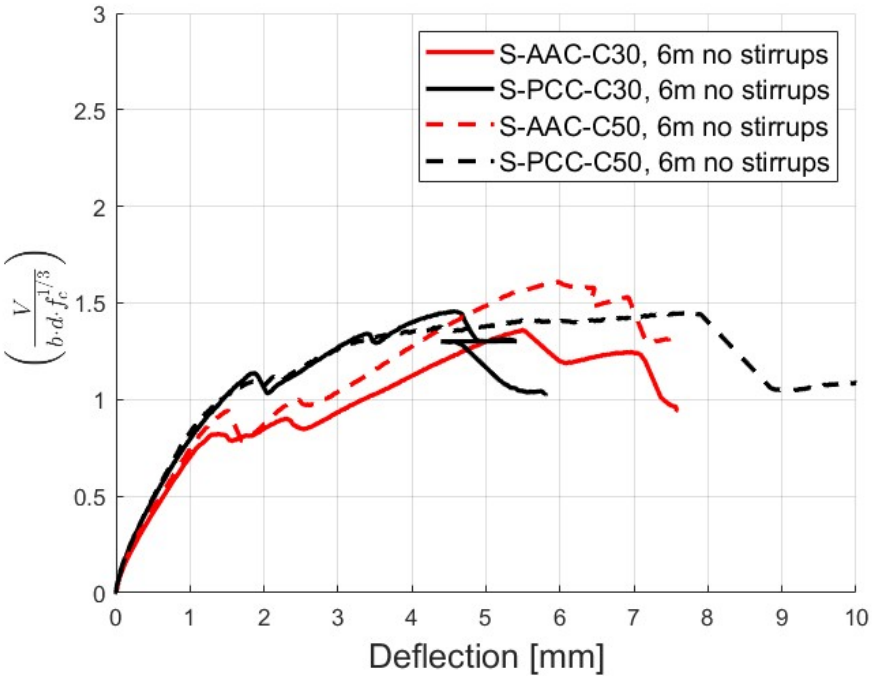

(b)

Figure 4.43: Normalized stress ratio including compressive force $v = \frac{V}{b \cdot d \cdot f_c^{1/3}}$ of shear beams without stirrups tested at 28 days and 6 months: (a) beams tested at 28 days and (b) beams tested 6 months.

5

Interpretation and comparison of the experimental results

5.1. General understanding of shear behaviour of one RC beam

To get a better understanding of the shear behaviour of the tested beams, the development of shear cracks, as discussed in Section 2.5.3, is applied to one tested beam. The beam selected is S-AAC-C30, tested at 28 days.

5.1.1. Crack pattern

First, the crack pattern of one selected beam has been documented and analysed along the test-displacement curve (see Figure 5.1).

This analysis shows that the first bending cracks begin to develop, followed by their inclination, which leads to the formation of the first shear crack. A second shear crack subsequently forms. Once both shear cracks have developed, the load continues to increase, causing the cracks to lengthen and widen until the ultimate failure capacity is reached. Thereafter, additional cracks form and the load gradually decreases.

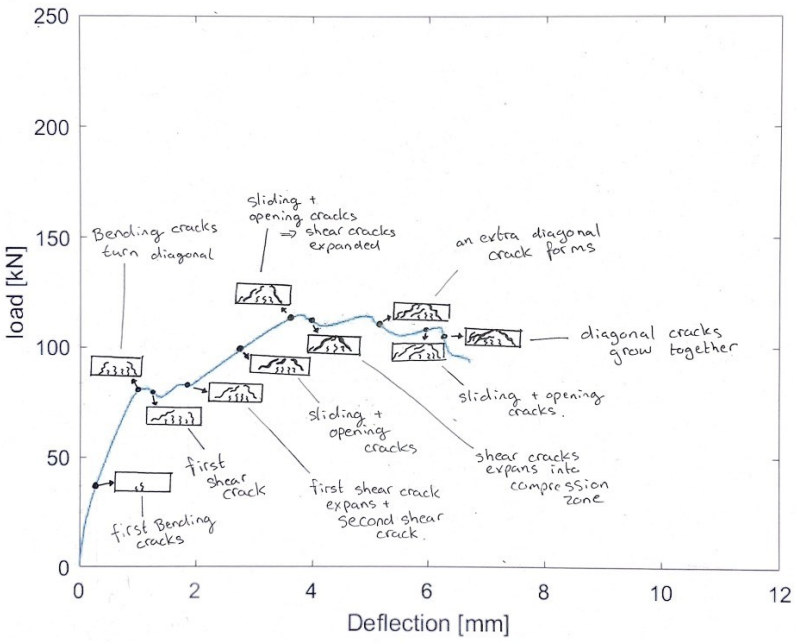

Figure 5.1: Load-deflection curve of S-AAC-C30, with figures of the crack pattern obtained form DIC.

5.1.2. Stages of shear failure

Secondly, the stages of shear failure discussed in section 2.5.3 (initial flexural cracks, inclination of flexural cracks, crack stabilization stage, failure and residual capacity) are placed along the load-deflection curve by using the crack pattern that was observed and the document before (see Figure 5.2).

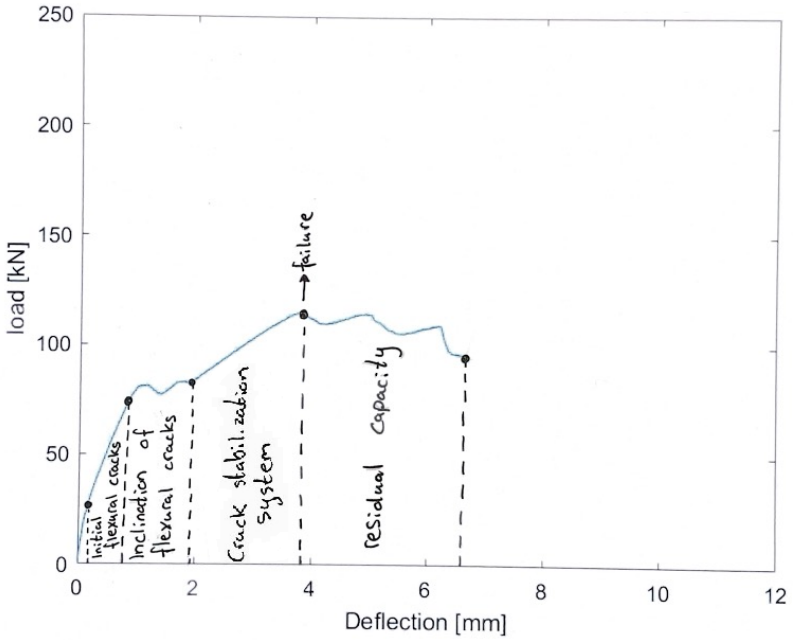

Figure 5.2: Load-deflection curve of S-AAC-C30-3, with stages of shear failure.

5.1.3. Role of material properties on structural behaviour

Finally, for all defined stages of shear failure, the corresponding material properties influencing each stage are listed along the load-deflection curve (see Figure 5.3).

This begins with the elastic modulus, which influences the stiffness of the specimen and can be calculated from the first linear part of the load-deflection curve. This is followed by the tensile strength, which can be determined from the first bending crack. Bending cracks start to appear when the tensile stresses caused by the load exceed the tensile resistance of the specimen. After that, shear stress and normal stresses contribute to the formation of shear cracks. Next, aggregate interlock, dowel action, and tensile softening behaviour ensure a load increase after the formation of shear cracks, until failure occurs. After failure, bond strength and compressive strength contribute to the remaining residual capacity.

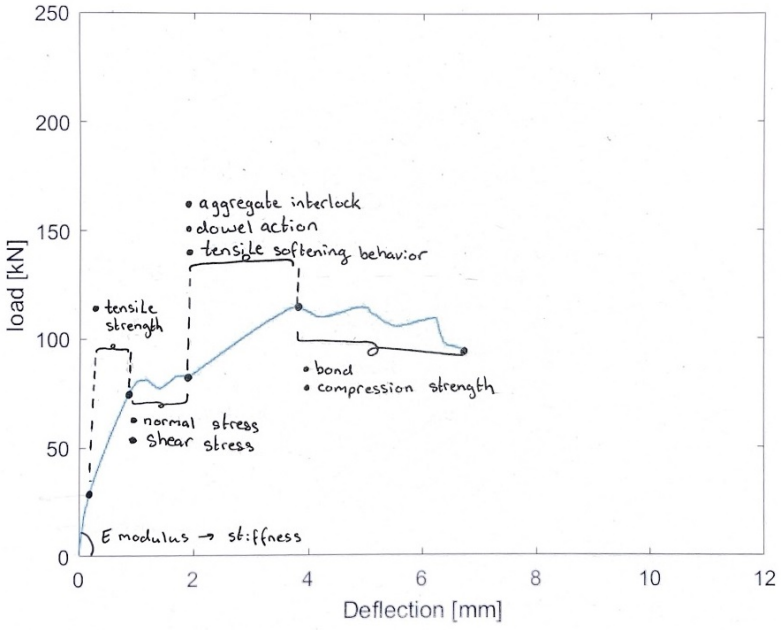

Figure 5.3: Load deflection curve of S-AAC-C30-3, with material influences.

5.2. Analysis of the shear behaviour of all tested RC beams.

5.2.1. Initial flexural cracks

Mixture S-AAC-C30

First, to better understand the experimental results of the shear test, the initial flexural cracks were investigated. This was done by documenting the DIC results of the concrete strains for the S-AAC-C30 mixtures tested at 28 days and 6 months, side by side for different load steps (10, 15, 20, 25, 30, 40, 50, 60, 70, and 80 kN), see Figure 5.4.

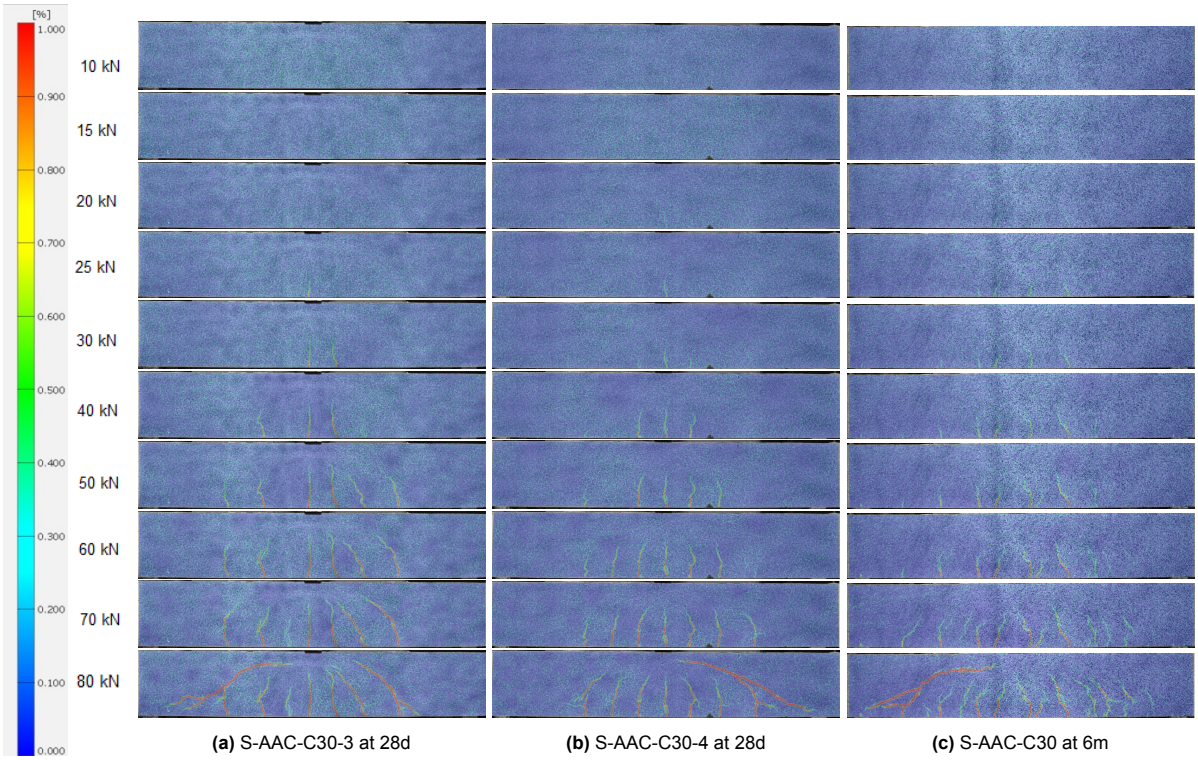

(a) S-AAC-C30-3 at 28d **(b)** S-AAC-C30-4 at 28d **(c)** S-AAC-C30 at 6m

Figure 5.4: Comparison of concrete strains for beam S-AAC-C30-3 and beam S-AAC-C30-4 tested at 28 days, and beam S-AAC-C30-6m tested at 6 months, under different load steps (10, 15, 20, 25, 30, 40, 50, 60, 70, and 80 kN) *[Scale: 0–1], [Unit:-].*

From the DIC results of the concrete strains, it can be concluded that the beams tested at 28 days show a similar crack path. Beam S-AAC-C30-3 tested at 28 days exhibits 7 bending cracks at 70 kN, with a mean length of 118 mm and a mean spacing of 87 mm. Beam S-AAC-C30-4 tested at 28 days shows 7 bending cracks at 70 kN, with a mean length of 111 mm and a mean spacing of 89 mm.

The DIC results of the concrete strain also reveal that the beam tested at 6 months shows a different crack path compared to the 28-day results. Beam S-AAC-C30-6m tested at 6 months shows 11 bending cracks at 70 kN, with a mean length of 100 mm and a mean spacing of 71 mm. This crack pattern indicates more cracks already at an early load of 25 kN, likely caused by micro-cracks introduced by shrinkage. As a result, there are more bending cracks on the specimen, with shorter crack lengths and smaller spacing between the cracks.

Secondly, to gain an understanding of the developments and material influences in the initial stage of flexural cracks, a zoom-in on the load-displacement graph has been made (see Figure 5.5). The first initial bending cracks and elastic modulus can be obtained from these curves.

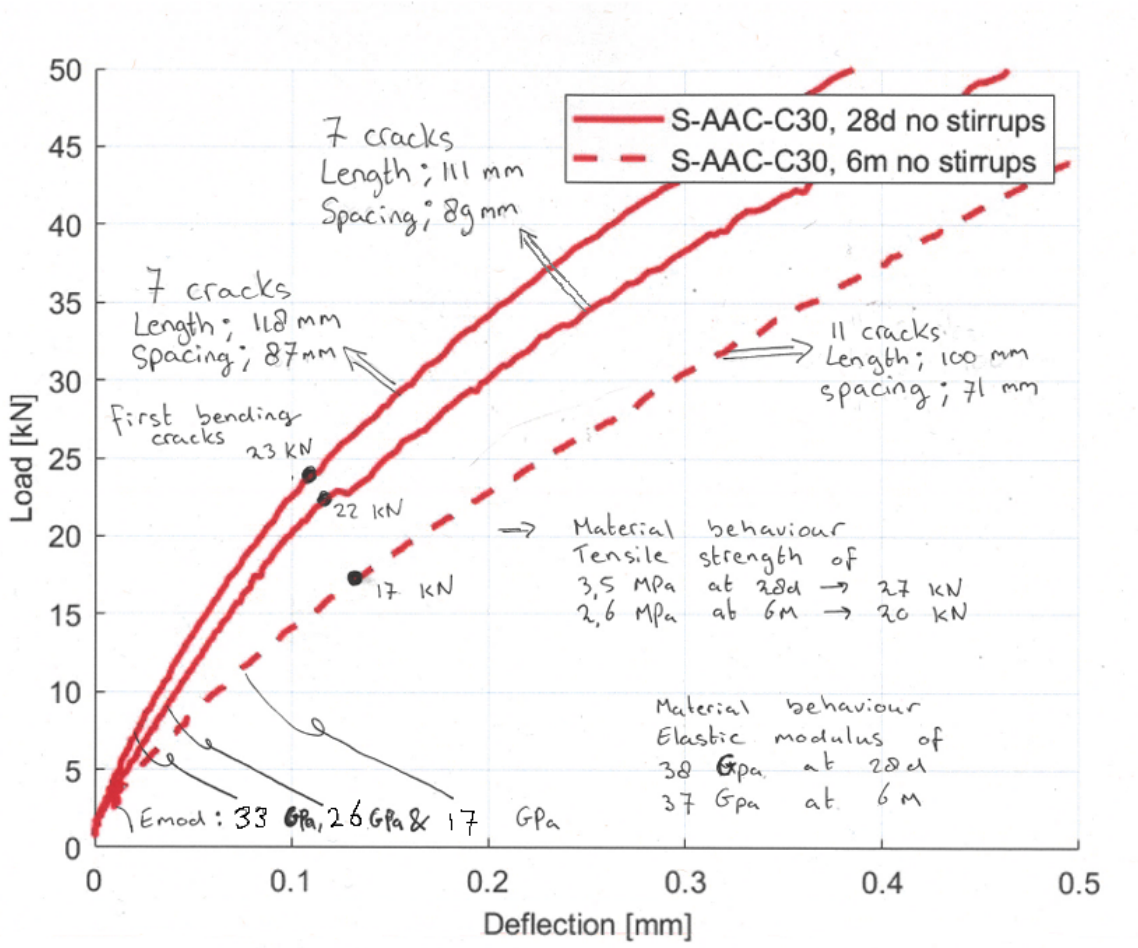

Figure 5.5: Zoom of the load-deflection curves of the beams from mixture S-AAC-C30, with two tested at 28 days and one tested at 6 months.

Firstly, the elasticity modulus can be determined and compared to the modulus obtained experimentally when testing the material behaviour (see Section 4.1.3). The elastic modulus obtained for the shear test is done at 10 kN. The elastic modulus obtained from the shear beams is 33, 26, and 17 GPa for the beams S-AAC-C30-3 tested at 28 days, S-AAC-C30-4 tested at 28 days, and S-AAC-C30-6m tested at 6 months, respectively. The elastic modulus from the material behaviour test was 38 GPa at 28 days and 37 GPa at 6 months. It can be noted that in the shear behaviour test, the elastic modulus decreases over six months, by -43%. This behaviour differs from the material behaviour test, where the elastic modulus remains similar over time.

Secondly, the first bending cracks can be identified on the load-displacement graph (see figure 5.6. Initial flexural cracks form when the tensile stresses caused by the load exceed the tensile stress resistance of the material. The results from the material behaviour test are a tensile resistance of 3.5 MPa (27 kN) at 28 days and 2.6 MPa (20 kN) at 6 months (see Section 4.1.2). The first bending cracks observed from the DIC analysis of the shear experiments occurred at 23 kN, 22 kN, and 17 kN for the beams S-AAC-C30-3 tested at 28 days, S-AAC-C30-4 tested at 28 days, and S-AAC-C30-6m tested at 6 months, respectively. When comparing these results it can be concluded that the results of the shear behaviour test show a reduction of -15% at 28 days and -15% at 6 months.

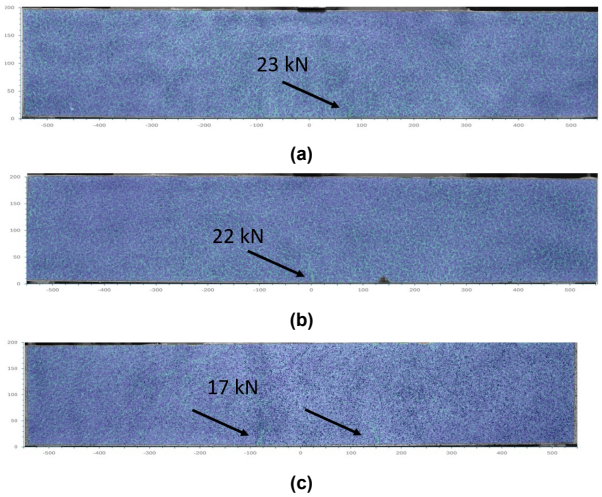

Figure 5.6: First crack from the DIC. a) beam S-AAC-C30-2 at 23 kN tested at 28 days, b) beam S-AAC-C30-3 at 22 kN tested at 28 days and c) beam S-AAC-C30-6m at 17 kN tested at 6 months

Mixture S-PCC-C30

To make a proper comparison to the S-AAC-C30 mixture, the initial flexural cracks of the S-PCC-C30 mixtures were also investigated. This was first done by documenting the DIC results of the concrete strains for the S-PCC-C30 mixtures tested at 28 days and 6 months, side by side for different load steps (10, 15, 20, 25, 30, 40, 50, 60, 70, and 80 kN), as shown in Figure 5.7. Unfortunately, one S-PCC-C30 beam tested at 28 days had missing DIC images for smaller load steps, which is why only one 28-day beam is documented in the figure.

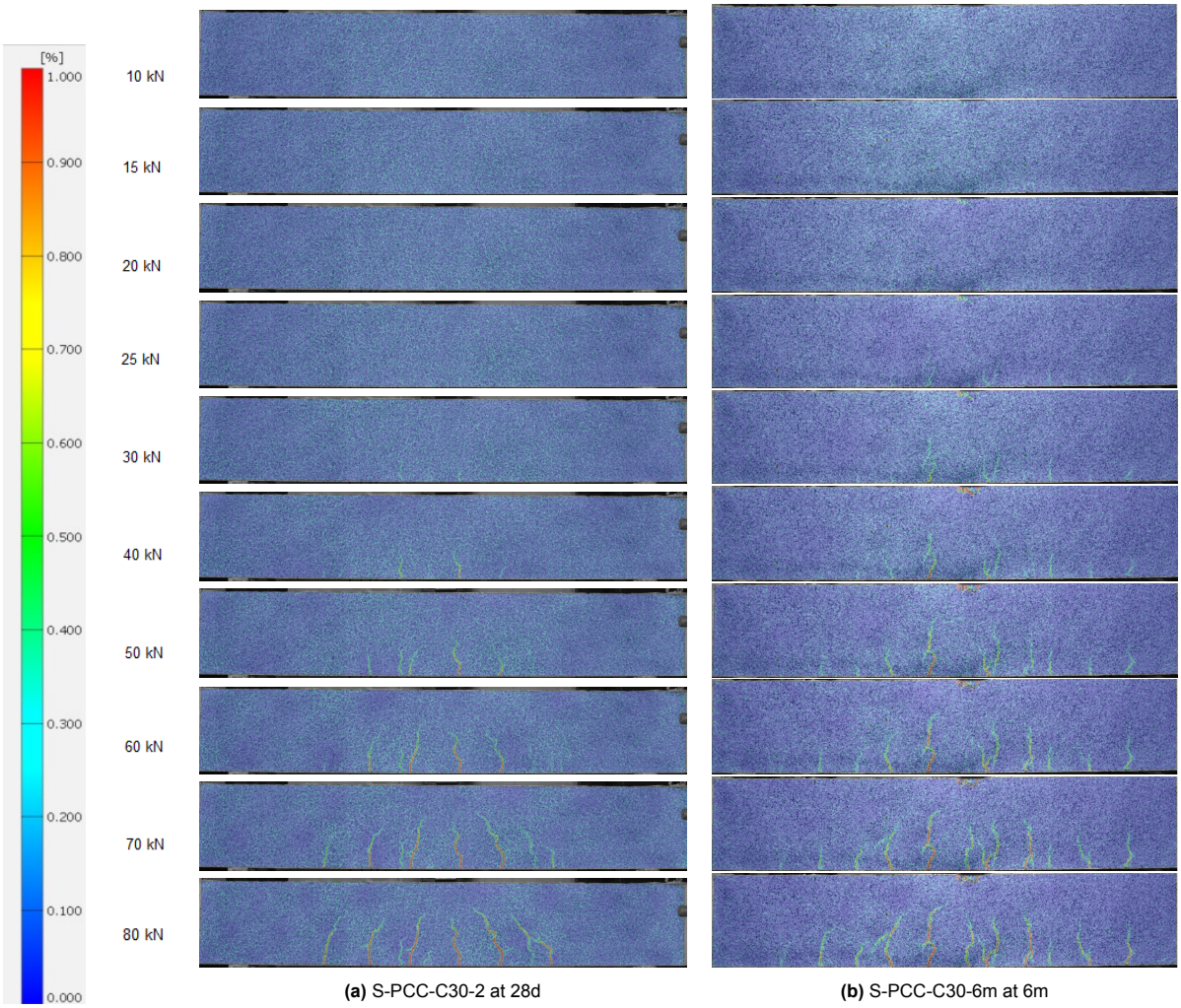

(a) S-PCC-C30-2 at 28d **(b)** S-PCC-C30-6m at 6m

Figure 5.7: Comparison of concrete strains for beam S-PCC-C30-2 tested at 28 days and beam S-PCC-C30-6m tested at 6 months, under different load steps (10, 15, 20, 25, 30, 40, 50, 60, 70, and 80 kN) *[Scale: 0–1], [Unit:-].*

The DIC results of the concrete strain show a difference in the crack path between the 28-day and 6-month results. The beam S-PCC-C30-2 tested at 28 days shows 6 bending cracks at 70 kN, with a mean length of 124 mm and a spacing of 105.7 mm between the cracks. In comparison, the beam S-PCC-C30-6m tested at 6 months shows 9 bending cracks at 70 kN, with a length of 110 mm and a spacing of 85 mm. Similar to the S-AAC-C30 tested at 6 months, the S-PCC-C30 beam tested at 6 months also shows more cracks at an early load of 25 kN compared to the 28-day results. The reason for this is likely micro-cracks introduced by shrinkage also for the S-PCC-C30 beam.

Furthermore, Also for the S-PCC-C30 mixture, a zoom-in of the load-displacement curves has been made (see Figure 5.8).

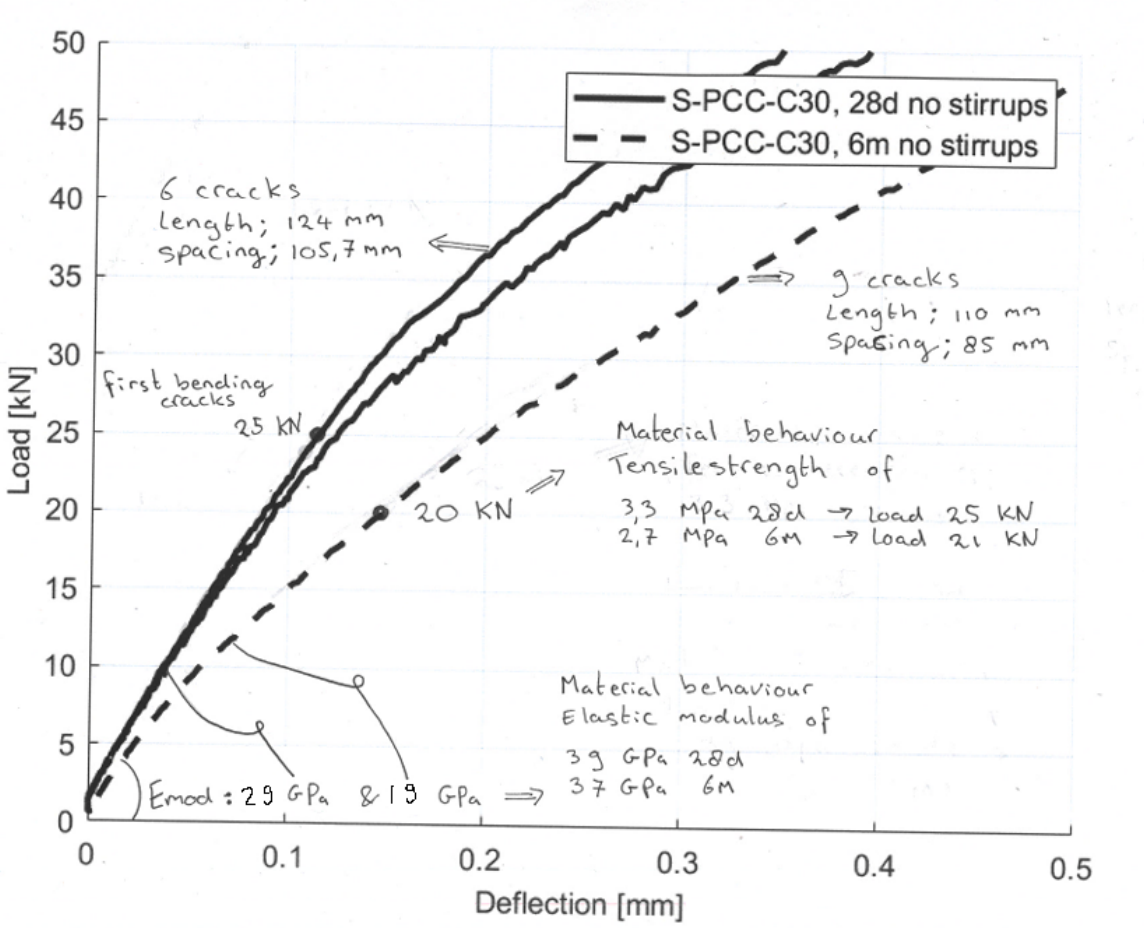

Figure 5.8: Zoom of the load-deflection curves of the beams from mixture S-PCC-C30, with two beams tested at 28 days and one beam tested at 6 months.

Firstly, the elastic modulus can be determined and compared to the values obtained experimentally from material behaviour tests. The elastic modulus from the shear behaviour test is 29 GPa for the beam S-PCC-C30-2 tested at 28 days and 19 GPa for the beam S-PCC-C30-6m tested at 6 months. In contrast, the elastic modulus obtained from the experimental material behaviour tests is 39 GPa and 37 GPa for the 28-day and 6-month tests, respectively. Similar to the S-AAC-C30 mixture, the elastic modulus obtained from the shear behaviour test decreases over six months. However, for the S-PCC-C30 mixture, this decrease is slightly less pronounced compared to the S-AAC-C30 mixture, namely -34%.

Secondly, the first bending cracks can be identified on the load-displacement graphs and compared to the results from the material behaviour test for direct tensile strength. The direct tensile strength test results are a maximum of 3.3 Mpa (25 kN) for 28 days and 2.7 MPa (21 kN). The DIC results show that first bending cracks are at 25 kN for the 28 results and 20 kN for the 6-month results (see figure 5.9). These are similar to the results obtained from the material behaviour test.

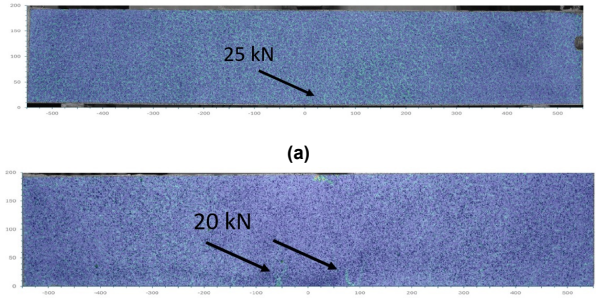

Figure 5.9: First crack from the DIC. a) beam S-PCC-C30-2 at 25 kN tested at 28 days, and b) beam S-PCC-C30-6m at 20 kN tested at 6 months

Comparison of S-AAC-C30 and S-PCC-C30 mixtures

To better understand the differences and/or similarities in the initial bending cracks between the S-AAC-C30 and S-PCC-C30 mixtures at 28 days, the load paths of the concrete strains obtained from DIC are visualized side by side (see Figure 5.10).

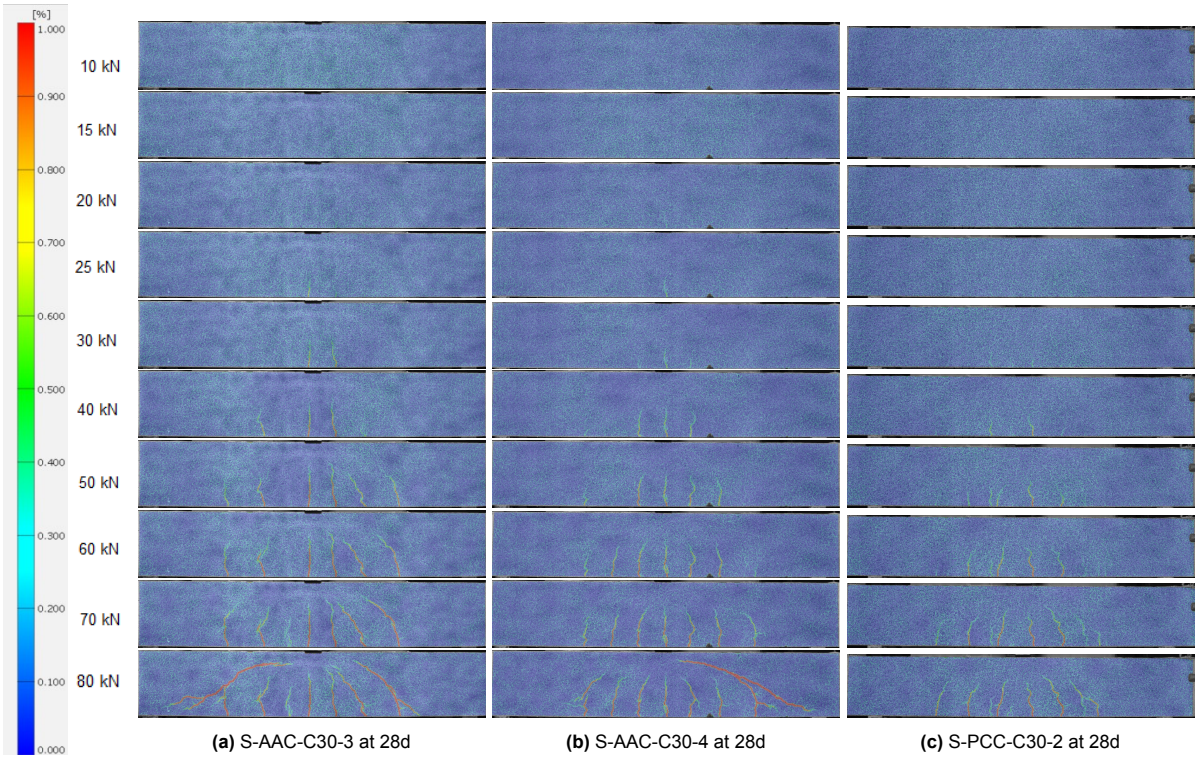

Figure 5.10: Comparison of concrete strains for beam S-AAC-C30-3, beam S-AAC-C30-4 and beam S-PCC-C30-2 tested at 28 days, under different load steps (10, 15, 20, 25, 30, 40, 50, 60, 70, and 80 kN) *[Scale: 0–1], [Unit:-].*

To better understand the differences and/or similarities in the initial bending cracks of the S-AAC-C30 and S-PCC-C30 mixtures at 6 months, the load paths of the concrete strains obtained from DIC are visualised side by side (see Figure 5.11).

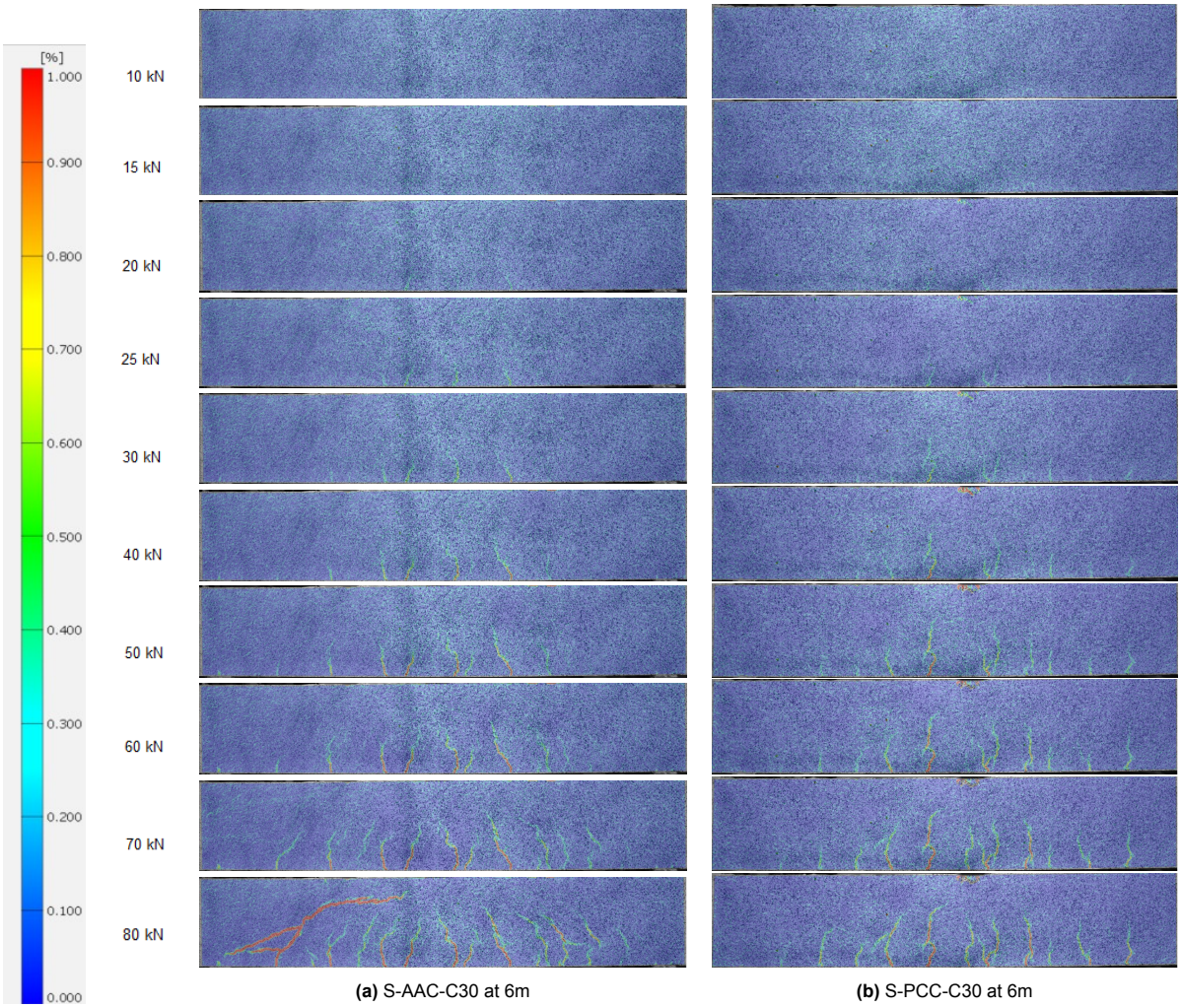

(a) S-AAC-C30 at 6m **(b)** S-PCC-C30 at 6m

Figure 5.11: Comparison of concrete strains for beam S-AAC-C30-6m and S-PCC-C30-6m tested tested at 6 months, under different load steps (10, 15, 20, 25, 30, 40, 50, 60, 70, and 80 kN) *[Scale: 0–1], [Unit:-]*.

When comparing the first bending crack for both mixtures, the following observations can be made: for the S-AAC-C30 mixture, the first bending cracks occur at 23 kN at 28 days and at 17 kN at 6 months. In contrast, for the S-PCC-C30 mixture, the first bending cracks occur at 25 kN at 28 days and at 20 kN at 6 months. The load difference between the mixtures is very small therefore, it can be considered to be similar for both mixtures.

Secondly, when looking at the elastic modulus determined at a load of 10 kN, it can be considered similar for both mixtures. The 28-day results align with the material behaviour tests for elastic modulus discussed in Section 4.1.3. However, the material behaviour tests reveal no significant differences between the 28-day and 6-month results for either mixture. In contrast, the shear test indicates a reduction of 42% and 34% in the elastic modulus for the mixtures S-AAC-C30 and S-PCC-C30 at 6 months. This reduction could be attributed to shrinkage over time, as both mixtures experienced autogenous and drying shrinkage over the 6 months (see Sections 4.2.2 and 4.2.3). The specimens tested for elastic modulus were unrestrained to shrink, while the longitudinal reinforcement in the shear beams restricted shrinkage, leading to the formation of microcracks. If microcracks are present, the elastic modulus cannot be accurately determined at 10 kN because the concrete has already sustained damage.

Furthermore, when comparing the number of cracks at 70 kN, both mixtures exhibit similar results at both 28 days and 6 months. The spacing between cracks is also comparable for both mixtures at these time intervals. However, differences are observed in crack length: the S-AAC-C30 mixtures

show longer cracks at both 28 days and 6 months. Variations in crack length may be influenced by the tensile strength or residual tensile strength of the mixtures. The material behaviour discussed in Section 4.1.2 indicates a higher tensile strength at 28 days for the S-AAC-C30 mixture compared to the S-PCC-C30 mixture, which would suggest shorter cracks in the S-AAC-C30 mixture. However, the longer cracks observed in the S-AAC-C30 mixture could be attributed to increased shrinkage compared to the S-PCC-C30 mixture. This shrinkage, coupled with the restrained shrinkage of the shear beams due to longitudinal reinforcement, may lead to the formation of microcracks and reduction of the tensile strength over time resulting in longer crack lengths.

Mixture S-AAC-C50

Also for the S-AAC-C50 mixtures the initial flexural cracks were investigated. This was done by documenting the DIC results of the concrete strains for the S-AAC-C50 mixtures tested at 28 days and 6 months, side by side for different load steps (10, 15, 20, 25, 30, 40, 50, 60, 70, and 80 kN), see Figure 5.12.

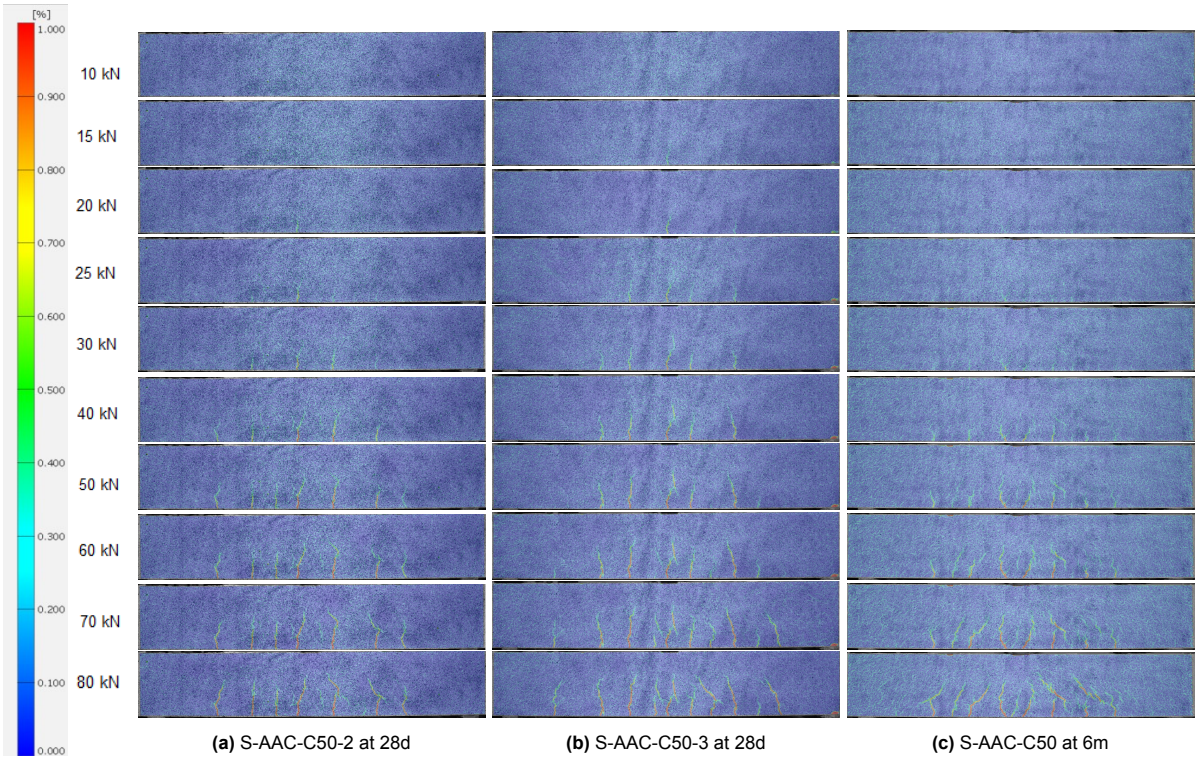

(a) S-AAC-C50-2 at 28d **(b)** S-AAC-C50-3 at 28d **(c)** S-AAC-C50 at 6m

Figure 5.12: Comparison of concrete strains for beam S-AAC-C50-2 and beam S-AAC-C50-3 tested at 28 days, and beam S-AAC-C50-6m tested at 6 months, under different load steps (10, 15, 20, 25, 30, 40, 50, 60, 70, and 80 kN) *[Scale: 0–1], [Unit:-].*

From the DIC results of the concrete strains, it can be concluded that the beams tested at 28 days exhibit some differences in the crack paths. While the length of the cracks is similar, the number of cracks and their spacing differ between the beams. Beam S-AAC-C50-2, tested at 28 days, shows 7 bending cracks at a load of 70 kN, with an average crack length of 107 mm and a spacing of 101 mm. In contrast, Beam S-AAC-C50-3, also tested at 28 days, exhibits 9 bending cracks at the same load, with a crack length of 101 mm and a spacing of 88 mm.

When comparing the 28-day results with the 6-month results, differences in the timing of the first cracks can be observed. For the 28-day beams, cracks begin to form around 15 kN, whereas for the 6-month beam, the first cracks appear after 20 kN. Additionally, the cracking pattern differs: the 28-day beams initially develop one crack, which gradually leads to multiple cracks. In contrast, the 6-month beam exhibits multiple small cracks forming simultaneously. These cracks eventually develop into 7, 9, and 9 cracks for beams S-AAC-C50-2, S-AAC-C50-3, and S-AAC-C50-6m, respectively.

Furthermore, for the S-PCC-C50 mixture, a zoom-in of the load-displacement curves has been made (see Figure 5.13).

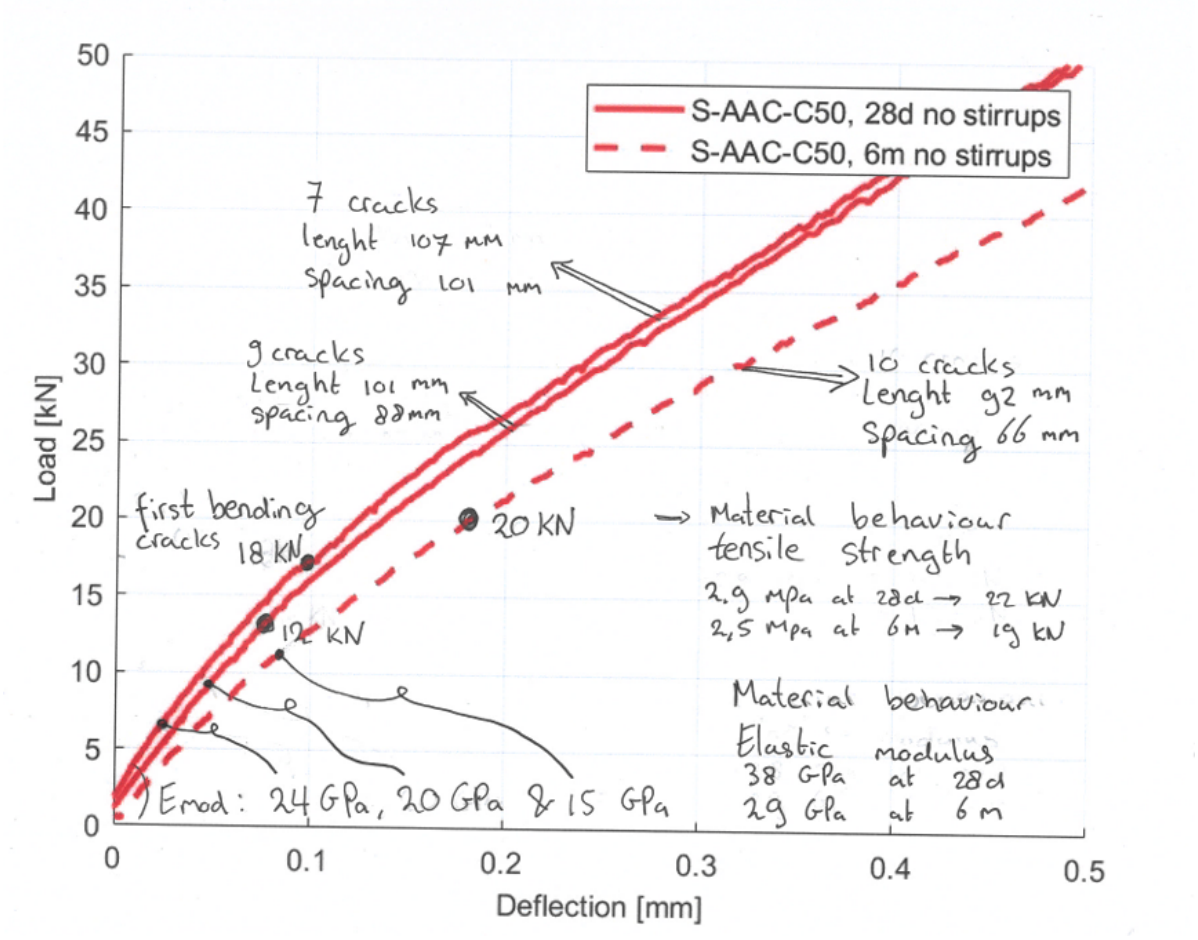

Figure 5.13: Zoom of the load-deflection curves of the beams from mixture S-AAC-C50, with two beams tested at 28 days and one beam tested at 6 months.

In this zoomed-in load-displacement curve, the first bending cracks (see Figure 5.14) are observed at 18 kN, 12 kN, and 20 kN for beams S-AAC-C50-2, S-AAC-C50-3, and S-AAC-C50-6m, respectively. The 28-day results are slightly lower than the tensile strength predicted by the material behaviour test, which estimated the first bending cracks at 22 kN. However, the 6-month results align closely with the material behaviour test, which predicted the first bending cracks at 19 kN.

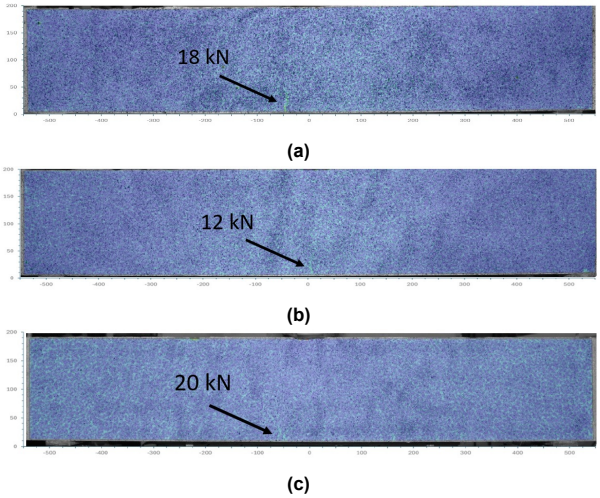

Figure 5.14: First crack from the DIC. a) beam S-AAC-C50-1 tested at 28 days, b) beam S-AAC-C50 tested at 28 days and c) beam S-AAC-C50-6m tested at 6 months

Furthermore, the elastic modulus was calculated at a load of 10 kN, resulting in values of 24 GPa, 20 GPa, and 15 GPa for beams S-AAC-C50-2, S-AAC-C50-3, and S-AAC-C50-6m, respectively. These values are slightly lower than those obtained from the material behaviour tests, which reported elastic modulus of 38 GPa at 28 days and 29 GPa at 6 months.

The lower elastic modulus and difference in crack pattern can again be attributed to shrinkage. The S-AAC-C50 mixture exhibited the highest amount of shrinkage compared to the S-AAC-C30, S-PCC-C30, and S-PCC-C50 mixtures.

Mixture S-PCC-C50

To make a good comparison to the S-AAC-C50 mixture, the initial flexural cracks of the S-PCC-C50 mixture are also investigated. This was done by documenting the DIC results of the concrete strains for the S-PCC-C50 mixtures tested at 28 days and 6 months, side by side for different load steps (10, 15, 20, 25, 30, 40, 50, 60, 70, and 80 kN), see Figure 5.15.

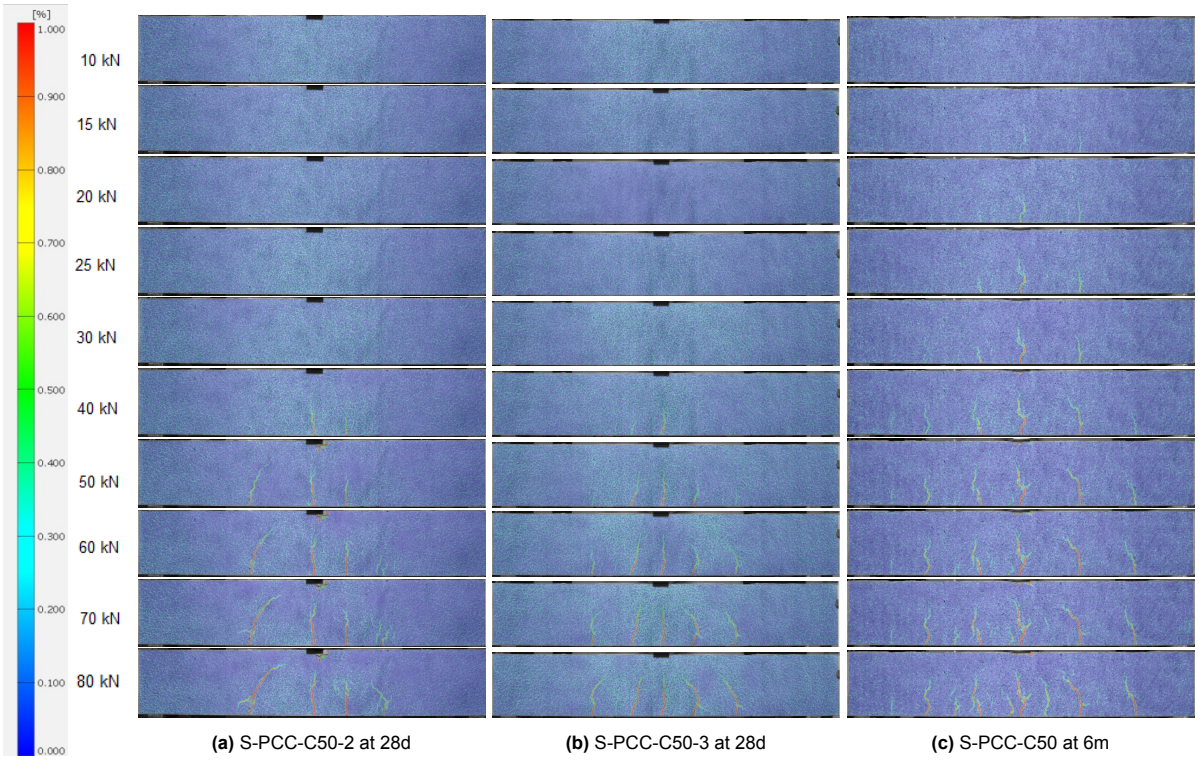

(a) S-PCC-C50-2 at 28d **(b)** S-PCC-C50-3 at 28d **(c)** S-PCC-C50 at 6m

Figure 5.15: Comparison of concrete strains for beam S-PCC-C50-2 and beam S-PCC-C50-3 tested at 28 days, and beam S-PCC-C50-6m tested at 6 months, under different load steps (10, 15, 20, 25, 30, 40, 50, 60, 70, and 80 kN) *[Scale: 0–1], [Unit:-].*

From the DIC results of the concrete strains, it can be concluded that the beams tested at 28 days show a similar crack path. Beam S-PCC-C50-2 tested at 28 days exhibits 4 bending cracks at 70 kN, with a mean length of 113 mm and a mean spacing of 138 mm. Beam S-PCC-C50-3 tested at 28 days shows 5 bending cracks at 70 kN, with a mean length of 123 mm and a mean spacing of 119 mm.

The DIC results of the concrete strain also reveal that the beam tested at 6 months shows a different crack path compared to the 28-day results. Beam S-PCC-C50-6m tested at 6 months shows 7 bending cracks at 70 kN, with a mean length of 105 mm and a mean spacing of 66 mm. This crack pattern indicates more cracks already at an early load of 15 kN, likely caused by micro-cracks introduced by shrinkage. As a result, there are more bending cracks on the specimen, with shorter crack lengths and smaller spacing between the cracks.

Furthermore, for the S-PCC-C50 mixture, a zoom/in of the load-displacement curves has been made (see Figure 5.16).

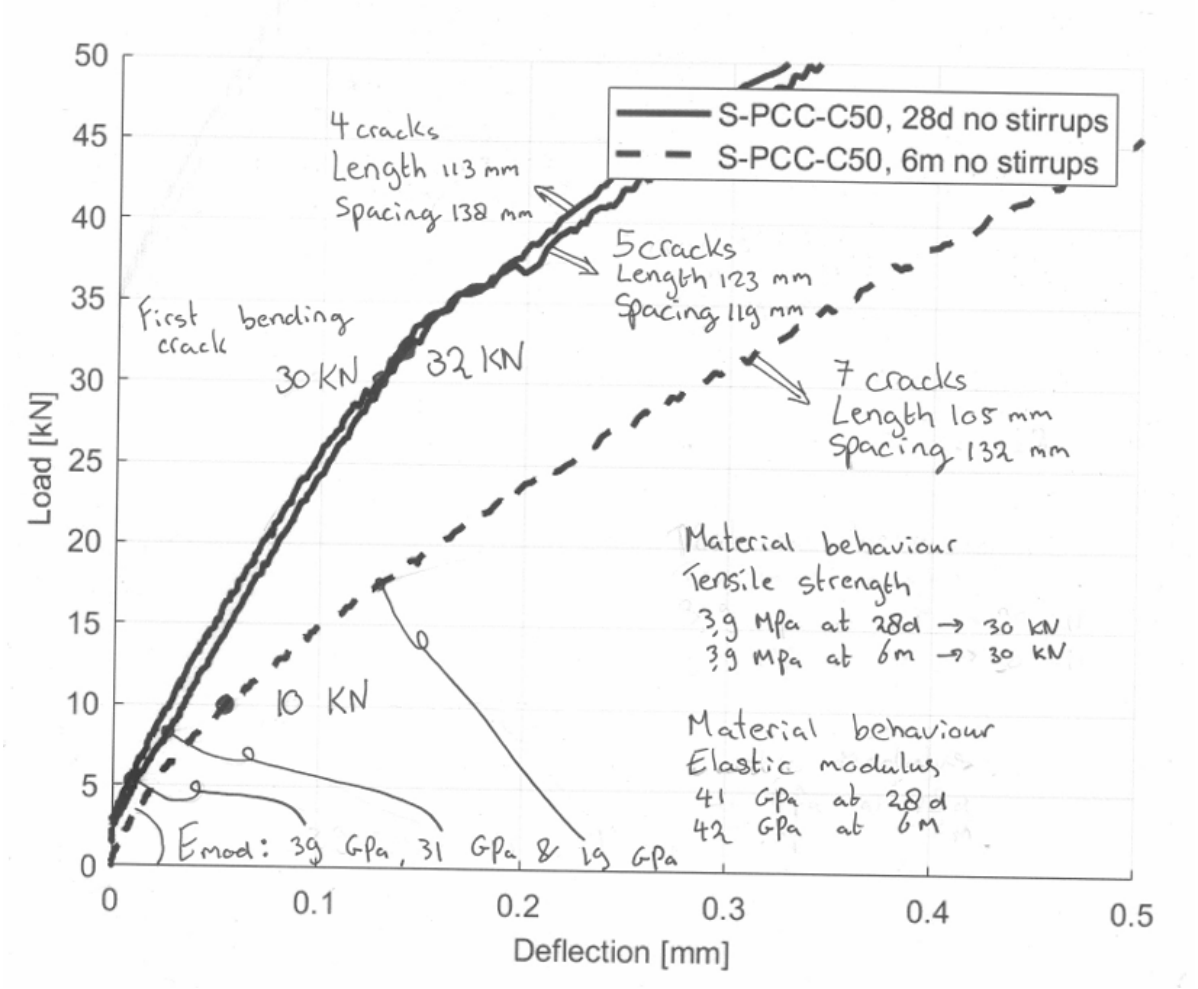

Figure 5.16: Zoom of the load-deflection curves of the beams from mixture S-PCC-C50, with two beams tested at 28 days and one beam tested at 6 months.

In this zoomed-in load-displacement curve, the first bending cracks (see Figure 5.9) are observed from DIC at 30 kN, 32 kN, and 10 kN for beams S-PCC-C50-2, S-PCC-C50-3, and S-PCC-C50-6m, respectively. The 28-day results are slightly similar to the tensile strength predicted by the material behaviour test, which estimated the first bending cracks at 30 kN. However, the 6-month results do not align with the material behaviour test, which predicted the first bending cracks at 30 kN.

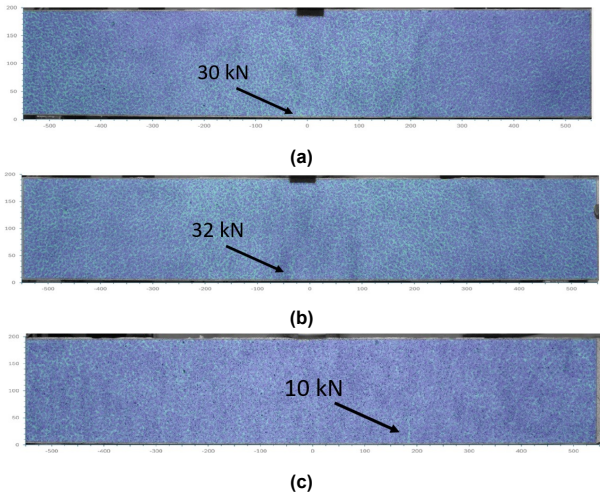

Figure 5.17: First crack from the DIC. a) beam S-PCC-C50-1 tested at 28 days, b) beam S-PCC-C50 tested at 28 days and c) beam S-PCC-C50-6m tested at 6 months

Furthermore, the elastic modulus was calculated at a load of 10 kN, resulting in values of 39 GPa, 31 GPa, and 19 GPa for beams S-PCC-C50-2, S-PCC-C50-3, and S-PCC-C50-6m, respectively. These values are slightly lower than those obtained from the material behaviour tests, which reported an elastic modulus of 41 GPa at 28 days and 42 GPa at 6 months.

Comparison of S-AAC-C50 and S-PCC-C50 mixtures

To better understand the differences and/or similarities in the initial bending cracks of the S-AAC-C50 and S-PCC-C50 mixtures at 28 days, the load paths of the concrete strains obtained from DIC are visualized side by side (see Figure 5.18).

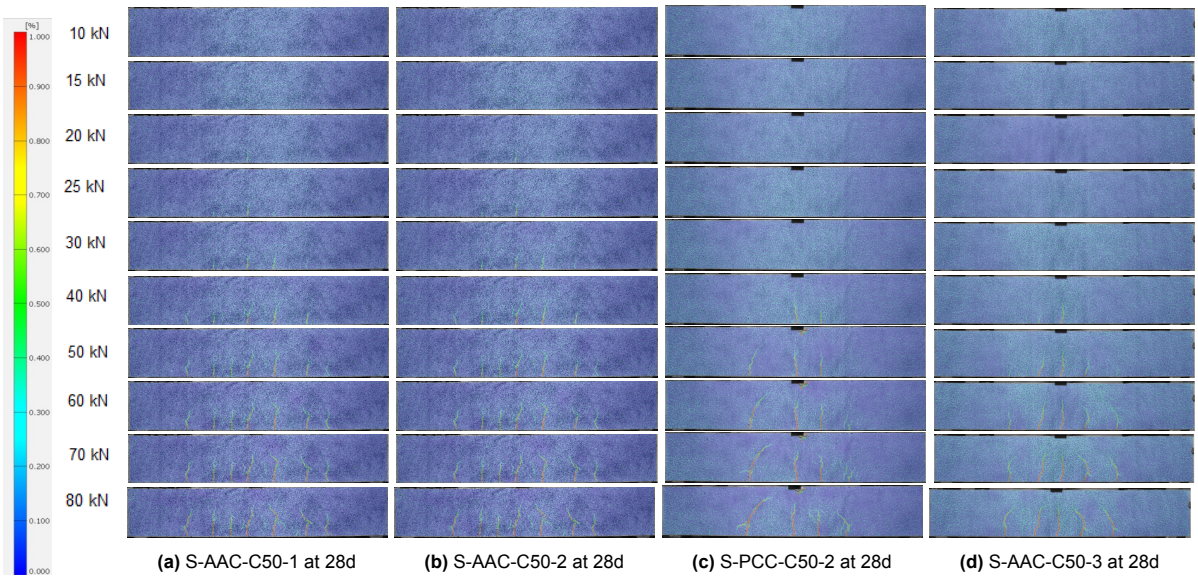

Figure 5.18: Comparison of concrete strains for beam S-AAC-C50-1, S-AAC-C50-2, beam S-PCC-C50-2 and beam S-PCC-C30-3 tested at 28 days, under different load steps (10, 15, 20, 25, 30, 40, 50, 60, 70, and 80 kN) *[Scale: 0–1], [Unit:-].*

A difference in crack pattern between the S-AAC-C50 mixture and the S-PCC-C50 mixture tested at 28 days is very clear. The S-AAC-C50 mixture shows more cracks 7 compared to S-PCC-C50 which shows 4-5 cracks. The length of the cracks from the S-AAC-C50 mixture is 101-107 mm compared to a similar length of 105-123 mm for the S-PCC-C50 mixture. The S-AAC-C50 mixture shows there first crack at a load of 15 kN compared to the S-PCC-C50 mixture at 30 kN. From this can be concluded that

the S-AAC-C50 mixture experiences strength loss due to micro-cracks already at an early age, before 28 days.

To better understand the differences and/or similarities in the initial bending cracks of the S-AAC-C50 and S-PCC-C50 mixtures at 6 months, the load paths of the concrete strains obtained from DIC are visualised side by side (see Figure 5.19).

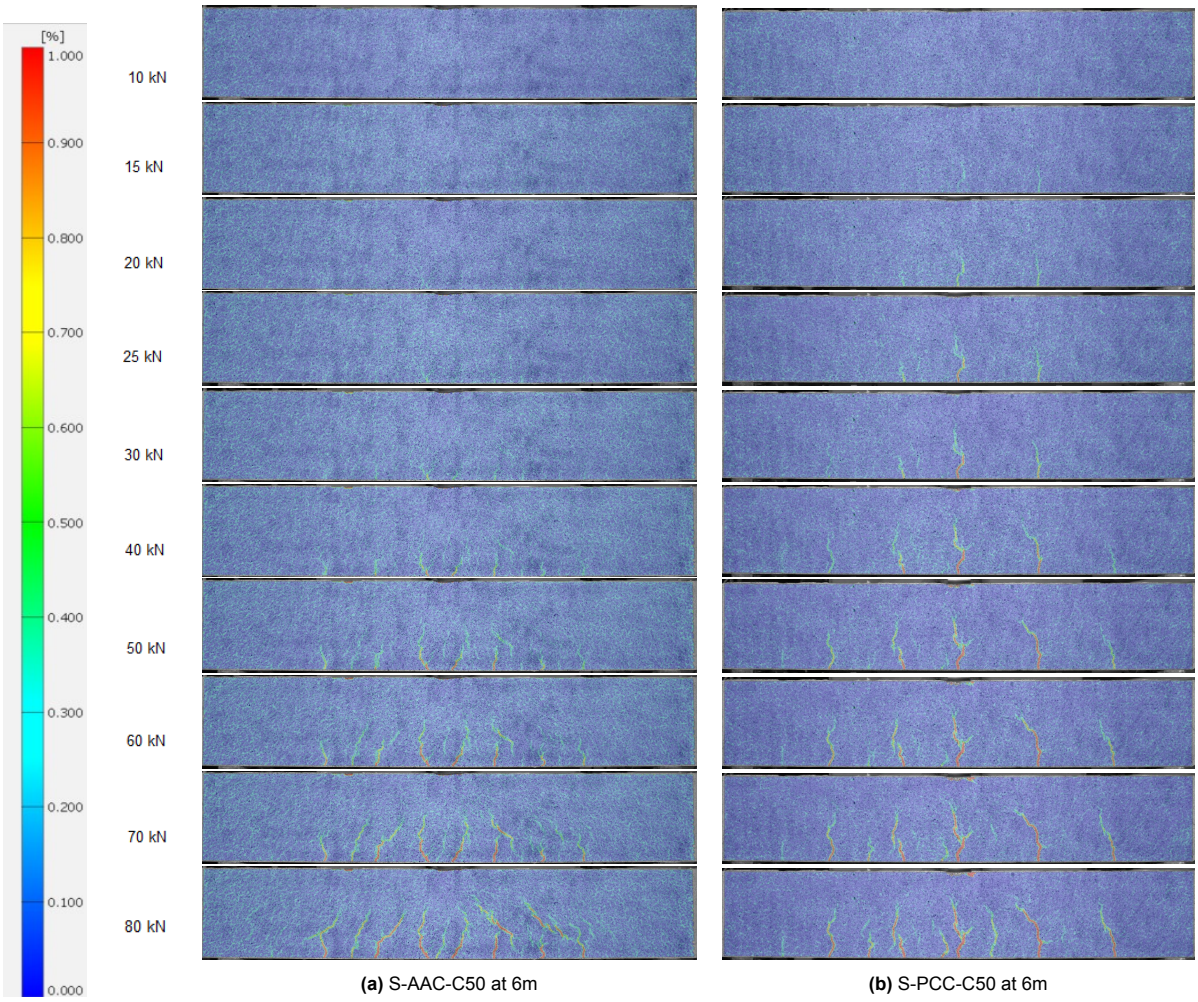

(a) S-AAC-C50 at 6m **(b)** S-PCC-C50 at 6m

Figure 5.19: Comparison of concrete strains for beam S-AAC-C50-6m and S-PCC-C50-6m tested tested at 6 months, under different load steps (10, 15, 20, 25, 30, 40, 50, 60, 70, and 80 kN) *[Scale: 0–1], [Unit:-]*.

When comparing the load path for the S-AAC-C50 and S-PCC-C50 beams tested at 6 months, both exhibit 8 cracks. For the S-AAC-C50 beam, the crack length is 92 mm, and the crack spacing is 66 mm. For the S-PCC-C50 beam, the crack length is 105 mm, with the same spacing of 66 mm. However, the S-AAC-C50 mixtures start to show first bending cracks at a load of 20 kN and the S-PCC-C50 mixture at a load of 10 kN.

When examining the first bending crack for both mixtures, it occurs earlier—by 15 kN—in the S-AAC-C50 mixture at 28 days compared to the S-PCC-C50 mixture. For the 6-month results, the first bending crack occurs earlier, by 10 kN, in the S-PCC-C50 mixture compared to the S-AAC-C50 mixture. Comparing these results to the material behaviour at 28 days and 6 months for tensile strength, as discussed in Section 4.1.2, we see alignment. In that section, the S-AAC-C50 mixture exhibits a lower tensile strength at 28 days (2.9 MPa, resistance of 22 kN) compared to the S-PCC-C50 mixture (3.9 MPa, resistance of 30 kN). This is consistent with the results. For the 6-month results, the tensile strength from the material behaviour test shows a reduction for the S-AAC-C50 mixture (2.5 MPa, resistance of 19 kN), which is in line with the results from the shear test. However, for the S-PCC-C50 mixture,

the material behaviour test showed a similar tensile strength to that observed at 28 days (3.9 MPa, resistance of 30 kN), which does not align with the shear experiment results. Doubts can be raised as to whether the shear beam of S-PCC-C50 at 6 months is truly representative; more beams should be tested to confirm this.

Secondly, when evaluating the elastic modulus determined at a load of 10 kN, it can be considered similar for both mixtures. The 28-day results align with the material behaviour tests for elastic modulus discussed in Section 4.1.3. However, the material behaviour tests reveal no significant differences between the 28-day and 6-month results for either mixture. In contrast, the shear test indicates a reduction of 32% and 44% in the elastic modulus. This reduction could be attributed to shrinkage over time, as both mixtures experienced autogenous and drying shrinkage over the 6 months (see Sections 4.2.2 and 4.2.3).

5.2.2. Formation of diagonal cracks

Furthermore, to better understand the experimental results of the shear test, the first shear crack are observed and documented using DIC.

For the S-AAC-C30 mixture, the first shear crack appears at a load of 80 kN for both beams tested at 28 days, and at 87 kN for the beam tested at 6 months

For the S-PCC-C30 mixture, the first shear crack appears at a load of 90 kN for the beam tested at 28 days, and at 113 kN for the beams tested at 6 months.

In analyzing the inclination of the flexural cracks under shear between the S-AAC-C30 and S-PCC-C30 mixtures, the S-AAC-C30 mixture shows the first shear crack earlier, both at 28 days (10 kN difference) and 6 months (26 kN difference). Both mixtures show an increase in load from the 28-day results to the 6-month results, with an increase of 7 kN for the S-AAC-C30 mixture and 23 kN for the S-PCC-C30 mixture.

For the S-AAC-C50 mixture, the first shear crack appears at a load of 93 kN and 108 kN for the beams tested at 28 days, and at 88 kN for the beams tested at 6 months.

For the S-PCC-C50 mixture, the first shear crack appears at a load of 97 kN and 105 kN for the beams tested at 28 days, and at 90 kN for the beams tested at 6 months.

In analyzing the inclination of the flexural cracks under shear between the S-AAC-C50 and S-PCC-C50 mixtures, the S-AAC-C50 mixture shows the first shear crack at a similar load compared to the S-PCC-C50 mixture for both 28 days and 6 months. Both mixtures exhibit a decrease in load from the 28-day results to the 6-month results. The S-AAC-C50 mixture shows a decrease of 12.5 kN, while the S-PCC-C50 mixture shows a decrease of 11 kN.

5.2.3. Crack stabilization stage

The crack stabilization stage refers to the stage after both shear cracks have formed but before the beam reaches the ultimate failure load capacity. In this stage, cracks keep on growing in width and length. Here the mechanisms of shear transfer in uncracked concrete, aggregate interlock, dowel action, and residual tensile stresses in cracks play a role. As early mentioned there is no agreement yet on how those components influence the overall shear failure process, and which one is the governing mechanism in the failure process.

For the mixture S-AAC-C30 the results are shown in figure 5.20. The stabilization stage of cracks is 30 kN at 28 days and 55 kN at 6 months.

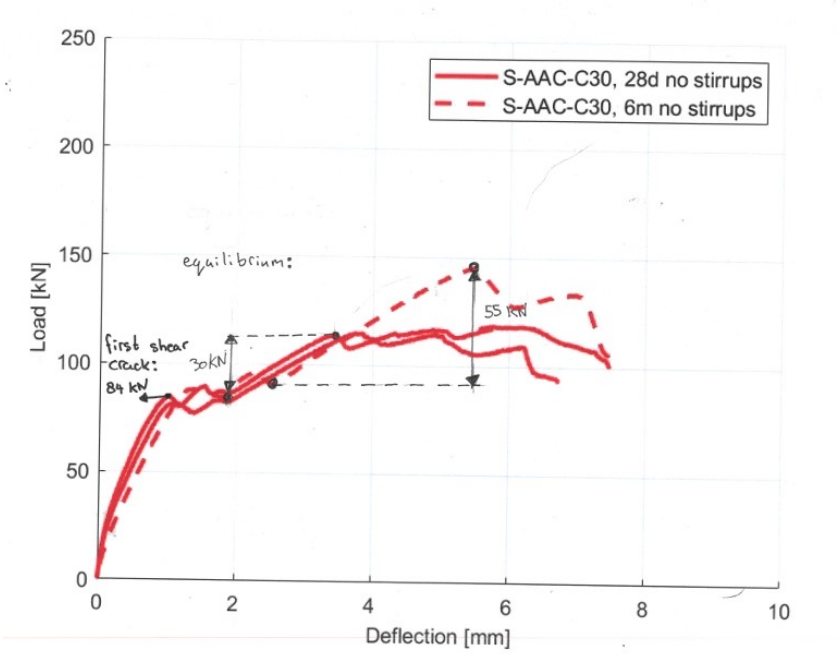

Figure 5.20: The of cracks for the beam S-AAC-C30 is 30 kN at 28 days and 55 kN at 6 months.

For the mixture S-PCC-C30 the results are shown in figure 5.21. The of cracks is 28 kN at 28 days and 41 kN at 6 months.

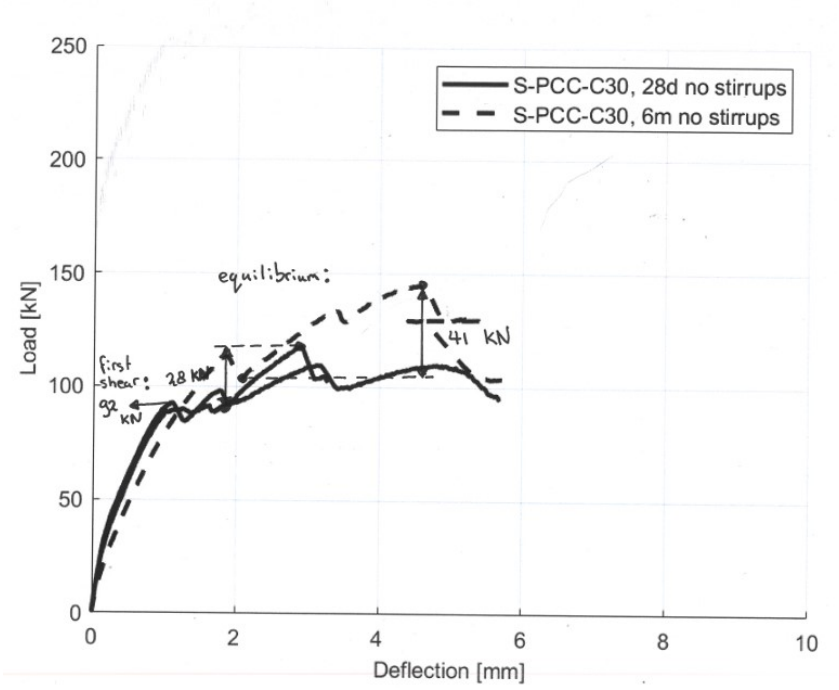

Figure 5.21: The of cracks for the beam S-PCC-C30 is 28 kN at 28 days and 41 kN at 6 months.

A comparison between the S-AAC-C30 mixture and the S-PCC-C30 mixture shows that the of cracks for the S-AAC-C30 mixture is similar at 28 days. Over time, the of cracks increases by 25 kN for S-AAC-C30 and 13 kN for S-PCC-C30. Therefore, the S-AAC-C30 mixture is 14 kN higher at 6 months compared to the S-PCC-C30 mixture.

For the mixture S-AAC-C50 the results are shown in figure 5.22. The of cracks is 45 kN at 28 days and 62 kN at 6 months.

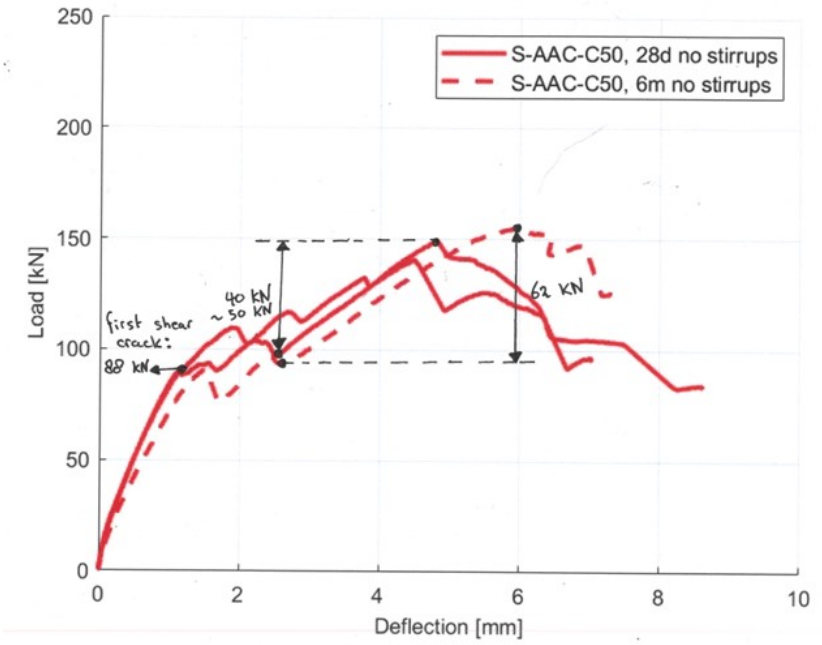

Figure 5.22: The of cracks for the beam S-AAC-C30 is 45 kN at 28 days and 62 kN at 6 months.

For the mixture S-PCC-C50 the results are shown in figure 5.23. The of cracks is 45 kN at 28 days and 34 kN at 6 months.

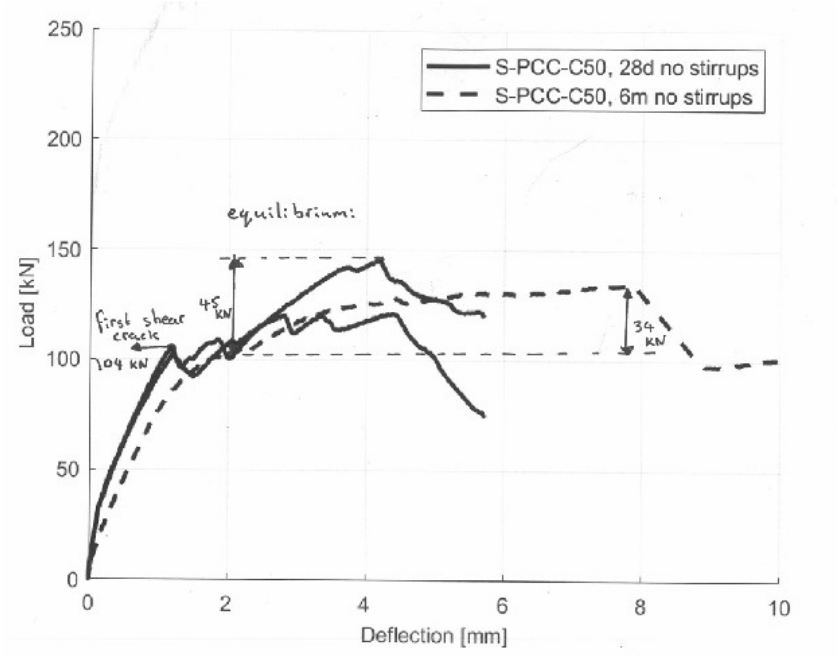

Figure 5.23: The of cracks for the beam S-PCC-C30 is 45 kN at 28 days and 34 kN at 6 months. T

A comparison between the S-AAC-C30 mixture and the S-PCC-C30 mixture shows that the of cracks for the S-AAC-C30 mixture is similar at 28 days. Over time, the of cracks increases by 25 kN for S-AAC-C30 and 13 kN for S-PCC-C30. Therefore, the S-AAC-C30 mixture shows a bigger increase by

14 kN at 6 months compared to the S-PCC-C30 mixture.

A comparison between the S-AAC-C50 mixture and the S-PCC-C50 mixture shows that the of cracks for the S-AAC-C50 mixture is similar at 28 days. The S-AAC-C50 mixture shows an increase of 17 kN over time (6 months), while the S-PCC-C50 mixture shows a reduction of -10 kN over time.

5.3. Additional comparison

5.3.1. Crack opening and slip measurements

From the DIC analysis, the crack opening and sliding along the shear crack plane can be analysed. This analysis was performed for one AAC beam, S-AAC-C30 and one PCC beam, S-PCC-C30-3, both tested at 28 days. Four groups were placed along the dominant shear crack on the beam. Refer to Figure 5.24 for the placement of these groups.

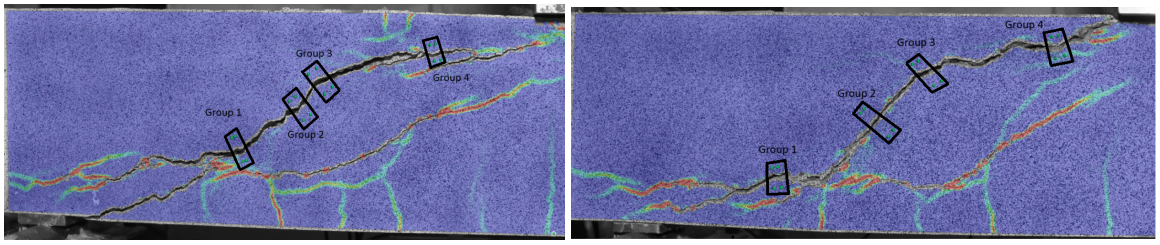

(a) (b)

Figure 5.24: Placement of groups 1, 2, 3 and 4. A) on a AAC beam S-AAC-C30-3 and b) on a PCC beam S-PCC-C30-3

The results from the crack opening and sliding calculations for the AAC beam are shown in Figure 5.25a. Group 1 exhibits the largest crack opening, measuring 4.3 mm, and relatively less sliding at 2.9 mm. Groups 2 and 3 display similar crack opening and sliding behaviours, with the highest sliding values among the groups, at 4 mm. At the beginning of the test, the sliding and crack openings progress together. However, after the beam reaches its ultimate load capacity, there is more sliding along Groups 2 and 3 than crack opening. Finally, Group 4 shows the smallest crack opening, at 3 mm, and the least sliding, measuring just 0.7 mm along the crack.

The results from the crack opening and sliding calculations for the PCC beam are shown in Figure 5.25b. Groups 2 and 3 also show similar opening and sliding behaviour. However, Groups 2 and 3 exhibit more sliding compared to the AAC beam, with less crack opening. Furthermore, Group 4 has the most crack opening, at 5 mm, and sliding begins only after ultimate failure. Group 1 shows the least sliding and a crack opening of 4 mm.

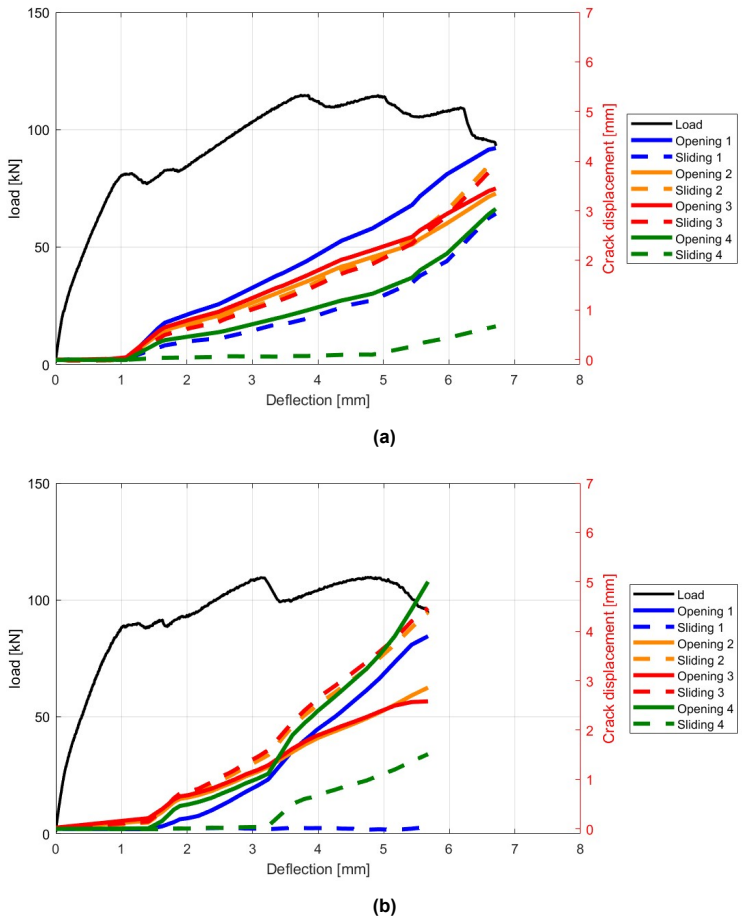

Figure 5.25: Load-displacement relationship (right black axis) and crack opening with slip-displacement relationships (left red axis). Figure a) AAC beam S-AAC-C30-3 and figure b) PCC beam S-PCC-C30-3.

The study of Y. Yang, 2014 mentioned the behaviour of the location of the critical inclined crack in reinforced concrete beams under shear forces. The research explained that beams with a low M/Vd ratio, where M is the bending moment, V is the shear force, and d is the effective depth, are less capable of carrying shear forces in sections closer to the support. Reason for this is when a beam is subjected to shear, cracks develop at specific angles, and their orientation significantly influences shear capacity. Cracks near the loading point often become critical first, as they reach the critical shear displacement earlier. The M/Vd ratio affects the inclination of these cracks: a higher ratio increases shear displacement while a lower ratio results in steeper cracks closer to the support that typically carry less shear force. For beams with a large shear slenderness ratio, the critical section is generally near the loading point. Conversely, for shorter spans, the critical crack may form closer to the support, reflecting the complex relationship between load distribution, crack inclination and structural capacity.

The beams tested in this study exhibited a high M/Vd ratio (M/Vd = 3.0), which can be calculated based on shear force and deflection, likely due to the substantial amount of longitudinal reinforcement. Consequently, it can be assumed that the critical shear crack may form closer to the loading point. An analysis of the crack opening and slip-displacement calculations revealed more critical behaviour at the midpoint (Groups 2 and 3) of the developed shear crack, aligning with theoretical expectations.

5.3.2. Bond strength

The bond between steel and concrete is a key parameter in studying shear behaviour. This bond influences several factors, including the formation of initial bending cracks, aggregate interlock, and dowel action.

By examining the initial bending cracks, conclusions about the bond strength can be drawn. In theory,

a stronger bond reduces the transfer length, see figure 5.26, between steel and concrete, resulting in smaller crack spacing. In other words, a higher bond strength leads to smaller crack spacing.

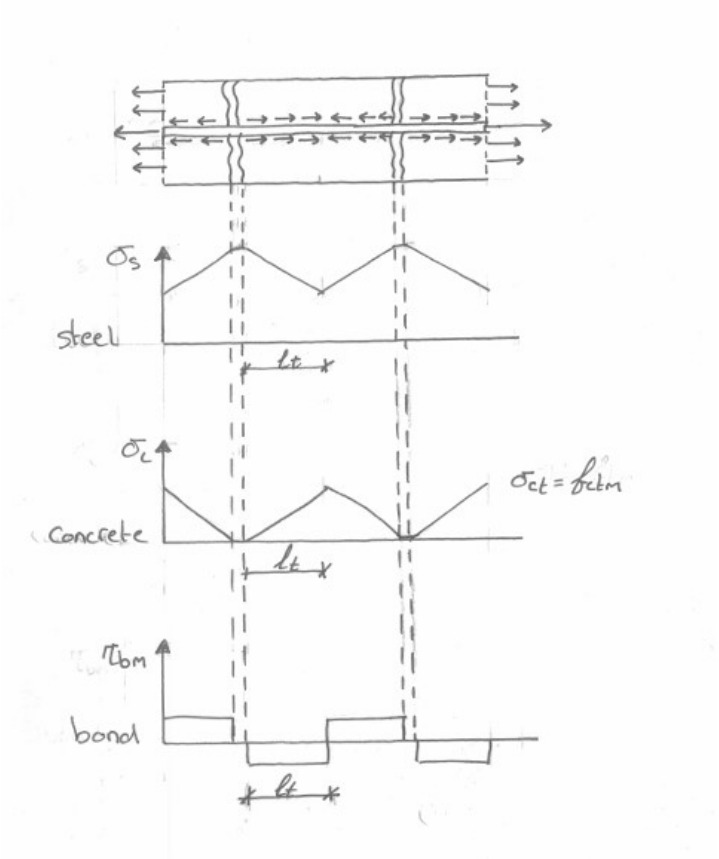

Figure 5.26: Transfer length of the bond between steel and concrete. Showing the development of steel stress along the cracked area, showing the development of concrete tensile stress along the cracked area and showing the development of bond stress along the cracked area

When examining the AAC shear beams tested in this study, more cracks with smaller crack spacing were observed over a period of six months. Can we then conclude that the bond becomes stronger over time? No, because the study also showed that the AAC beams experienced significant shrinkage over time. It is expected that shrinkage would reduce bond strength due to the formation of micro-cracks. While more cracks may appear over time with smaller crack spacing, this is likely due to micro-cracking caused by shrinkage. Therefore, due to the effects of shrinkage on the beams, drawing conclusions about bond strength based on the results of this study is difficult and not further investigated.

6

Discussion

6.1. Shear behaviour versus material behaviour

To provide the readers with a clear overview of all the results obtained from the experiments see Table 6.1.

Table 6.1: Overview of all the experimental results obtained on material behaviour, shrinkage, and shear behaviour test for the mixtures S-AAC-C30, S-PCC-C30, S-AAC-C50, and S-PCC-C50.

		Time	Unit	S-AAC-C30	S-PCC-C30	S-AAC-C50	S-PCC-C50
Material behaviour	Compression strength	28d	[Mpa]	45	43	68	58
		6m	[Mpa]	62	55	85	68
	Tensile strength	28d	[Mpa] / [kN]	3.5 / 27	3.3 / 25	2.9 / 22	4.7 / 30
		6m	[Mpa] / [kN]	2.6 / 20	2.7 / 21	2.5 / 19	3.9 / 30
	Elastic modulus	28d	[Gpa]	38	39	38	41
		6m	[Gpa]	37	37	29	42
Shrinkage	Autogenous shrinkage	28d	$[\mu mm/mm]$	183	90	33	119
		6m	$[\mu mm/mm]$	370	200	489	200
	Drying shrinkage	6m	$[\mu mm/mm]$	273	186	310	225
Shear behaviour	Elastic modulus	28d	[Gpa]	30	29	22	35
		6m	[Gpa]	17	19	15	19
	Initial flexural cracks load	28d	[kN]	22	25	15	31
		6m	[kN]	17	20	20	10
	Initial flexural cracks num. of cracks	28d	[-]	7	6	8	5
		6m	[-]	11	9	10	7
	Initial flexural cracks lenght	28d	[mm]	115	106	105	120
		6m	[mm]	100	110	92	105
	First shear crack	28d	[kN]	80	90	101	105
		6m	[kN]	87	113	88	90
	Crack stabilization stage	28d	[kN]	30	28	45	45
		6m	[kN]	55	41	62	34
	Ultimate failure load	28d	[kN]	116	114	144	134
		6m	[kN]	146	146	156	134

Shrinkage

The most significant difference between the AAC mixtures and the PCC mixtures, as observed in the material behaviour test, is the higher amount of shrinkage measured in the AAC mixtures, even more in the S-AAC-C50 mixture. This is crucial because, during the shear strength test, the specimens contained longitudinal reinforcement, preventing them from freely shrinking. As a result, internal stresses developed within the concrete. If these stresses exceeded the tensile strength capacity of the concrete, they led to the formation of micro-cracks. These micro-cracks can reduce the strength and stiffness of the concrete, making shrinkage a key factor influencing the shear test results.

The impact of this high shrinkage became apparent in the AAC mixtures when comparing the material behaviour test (tensile strength and elastic modulus) with the shear behaviour test (the first initial bending crack and elastic modulus).

Tensile strength

To assess this effect, the tensile strength obtained from the material behaviour test was compared with the first initial bending crack. The results showed that the AAC mixtures exhibited a reduction in tensile strength in the shear behaviour test. In contrast, the PCC mixtures displayed similar tensile strength values in both the material and shear behaviour tests.

For the S-AAC-C30 mixture, a lower tensile strength of −19% at 28 days and −15% at 6 months was observed in the shear behaviour test. In comparison, the S-PCC-C30 mixture maintained similar tensile strength values at both 28 days and 6 months in the shear behaviour test.

For the S-AAC-C50 mixture, a lower tensile strength of −47% at 28 days was observed in the shear behaviour test. At 6 months, the tensile strength from the material behaviour test had already shown a reduction of −14%, which was consistent with the shear behaviour test. Conversely, the S-PCC-C50 mixture exhibited similar tensile strength at 28 days in the shear behaviour test. However, at 6 months, a significant reduction of −67% was observed in the shear behaviour test.

Elastic modulus

Following this, the elastic modulus obtained from the material behaviour test was compared with the elastic modulus obtained from the shear behaviour test at 10 kN. The results show a reduction in the elastic modulus from the shear behaviour test for all mixtures. This reduction becomes more pronounced over time, 6 months, see figure 6.1. It is also important to consider that part of this reduction may be related to the calculation method of drawing a linear line up to 10 kN. If the specimen already showed cracks beyond 10 kN, the line would no longer be linear. However, the conclusion that can be drawn from this is that, at both 28 days and 6 months, the S-AAC-C30 and S-PCC-C30 specimens show a similar reduction in elastic modulus. For the S-AAC-C50 mixture, the reduction in elastic modulus is already more significant at 28 days, whereas the S-PCC-C50 mixture begins to show a reduction only at 6 months. At 6 months, a similar reduction in elastic modulus between the S-PCC-C50 and S-AAC-C50 mixtures is observed.

For the S-AAC-C30 mixture, the elastic modulus from the shear behaviour test shows a reduction of −21% at 28 days and −54% at 6 months. In comparison, the S-PCC-C30 mixture shows a reduction of −26% at 28 days and −49% at 6 months.

hspace*2em For the S-AAC-C50 mixture, the elastic modulus from the shear behaviour test shows a reduction of −42% at 28 days and −48% at 6 months. In comparison, the S-PCC-C50 mixture shows a reduction of −15% at 28 days and −55% at 6 months.

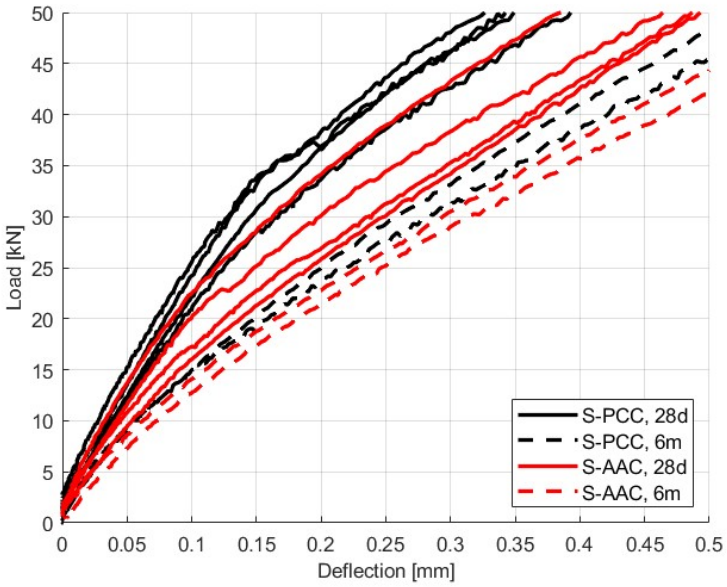

Figure 6.1: Zoom of the load-displacement curve for all RC beams tested without stirrups at 28 days and 6 months. A decrease in stiffness over time can be noted for both the AAC and PCC mixtures. The red lines represent the AAC mixtures and the black lines represent the PCC mixtures. The solid lines correspond to beams tested at 28 days, while the dotted lines correspond to beams tested at 6 months.

Crack stabilization stage

Furthermore, it is important to discuss the comparison of the difference in height of the crack stabilization stage. The results show a significant increase in the stabilization stage over time for the AAC mixtures. This increase is higher for the AAC mixtures compared to the PCC mixtures.

For the S-AAC-C30 mixture, the crack stabilization stage is 30 kN at 28 days and 55 kN at 6 months, representing an increase of +83%. In comparison, the S-PCC-C30 mixture shows a crack stabilization stage of 28 kN at 28 days and 41 kN at 6 months, an increase of +46%.

For the S-AAC-C50 mixture, the crack stabilization stage is 45 kN at 28 days and 62 kN at 6 months, representing an increase of +38%. In comparison, the S-PCC-C50 mixture shows a crack stabilization stage of 45 kN at 28 days and 34 kN at 6 months, a decrease of −24%.

Ultimate failure capacity

Finally, a comparison of the ultimate failure load can be made for the beams tested in shear behaviour. The S-AAC-C30 beams show similar results to the S-PCC-C30 beams, with an increase in shear capacity over 6 months of 28%. The S-AAC-C50 beam shows a higher shear capacity at both 28 days and 6 months compared to the S-PCC-C50 mixture, with an increase over 6 months of 8%.

For the S-AAC-C30 mixture, the ultimate failure load is 116 kN at 28 days and 146 kN at 6 months, resulting in a shear capacity of 58 kN at 28 days and 73 kN at 6 months. In comparison, the S-PCC-C30 mixture shows an ultimate failure load of 114 kN at 28 days and 146 kN at 6 months, resulting in a shear capacity of 57 kN at 28 days and 73 kN at 6 months.

For the S-AAC-C50 mixture, the ultimate failure load is 144 kN at 28 days and 156 kN at 6 months, resulting in a shear capacity of 72 kN at 28 days and 78 kN at 6 months. In comparison, the S-PCC-C50 mixture shows an ultimate failure load of 134 kN at 28 days and 134 kN at 6 months, resulting in a shear capacity of 67 kN at both 28 days and 6 months.

Critical Review

An attentive reader might have noted that the AAC mixtures show a decrease in tensile strength and elastic modulus but an increase in the crack stabilization stage, which increases the ultimate shear capacity of both AAC mixtures. Therefore, it can be concluded that the crack stabilization stage is the primary factor contributing to the increase in ultimate shear failure capacity.

One might be tempted to think that we should use AAC right now because it shows similar or even better ultimate failure capacity than PCC at both 28 days and 6 months. However, it is crucial to remain critical and consider the entire picture.

It is, however, essential to further investigate the AAC mixtures over a long period to determine whether the crack stabilization stage continues to increase, remains stable, or starts to decrease. Potential reasons for a change in the crack stabilization stage can be illustrated with two examples:

Example 1: The mechanism of aggregate interlock depends, among other factors, on the roughness of the surface. A rougher surface results in better aggregate interlock. The material behaviour test has shown a linear crack through the aggregates in the direct tensile test, which creates a smoother surface and harms the aggregate interlock. This linear crack through the aggregates is caused by a strong bond in the ITZ zone. Over time, shrinkage plays a role, causing micro-cracks that weaken the bond in the ITZ. This may eventually lead to cracks forming around the aggregates, creating a rougher surface, which could improve aggregate interlock. But what will happen if micro-cracks continue to develop? What is the optimum surface roughness for the best aggregate interlock?

Example 2: The mechanism of dowel action depends, among other factors, on the bond strength; a stronger bond results in better dowel action. The linear crack through the aggregates indicates a strong bond in the ITZ. A strong bond has a positive influence on bond strength, but over time, the formation of micro-cracks could weaken this bond, resulting in a negative effect on bond strength. Over time, how much weaker will the bond become? How much influence will this have on the crack stabilization stage?

6.2. Relations between material behaviour and shear behaviour

First, to get a better understanding of whether there is a relation between the compressive strength and shear strength of a mixture, the experimental results of compressive strength are displayed compared

to the maximum shear stress of the mixtures (See Figure 6.2). The results indicate that a higher compressive strength results in a higher maximum shear stress for both PCC and ACC mixtures.

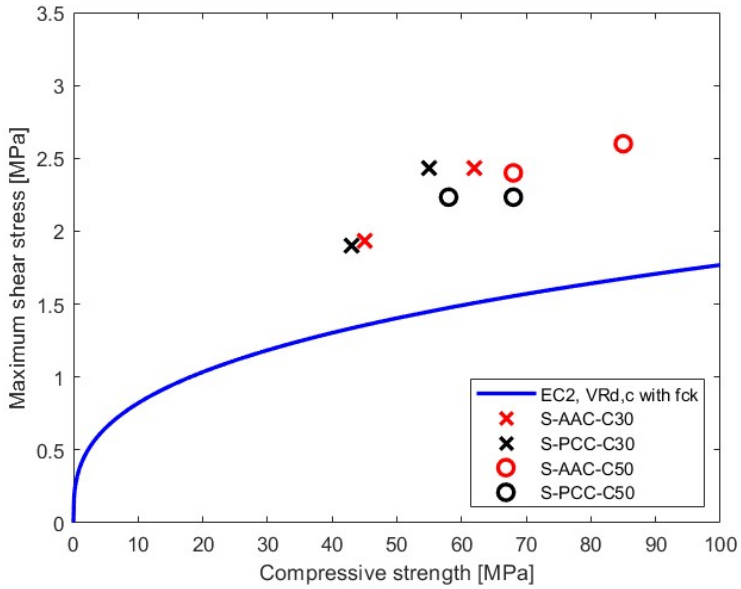

Figure 6.2: Relation between the experimental results of compressive strength versus maximum shear stress for beams with no stirrups compared with the EC2, NEN-EN 1992-1-1, 2015.

Secondly, to get a better understanding of whether there is a relation between the tensile strength and shear strength of a mixture, the experimental results of direct tensile strength are displayed compared to the maximum shear stress of the mixtures (See Figure 6.3. The results indicate that a lower tensile strength results in a higher maximum shear stress, especially for the ACC mixtures. Reasons for this can be that a lower tensile strength results in more cracks and possibly rougher cracks, a less strong ITZ zone, thereby influencing dowel action and aggregate interlock.

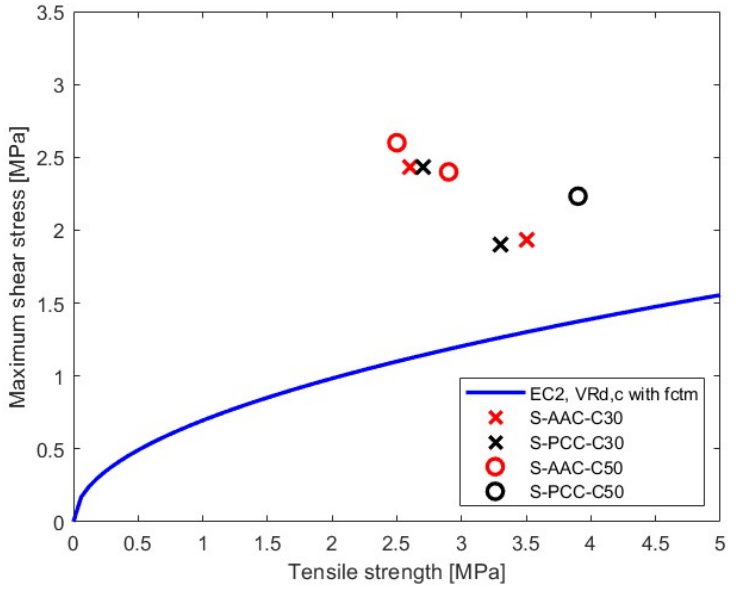

Figure 6.3: Relation between the experimental results of tensile strength versus maximum shear stress for beams with no stirrups compared with the EC2, NEN-EN 1992-1-1, 2015.

Thirdly, to get a better understanding of whether there is a relationship between shrinkage and tensile strength, the experimental results of autogenous shrinkage and direct tensile strength are displayed in Figure 6.4. The results that show high amounts of autogenous shrinkage have a lower tensile strength.

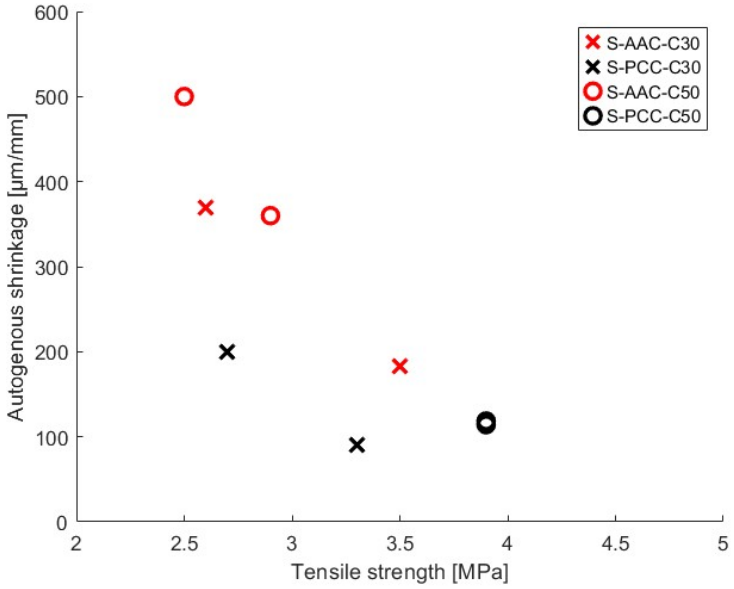

Figure 6.4: Relation between the experimental results of tensile strength versus autogenous shrinkage.

Finally, to better understand the relationship between shrinkage and ultimate shear stress, the experimental results of autogenous shrinkage and shear stress are displayed in Figure 6.5. The results show that mixtures that experienced greater autogenous shrinkage exhibited higher maximum shear stress, especially for the AAC mixtures.

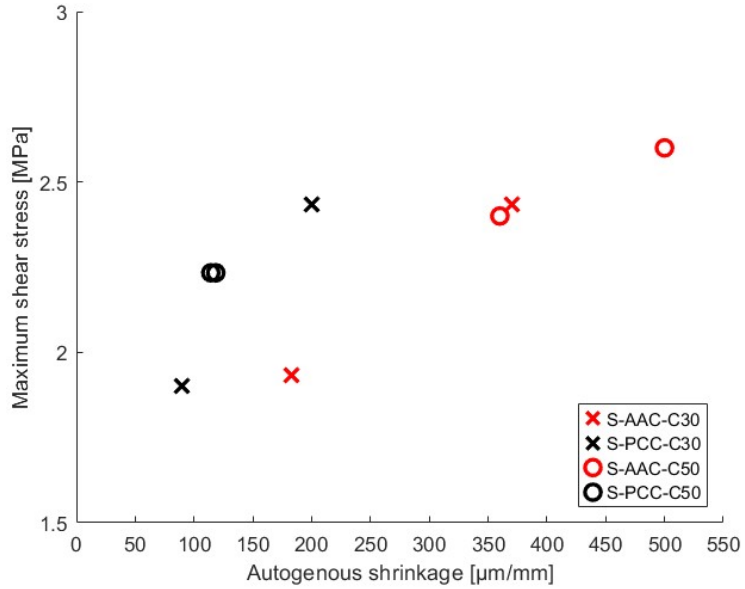

Figure 6.5: Relation between the experimental results of autogenous shrinkage versus maxiumum shear stress for beams with no stirrups.

6.3. Strength classes

For a comparison between the C30 and C50 mixtures, the elastic modulus is first displayed in Figure 6.6. The AAC mixtures (Figure 6.6a) show a higher elastic modulus for the C30 beams compared to the C50 beams at both 28 days and 6 months. This behaviour is different from that observed in the PCC mixtures (Figure 6.6b), where the C50 mixture exhibits a stiffer material compared to the C30 mixture at both 28 days and 6 months.

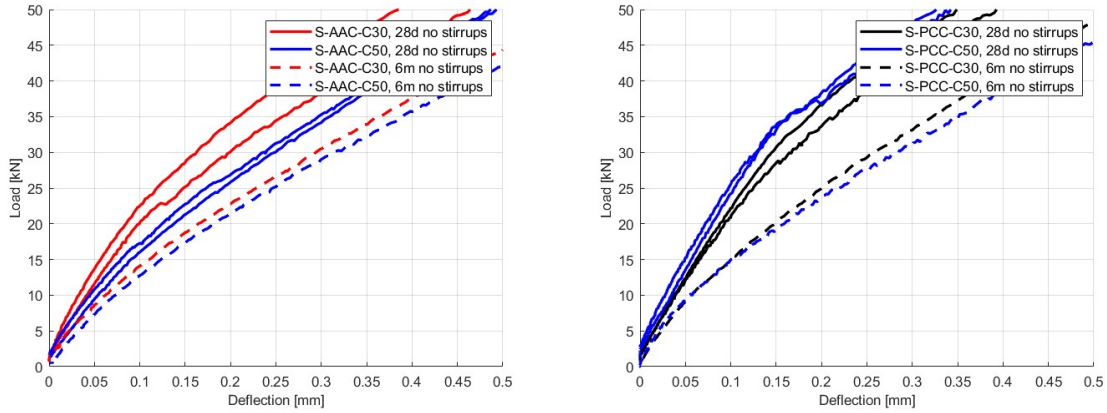

Figure 6.6: Zoom of the load-deflection curves. (a) represents the AAC mixtures, and (b) represents the PCC mixtures.

Furthermore, for a comparison between the C30 and C50 mixtures, the full load-deflection curves are displayed in Figure 6.7. The AAC mixtures (Figure 6.7a) show that the C50 mixture has a higher ultimate failure capacity compared to the C30 mixture, with both mixtures exhibiting an increase in shear strength over 6 months. The PCC mixtures (Figure 6.7b) show a similar behaviour.

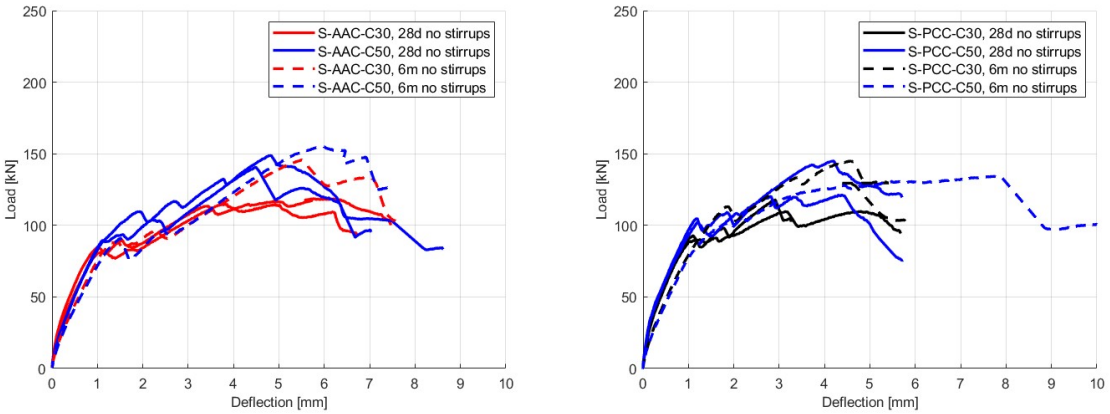

Figure 6.7: The load-deflection curves. (a) represents the AAC mixtures, and (b) represents the PCC mixtures.

6.4. Experimental results compared with literature

6.4.1. Material behaviour

Tensile strength

Firstly, The experimental results of the direct tensile test compared with the formula from the Eurocode 2, NEN-EN 1992-1-1, 2015.

The formula used from Eurocode 2 is given in Equation 6.1. This formula uses the experimental com-

pressive strength (cylindrical) to predict the tensile strength of the mixtures.

$$f_{ctm} = 0.3 \cdot f_{cm}^{2/3} \leq \text{C50/60} \tag{6.1}$$

The results are presented in Figure 6.8. The experimental study shows a decrease in tensile strength over time for the mixtures S-AAC-C30, S-AAC-C50, and S-PCC-C30. The predicted values, based on compressive strength, show an increase over time, which is very different from the experimental findings. Furthermore, it can be noted that the S-AAC-C50 mixture already shows a very low experimental value at 28 days compared to the prediction, with this difference only increasing over time as the experimental values continue to decrease further.

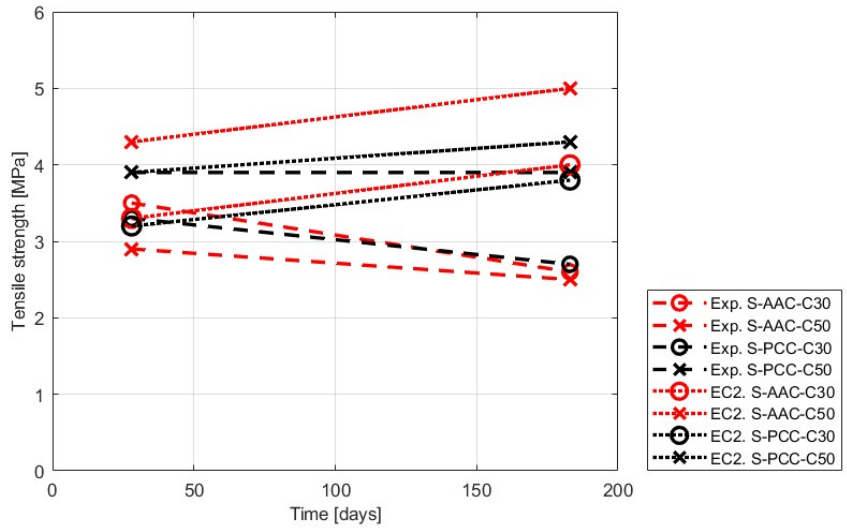

Figure 6.8: Experimental direct tensile strength is compared with Eurocode 2 NEN-EN 1992-1-1, 2015 at both 28 days and 6 months for the mixtures S-AAC-C30, S-PCC-C30, S-AAC-C50, and S-PCC-C50.

Secondly, The experimental results of the direct and splitting tensile strength tests are compared with experimental results found in the literature (See figure 6.9)

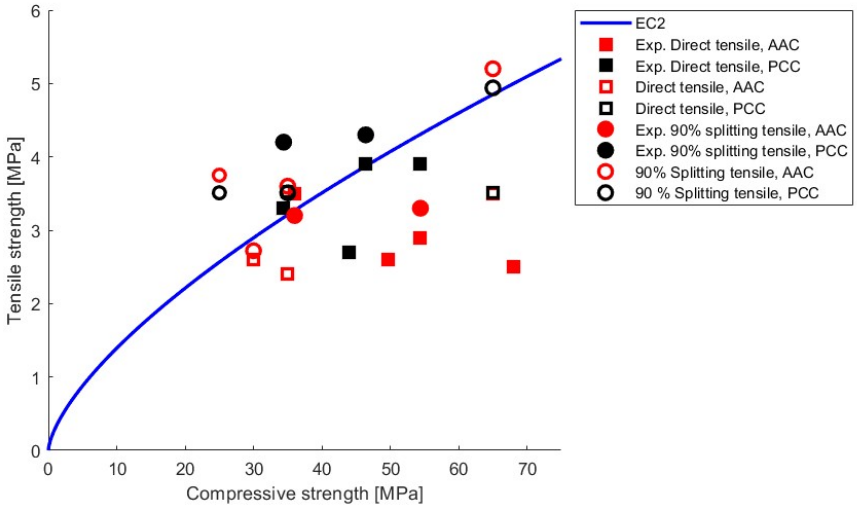

Figure 6.9: Experimental results for tensile stress compared with studies found in literature.

The results of the AAC mixtures show a large variation in tensile strength. There is no increase in tensile strength as the compressive strength increases. Therefore, it can be concluded that the relationship between tensile strength and compressive strength does not apply. The reasons for this large variation in results could be due to the influence of different activators or curing conditions.

Elastic modulus

Firstly, the experimental results of the elastic modulus are compared with the formula from the Eurocode 2, NEN-EN 1992-1-1, 2015.

The formula used from Eurocode 2 is given in Equation 6.2. This formula uses the experimental compressive strength (cylindrical) to predict the elastic modulus of the mixtures.

$$E_{cm} = 22 \left(\frac{f_{cm}}{10} \right)^{0.3} \tag{6.2}$$

The results are presented in Figure 6.10. The results show that at 28 days, the experimental values are higher than the predictions made using Eurocode 2 NEN-EN 1992-1-1, 2015. However, over time, the predictions show an increase in elastic modulus, while the experimental results show little change or even a decrease. Notably, the S-AAC-C50 mixture exhibits a significant decrease over time, which is not in line with the prediction.

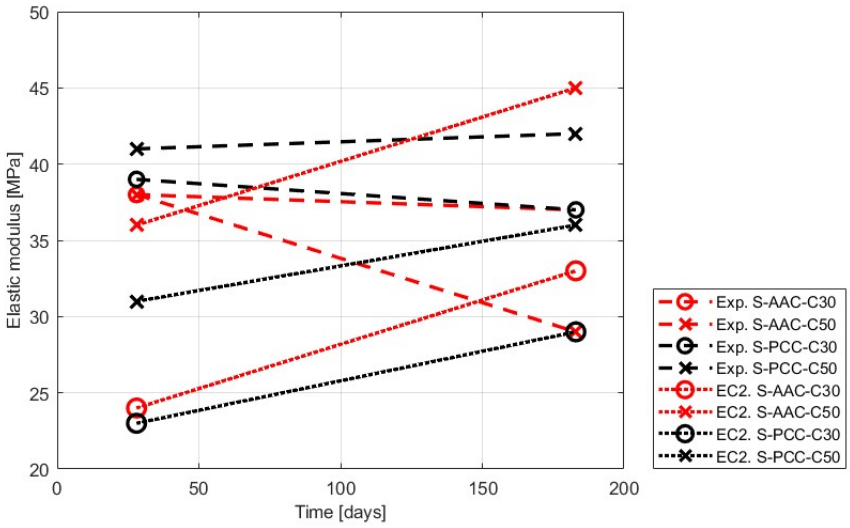

Figure 6.10: Experimental elastic modulus is compared with Eurocode 2 NEN-EN 1992-1-1, 2015 at both 28 days and 6 months for the mixtures S-AAC-C30, S-PCC-C30, S-AAC-C50, and S-PCC-C50.

Secondly, for a comparison of the elastic modulus, two studies from literature are compared (See Figure 6.11).

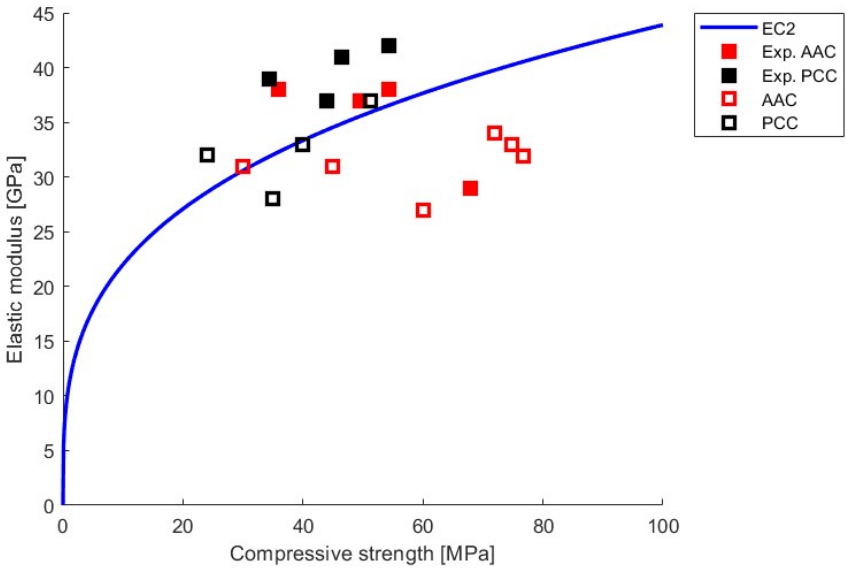

Figure 6.11: Experimental results for elastic modulus compared with studies found in literature.

The results indicated that the AAC mixtures show a lower elastic modulus for mixtures with a higher compressive strength, even lower than predicted by EC2, NEN-EN 1992-1-1, 2015.

Different strength classes

Furthermore, the results of the elastic modulus have been compared to the study by Prinsse, 2017. In this study, a mixture (S100) consisting of 100% BFS with a cubic compressive strength of 93 MPa at 28 days was tested. The results are shown in Figure 6.12. The findings indicate that the elastic modulus of a stronger mixture is lower compared to the C30 and C50 AAC mixtures. This trend aligns with the results observed between the C30 and C50 mixtures, where higher compressive strengths correspond to lower stiffness, with stiffness decreasing over time. However, the rate of decrease is similar to that of the C50 mixture.

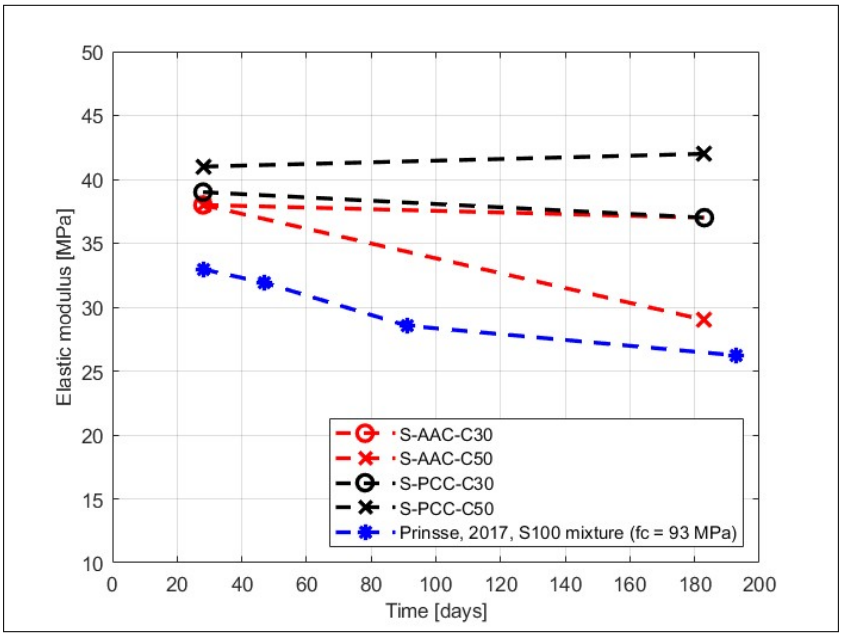

Figure 6.12: Elastic modulus of the experimental study compared with the study of Prinsse, 2017 over time.

6.4.2. Shear behaviour

Eurocode 2, NEN-EN 1992-1-1, 2015

The experimental results of the shear test are firstly compared with two formulas of Eurocode 2, NEN-EN 1992-1-1, 2015.

formulas The first formula $v_{Rd,c}$ represents the design value of the punching shear resistance for a slab without punching shear reinforcement along the considered control section (See Equation 6.3).

$$v_{Rd,c} = C_{Rd,c} \cdot k \cdot (100 \cdot \rho_l \cdot f_{ck})^1 3 \tag{6.3}$$

Where $V_{Rd,c}$ is the design shear resistance of the member without shear reinforcement in N, $C_{Rd,c}$, k are a calculation coefficient, ρ_l is the reinforcement ratio, f_{cm} is the mean compression strength in MPa, b_w is the smallest width of the cross-section in the tensile area in mm and d is the effective depth of the cross-section in mm.

The second formula v_{min} is for calculating the minimum shear stress without shear reinforcement (See Equation 6.4)

$$v_{min} = 0.035 \cdot k^{\frac{3}{2}} \cdot f_{ck}^{\frac{1}{2}} \tag{6.4}$$

The results are presented in Figure 6.13. They indicate that Eurocode 2 is very conservative. Furthermore, for both equations used, $v_{Rd,c}$ and v_{min}, a slight increase in ultimate shear capacity over time is observed for all mixtures, based on compressive strength. In the experimental results, the increase is more pronounced for the AAC mixtures than predicted by the Eurocode equations. A similar trend is also observed for the S-PCC-C30 mixtures.

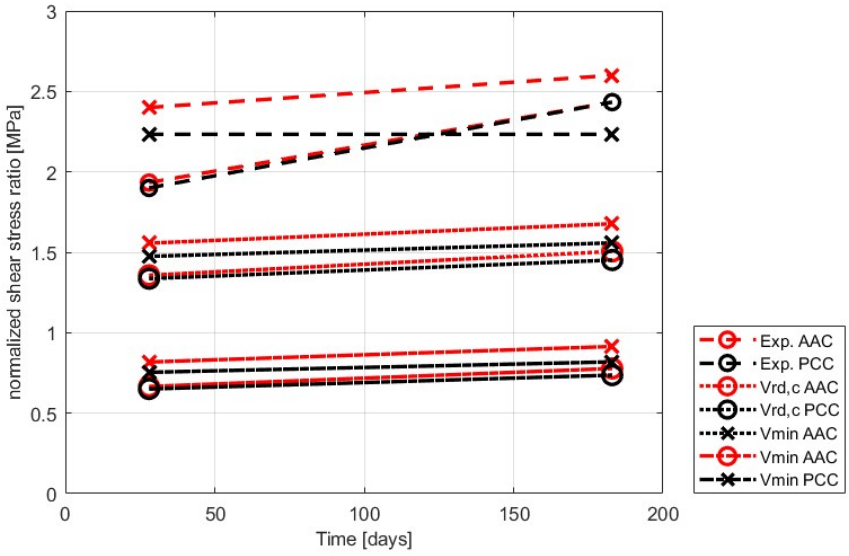

Figure 6.13: Experimental ultimate shear capacity compared with the Eurocode 2, NEN-EN 1992-1-1, 2015 at 28 days and 6 months for the mixtures S-AAC-C30, S-PCC-C30, S-AAC-C50, and S-PCC-C50.

28-day results without stirrups

The results are compared with the thesis of Teeuwen, 2024. In this thesis, an RC beam (200 x 150 x 1650 mm^3) without stirrups in strength class C30 of mixture PCC has been tested. The results (see Figure 6.14) show a similar elastic modulus, with the first shear crack occurring around the same load of 80 kN. However, the results of this report show a higher ultimate shear capacity of 128 kN, 91% of the shear capacity of the beams tested in this study. This difference is acceptable.

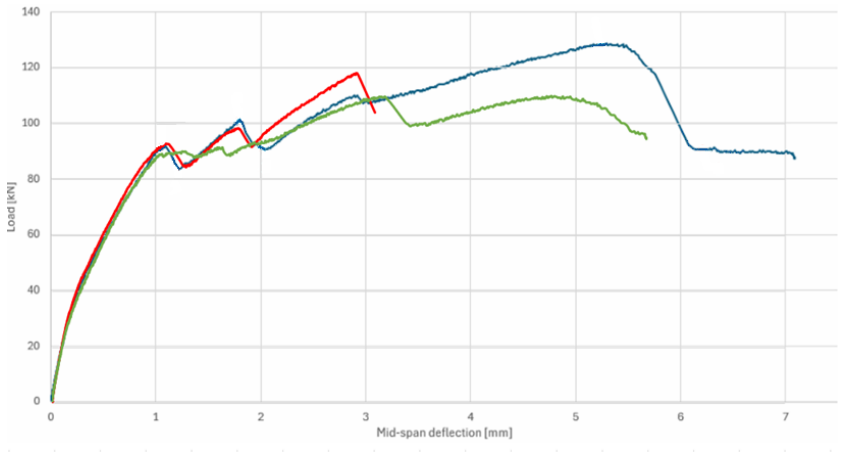

Figure 6.14: Load-displacement graph of the S-PCC-C30 beams, tested at 28 days, where the red line represents beam S-PCC-C30-1, the green line represents beam S-PCC-C30-2 from the experimental study in this report, and the blue line represents the beam from the thesis of Teeuwen, 2024.

Different concrete/steel ratios

Furthermore, the experimental results are compared with the study executed by Huang et al., 2023. In this study two reference beams (100 x 200 x 1400 mm^3) of a strength class C20/25 (w/c ratio 0.60) are tested in shear failure in a 3-point bending test, where the supports are placed 1000 mm apart.

The dimensions of the beam and the concrete strength class are different from those applied in this report. Therefore the results have been plotted deflection by $\frac{v}{f_c^{1/3}}$, where the shear stress is calculated by $v = \frac{F}{b \cdot d}$ in MPa and for f_c the compressive strength obtained at 28 days is used in MPa. See Figure 6.15 for the comparison.

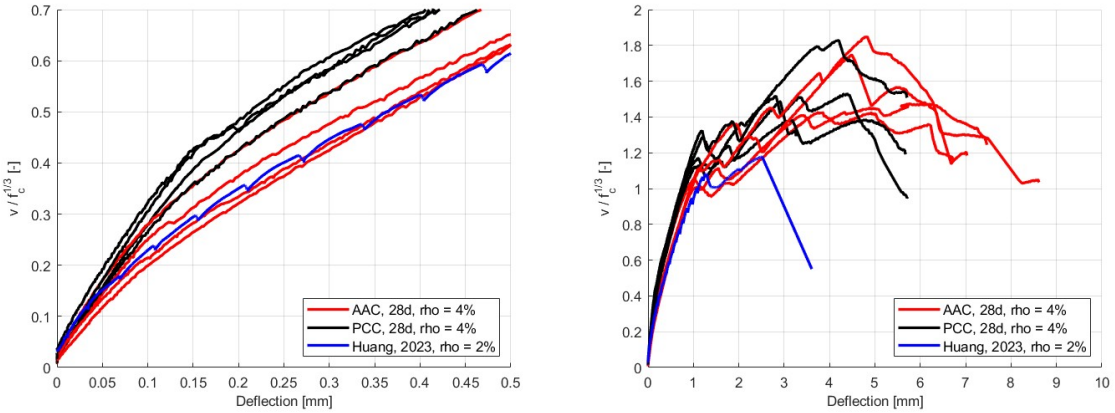

Figure 6.15: Shear stress / compressive strength$^{1/3}$ versus displacement graph of PCC and AAC beams, tested at 28 days, and beam of the experimental study of Huang et al., 2023. a) zoom of the graph and b) full graph.

The results obtained from the paper of Huang et al., 2023 initially show a some what similar elastic modulus compared to the PCC and AAC beams. However, the first bending cracks appear at an early load, which can be explained by the use of a lower-strength concrete mixture. Furthermore, it can be observed that the first shear crack occurs at a somewhat similar moment. The most significant difference, however, is that the beam from the study by Huang et al., 2023 has a much shorter crack stabilization stage. This could be due to a lower amount of reinforcement in the beam, which can result in affecting the crack width and dowel action.

Simplified M-k diagram

Finally, the 28-day and 6-month results are compared using a simplified M-k diagram. The Excel model used in this study was provided by Dr. ir. Mladena Luković and is also referenced in Prinsse, 2017.

The model considers four stages of failure: (1) before concrete cracking, (2) after concrete cracking, (3) the plastic zone, and (4) steel yielding. For each stage, the moment M and kappa k can be calculated (see Table 6.2).

Stage		Moment M	Kappa k
1	before cracking	$M_{cr} = 1/6 \cdot f_{ctm,fl} \cdot h^2 \cdot w$	$k = \frac{\varepsilon_c + \varepsilon_c}{h}$
2	after cracking concrete	$M_{cr} = 1/6 \cdot f_{ctm,fl} \cdot h^2 \cdot w$	$k = \frac{\varepsilon_c + \varepsilon_s}{d}$
3	plastic zone	$M_{cr} = M_{cpl} = (d - \frac{x}{3}) \cdot A_s \cdot \varepsilon_s \cdot E_{cm}$	$k = \frac{\varepsilon_s}{d-x}$
4	yielding steel	$M_{cr} = M_{rd} = (d - t_{ez} \cdot x_u) \cdot x_u$	$k = \frac{\varepsilon_s}{d-x_u}$

Table 6.2: Four different stages of the M-K diagram, with corresponding M and k equations

Using ”vergeet-me-nietjes” for a three-point bending test, the load and deflection can be calculated. The model determines the load based on the moment M using Equation 6.5, while the deflection is derived from kappa k using Equation 6.6.

$$M = \frac{1}{4} \cdot F \cdot l \rightarrow P = \frac{4 \cdot M}{l} \tag{6.5}$$

Where M is the moment in N, l is the length between the supports in mm.

$$w = \frac{1}{48} \cdot \frac{F \cdot l^3}{EI} = \frac{1}{48} \cdot \frac{\frac{4 \cdot M}{l} \cdot l^3}{EI} = \frac{1}{12} \cdot k \cdot l \tag{6.6}$$

Where $k = \frac{M}{EI}$ moment divided by stiffness and l is the length between the supports in mm.

The results for the PCC mixtures (see Figure 6.16 and 6.17) indicate that, for the 28-day results, the elastic modulus from the M-K diagram is perpendicular to that of the experimental results. Additionally, the first bending cracks appear at a similar load in both the M-K diagram and the experiments, suggesting that the model provides a reasonable approximation. However, the M-K diagram predicts a higher failure load, primarily due to the yielding of steel, whereas, in the experiments, concrete failure is the governing factor. This discrepancy indicates that the M-K diagram does not accurately predict failure behaviour. Furthermore, the six-month results deviate significantly, as the elastic modulus is no longer perpendicular to the M-K diagram, and the first bending cracks do not form at the same load as observed in the experimental results. These inconsistencies suggest that the M-K diagram is less reliable for predicting long-term behaviour, because of the effects of shrinkage.

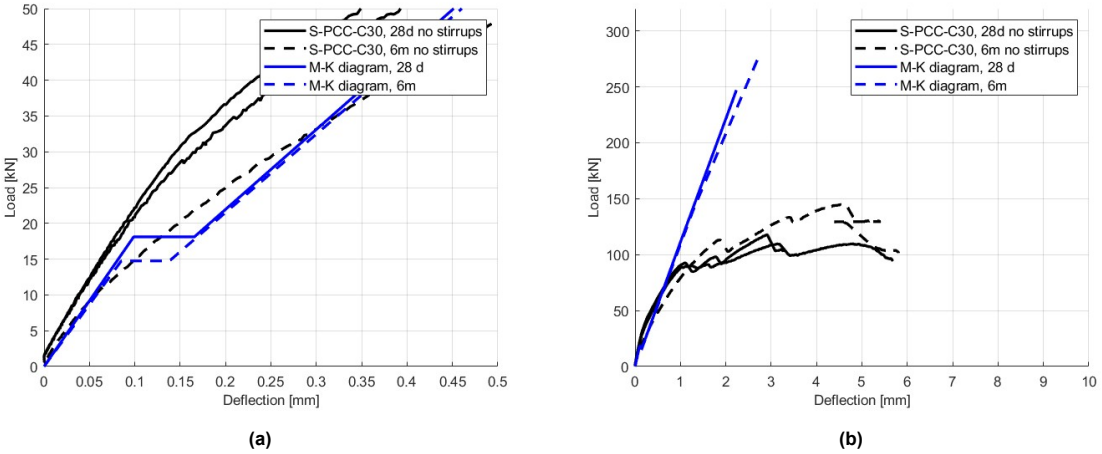

Figure 6.16: Force-deflection graph based on the M-k diagram for mixture S-PCC-C30 a) zoom of the graph and b) full graph.

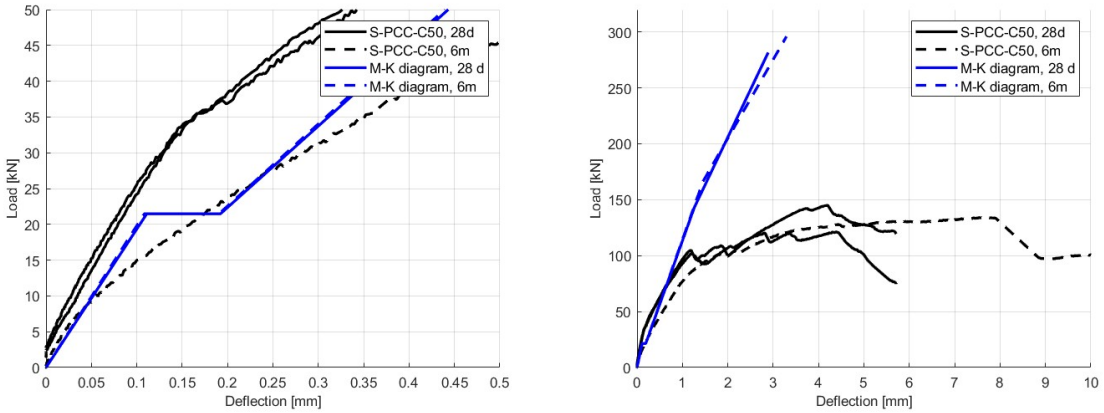

Figure 6.17: Shear results compared with force-deflection graph based on the M-k diagram for mixture S-PCC-C50 a) zoom of the graph [0, 0.5] and b) full graph [0, 10].

The results for the AAC mixtures (see Figure 6.18 and 6.19) indicate that, for the 28-day results, the elastic modulus from the M-K diagram is not perpendicular to that of the experimental results, with the largest difference observed in the S-AAC-C50 mixture. In this case, the effects of shrinkage on the experimental results are already noticeable. Furthermore, the first bending cracks do not form at the predicted load. Therefore, it can be concluded that the M-K diagram predicts the results for AAC mixtures less accurately, as these mixtures are more influenced by shrinkage at an early age.

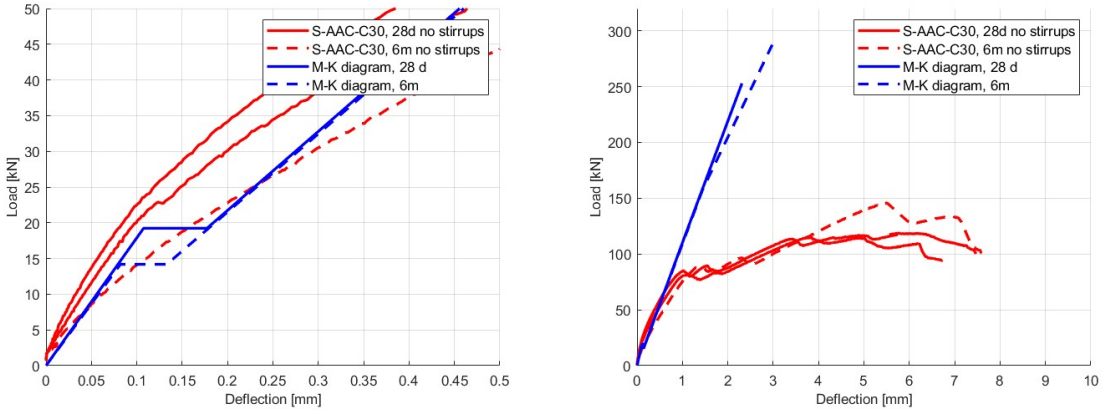

Figure 6.18: Shear results compared with force-deflection graph based on the M-k diagram for mixture S-AAC-C30 a) zoom of the graph and b) full graph.

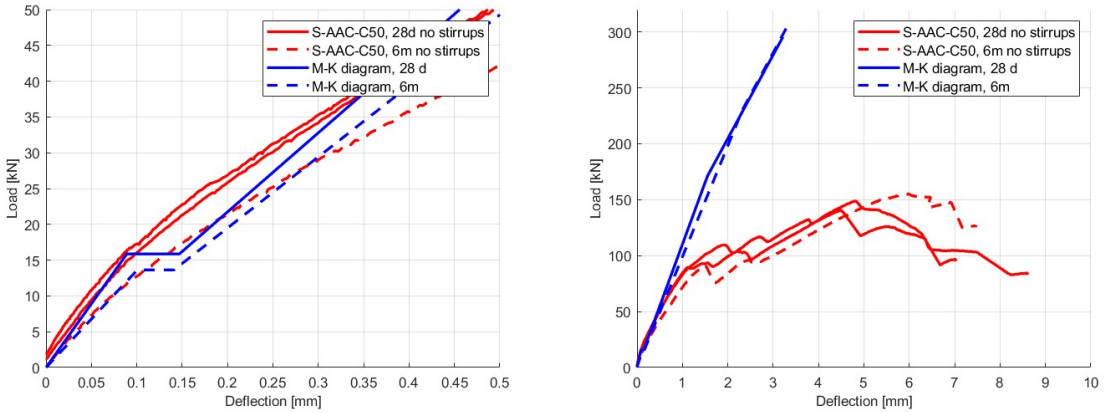

Figure 6.19: Shear results compared with force-deflection graph based on the M-k diagram for mixture S-AAC-C50 a) zoom of the graph and b) full graph.

6.5. Limitations

Some of the main limitations of the study include: 1) the number of shear beams tested, 2) the high amount of longitudinal steel reinforcement applied in the shear beams, 3) the duration of the study and 4) the AAC mixtures are experimentally compared to PCC mixtures and not to OPCC mixtures.

The first limitation of the study is the number of shear beams tested. In this study, two beams without stirrups and one beam with stirrups were tested at 28 days, followed by one beam without stirrups at six months for each mixture. By testing only one or two beams per type and age, there is a higher risk that results may be affected by random variations such as mix inconsistencies, curing conditions, reinforcement placement, or testing errors. Testing multiple beams (suggested: 5–10 samples) can help eliminate random variation and provide more confidence in the results. Based on testing only two beams, the highest standard deviation found is 5.92 corresponding to a coefficient of variation of 8.88 for the beams of the S-PCC-C50 mixture.

The second limitation of the study is the high amount of longitudinal steel reinforcement applied to the shear beams. The samples used for the shear tests contained 4% longitudinal steel reinforcement, which is above average. Over-reinforcing the shear specimens can affect the results by delaying the formation of diagonal shear cracks and reducing the shear crack width. This leads to improvements in aggregate interlock and dowel action capacity, ultimately influencing the shear failure capacity.

The third limitation of the study is its duration. The long-term behaviour of the shear beams was assessed over six months. While it is beneficial that this research provides insight beyond the typical 28-day period, a structure is designed to last 50 to 100 years. To fully understand the long-term shear behaviour, studies spanning multiple years should be conducted. Extending the investigation over an even longer period would provide a more complete understanding of shear behaviour over time.

Furthermore, a limitation of the study is that the specimens were made and stored under laboratory conditions. From 1 to 28 days, all specimens were placed in the fog room at a temperature of 20°C and relative humidity of >95%. Samples tested at 6 months were placed, after 28 days, in a room with a temperature of 20°C and relative humidity of 55%. These conditions differ from those typically found in real-world, outdoor environments. If AAC is exposed to weather conditions such as wind and sun, this could also affect the shrinkage behaviour of the concrete, ultimately influencing the shear behaviour.

Moreover, the study compared the AAC with PCC, not with OPCC. The knowledge and formulas available are mostly based on OPCC. Therefore, the results with PCC may differ from comparison with codes and formulas.

7

Conclusion and recommendations

7.1. Conclusion

The main goal of this study was to find an answer to the question: ***"What is the difference in shear behaviour of reinforced beams made of slag-based alkali-activated concrete versus Portland cement concrete, including the influence of age, shrinkage and strength class?"*** To answer this question, the sub-questions are addressed first, followed by the main research question.

7.1.1. Material properties

What are the differences in material properties influencing shear behaviour, namely tensile strength, elastic modulus and shrinkage, between slag-based alkali-activated concrete and Portland cement concrete mixtures?

Tensile strength

- The C30 mixtures exhibit similar tensile strength development over time for PCC and ACC. At 28 days, the tensile strengths are 3.5 MPa and 3.3 MPa, respectively, while at 6 months, they decrease to 2.6 MPa and 2.7 MPa. This represents a 26% reduction in tensile strength over six months.
- The C50 mixtures show differences in tensile strength at 28 days and 6 months. The S-AAC-C50 mixture has a lower tensile strength at 28 days (2.9 MPa) than the S-PCC-C50 mixture (3.9 MPa). Over 6 months, the tensile strength of the S-AAC-C50 mixture decreases by 14% to 2.5 MPa, while the S-PCC-C50 mixture remains constant.

The lowest tensile strength is measured in the following order:

1. S-AAC-C50 mixture (with a 14% reduction over 6 months)
2. S-AAC-C30 / S-PCC-C30 mixture (with a 26% reduction over 6 months)
3. S-PCC-C50 mixture

These results are interesting because the AAC mixture with the highest strength class does not result in the highest tensile strength. This outcome is different dan expected and different than described in the EC2, NEN-EN 1992-1-1, 2015.

Furthermore, from the direct tensile test, it is observed that the AAC mixtures show smooth cracks through the aggregate, while PCC mixtures show cracks around the aggregate. Therefore, it can be concluded that the bond in the ITZ zone is stronger for the AAC mixtures.

Elastic modulus

- The elastic modulus of the S-AAC-C30 and S-PCC-C30 mixtures is similar at both 28 days and 6 months, measuring 38 GPa and 39 GPa at 28 days, and 37 GPa for both mixtures at 6 months.

- The elastic modulus of the S-AAC-C50 mixture at 28 days is lower than that of the S-PCC-C50 mixture, measuring 38 GPa and 41 GPa, respectively. Over 6 months, the S-AAC-C50 mixture exhibits a 24% reduction in elastic modulus, decreasing to 29 GPa, while the elastic modulus of the S-PCC-C50 mixture remains unchanged.

The lowest stiffness is measured in the following order:

1. S-AAC-C50 mixture (with a 24% reduction over 6 months)
2. S-AAC-C30 / S-PCC-C30 mixture
3. S-PCC-C50 mixture

These results are consistent with the tensile strength measurements.

Autogenous shrinkage

- In the S-AAC-C30 mixture more autogenous shrinkage (+103% at 28d and +45% at 6m) is observed than in the S-PCC-C30 mixture. The values are 183 $\mu mm/mm$ and 90 $\mu mm/mm$ at 28 days, and 370 and 200 $\mu mm/mm$ at 6 months, for the S-AAC-C30 and S-PCC-C30 mixtures, respectively.
- In the S-AAC-C50 mixture more autogenous shrinkage (+205% at 28d and +145% at 6m) is observed than in the S-PCC-C50 mixture. The values are 363 $\mu mm/mm$ and 119 $\mu mm/mm$ at 28 days, and 489 $\mu mm/mm$ and 200 $\mu mm/mm$ at 6 months, for the S-AAC-C50 and S-PCC-C50 mixtures, respectively.

Both AAC mixtures exhibited higher autogenous shrinkage compared to PCC mixtures. For the higher strength mixtures, this was 2–3 times higher. The effect of higher measured autogenous shrinkage can be micro-cracks leading to a reduction in strength, stiffness and bond.

Drying shrinkage

- In the S-AAC-C30 mixture more drying shrinkage (+47% at 6m) is observed than in the S-PCC-C30 mixture, being 273 $\mu mm/mm$ and 186 $\mu mm/mm$ at 6 months, for the S-AAC-C30 and S-PCC-C30 mixtures, respectively.
- In the S-AAC-C50 mixture more drying shrinkage (+38% at 6m) is observed than in the S-PCC-C50 mixture, being 310 $\mu mm/mm$ and 225 $\mu mm/mm$ at 6 months, for the S-AAC-C50 and S-PCC-C50 mixtures, respectively.

Both AAC mixtures exhibited higher drying shrinkage compared to the PCC mixtures. For the higher-strength mixtures. The effect of higher measured drying shrinkage can be micro-cracks leading to a reduction in strength, stiffness and bond.

7.1.2. Effect of age

What is the effect of age on the material properties and structural behaviour of slag-based alkali-activated concrete?

The effect of aging is shown in Figure 7.1. The graphs illustrate the evolution of material properties (a, b, c) and structural behaviour (d) over a period from 28 days to 6 months for different mixtures: S-AAC-C30, S-PCC-C30, S-AAC-C50, and S-PCC-C50.

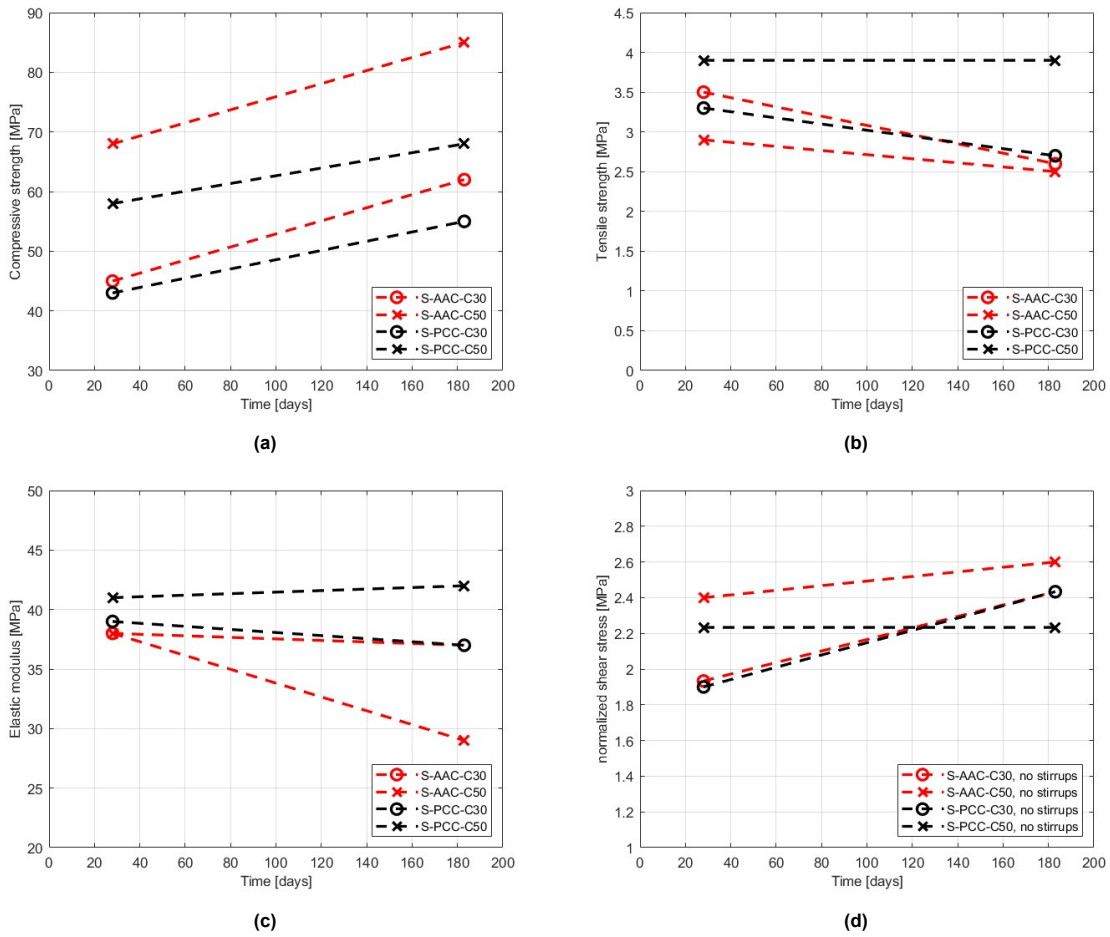

Figure 7.1: Material properties and structural behaviour versus time at 28 days and 6 months for the mixtures S-AAC-C30, S-PCC-C30, S-AAC-C50, and S-PCC-C50. a) compressive strength, b) tensile strength, c) elastic modulus and d) normalized shear stress.

The results for compressive strength (Figure 7.1a) show a general increase over time for all mixtures. The S-AAC-C30 and S-AAC-C50 mixtures exhibit a steeper increase compared to their PCC counterparts, indicating a more pronounced strength gain in AAC mixtures over time. Among all mixtures, S-AAC-C30 shows the highest increase.

The tensile strength results (Figure 7.1b) reveal either a reduction or stabilization over time. The S-AAC-C30 mixture experiences the most significant decrease in tensile strength, while the PCC mixtures show relatively minor changes. This suggests that AAC mixtures might be more susceptible to long-term reductions in tensile capacity compared to PCC mixtures.

For the elastic modulus (Figure 7.1c), the results indicate either stability or a decline over time. The most notable reduction is observed in the S-AAC-C50 mixture, while other mixtures show relatively smaller changes. This suggests that the stiffness of AAC mixtures, especially at higher strength grades (C50), tends to degrade more over time compared to PCC mixtures.

The results for the ultimate shear load (Figure 7.1d) indicate an overall increase over time, with the C30 mixtures showing the most significant improvement. The AAC and PCC mixtures follow a similar trend, but the rate of increase appears to be slightly higher for PCC mixtures. This suggests that shear capacity improves over time, with PCC mixtures potentially retaining a more stable structural response compared to AAC mixtures.

These findings highlight that while AAC mixtures demonstrate significant compressive strength gains over time, they also experience reductions in tensile strength and stiffness. PCC mixtures, on the other

hand, show more stable mechanical properties over the aging period.

7.1.3. Concrete strength class

What is the effect of concrete strength class on the shear behaviour of slag-based alkali-activated concrete?

When comparing the differences in the shear behaviour of the S-AAC-C30 mixture and the S-AAC-C50 mixture (Figure 7.2), the following observations were made:

- The first initial flexural crack for the S-AAC-C30 and S-AAC-C50 mixtures, tested at 28 days and 6 months, forms at approximately the same load: 22 kN and 18 kN at 28 days, and 17 kN and 20 kN at 6 months, respectively. Those results are lower than the material behaviour test at 28 days and 6 months.
- The elastic modulus obtained from the shear test results is higher for the S-AAC-C30 mixture at 28 days (+36%) and 6 months (+13%). Specifically, at 28 days, it is 30 GPa and 22 GPa, and at 6 months, it is 17 GPa and 15 GPa for the S-AAC-C30 and S-AAC-C50 mixtures, respectively. The results for 28 days are in line with the material behaviour test, the 6-month results are not in line with the material behaviour test.
- The first shear crack appears earlier (by 20 kN) for the S-AAC-C30 mixture at 28 days, but at a similar load at 6 months. Specifically, it occurs at 80 kN and 101 kN at 28 days for the S-AAC-C30 and S-AAC-C50 mixtures, respectively. At 6 months, it occurs at 87 kN for the S-AAC-C30 mixture and 88 kN for the S-AAC-C50 mixture.
- The crack stabilization stage (aggregate interlock, dowel action and residual tensile stress) is greater for the S-AAC-C50 mixture, by 50% at 28 days and 12% at 6 months. The S-AAC-C50 mixture has a crack stabilization stage of 45 kN at 28 days and 62 kN at 6 months, compared to 30 kN at 28 days and 55 kN at 6 months for the S-AAC-C30 mixture.
- The ultimate failure capacity is higher and increases over time (6 months) for the S-AAC-C50 mixture. Specifically, failure occurs at 144 kN at 28 days and 156 kN at 6 months, compared to 116 kN at 28 days and 146 kN at 6 months for the S-AAC-C30 mixture.

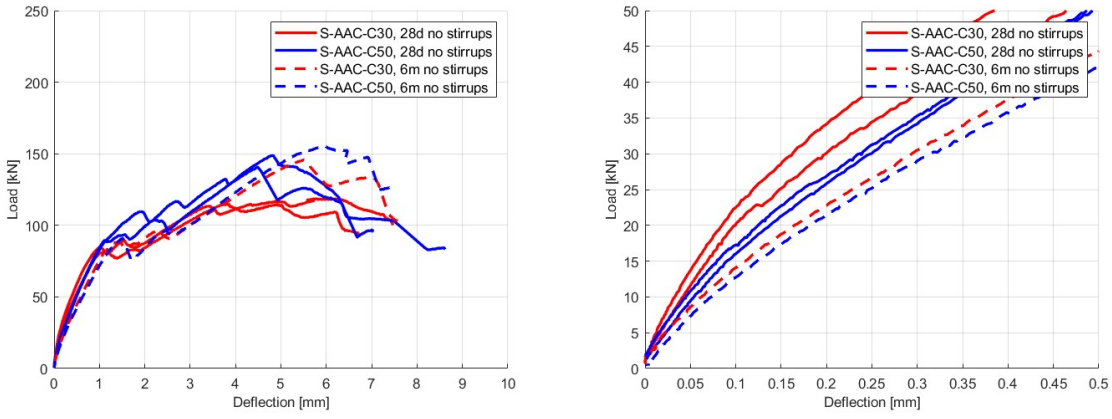

Figure 7.2: Load-displacement curves of S-AAC-C30 compared to S-AAC-C50.a) full graph and b) zoomed-in view from 0 mm to 0.5 mm deflection.

From these results, it can be observed that using a higher strength class of AAC concrete (from C30 to C50) does not lead to higher tensile strength, as the initial flexural cracks formed at the same load. It also does not result in a stiffer material, as the elastic modulus obtained from the shear test results was lower for the S-AAC-C50 mixture. Over time (6 months), it does not lead to a later formation of the first shear failure crack. However, the S-AAC-C50 mixture shows a increase in the crack stabilization stage (aggregate interlock, dowel action and residual tensile stress), which continues to grow over time (6 months), resulting in a greater ultimate shear failure capacity. This behaviour is different from that

found for the S-PCC-C30 and S-PCC-C50 beams, where a higher strength class leads to an increase in tensile strength, higher stiffness and later formation of the first shear crack and growth in the crack stabilization stage.

7.1.4. Shear behaviour of reinforced beams

"What is the difference in shear behaviour of reinforced beams made of slag-based alkali-activated concrete versus Portland cement concrete, including the influence of age, shrinkage and strength class?"

- The **strength class** of AAC mixtures influences the shear test results (See figure 7.4. A higher strength class does not result in a higher tensile strength, leading to early flexural cracks and a crack pattern with more cracks of shorter length for the S-AAC-C50 mixture. Additionally, for the S-AAC-C50 mixture, the elastic modulus is the lowest, which decreases the stiffness of the RC beams.
- The most significant difference over time between the AAC mixtures and the PCC mixtures is the higher amount of **shrinkage** measured in the AAC mixtures, even more in the S-AAC-C50 mixture. This is crucial because, during the shear strength test, the specimens contained longitudinal reinforcement, preventing them from freely shrinking. As a result, internal stresses developed within the concrete. If these stresses exceeded the tensile strength capacity of the concrete, they led to the formation of micro-cracks. These micro-cracks can reduce the strength and stiffness of the concrete, making shrinkage a key factor influencing the shear test results.
- Evidence of **micro-cracks** were found at 6 months in the S-AAC-C50 mixtures through UPV testing. The results show a lower velocity for the S-AAC-C50 mixture compared to the S-PCC-C50 mixture, indicating the presence of flaws such as micro-cracks in the concrete mixture S-AAC-C50.
- Final results from the shear test indicate a similar or higher **ultimate shear load capacity** for the AAC mixtures compared to the PCC mixtures at 28 days and 6 months.
- The AAC mixtures show a decrease in tensile strength and elastic modulus but an increase in ultimate shear capacity, due to a bigger increase of **crack stabilization stage** (aggregate interlock, dowel action and residual tensile stress) over time, 6 months, compared to the PCC mixtures. For the S-AAC-C30 mixture, the crack stabilization stage is 30 kN at 28 days and 55 kN at 6 months, representing an increase of +83%. The S-PCC-C30 mixture shows an stabilization stage of cracks of 28 kN at 28 days and 41 kN at 6 months, an increase of +46%. For the S-AAC-C50 mixture, the crack stabilization stage is 45 kN at 28 days and 62 kN at 6 months, representing an increase of +38%. The S-PCC-C50 mixture shows a crack stabilization stage of 45 kN at 28 days and 34 kN at 6 months, a decrease of −24%.

The results show that the AAC mixtures show a decrease in tensile strength and elastic modulus compared to the PCC mixtures, but an increase in the crack stabilization stage (aggregate interlock, dowel action and residual tensile stress), which improves the ultimate shear capacity of both AAC mixtures. Therefore, it can be concluded that the crack stabilization stage is the primary factor contributing to the increase in ultimate shear failure capacity for both AAC mixtures. As previously discussed, this stabilization stage depends on dowel action, aggregate interlock and residual tensile stress. However, there is no clear agreement on how these components influence the overall shear failure process or which mechanism governs failure. Consequently, it is difficult to determine which of these three factors contributes to the observed increase and whether the increase in the crack stabilization stage will continue over time or eventually decline. Additionally, the role of shrinkage in this increase in the stabilization stage is not clear from the results and should be further investigated.

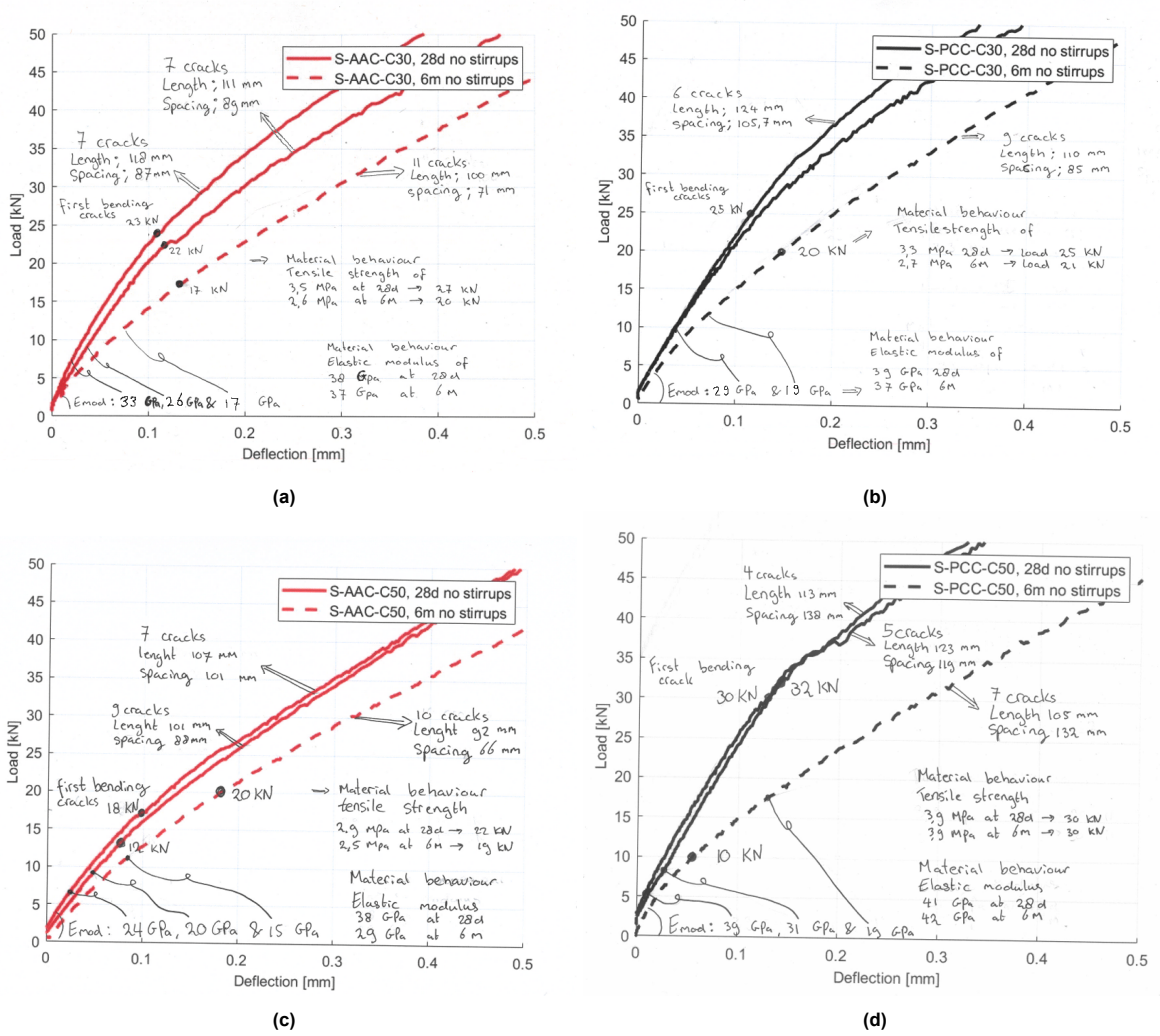

Figure 7.3: Zoom-in view of the load-displacement graphs, comparing the elastic modulus and tensile strength of the shear beams with the material behaviour test. a) S-AAC-C30 mixture, b) S-PCC-C30 mixture, c) S-AAC-C50 mixture and d) S-PCC-C50 mixture.

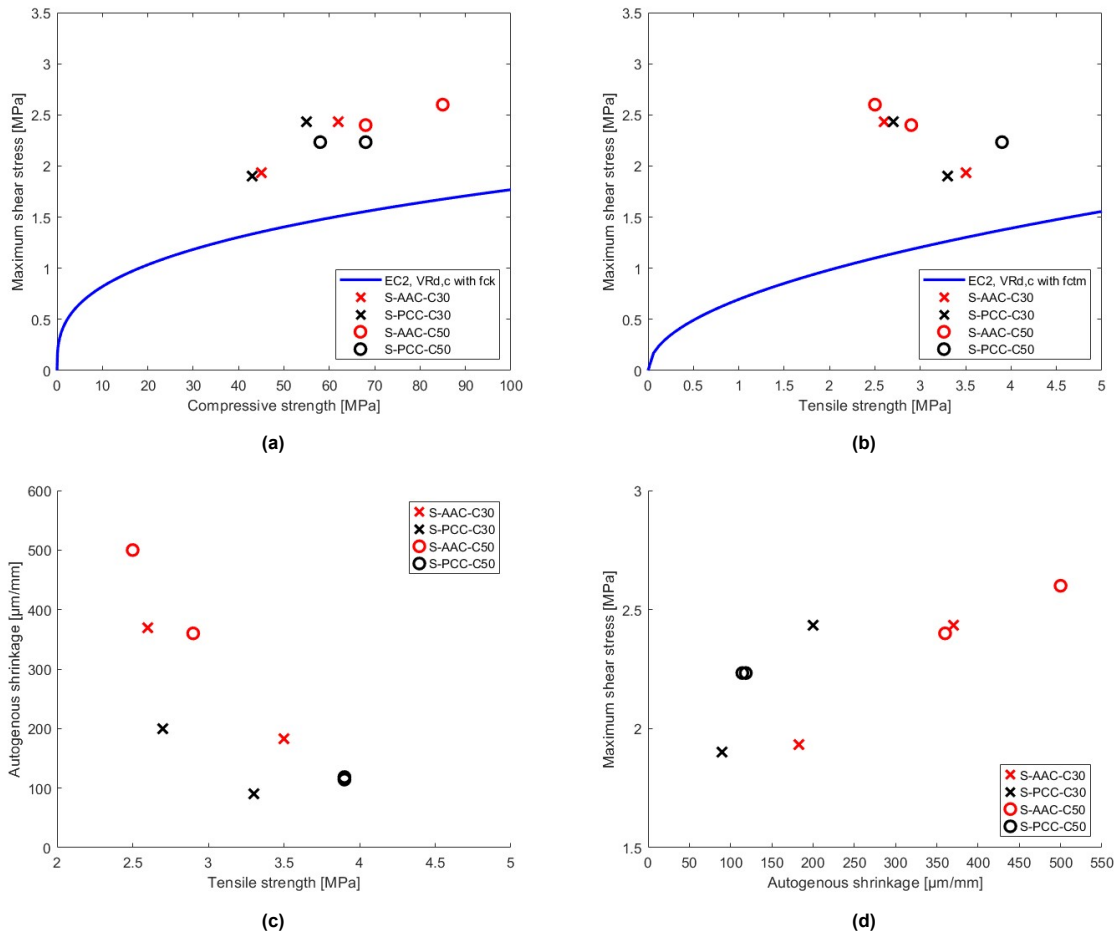

Figure 7.4: Relations between the experimental material behaviour and stuctural behaviour. a) Compressive strength and maximum shear stress, b) Tensile strength and maximum shear stress, c) Tensile strength and autogenous shrinkage and d) Autogenous shrinkage and maximum shear stress.

7.2. Recommendations

7.2.1. Future studies

To further investigate AAC and advance its application in the structural field, the following recommendations for future studies are made:

1. Bond strength of AACs and the influence of shrinkage

During the study, the importance of bond strength and its influence on the shear mechanism, including dowel action and aggregate interlock, is mentioned. To better understand the variations in aggregate interlock and dowel action, it is crucial to have a clear understanding of the bond strength of AAC and how it develops over time, particularly in relation to shrinkage effects.

2. Variation with different levels of reinforcement

One of the limitations of the study is the high amount of reinforcement used (4%). The results of the study show that a similar or higher amount of ultimate shear capacity comes mainly from the crack stabilization stage. It would be interesting to investigate to what extent reinforcement plays a role in this behaviour influencing the aggregate interlock and dowel action. The results have been compared to one study with less reinforcement (2%), the study of Huang et al., 2023 (See Section 6.4.2 and figure 6.15).

3. Long-term investigation

This study documented the shear behaviour of AAC for up to six months. It would be interesting to investigate a longer period to determine whether the shear capacity of AAC beams continues to increase

or if there is an optimum point for the crack stabilization stage. If the crack stabilization stage begins to weaken, the ultimate shear capacity will also decrease rapidly. This is particularly relevant because the construction design lifespan ranges from 50 to 100 years.

4. Analytical and numerical modelling of AAC behaviour
It would be interesting to investigate whether the material behaviour and shear behaviour of AAC can be accurately captured using analytical and numerical models. This study has already taken an initial step by comparing the results with existing analytical models, including NEN-EN 1992-1-1, 2015 and the General Shear Design Method (GSDM). See Appendix D for the detailed execution.

7.2.2. Application in the structural field

When applying AAC in the structural field, the following recommendations should be taken into account:

1. The analytical formulas for OPCC do not apply
The study showed that the analytical formulas obtained from EC2, NEN-EN 12390-6, 2023, did not correctly predict the tensile strength, elastic modulus and shrinkage for the AAC mixtures. Therefore, it is important to take into account that the relationship between compressive strength and other material properties does not necessarily apply to new types of concrete and should be reassessed before application.

2. Effects of shrinkage
The study showed that the high shrinkage measured in AAC affects its long-term material properties under restrained conditions. Therefore, when applying AAC, the impact of shrinkage should be considered, as excessive shrinkage in restrains conditions can lead to micro-cracks, reducing the strength and stiffness of the material.

Bibliography

ASCE-ACI Committee 445. (1998). Recent approaches to shear design of structural concrete. *Journal of Structural Engineering*, *124*(12), 1375–1417. https://doi.org/10.1061/(ASCE)0733-9445(1998)124:12(1375)

Awasthy, N., Schlangen, E., Hordijk, D., Šavija, B., & Luković, M. (2023). The role of eigen-stresses on apparent strength and stiffness of normal, high strength, and ultra-high performance fibre reinforced concrete. *Developments in the Built Environment*, *16*, 100277. https://doi.org/https://doi.org/10.1016/j.dibe.2023.100277

Awoyera, P. O., Babalola, O. E., & Aluko, O. G. (2022). 7 - the use of slags in recycled aggregate concrete. In P. O. Awoyera, C. Thomas, & M. S. Kirgiz (Eds.), *The structural integrity of recycled aggregate concrete produced with fillers and pozzolans* (pp. 145–170). Woodhead Publishing. https://doi.org/https://doi.org/10.1016/B978-0-12-824105-9.00009-3

Bendapudi, S. C. K., Ramesh, K., & Poluraju, P. (2017). An experimental investigation on flexural behavior of ggbs and metakaolin based geopolymer concrete. *Journal of engineering and applied sciences*, *12*. https://www.researchgate.net/publication/316934887_An_experimental_investigation_on_flexural_behavior_of_GGBS_and_Metakaolin_based_Geopolymer_concrete

Bezemer, H., Awasthy, N., & Luković, M. (2023). Multiscale analysis of long-term mechanical and durability behaviour of two alkali-activated slag-based types of concrete. *Construction and Building Materials*, *407*, 133507. https://doi.org/https://doi.org/10.1016/j.conbuildmat.2023.133507

Cartwright, C., Rajabipour, F., & Radlińska, A. (2015). Shrinkage characteristics of alkali-activated slag cements. *Journal of Materials in Civil Engineering*, *27*(7), B4014007. https://doi.org/10.1061/(ASCE)MT.1943-5533.0001058

Cembureau. (2024). *Cementing the european green deal* (tech. rep.). Cembureau The European Cement Association.

Cladera, A., & Marí, A. (2004a). Shear design procedure for reinforced normal and high-strength concrete beams using artificial neural networks. part i: Beams without stirrups. *Engineering Structures*, *26*(7), 917–926. https://doi.org/https://doi.org/10.1016/j.engstruct.2004.02.010

Cladera, A., & Marí, A. (2004b). Shear design procedure for reinforced normal and high-strength concrete beams using artificial neural networks. part ii: Beams with stirrups. *Engineering Structures*, *26*(7), 927–936. https://doi.org/https://doi.org/10.1016/j.engstruct.2004.02.011

Collins, F., & Sanjayan, J. (1999). Workability and mechanical properties of alkali activated slag concrete. *Cement and Concrete Research*, *29*(3), 455–458. https://doi.org/https://doi.org/10.1016/S0008-8846(98)00236-1

Ding, Y., Dai, J.-G., & Shi, C.-J. (2016). Mechanical properties of alkali-activated concrete: A state-of-the-art review. *Construction and Building Materials*, *127*, 68–79. https://doi.org/https://doi.org/10.1016/j.conbuildmat.2016.09.121

Djobo, N. (2016). *What is the difference between geopolymer and alkali activated cement?* Retrieved March 24, 2025, from https://www.researchgate.net/post/What-is-the-difference-between-geopolymer-and-alkali-activated-cement

European Environment Agency. (2024). *Climate change is one of the biggest challenges of our time*. Retrieved April 24, 2024, from https://www.eea.europa.eu/themes/climate/climate-change-is-one-of

Faraj, R. H., Ahmed, H. U., Hama ali, H. F., & Sherwani, A. F. H. (2022). 8 - fresh and mechanical properties of concrete made with recycled plastic aggregates. In F. Colangelo, R. Cioffi, & I. Farina (Eds.), *Handbook of sustainable concrete and industrial waste management* (pp. 167–185). Woodhead Publishing. https://doi.org/https://doi.org/10.1016/B978-0-12-821730-6.00023-1

Farhan, N. A., Sheikh, M. N., & Hadi, M. N. (2019). Investigation of engineering properties of normal and high strength fly ash based geopolymer and alkali-activated slag concrete compared to

ordinary portland cement concrete. *Construction and Building Materials*, *196*, 26–42. https://doi.org/https://doi.org/10.1016/j.conbuildmat.2018.11.083

Fenwick, R. C., & Paulay, T. (1968). Mechanisms of shear resistance of concrete beams. *Journal of the Structural Division*, *94*(10), 2325–2350. https://doi.org/10.1061/JSDEAG.0002092

Hordijk, D. (1991). *Local approach to fatigue of concrete* [Dissertation (TU Delft)]. Delft University of Technology.

Huang, Y., Gu, D., Mustafa, S., Grünewald, S., & Luković, M. (2023). Shear behaviour of reinforced concrete beams strengthened with ultra-high performance fiber reinforced concrete (uhpfrc). *Case Studies in Construction Materials*, *19*, e02441. https://doi.org/https://doi.org/10.1016/j.cscm.2023.e02441

Huber, T., Huber, P., & Kollegger, J. (2019). Influence of aggregate interlock on the shear resistance of reinforced concrete beams without stirrups. *Engineering Structures*, *186*, 26–42. https://doi.org/https://doi.org/10.1016/j.engstruct.2019.01.074

Jeli, I., Pavlović, M. N., & Kotsovos, M. D. (1999). A study of dowel action in reinforced concrete beams. *Magazine of Concrete Research*, *51*(2), 131–141. https://doi.org/10.1680/macr.1999.51.2.131

Kalyan, T. S., & Kishen, J. M. C. (2016). Experimental evaluation of cracks in concrete by ultrasonic pulse velocity. https://api.semanticscholar.org/CorpusID:29797934

Kani, G. N. J. (1964). The riddle of shear failure and its solution. *Journal of the american concrete instiute*, 441–468. https://doi.org/10.14359/7791

Li, Z., Zhang, S., Liang, X., & Ye, G. (2020). Cracking potential of alkali-activated slag and fly ash concrete subjected to restrained autogenous shrinkage. *Cement and Concrete Composites*, *114*, 103767. https://doi.org/https://doi.org/10.1016/j.cemconcomp.2020.103767

Liang, M., Chang, Z., Zhang, Y., Cheng, H., He, S., Schlangen, E., & Šavija, B. (2023). Autogenous deformation induced- stress evolution in high-volume ggbfs concrete: Macro-scale behavior and micro-scale origin. *Construction and Building Materials*, *370*, 130663. https://doi.org/https://doi.org/10.1016/j.conbuildmat.2023.130663

Liu, Y., Zhou, F., Shen, Y., Hwang, H.-J., Du, Y., Mao, Y., & Shi, C. (2023). Shear transfer strength of alkali-activated slag-based concrete. *Journal of Building Engineering*, *70*, 106304. https://doi.org/https://doi.org/10.1016/j.jobe.2023.106304

Lu, T., Liang, X., Liu, C., Chen, Y., & Li, Z. (2023). Experimental and numerical study on the mitigation of autogenous shrinkage of cementitious material. *Cement and Concrete Composites*, *141*, 105147. https://doi.org/https://doi.org/10.1016/j.cemconcomp.2023.105147

Mors, R. (2011). *Autogenous shrinkage. cementitious materials containing bfs* [Doctoral dissertation, Delft University of Technology].

Mörsch, E. (1909). *Concrete-streel construction (der eisenbetonbau)*. E.P Goodrich consulting engineer.

Nasir, M., Mahmood, A. H., & Bahraq, A. A. (2024). History, recent progress, and future challenges of alkali-activated binders – an overview. *Construction and Building Materials*, *426*, 136141. https://doi.org/https://doi.org/10.1016/j.conbuildmat.2024.136141

Nedeljković, M., Ghiassi, B., van der Laan, S., Li, Z., & Ye, G. (2019). Effect of curing conditions on the pore solution and carbonation resistance of alkali-activated fly ash and slag pastes. *Cement and Concrete Research*, *116*, 146–158. https://doi.org/https://doi.org/10.1016/j.cemconres.2018.11.011

NEN-EN 12390-13. (2021). *Testing hardened concrete - part 13: Determination of secant modulus of elasticity in compression* (tech. rep.). European committee for standardization. Brussels.

NEN-EN 12390-3. (2019). *Testing hardened concrete- part 3: Compressive strength of test speciments* (tech. rep.). European committee for standardization. Brussels.

NEN-EN 12390-6. (2023). *Testing hardened concrete- part 6: Tensile splitting strength of test specimens* (tech. rep.). European committee for standardization. Brussels.

NEN-EN 1992-1-1. (2015). *Eurocode 2: Design of concrete structures - part 1-1: General rules and rules for buildings* (tech. rep.). European committee for standardization. Brussels.

Olivier, J., & Peters, J. (2020). *Trends in global CO_2 and total greenhouse gas emissions* (tech. rep.). PBL Netherlands Environmental Assessment Agency.

Ouyang, X., Yong, H., Xiang, H., Yin, J., & Shi, C. (2024). 5. evaluation of tensile failure behavior of ultra high performance concrete under double-edge wedge splitting and direct tension loadings. *Journal of building engineering*. https://doi.org/10.1016/j.jobe.2024.109480

Prinsse, S. (2017). *Alkaliactivated concrete: Development of material properties (strength and stiffness) and flexural behaviour of reinforced beams over time* [Doctoral dissertation, Delft University of Technology].

Prinsse, S., Hordijk, D. A., Ye, G., Lagendijk, P., & Luković, M. (2020). Time-dependent material properties and reinforced beams behavior of two alkali-activated types of concrete. *Structural Concrete*, *21*, 642–658.

Provis, J. L. (2014). Geopolymers and other alkali activated materials: Why, how, and what? *Materials and structures*, *47*, 11–25.

Ridtirud, C., Chindaprasirt, P., & Pimraksa, K. (2011). Factors affecting the shrinkage of fly ash geopolymers. *International Journal of Minerals, Metallurgy, and Materials*, *18*(1).

Samad, A. A. A., N. Mohamad, J. J., N. Ali, & Mendis, P. (2016). *Rehabilitation of continuous reinforced concrete beams in shear by external bonding of carbon fiber reinforced polymer strips for sustainable construction.* https://www.researchgate.net/publication/308182442_Rehabilitation_of_Continuous_Reinforced_Concrete_Beams_in_Shear_by_External_Bonding_of_Carbon_Fiber_Reinforced_Polymer_Strips_for_Sustainable_Construction

Sarkhosh, R. (2014). *Shear resistance of reinforced concrete beams without shear reinforcement under sustained loading* [Dissertation (TU Delft)]. Delft University of Technology.

Shah, A., & Shah, C. (2017). Comparison of load displacement relationship and crack development in reinforced geopolymer concrete. *In International Conference on Advances in Construction Materials and Systems*. https://www.researchgate.net/publication/344689283_COMPARISON_OF_LOAD_DISPLACEMENT_RELATIONSHIP_AND_CRACK_DEVELOPMENT_MECHANISM_IN_REINFORCED_GEOPOLYMER_CONCRETE_BEAMS_WITH_THAT_OF_REGULAR_REINFORCED_CONCRETE_BEAMS#fullTextFileContent

Shen, Q., Chen, W., Liu, C., Zou, W., & Pan, L. (2019). 1. the tensile strength and damage characteristics of two types of concrete and their interface. *Materials*. https://doi.org/10.3390/MA13010016

Soomro, M., Tam, V. W., & Jorge Evangelista, A. C. (2023). 2 - production of cement and its environmental impact. In V. W. Tam, M. Soomro, & A. C. Jorge Evangelista (Eds.), *Recycled concrete* (pp. 11–46). Woodhead Publishing. https://doi.org/https://doi.org/10.1016/B978-0-323-85210-4.00010-2

ST sentech. (2023). *How does a lvdt sensor work?* Retrieved January 14, 2025, from https://www.sentechsensors.com/news/how-does-a-lvdt-sensor-work#:~:text=It%20works%20by%20converting%20the,that%20moves%20within%20the%20coils.

Tang, S., Huang, D., & He, Z. (2021). A review of autogenous shrinkage models of concrete. *Journal of Building Engineering*, *44*, 103412. https://doi.org/https://doi.org/10.1016/j.jobe.2021.103412

Teeuwen, S. B. (2024). *Shear capacity of concrete beams reinforced with basalt fiber-reinforced polymer stirrups* [Doctoral dissertation, Delft University of Technology].

van Breugel, K. (2023). *Invloed kruip op autogene krimp*. Retrieved March 21, 2025, from https://www.cementonline.nl/artikelen/invloed-kruip-op-autogene-krimp

Visintin, P., Mohamed Ali, M., Albitar, M., & Lucas, W. (2017). Shear behaviour of geopolymer concrete beams without stirrups. *Construction and Building Materials*, *148*, 10–21. https://doi.org/https://doi.org/10.1016/j.conbuildmat.2017.05.010

Wang, L., Wang, L., Li, Y., & Wang, J. (2023). A century-long analysis of global warming and earth temperature using a rondom walk with drift approach. *Elsevier*, *7*.

Wardhono, A., Gunasekara, C., Law, D. W., & Setunge, S. (2017). Comparison of long term performance between alkali activated slag and fly ash geopolymer concretes. *Construction and Building Materials*, *143*, 272–279. https://doi.org/https://doi.org/10.1016/j.conbuildmat.2017.03.153

Wu, C., Hwang, H.-J., Shi, C., Li, N., & Du, Y. (2020). Shear tests on reinforced slag-based geopolymer concrete beams with transverse reinforcement. *Engineering Structures*, *219*, 110966. https://doi.org/https://doi.org/10.1016/j.engstruct.2020.110966

Yang, R., He, Y., & Zhang, H. (2016). Progress and trends in nondestructive testing and evaluation for wind turbine composite blade. *Renewable and Sustainable Energy Reviews*, *60*, 1225–1250. https://doi.org/https://doi.org/10.1016/j.rser.2016.02.026

Yang, Y. (2014). *Shear behaviour of reinforced concrete members without shear reinforcement: A new look at an old problem* [Dissertation (TU Delft)]. Delft University of Technology. Yuguang YANG. https://doi.org/10.4233/uuid:ac776cf0-4412-4079-968f-9eacb67e8846

A

Verification of the DIC measurements with the LVDT measurements

S-AAC-C30-1 at 28 days

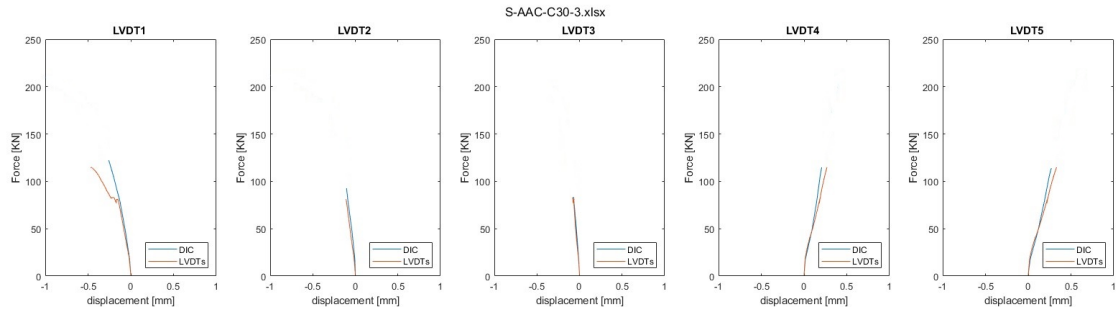

Figure A.1: Verification of the DIC measurements with the LVDT measurements

S-AAC-C30-2 at 28 days

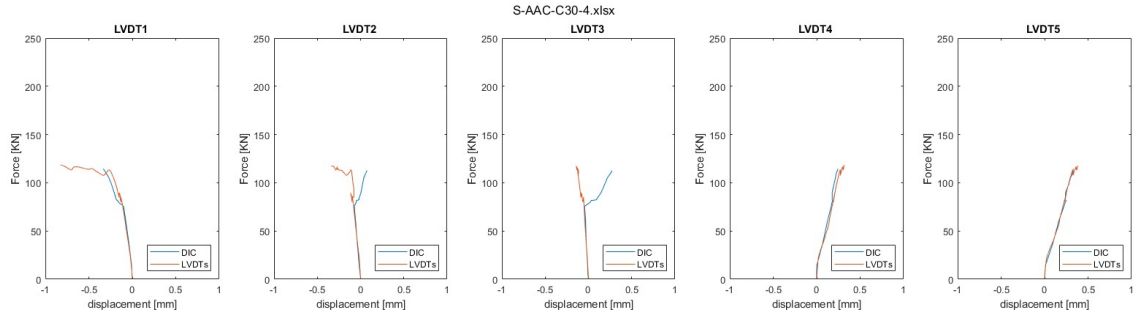

Figure A.2: Verification of the DIC measurements with the LVDT measurements

S-AAC-C30 with stirrups at 28 days

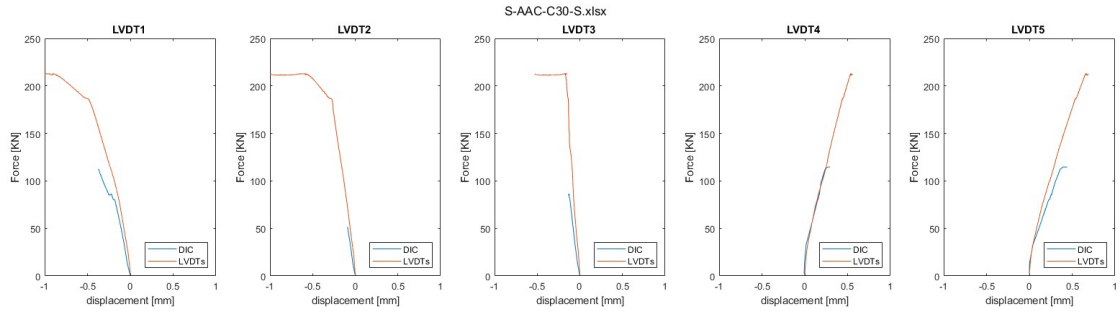

Figure A.3: Verification of the DIC measurements with the LVDT measurements

S-AAC-C30 at 6 months

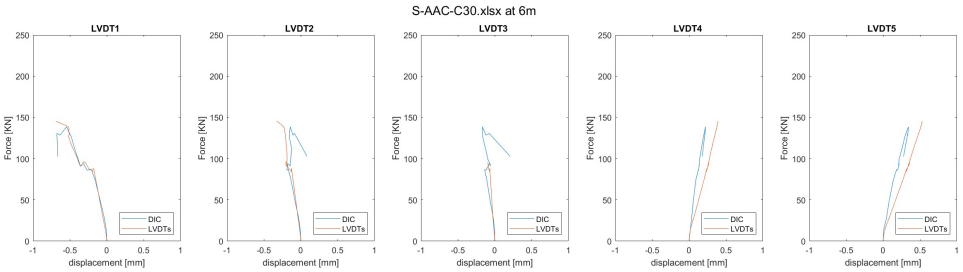

Figure A.4: Verification of the DIC measurements with the LVDT measurements

S-PCC-C30-1 at 28 days

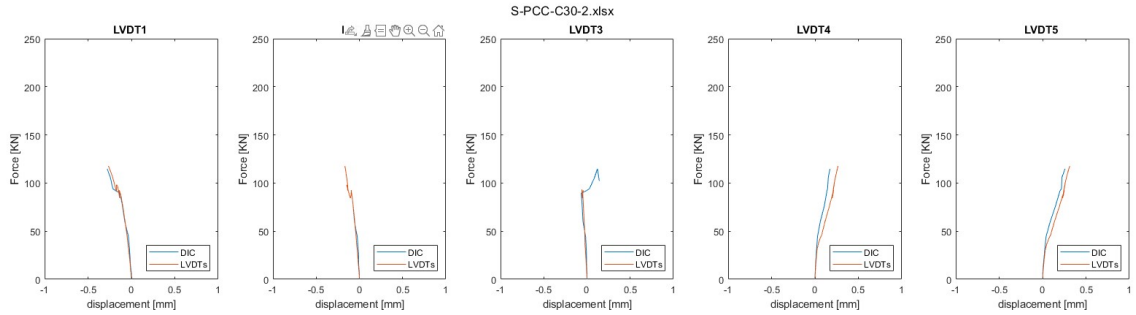

Figure A.5: Verification of the DIC measurements with the LVDT measurements

S-PCC-C30-2 at 28 days

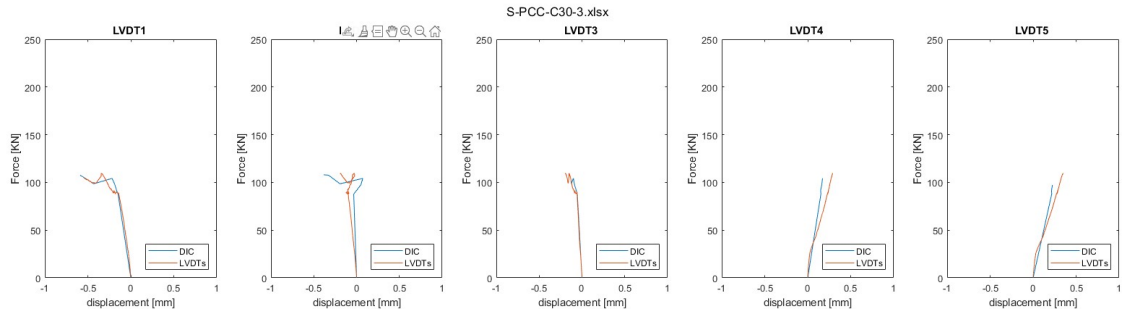

Figure A.6: Verification of the DIC measurements with the LVDT measurements

S-PCC-C30 with stirrups at 28 days

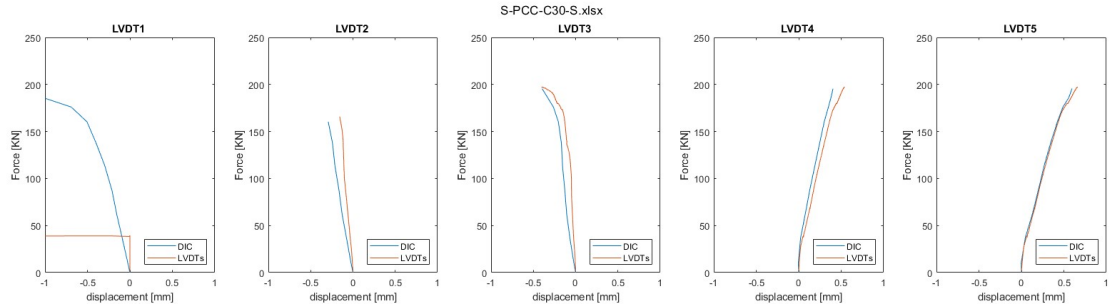

Figure A.7: Verification of the DIC measurements with the LVDT measurements

S-PCC-C30 at 6 months

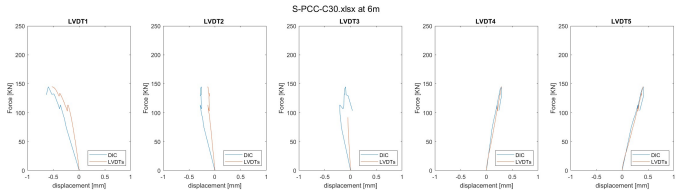

Figure A.8: Load-deflection curve of beam S-PCC-C30-6m

S-AAC-C50-1 at 28 days

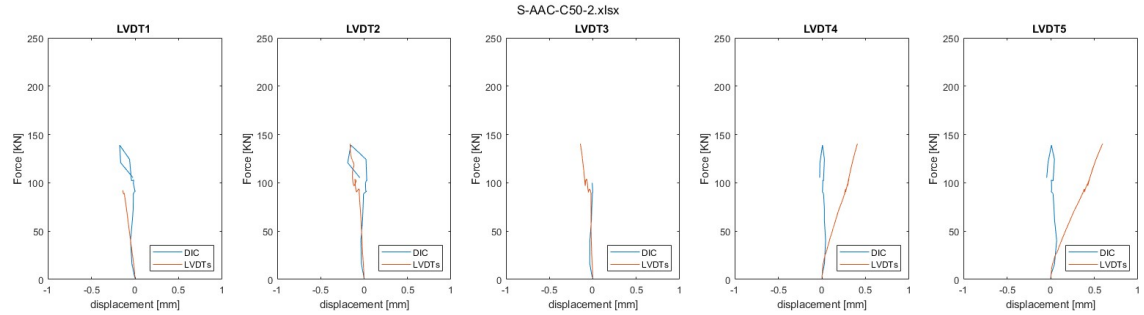

Figure A.9: Verification of the DIC measurements with the LVDT measurements

S-AAC-C50-2 at 28 days

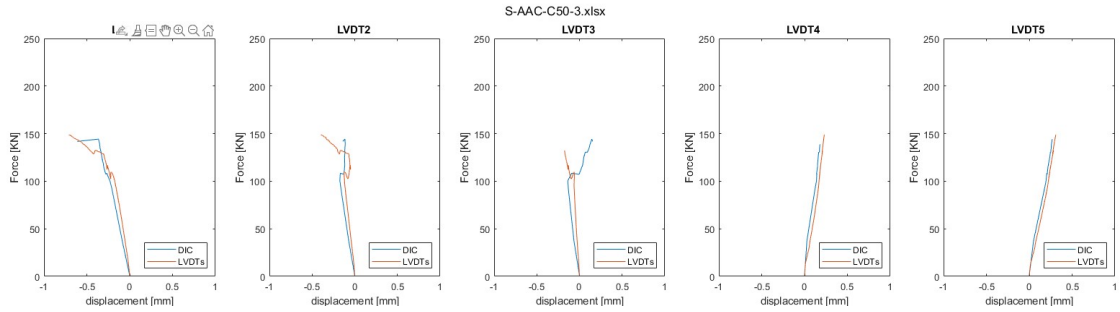

Figure A.10: Verification of the DIC measurements with the LVDT measurements

S-AAC-C50 with stirrups at 28 days

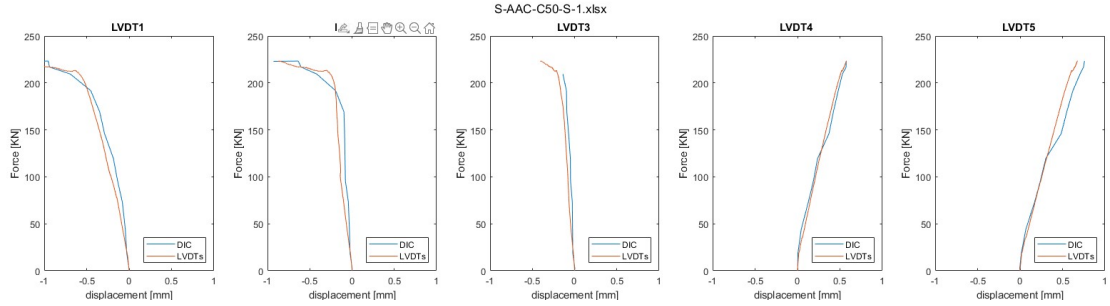

Figure A.11: Verification of the DIC measurements with the LVDT measurements

S-AAC-C50 at 6 months

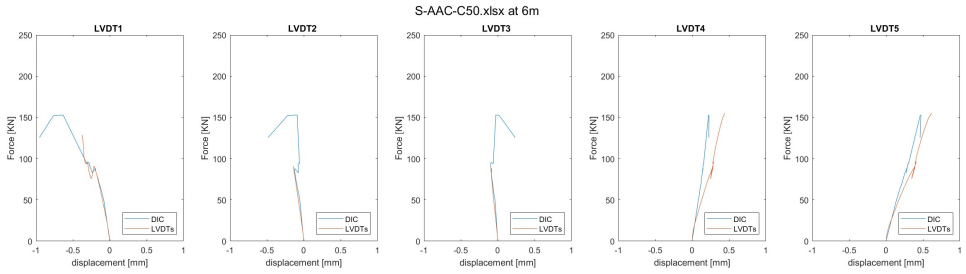

Figure A.12: Verification of the DIC measurements with the LVDT measurements

S-PCC-C50-1 at 28 days

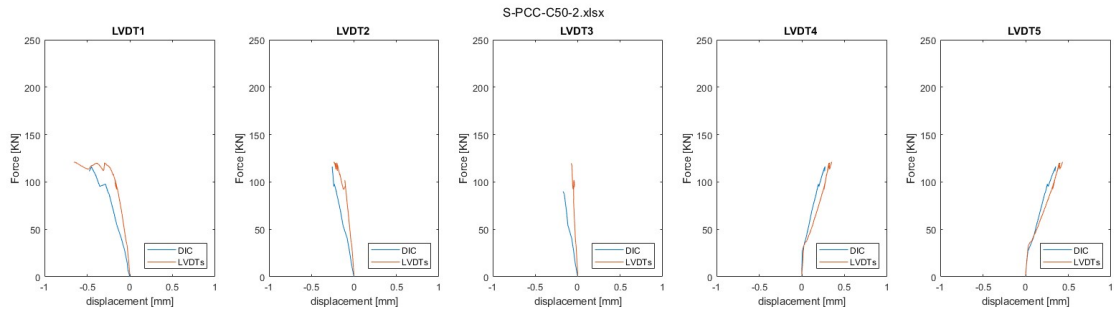

Figure A.13: Verification of the DIC measurements with the LVDT measurements

S-PCC-C50-2 at 28 days

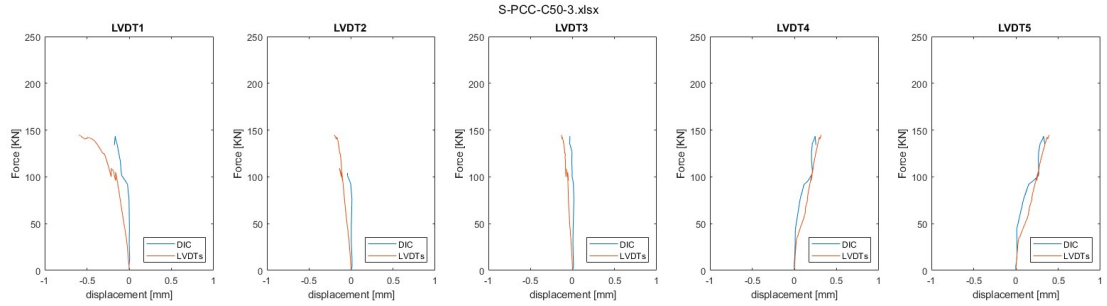

Figure A.14: Verification of the DIC measurements with the LVDT measurements

S-PCC-C50 with stirrups at 28 days

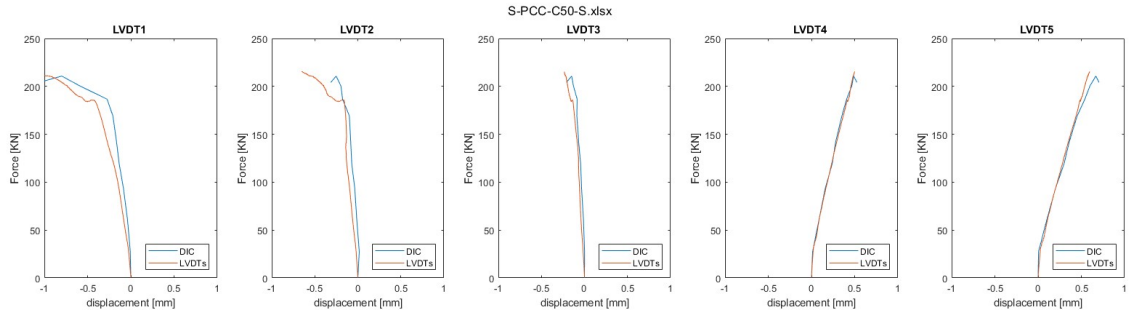

Figure A.15: Verification of the DIC measurements with the LVDT measurements

S-PCC-C50 at 6 months

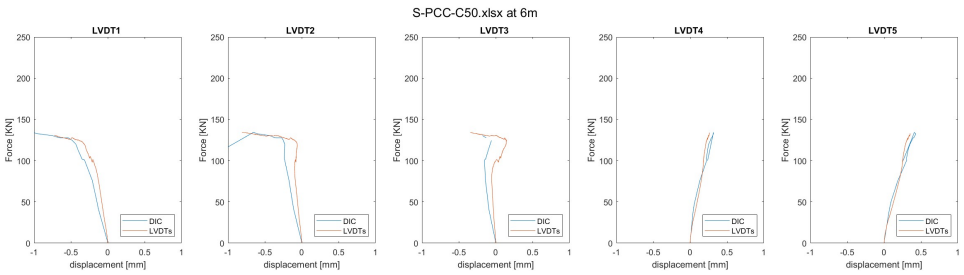

Figure A.16: Verification of the DIC measurements with the LVDT measurements

B

Images of direct tensile test specimens

B.1. S-AAC-C30 dogbones

S-AAC-C30-S1 tested at 28 days

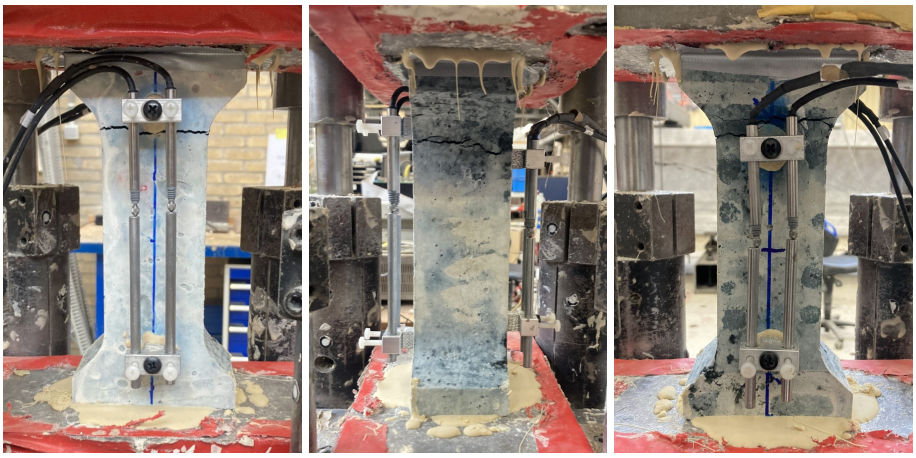

(a) Front **(b)** Side **(c)** Back

Figure B.1: Dogbone S-AAC-C30-S1 after failure

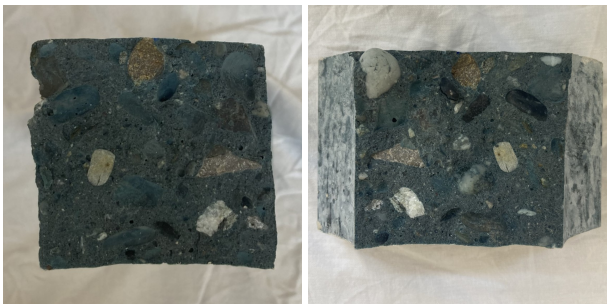

(a) Bottom part **(b)** Top part

Figure B.2: Cross-section of the crack of dogbone S-AAC-C30-S1

S-AAC-C30-S2 tested at 28 days

(a) Front **(b)** Side **(c)** Back

Figure B.3: Dogbone S-AAC-C30-S2 after failure

(a) Bottom part **(b)** Top part

Figure B.4: Cross-section of the crack of dogbone S-AAC-C30-S2

S-AAC-C30-S3 tested at 28 days

(a) Front **(b)** Side **(c)** Back

Figure B.5: Dogbone S-AAC-C30-S3 after failure

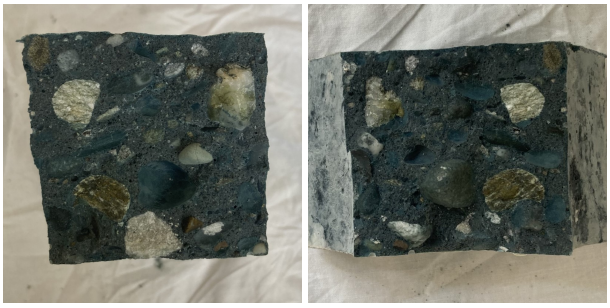

(a) Bottom part **(b)** Top part

Figure B.6: Cross-section of the crack of dogbone S-AAC-C30-S3

S-AAC-C30-S4 tested at 28 days

(a) Front **(b)** Side **(c)** Back

Figure B.7: Dogbone S-AAC-C30-S4 after failure

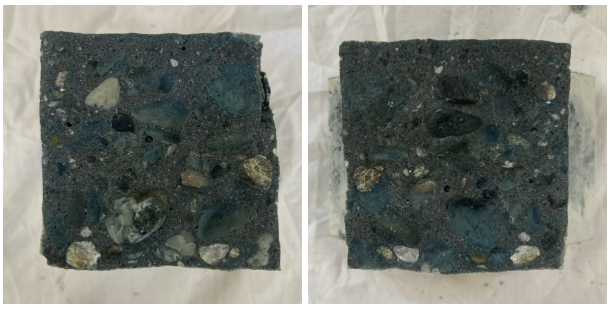

(a) Bottom part **(b)** Top part

Figure B.8: Cross-section of the crack of dogbone S-AAC-C30-S4

S-AAC-C30-S2 tested at 6 months

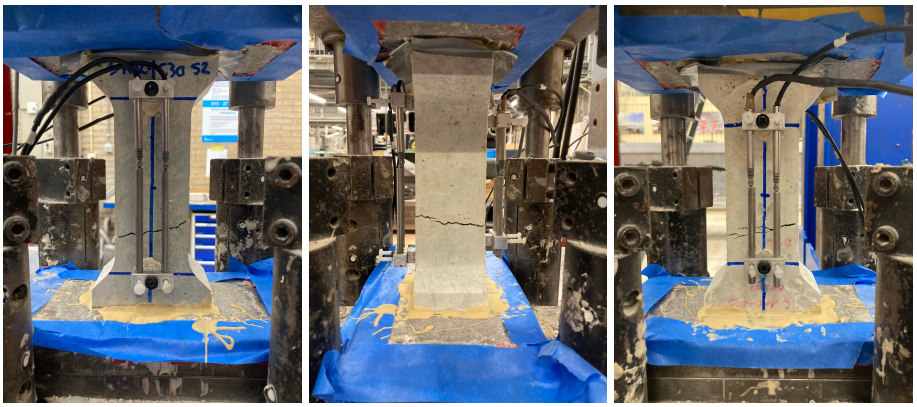

(a) Front **(b)** Side **(c)** Back

Figure B.9: Dogbone S-AAC-C30-S2 after failure at 6m

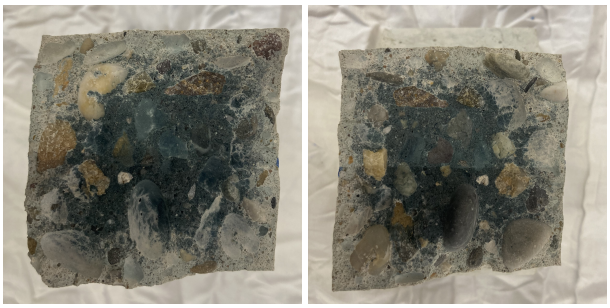

(a) Bottom part **(b)** Top part

Figure B.10: Cross-section of the crack of dogbone S-AAC-C30-S2 at 6m

S-AAC-C30-S2 tested at 6 months

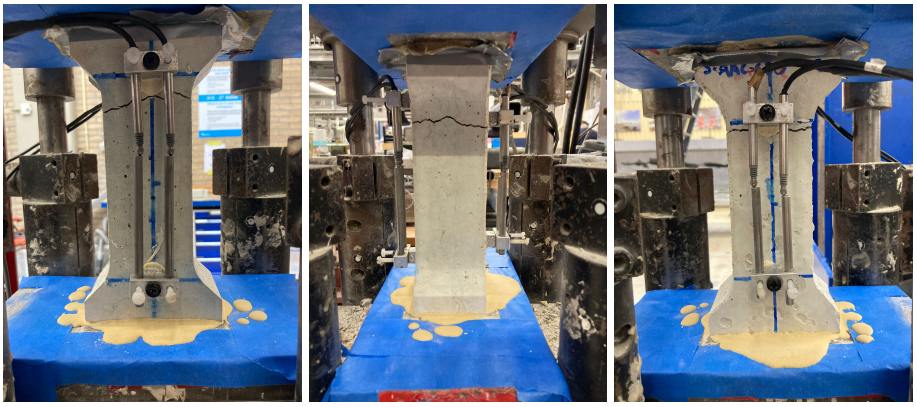

(a) Front **(b)** Side **(c)** Back

Figure B.11: Dogbone S-AAC-C30-S3 after failure at 6m

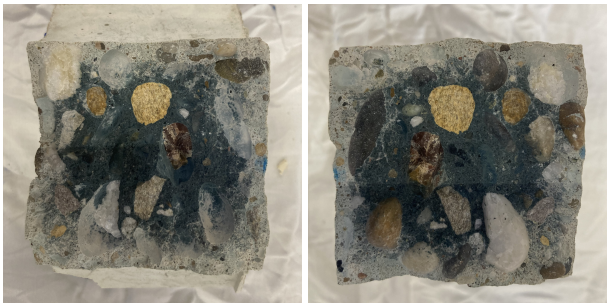

(a) Bottom part **(b)** Top part

Figure B.12: Cross-section of the crack of dogbone S-AAC-C30-S3 at 6m

S-AAC-C30-S4 tested at 6 months

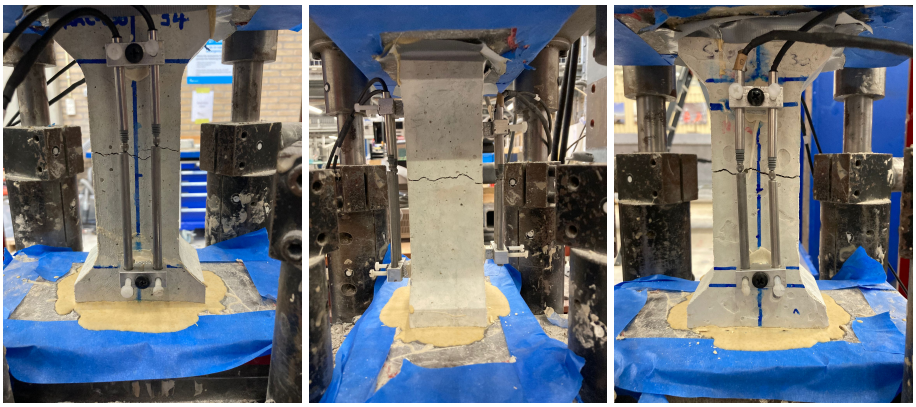

(a) Front **(b)** Side **(c)** Back

Figure B.13: Dogbone S-AAC-C30-S4 after failure at 6m

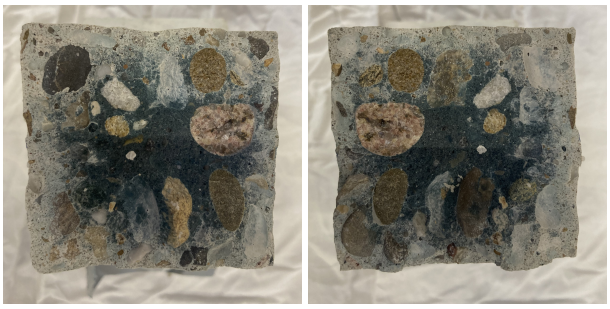

(a) Bottom part **(b)** Top part

Figure B.14: Cross-section of the crack of dogbone S-AAC-C30-S4 at 6m

B.2. S-PCC-C30 dogbones

S-PCC-C30-S1 tested at 28 days

(a) Front **(b)** Side **(c)** Back

Figure B.15: Dogbone S-PCC-C30-S1 after failure

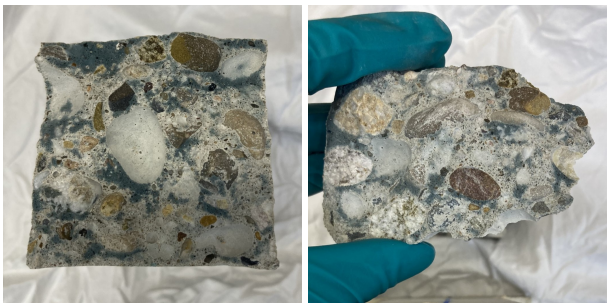

(a) Bottom part **(b)** Top part

Figure B.16: Cross-section of the crack of dogbone S-PCC-C30-S1

S-PCC-C30-S2 tested at 28 days

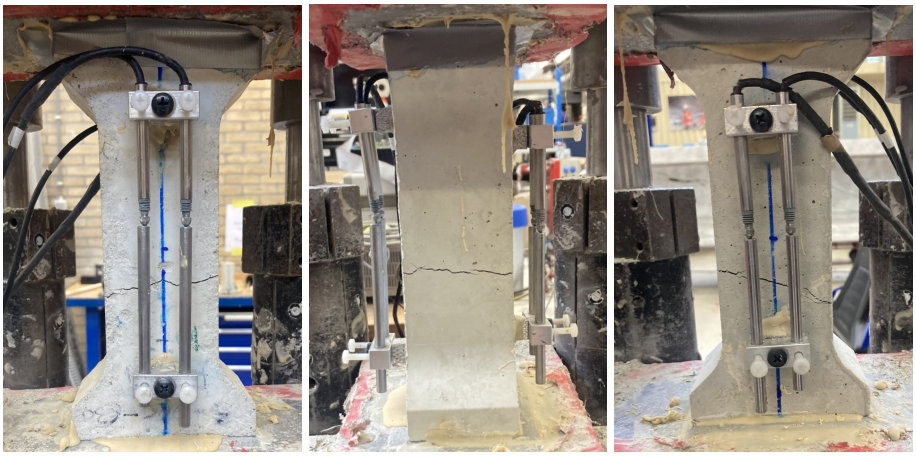

(a) Front **(b)** Side **(c)** Back

Figure B.17: Dogbone S-PCC-C30-S2 after failure

(a) Bottom part **(b)** Top part

Figure B.18: Cross-section of the crack of dogbone S-PCC-C30-S2

S-PCC-C30-S3 tested at 28 days

(a) Front **(b)** Side **(c)** Back

Figure B.19: Dogbone S-PCC-C30-S3 after failure

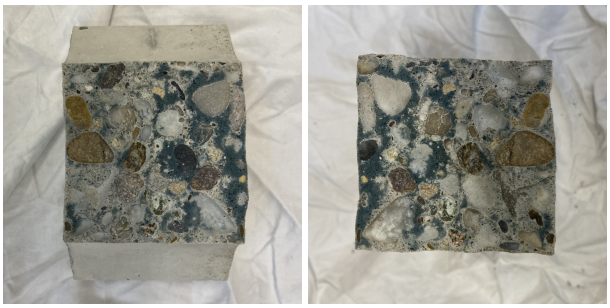

(a) Bottom part **(b)** Top part

Figure B.20: Cross-section of the crack of dogbone S-PCC-C30-S3

S-PCC-C30-S4, tested at 28 days

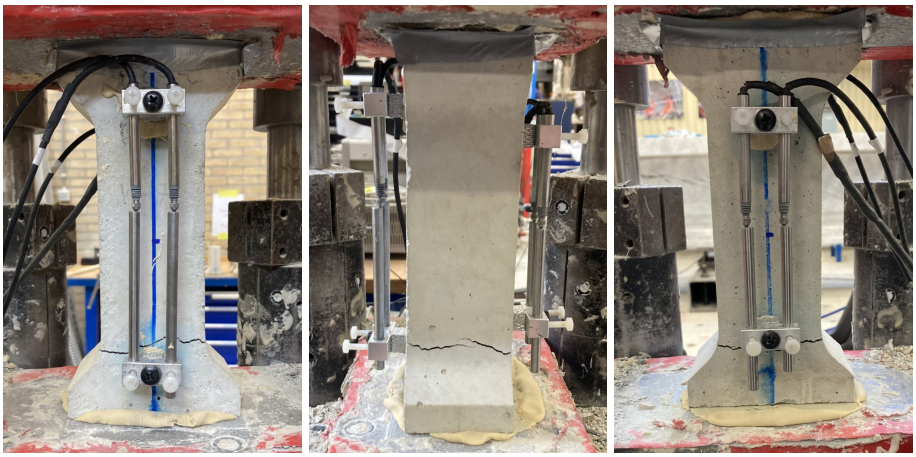

(a) Front **(b)** Side **(c)** Back

Figure B.21: Dogbone S-PCC-C30-S4 after failure

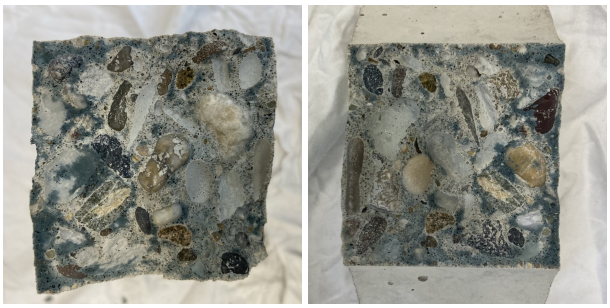

(a) Bottom part **(b)** Top part

Figure B.22: Cross-section of the crack of dogbone S-PCC-C30-S4

S-PCC-C30-S1 tested at 6 months

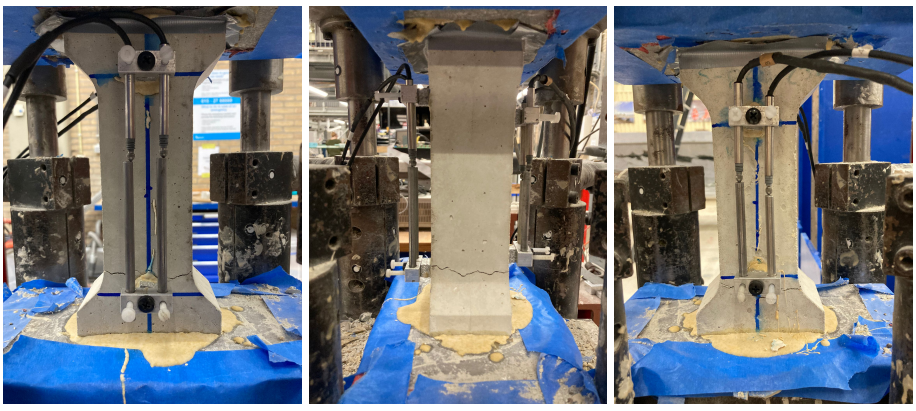

(a) Front **(b)** Side **(c)** Back

Figure B.23: Dogbone S-PCC-C30-S1 after failure at 6m

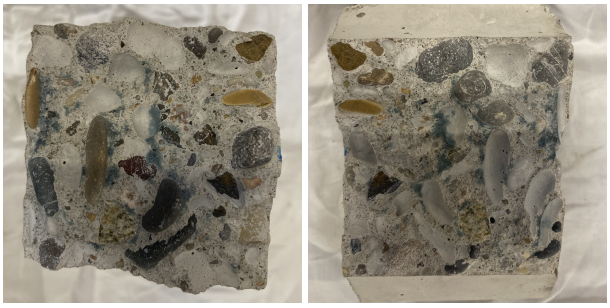

(a) Bottom part **(b)** Top part

Figure B.24: Cross-section of the crack of dogbone S-PCC-C30-S1 at 6m

S-PCC-C30-S2 tested at 6 months

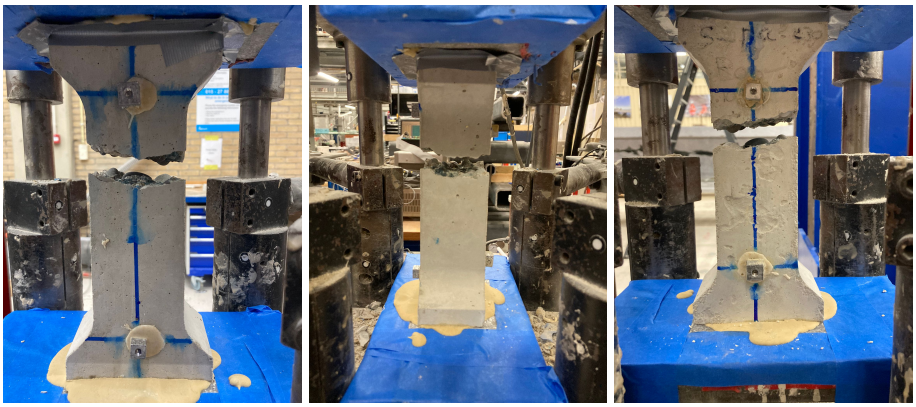

(a) Front **(b)** Side **(c)** Back

Figure B.25: Dogbone S-PCC-C30-S2 after failure at 6m

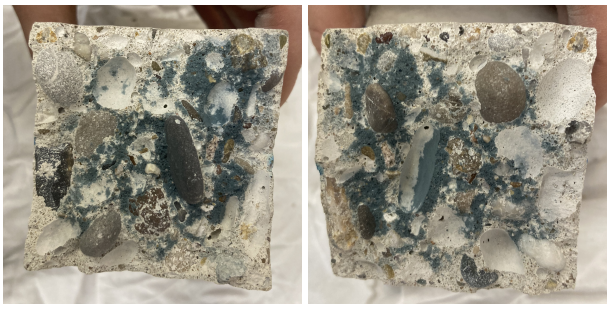

(a) Bottom part **(b)** Top part

Figure B.26: Cross-section of the crack of dogbone S-PCC-C30-S2 at 6m

S-PCC-C30-S3 tested at 6 months

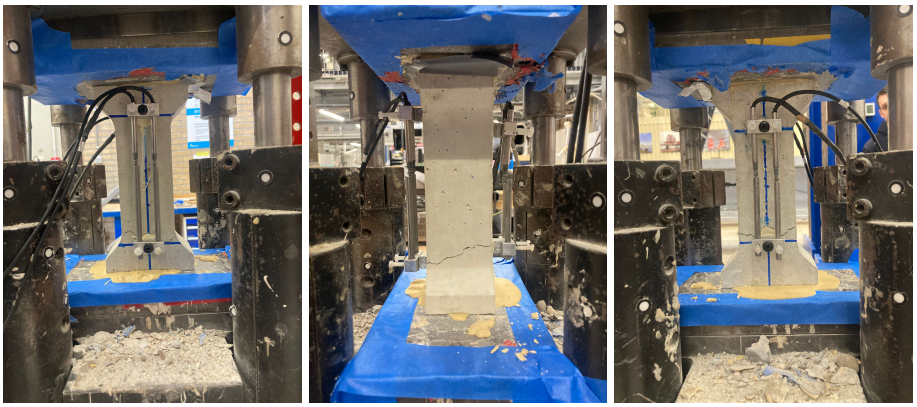

(a) Front **(b)** Side **(c)** Back

Figure B.27: Dogbone S-PCC-C30-S3 after failure at 6m

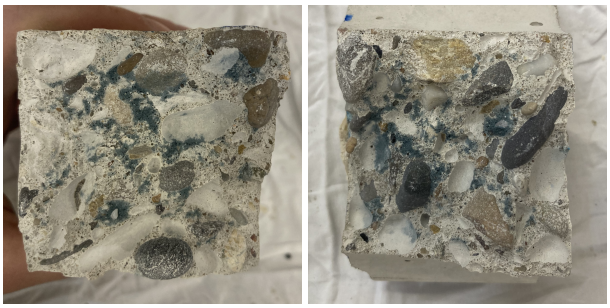

(a) Bottom part **(b)** Top part

Figure B.28: Cross-section of the crack of dogbone S-PCC-C30-S3 at 6m

S-PCC-C30-S4 tested at 6 months

(a) Front **(b)** Side

Figure B.29: Dogbone S-PCC-C30-S4 after failure at 6m

(a) Bottom part **(b)** Top part

Figure B.30: Cross-section of the crack of dogbone S-PCC-C30-S4 at 6m

C

Shear behaviour test results

C.1. Experimental results

Table C.1: Overview experimental results shear test, beams with no stirrups at 28 days

	First crack		Maximum capacity		
	Force	Mid-span defl.	Force	Mid-span defl.	Shear capacity
Beam	F_{max} [kN]	δ [mm]	F_{max} [kN]	δ [mm]	V [kN] [mm]
S-AAC-C30-1	80.65	1.05	114.76	3.80	57.38
S-AAC-C30-2	85.27	1.02	118.86	5.77	59.43
mean	82.96	1.04	116.81	4.79	58.41
std	2.31	0.02	2.05	0.99	1.03
CoV	2.78	1.45	1.75	20.59	1.75
S-PCC-C30-1	92.52	1.12	117.84	2.90	58.92
S-PCC-C30-2	89.23	1.02	109.85	4.77	54.92
mean	90.88	1.07	113.85	3.53	56.92
std	1.65	0.05	4.00	1.24	2.00
CoV	1.81	4.67	3.51	35.13	3.51
S-AAC-C50-1	89.40	1.12	140.77	4.49	70.38
S-AAC-C50-2	109.62	1.87	148.27	4.83	74.47
mean	99.51	1.50	144.52	4.66	72.43
std	10.11	0.38	3.75	0.17	2.05
CoV	10.16	25.08	2.59	3.65	2.82
S-PCC-C50-1	100.31	1.44	121.38	4.38	60.69
S-PCC-C50-2	105.01	1.19	145.05	4.16	72.52
mean	102.66	1.32	133.22	4.27	66.61
std	2.35	0.13	11.84	0.11	5.92
CoV	2.29	9.51	8.88	2.58	8.88

Table C.2: Overview experimental results shear test, beams with no stirrups at 6 months

	First crack		Maximum capacity		
	Force	Mid-span defl.	Force	Mid-span defl.	Shear capacity
Beam	F_{max} [kN]	δ [mm]	F_{max} [kN]	δ [mm]	V [kN] [mm]
S-AAC-C30-6m	86.90	1.49	145.80	5.50	72.90
S-PCC-C30-6m	112.80	1.89	145.03	4.58	72.52
S-AAC-C50-6m	91.10	1.51	155.38	5.98	77.69
S-PCC-C50-6m	101.31	1.85	134.25	7.75	67.12

Table C.3: Overview experimental results shear test, beams with stirrups

	First crack		Maximum capacity		
	Force	Mid-span defl.	Force	Mid-span defl.	Shear capacity
Beam	F_{max} [kN]	δ [mm]	F_{max} [kN]	δ [mm]	V [kN]
S-AAC-C30-S	133.35	1.61	213.24	6.32	106.62
S-PCC-C30-S	140.2	2.49	197.73	5.98	98.87
S-AAC-C50-S	160.78	2.49	223.88	6.10	111.94
S-PCC-C50-S	136.40	1.94	215.55	5.53	107.77

C.2. Load-paths

C.2.1. S-AAC-C30

Beam S-AAC-C30-1 without stirrups, tested at 28 days

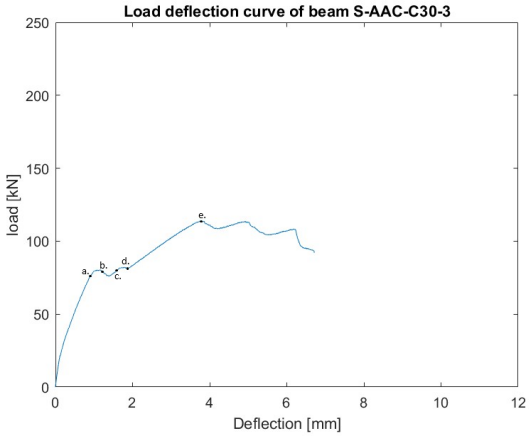

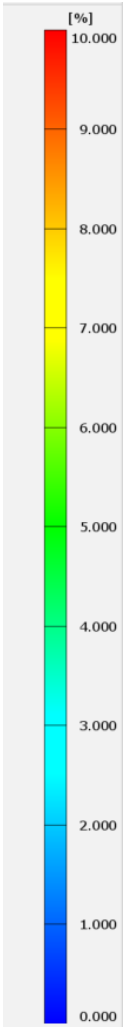

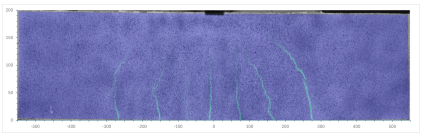

(a) Bending cracks expanding into a shear crack
[Load = 75.92 kN], [Deflection = 0.88 mm]

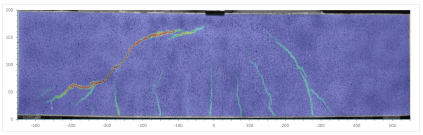

(b) Formation of diagonal shear crack
[Load = 79.73 kN], [Deflection = 1.24 mm]

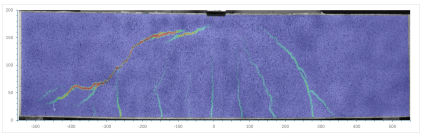

(c) Prior to formation of second diagonal shear crack
[Load = 81.71 kN], [Deflection = 1.63 mm]

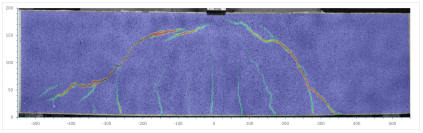

(d) Formation of second diagonal shear crack
[Load = 82.26 kN], [Deflection = 1.86 mm]

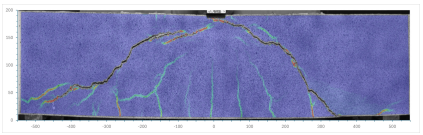

(e) Ultimate shear load
[Load = 114.35 kN], [Deflection = 3.77 mm]

Figure C.1: Load-deflection curve, scale and concrete strains

Beam S-AAC-C30-2 without stirrups, tested at 28 days

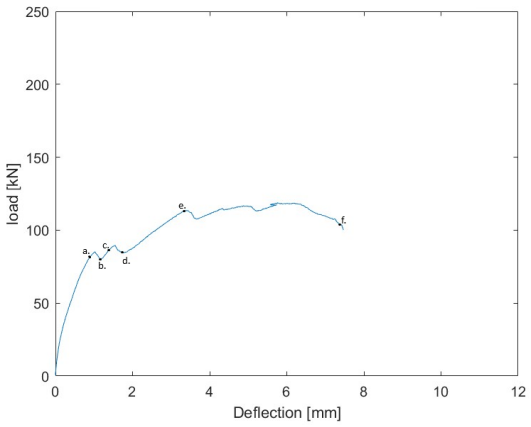

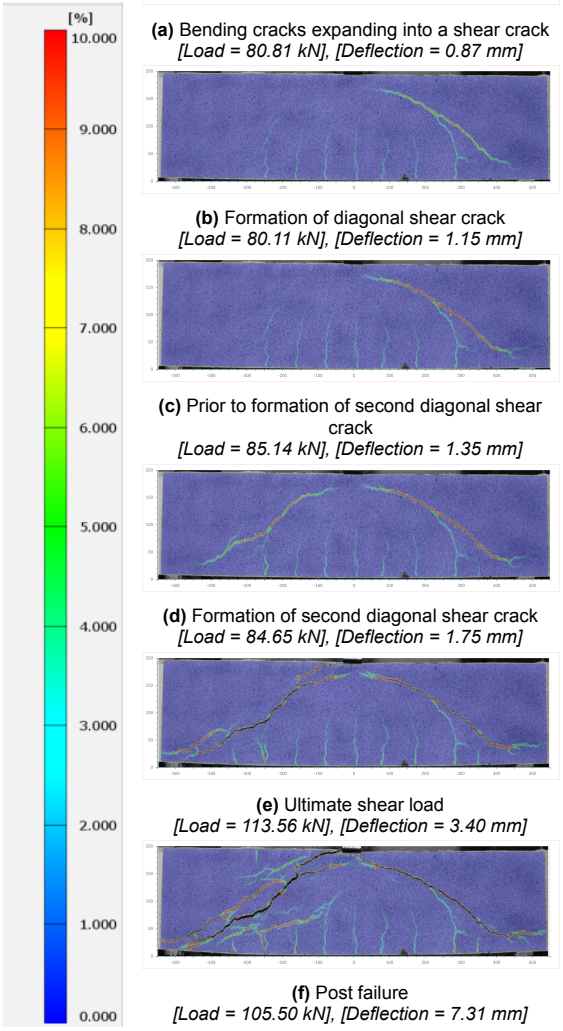

(a) Bending cracks expanding into a shear crack
[Load = 80.81 kN], [Deflection = 0.87 mm]

(b) Formation of diagonal shear crack
[Load = 80.11 kN], [Deflection = 1.15 mm]

(c) Prior to formation of second diagonal shear crack
[Load = 85.14 kN], [Deflection = 1.35 mm]

(d) Formation of second diagonal shear crack
[Load = 84.65 kN], [Deflection = 1.75 mm]

(e) Ultimate shear load
[Load = 113.56 kN], [Deflection = 3.40 mm]

(f) Post failure
[Load = 105.50 kN], [Deflection = 7.31 mm]

Figure C.2: Load-deflection curve, scale and concrete strains

Beam S-AAC-C30-S with stirrups, tested at 28 days

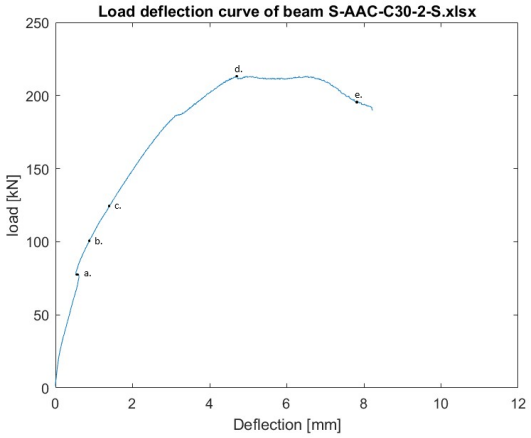

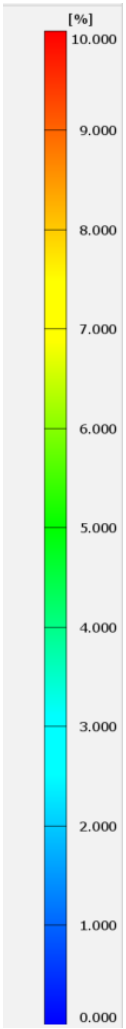

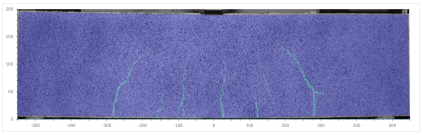

(a) First bending cracks
[Load = 77.62 kN], [Deflection = 0.54 mm]

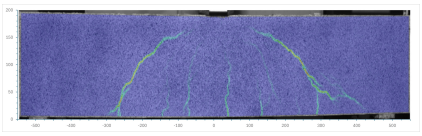

(b) Bending cracks expanding into two shear cracks
[Load = 106.49 kN], [Deflection = 0.99 mm]

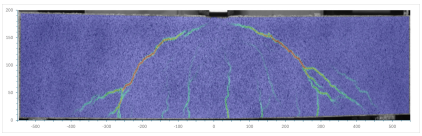

(c) Formation of two diagonal shear cracks
[Load = 133.35 kN], [Deflection = 1.61 mm]

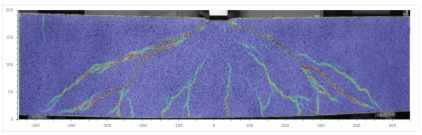

(d) Ultimate shear load
[Load = 211.59 kN], [Deflection = 4.72 mm]

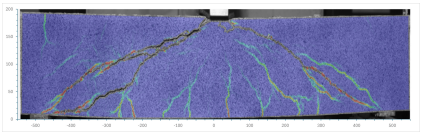

(e) Post failure
[Load = 195.3 kN], [Deflection = 7.83 mm]

Figure C.3: Load-deflection curve, scale and concrete strains

Beam S-AAC-C30-6m without stirrups, tested at 6 months

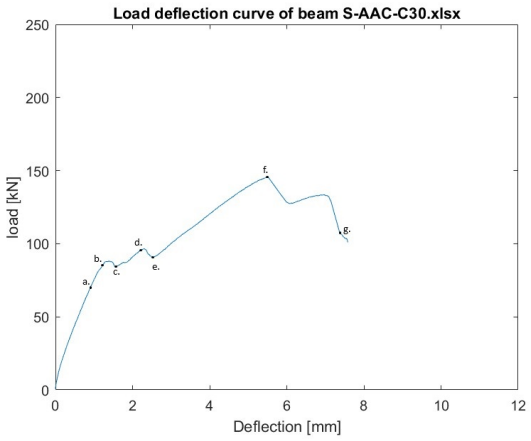

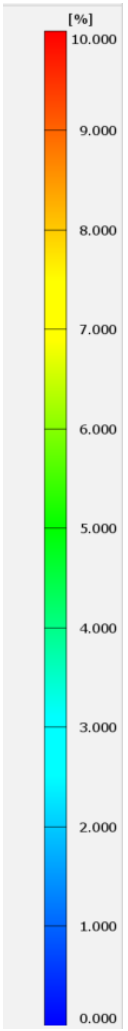

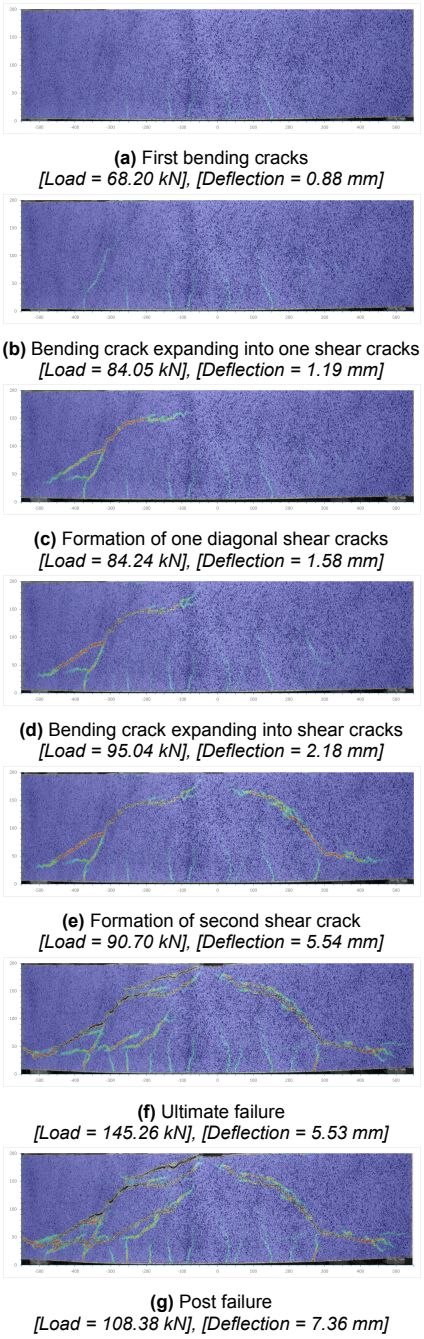

(a) First bending cracks
[Load = 68.20 kN], [Deflection = 0.88 mm]

(b) Bending crack expanding into one shear cracks
[Load = 84.05 kN], [Deflection = 1.19 mm]

(c) Formation of one diagonal shear cracks
[Load = 84.24 kN], [Deflection = 1.58 mm]

(d) Bending crack expanding into shear cracks
[Load = 95.04 kN], [Deflection = 2.18 mm]

(e) Formation of second shear crack
[Load = 90.70 kN], [Deflection = 5.54 mm]

(f) Ultimate failure
[Load = 145.26 kN], [Deflection = 5.53 mm]

(g) Post failure
[Load = 108.38 kN], [Deflection = 7.36 mm]

Figure C.4: Load-deflection curve, scale and concrete strains

C.2.2. S-PCC-C30

Beam S-PCC-C30-1 without stirrups, tested at 28 days

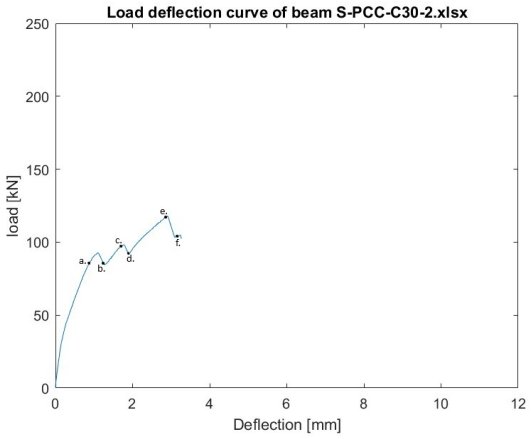

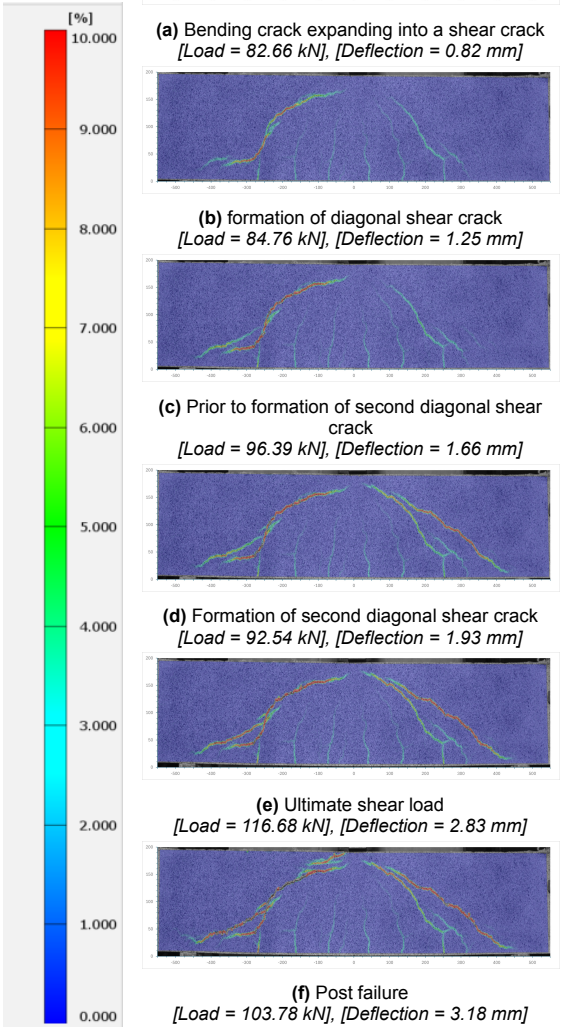

(a) Bending crack expanding into a shear crack
[Load = 82.66 kN], [Deflection = 0.82 mm]

(b) formation of diagonal shear crack
[Load = 84.76 kN], [Deflection = 1.25 mm]

(c) Prior to formation of second diagonal shear crack
[Load = 96.39 kN], [Deflection = 1.66 mm]

(d) Formation of second diagonal shear crack
[Load = 92.54 kN], [Deflection = 1.93 mm]

(e) Ultimate shear load
[Load = 116.68 kN], [Deflection = 2.83 mm]

(f) Post failure
[Load = 103.78 kN], [Deflection = 3.18 mm]

Figure C.5: Load-deflection curve, scale and concrete strains

Beam S-PCC-C30-2 without stirrups, tested at 28 days

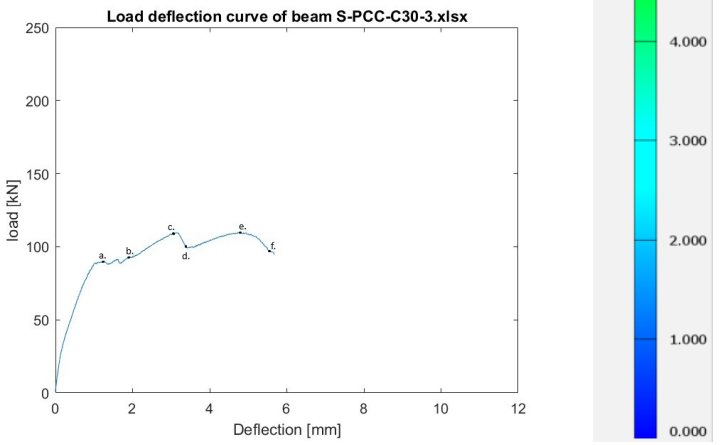

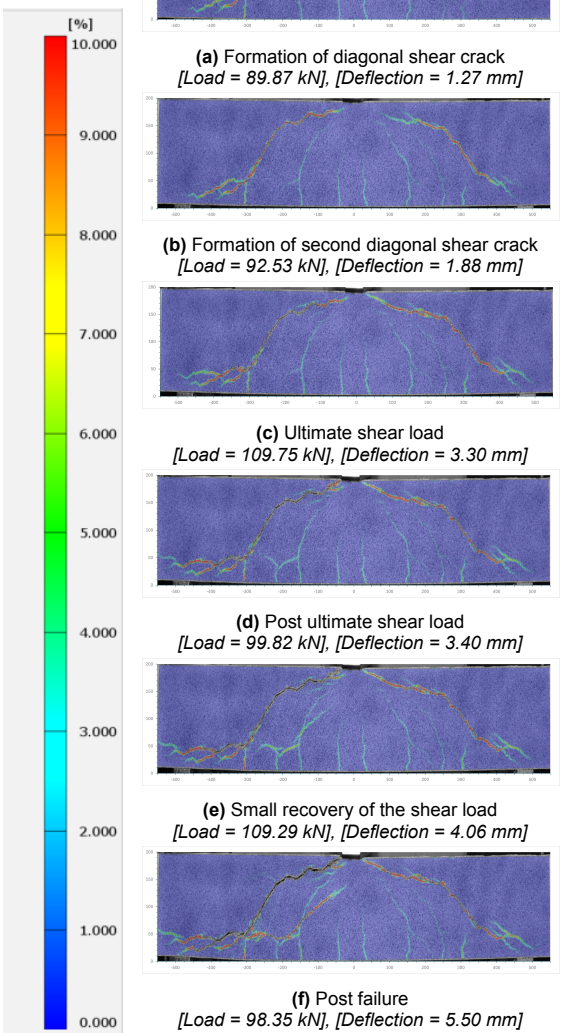

Figure C.6: Load-deflection curve, scale and concrete strains

Beam S-PCC-C30-S with stirrups, tested at 28 days

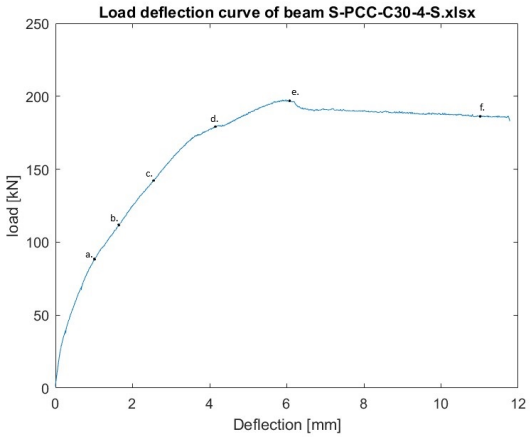

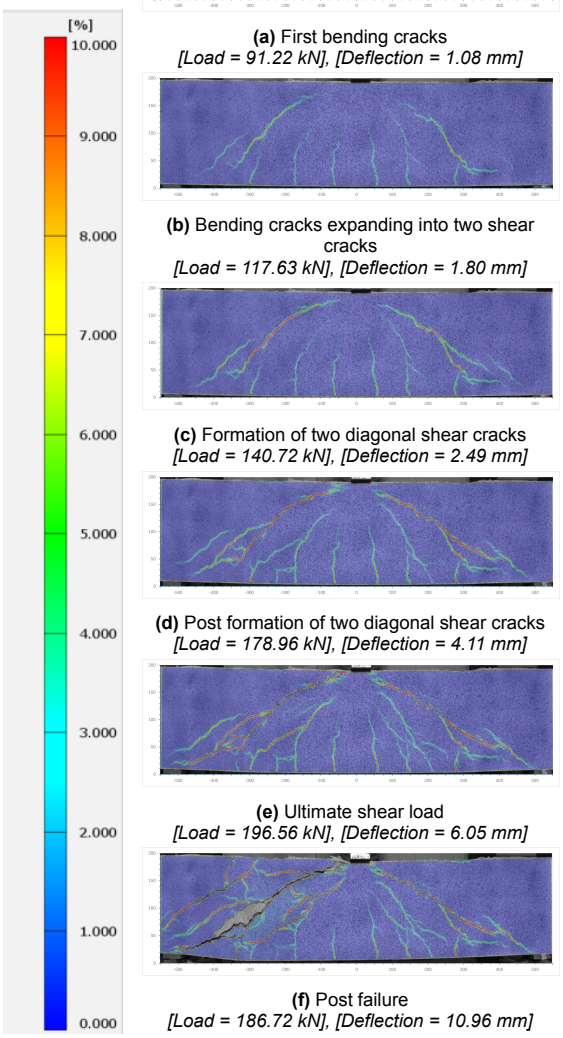

Figure C.7: Load-deflection curve, scale and concrete strains

Beam S-PCC-C30-6m without stirrups, tested at 6 months

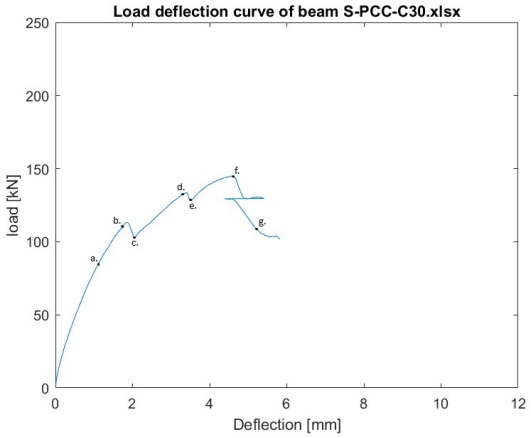

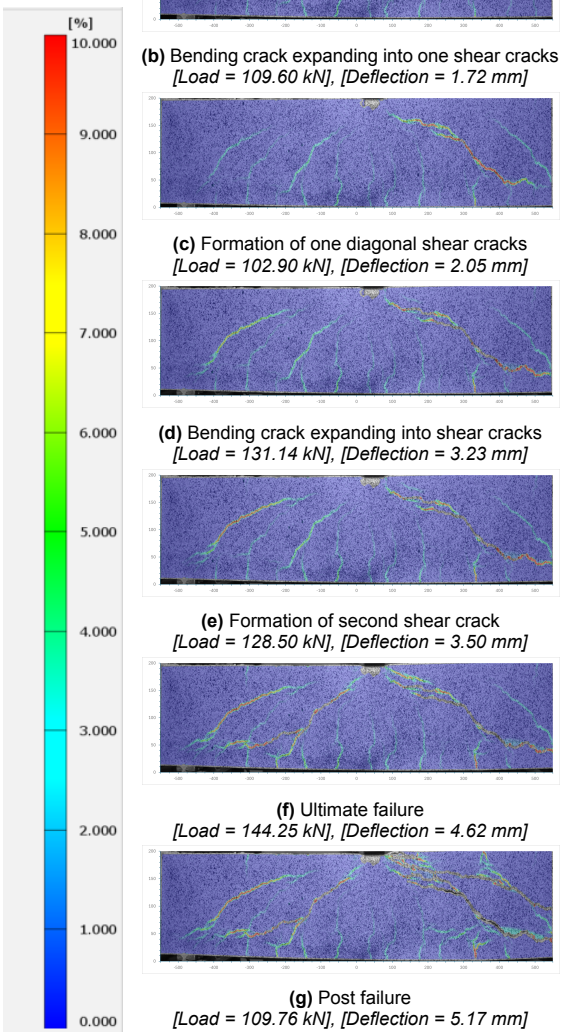

(a) First bending cracks
[Load = 85.59 kN], [Deflection = 1.13 mm]

(b) Bending crack expanding into one shear cracks
[Load = 109.60 kN], [Deflection = 1.72 mm]

(c) Formation of one diagonal shear cracks
[Load = 102.90 kN], [Deflection = 2.05 mm]

(d) Bending crack expanding into shear cracks
[Load = 131.14 kN], [Deflection = 3.23 mm]

(e) Formation of second shear crack
[Load = 128.50 kN], [Deflection = 3.50 mm]

(f) Ultimate failure
[Load = 144.25 kN], [Deflection = 4.62 mm]

(g) Post failure
[Load = 109.76 kN], [Deflection = 5.17 mm]

Figure C.8: Load-deflection curve, scale and concrete strains

C.2.3. S-AAC-C50

Beam S-AAC-C50-1 without stirrups, tested at 28 days

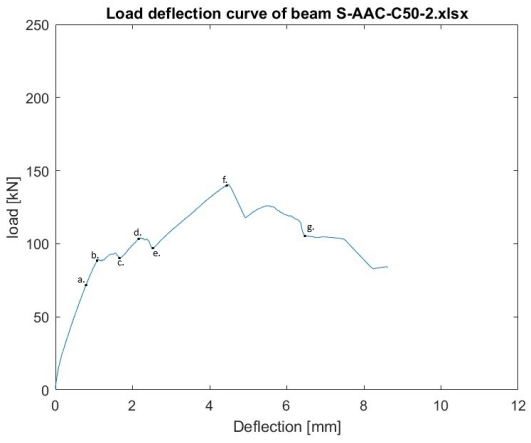

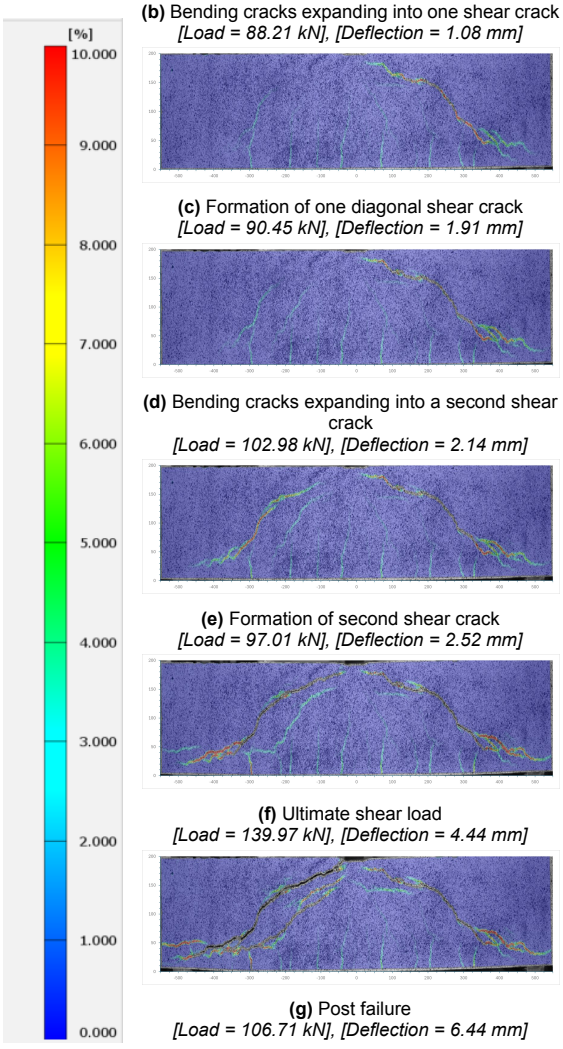

(a) First bending cracks
[Load = 73.31 kN], [Deflection = 0.82 mm]

(b) Bending cracks expanding into one shear crack
[Load = 88.21 kN], [Deflection = 1.08 mm]

(c) Formation of one diagonal shear crack
[Load = 90.45 kN], [Deflection = 1.91 mm]

(d) Bending cracks expanding into a second shear crack
[Load = 102.98 kN], [Deflection = 2.14 mm]

(e) Formation of second shear crack
[Load = 97.01 kN], [Deflection = 2.52 mm]

(f) Ultimate shear load
[Load = 139.97 kN], [Deflection = 4.44 mm]

(g) Post failure
[Load = 106.71 kN], [Deflection = 6.44 mm]

Figure C.9: Load-deflection curve, scale and concrete strains

Beam S-AAC-C50-2 without stirrups, tested at 28 days

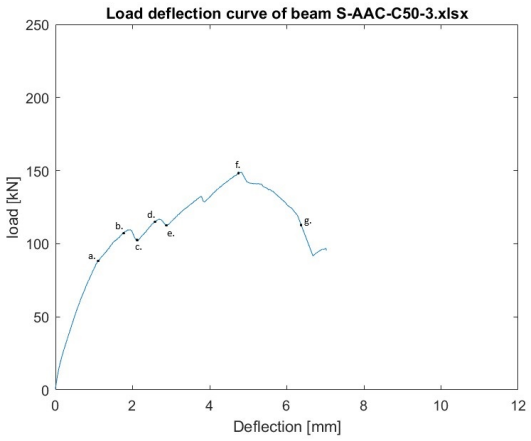

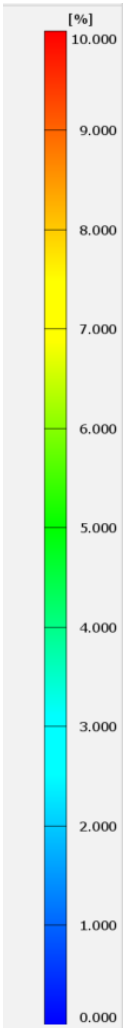

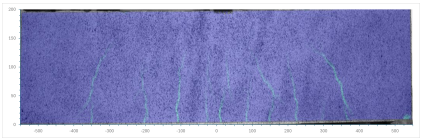

(a) First bending cracks
[Load = 91.69 kN], [Deflection = 1.22 mm]

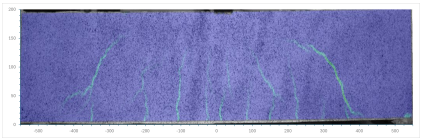

(b) Bending cracks expanding into one shear crack
[Load = 107.60 kN], [Deflection = 1.76 mm]

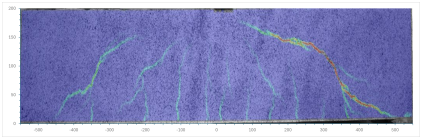

(c) Formation of one diagonal shear crack
[Load = 102.55 kN], [Deflection = 2.10 mm]

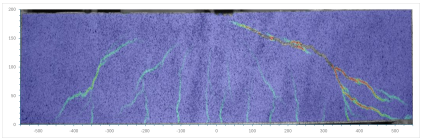

(d) Bending cracks expanding into a second shear crack
[Load = 116.31 kN], [Deflection = 2.63 mm]

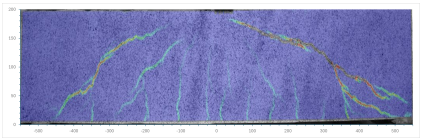

(e) Formation of second shear crack
[Load = 112.40 kN], [Deflection = 2.89 mm]

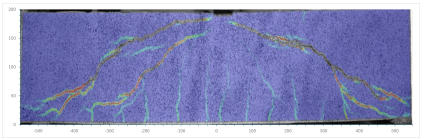

(f) Ultimate shear load
[Load = 148.50 kN], [Deflection = 4.77 mm]

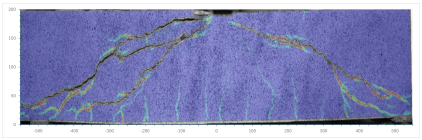

(g) Post failure
[Load = 119.27 kN], [Deflection = 6.28 mm]

Figure C.10: Load-deflection curve, scale and concrete strains

Beam S-AAC-C50-S with stirrups, tested at 28 days

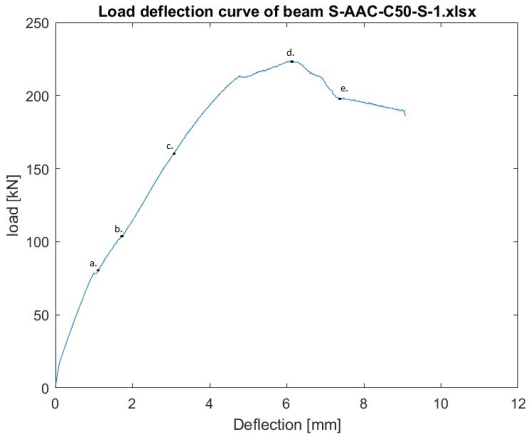

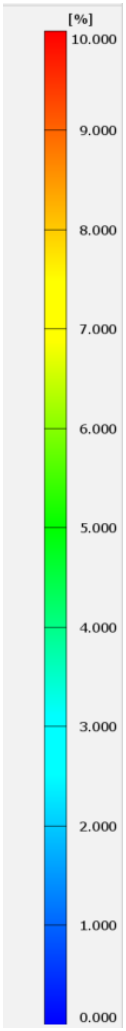

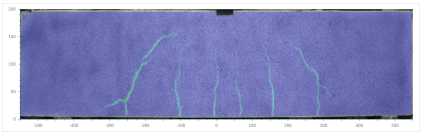

(a) First bending cracks
[Load = 85.64 kN], [Deflection = 1.24 mm]

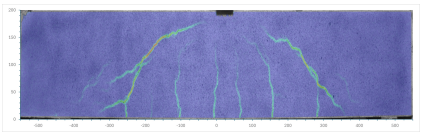

(b) Bending cracks expanding into two shear cracks
[Load = 106.49 kN], [Deflection = 1.80 mm]

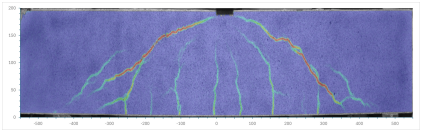

(c) Formation of two diagonal shear cracks
[Load = 160.78 kN], [Deflection = 2.49 mm]

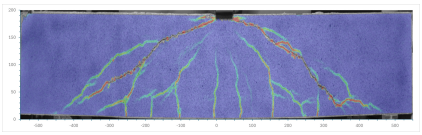

(d) Ultimate shear load
[Load = 223.12 kN], [Deflection = 6.05 mm]

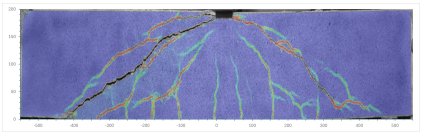

(e) Post failure
[Load = 198.01 kN], [Deflection = 7.34 mm]

Figure C.11: Load-deflection curve, scale and concrete strains

Beam S-AAC-C50-6m without stirrups, tested at 6 months

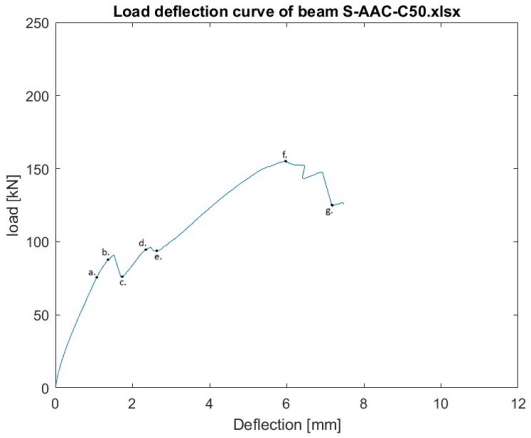

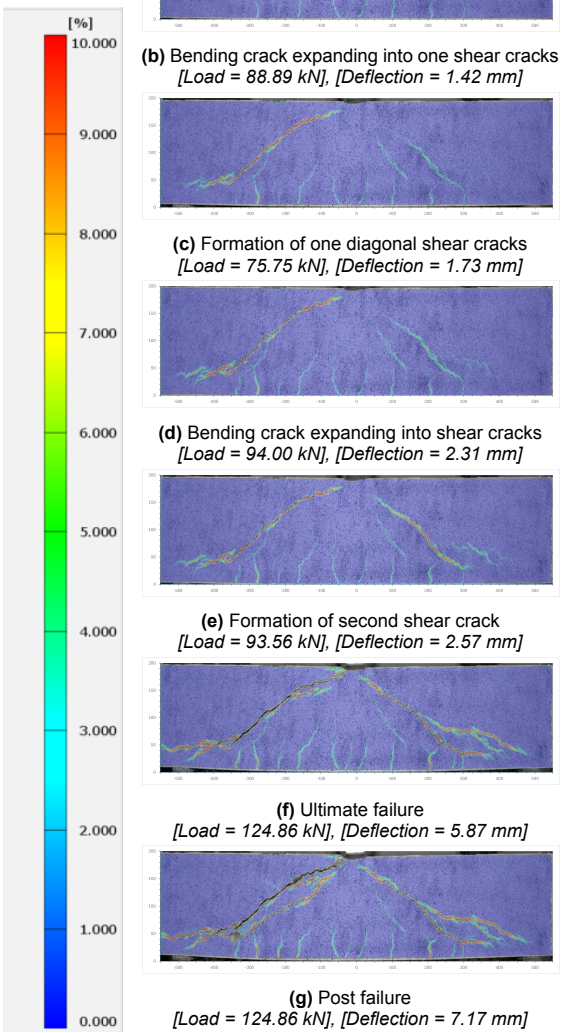

(a) First bending cracks
[Load = 73.35 kN], [Deflection = 1.03 mm]

(b) Bending crack expanding into one shear cracks
[Load = 88.89 kN], [Deflection = 1.42 mm]

(c) Formation of one diagonal shear cracks
[Load = 75.75 kN], [Deflection = 1.73 mm]

(d) Bending crack expanding into shear cracks
[Load = 94.00 kN], [Deflection = 2.31 mm]

(e) Formation of second shear crack
[Load = 93.56 kN], [Deflection = 2.57 mm]

(f) Ultimate failure
[Load = 124.86 kN], [Deflection = 5.87 mm]

(g) Post failure
[Load = 124.86 kN], [Deflection = 7.17 mm]

Figure C.12: Load-deflection curve, scale and concrete strains

C.2.4. S-PCC-C50

Beam S-PCC-C50-1 without stirrups, tested at 28 days

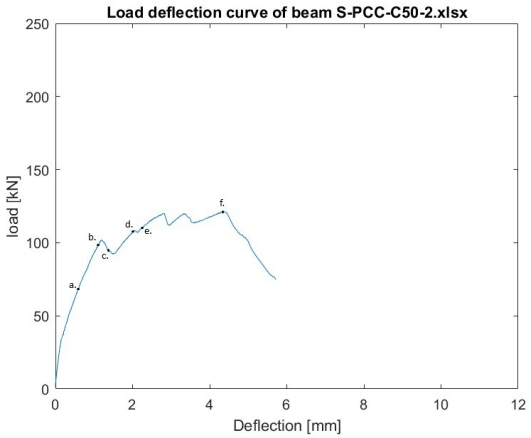

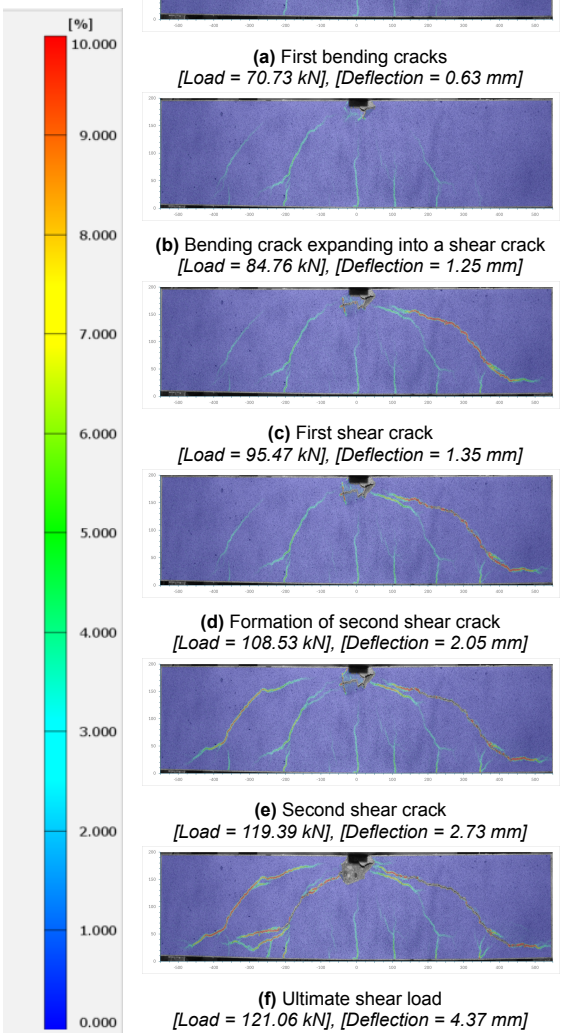

(a) First bending cracks
[Load = 70.73 kN], [Deflection = 0.63 mm]

(b) Bending crack expanding into a shear crack
[Load = 84.76 kN], [Deflection = 1.25 mm]

(c) First shear crack
[Load = 95.47 kN], [Deflection = 1.35 mm]

(d) Formation of second shear crack
[Load = 108.53 kN], [Deflection = 2.05 mm]

(e) Second shear crack
[Load = 119.39 kN], [Deflection = 2.73 mm]

(f) Ultimate shear load
[Load = 121.06 kN], [Deflection = 4.37 mm]

Figure C.13: Load-deflection curve, scale and concrete strains

Beam S-PCC-C50-2 without stirrups, tested at 28 days

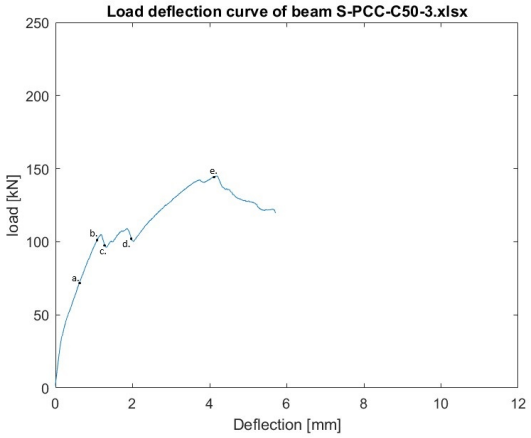

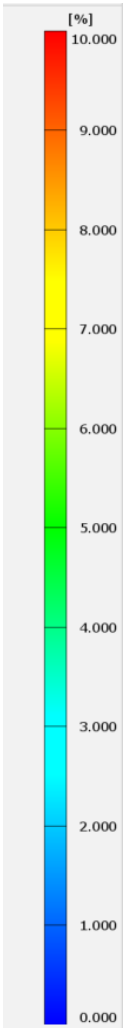

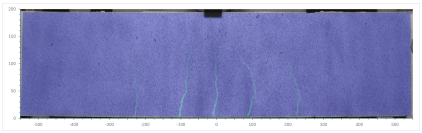

(a) First bending cracks
[Load = 73.15 kN], [Deflection = 0.64 mm]

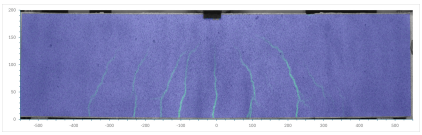

(b) Bending crack expanding into a shear crack
[Load = 102.4 kN], [Deflection = 1.11 mm]

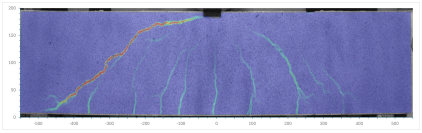

(c) First shear crack
[Load = 97.4 kN], [Deflection = 1.27 mm]

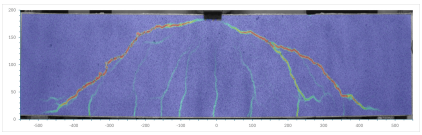

(d) Second shear crack
[Load = 100.99 kN], [Deflection = 1.98 mm]

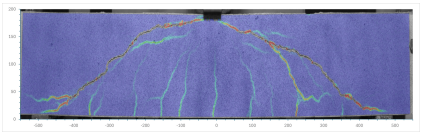

(e) Ultimate shear load
[Load = 144.63 kN], [Deflection = 4.15 mm]

Figure C.14: Load-deflection curve, scale and concrete strains

Beam S-PCC-C50-S with stirrups, tested at 28 days

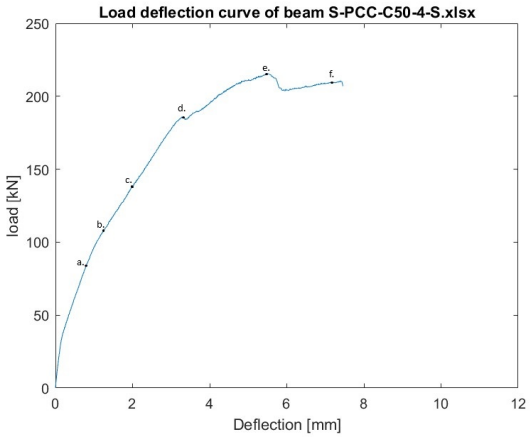

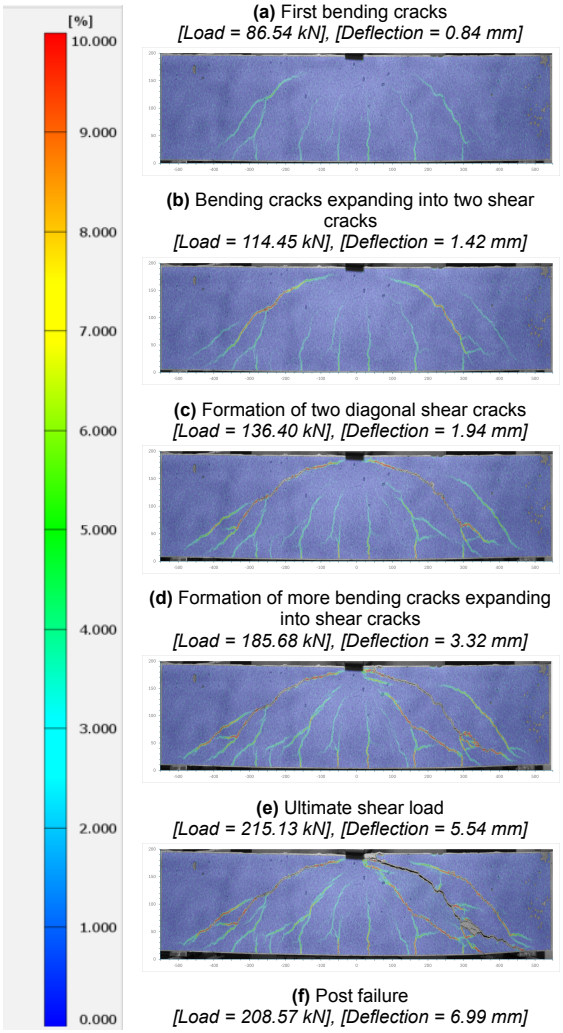

(a) First bending cracks
[Load = 86.54 kN], [Deflection = 0.84 mm]

(b) Bending cracks expanding into two shear cracks
[Load = 114.45 kN], [Deflection = 1.42 mm]

(c) Formation of two diagonal shear cracks
[Load = 136.40 kN], [Deflection = 1.94 mm]

(d) Formation of more bending cracks expanding into shear cracks
[Load = 185.68 kN], [Deflection = 3.32 mm]

(e) Ultimate shear load
[Load = 215.13 kN], [Deflection = 5.54 mm]

(f) Post failure
[Load = 208.57 kN], [Deflection = 6.99 mm]

Figure C.15: Load-deflection curve, scale and concrete strains

Beam S-PCC-C50-6m without stirrups, tested at 6 months

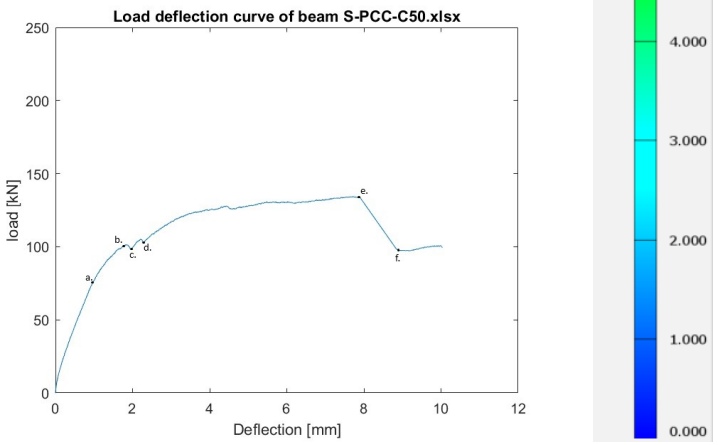

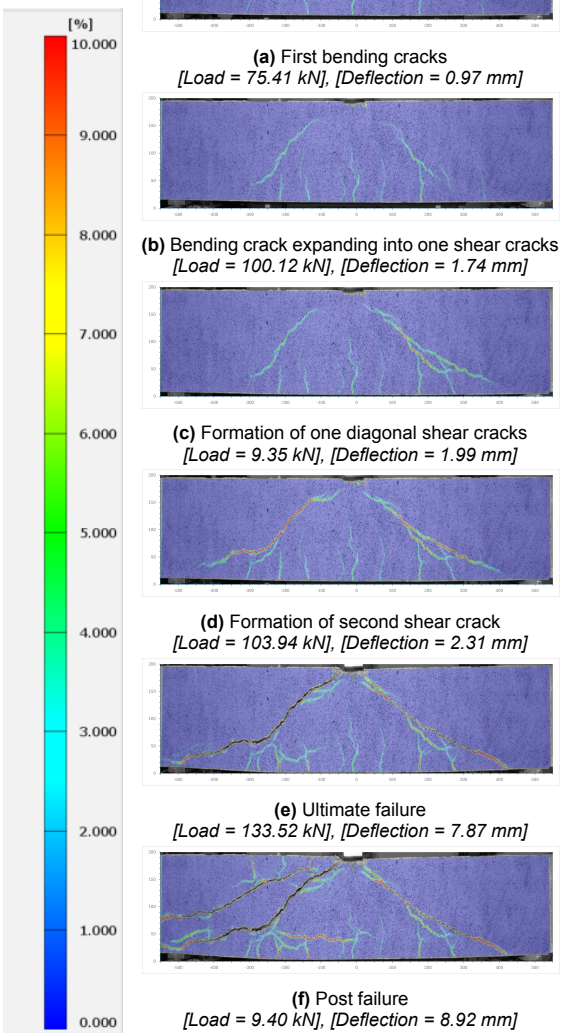

(a) First bending cracks
[Load = 75.41 kN], [Deflection = 0.97 mm]

(b) Bending crack expanding into one shear cracks
[Load = 100.12 kN], [Deflection = 1.74 mm]

(c) Formation of one diagonal shear cracks
[Load = 9.35 kN], [Deflection = 1.99 mm]

(d) Formation of second shear crack
[Load = 103.94 kN], [Deflection = 2.31 mm]

(e) Ultimate failure
[Load = 133.52 kN], [Deflection = 7.87 mm]

(f) Post failure
[Load = 9.40 kN], [Deflection = 8.92 mm]

Figure C.16: Load-deflection curve, scale and concrete strains

D

Comparison of experimental shear results with existing methods

D.1. NEN-EN 1992-1-1

Compressive strength

The 28-day compressive strength is the basis of Eurocode 2 (EC2), NEN-EN 1992-1-1, 2015. The EC2 uses the 28-day compressive cylinder strength to estimate other material properties. To convert the mean cube compressive strength obtained during the experimental study into a mean compressive cylinder strength, equation D.1 can be used.

$$f_{cm} = f_{cm,cylinder} = 0.8 \cdot f_{cm,cube} \tag{D.1}$$

Where f_{cm} is the main value of concrete compressive strength in MPa, $f_{cm,cylinder}$ is the mean value of concrete cylinder compressive strength in MPa and $f_{cm,cube}$ is the main value of concrete cubic compressive strength in MPa.

This results in the mean cylinder compressive strengths of 37, 34, 53, and 46 MPa for mixtures S-AAC-C30, S-PCC-C30, S-AAC-C50, and S-PCC-C50, respectively.

Tensile strength

The relationship between mean tensile strength and mean compressive strength described by NEN-EN 1992-1-1, 2015, is shown in equation D.2.

$$f_{ctm} = 0.3 \cdot f_{cm}^{\frac{2}{3}} \leq \text{C50/60} \tag{D.2}$$

Where f_{ctm} is the main tensile strength in MPa and f_{cm} is the main compressive strength in MPa.

Using the mean value of concrete compressive strength obtained in subsection D.1, this results in a mean tensile strength of 3.33, 3.14, 4.26 and 3.87 MPa for mixtures S-AAC-C30, S-PCC-C30, S-AAC-C50, and S-PCC-C50, respectively.

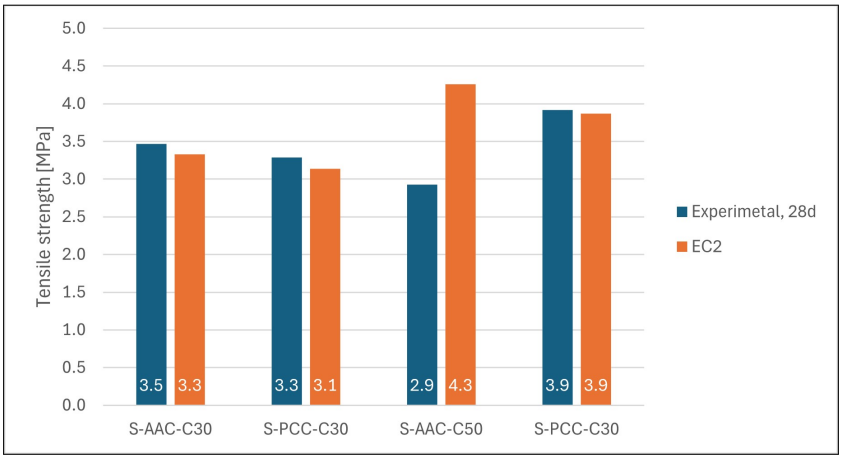

Figure D.1: Comparison of the experimental direct tensile strength in MPa at 28 days and the tensile strength obtained with NEN-EN 1992-1-1 in MPa for the mixtures S-AAC-C30, S-PCC-C30, S-AAC-C50, and S-PCC-C50.

The comparison with the experimental results obtained at 28 days (see figure D.1) shows that the S-AAC-C30, S-PCC-C30, and S-PCC-C50 mixtures can be accurately estimated using NEN-EN 1992-1-1, 2015. However, for the S-AAC-C50 mixture, this is not the case. NEN-EN 1992-1-1, 2015 shows an overestimation of the tensile strength compared to the experimental results.

Shear resistance without shear reinforcement

The relationship between compressive strength and shear resistance provided by NEN-EN 1992-1-1, 2015, is rewritten for f_{cm} and shown in equation D.3.

$$V_{Rd,c} = C_{Rd,c} \cdot k \cdot (100 \cdot \rho_l \cdot f_{cm})^{1/3} \cdot b_w \cdot d \tag{D.3}$$

Where $V_{Rd,c}$ is the design shear resistance of the member without shear reinforcement in N, $C_{Rd,c}$, k are a calculation coefficient, ρ_l is the reinforcement ratio, f_{cm} is the mean compression strength in MPa, b_w is the smallest width of the cross-section in the tensile area in mm and d is the effective depth of the cross-section in mm.

The effective depth of the cross-section can be calculated using equation D.4.

$$d = h - c - \frac{1}{2} \cdot ø = 200 - 25 - \frac{1}{2} \cdot 25 = 162.5\ [mm] \tag{D.4}$$

Where h is the height of the cross-section in mm, c is the concrete cover in mm and ø is the diameter of the reinforcement bars in the tensile zone in mm.

Coefficient $C_{Rd,c}$ and k can be calculated using equation D.5 and D.6.

$$C_{Rd,c} = \frac{0.18}{\gamma_c} = \frac{0.18}{1.5} = 0.12 \tag{D.5}$$

$$k = min[1 + \sqrt{\frac{200}{d}}; 2.0] = min[2.11; 2.0] = 2.0 \tag{D.6}$$

The area of tensile reinforcement can be calculated using equation D.7.

$$A_{sl} = n \cdot \frac{1}{4} \cdot \pi \cdot ø^2 = 2 \cdot \frac{1}{4} \cdot \pi \cdot 25^2 = 981.75\ [mm^2] \tag{D.7}$$

Finally, the reinforcement ratio for longitudinal reinforcement can be calculated using the equation D.8.

$$\rho_l = min\left[\frac{A_{sl}}{b_w d}; 0.02\right] = min[0.04; 0.02] = 0.02 \tag{D.8}$$

When using the 28-day mean compressive strength, the shear resistances are 24, 24, 28, and 26 kN for the S-AAC-C30, S-PCC-C30, S-AAC-C50, and S-PCC-C50 mixtures, respectively. When using the 6-month compressive strength, the shear resistances are 27, 27, 30, and 28 kN for the S-AAC-C30, S-PCC-C30, S-AAC-C50, and S-PCC-C50 mixtures, respectively. The shear resistance calculated using the formulas provided by EC2 approximates the experimental results at 28 days by 39%–42% and the experimental results at 6 months by 42%–46%. This is considered very conservative.

NEN-EN 1992-1-1, 2015 specifies a maximum reinforcement ratio of 2% for longitudinal reinforcement. However, the actual reinforcement ratio in the beams tested is 4%. By increasing $\rho_l = 0.04$, the shear resistances at 28 days become 31, 30, 35, and 33 kN, and at 6 months, they are 35, 34, 38, and 35 kN for the S-AAC-C30, S-PCC-C30, S-AAC-C50, and S-PCC-C50 mixtures, respectively. These calculated values are approximately 49%–53% of the experimental results at 28 days and 53%–58% at 6 months, which is still quite conservative.

See figure D.2 for the calculated results compared to the experimental results.

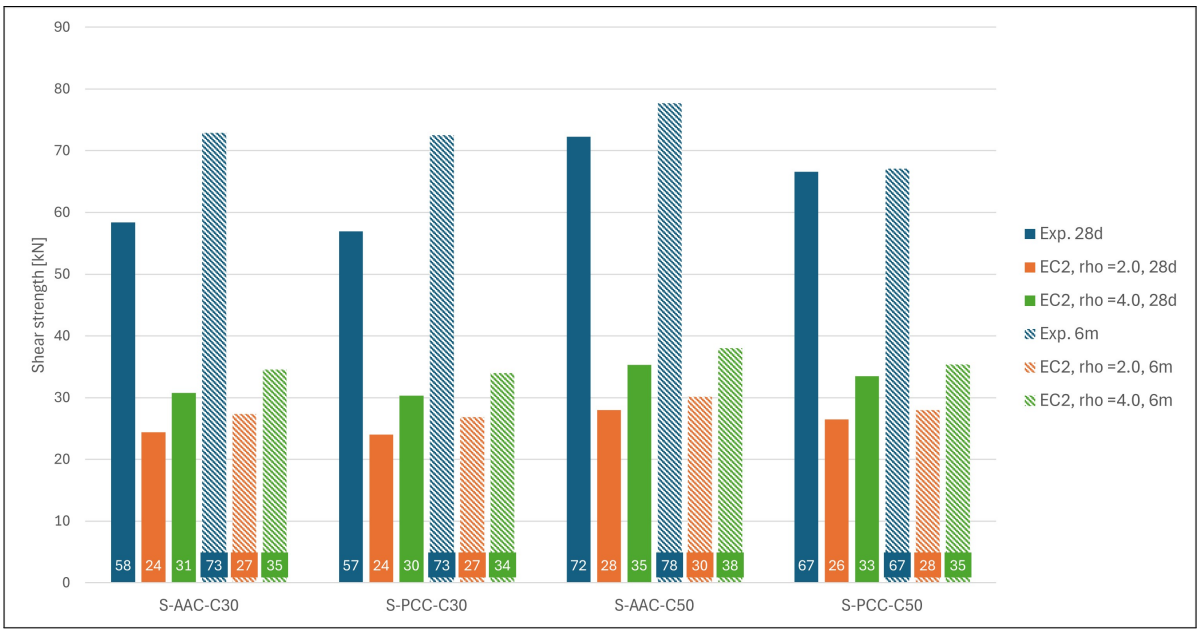

Figure D.2: Comparison of the experimental shear results without stirrups at 28 days and 6 months with the shear resistance obtained using NEN-EN 1992-1-1, 2015. The blue bars represent the experimental results, the orange bars represent the calculations with a reinforcement ratio of 2%, and the orange bars also represent the calculations with a reinforcement ratio of 4%. Solid bars represent the 28-day results, and striped bars represent the 6-month results.

Shear resistance with shear reinforcement

The formula specified in NEN-EN 1992-1-1, 2015, to calculate the shear resistance with shear reinforcement is shown in equations D.9 and D.10. Equation D.9 accounts for the crushing of the concrete, while equation D.10 accounts for the yielding of the stirrups. The minimum value of the two will determine the governing failure mode.

$$V_{Rd,s} = \frac{A_{sw}}{s} \cdot z \cdot f_{ym} \cdot cot(\theta) \tag{D.9}$$

Where $V_{Rd,s}$ is the design value of the shear force that can be sustained by the yielding shear reinforcement, A_{sw} is the cross-sectional area of the shear reinforcement in mm^2, s is the spacing of the stirrups in mm, f_{ym} is the yield strength of the shear reinforcement and θ is the angle between the concrete compression strut and the beam axis perpendicular to the shear force.

$$V_{Rd,max} = \frac{\alpha_{cw} \cdot b_w \cdot z \cdot \nu_1 \cdot f_{cm}}{cot(\theta) + tan(\theta)} \tag{D.10}$$

Where $V_{Rd,max}$ is the design value of the maximum shear force that can be sustained by the member, limited by the crushing of the compression struts, α_{cw} is a coefficient accounting for the state of stress in the compression chord, b_w is the smallest width of the cross-section in the tensile area in mm, z is the lever arm of internal forces in mm, v_1 is a strength reduction factor for concrete cracked in shear, f_{cm} is the mean compressive strength of the concrete and θ is the angle between the concrete compression strut and the beam axis perpendicular to the shear force.

For the calculation $\theta = 45^o$, $\alpha_{cw} = 1$ and $\nu_1 = 0.6$ are used.

The cross-sectional area of the shear reinforcement is calculated with equation D.11.

$$A_{sw} = n \cdot \frac{1}{4} \cdot \pi \cdot \text{ø}^2 = 2 \cdot \frac{1}{4} \cdot \pi \cdot 8^2 = 100.5 \; [mm^2] \tag{D.11}$$

The spacing of the stirrups has been calculated with equation D.12.

$$s = 150 + \frac{1}{2} \cdot 200 = 250 \; [mm] \tag{D.12}$$

Lever arm of internal forces has been calculated with equation D.13.

$$z = 0.9 \cdot d = 0.9 \cdot 162.5 = 146.25 \; [mm] \tag{D.13}$$

For S-PCC-C30 calculating $V_{Rd,s}$ and $V_{Rd,max}$ results into 33 kN and 223 kN, respectability.

$$V_{Rd,s} = \frac{A_{sw}}{s} \cdot z \cdot f_{ym} \cdot cot(\theta) = \frac{100.53}{250} \cdot 146.25 \cdot 1.12 \cdot 500 \cdot cot(45^o) = 32.93 \; [kN]$$

$$V_{Rd,max} = \frac{\alpha_{cw} \cdot b_w \cdot z \cdot \nu_1 \cdot f_{cm}}{cot(\theta) + tan(\theta)} = \frac{1 \cdot 150 \cdot 146.25 \cdot 0.6 \cdot 33.85}{cot(45) + tan(45)} = 222.76 \; [kN]$$

The minimum value is $V_{Rd,s}$, making the stirrup yield strength the limiting factor. The shear resistance according to NEN-EN 1992-1-1, 2015 will be 32.94 kN for all mixtures due to similar steel properties. The shear resistance calculated using the formulas provided by NEN-EN 1992-1-1, 2015 is approximately 30% of the experimental results, which is very conservative.

When examining the experimental results, shear cracks are observed between the load and the support. Therefore, a more realistic value of θ can be used, namely $\theta = 21.8°$. When implementing this, the shear resistance increases to 82.34 kN for all mixtures, approximating the experimental results by 75%. This angle is a more realistic value obtained from the experimental studies. See Figure D.3 for the results compared to the experimental studies.

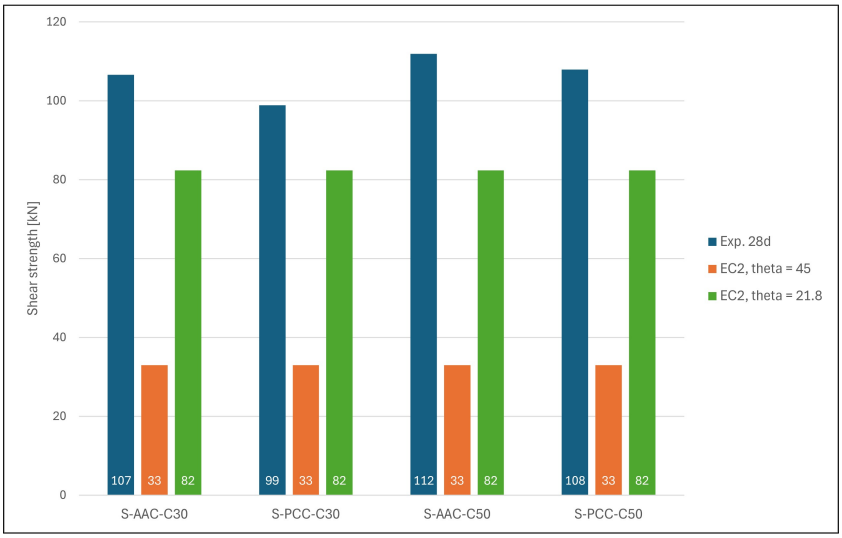

Figure D.3: Comparison of the experimental shear results with stirrups at 28 days with the shear resistance obtained using NEN-EN 1992-1-1, 2015. The blue bars represent the experimental results, the orange bars represent the calculations with the angle between the concrete compression strut of 45^o, and the orange bars also represent the calculations with the angle between the concrete compression strut of 21.8^o.

D.2. General shear design method (GSDM)

The General Shear Design Method (GSDM) is developed by Cladera and Marí, 2004a, providing an enhanced approach for predicting the shear strength of concrete beams, with shear reinforcement in part I and without shear reinforcement in part II. The authors used artificial neural networks to predict strength by analysing a large database of experimental results. This method captures complex relationships between variables such as concrete strength, beam dimensions, and reinforcement levels.

Based on their analysis, the authors proposed a general and simplified shear design method that accounts for various mechanisms, including aggregate interlock and dowel action, making the method more representative of the actual behaviour of concrete beams under shear forces. This approach contrasts with NEN-EN 1992-1-1, 2015, which can sometimes oversimplify these factors.

Without stirrups

The general shear design method proposed consists of equation D.14. This equation is valid for normal and high-strength concretes without web reinforcement (Cladera and Marí, 2004a).

$$V_c = \left(0.13 \cdot \xi \cdot (100 \cdot \rho_l)^{\frac{1}{2}} \cdot f_c^{\frac{1}{3}}\right) \cdot b_w \cdot d \tag{D.14}$$

Where V_c is the predicted shear resistance in N, ξ is the size effect, ρ_l is the reinforcement ratio, f_c is the compressive strength, b_w is the smallest width of the cross-section in the tensile area in mm and d is the effective depth of the cross-section in mm.

The size effect is calculated with equation D.15.

$$\xi = min\left[\left(\frac{135000 \cdot f_c^{-1.1}}{s_x}\right)^{0.25\left(1+\frac{f_c-25}{75}\right)}; 2.75\right] \tag{D.15}$$

Where S_x is the minimum of the internet lever arm, $z = 0.9 \cdot d = 146.25\ [mm]$ or the centre-to-centre distance of the longitudinal compression and tension reinforcement, $127.5\ [mm]$.

The reinforcement ratio is calculated with equation D.16.

$$\rho_l = min\left[\frac{A_l}{b_w \cdot d}; 0.02\left(1 + \frac{f_c}{100}\right)\right] \tag{D.16}$$

For S-PCC-C30, the calculation is:

$$\xi = min\left[\left(\frac{135000 \cdot 36.9^{-1.1}}{127.5}\right)^{0.25\left(1+\frac{36.9-25}{75}\right)}; 2.75\right] = min\left[2.38; 2.75\right] = 2.38$$

$$\rho_l = min\left[\frac{981.75}{150 \cdot 162.5}; 0.02\left(1+\frac{36.90}{100}\right)\right] = min\left[0.04; 0.03\right] = 0.03$$

$$V_c = \left(0.13 \cdot 2.38 \cdot (100 \cdot 0.03)^{\frac{1}{2}} \cdot 36.90^{\frac{1}{3}}\right) \cdot 150 \cdot 162.5 = 41.58\ [kN]$$

For the mixtures S-AAC-C30, S-PCC-C30, S-AAC-C50, and S-PCC-C50, the shear resistance using the GSDM at 28 days results in 41, 40, 52, and 47 kN, respectively. This corresponds to approximately 70%-72% of the experimental results. Using the 6-month compressive strength, the results obtained are 50, 48, 59, and 50 kN, respectively. This corresponds to approximately 66%–78% of the experimental results.

When increasing the reinforcement ratio to $\rho = 0.04$ using the GSDM, the results are 50, 49, 59, and 55 kN at 28 days, and 57, 56, 59, and 52 kN at 6 months for the mixtures S-AAC-C30, S-PCC-C30, S-AAC-C50, and S-PCC-C50, respectively. This corresponds to 82%-86% at 28 days and 76%-78% at 6 months of the experimental results.

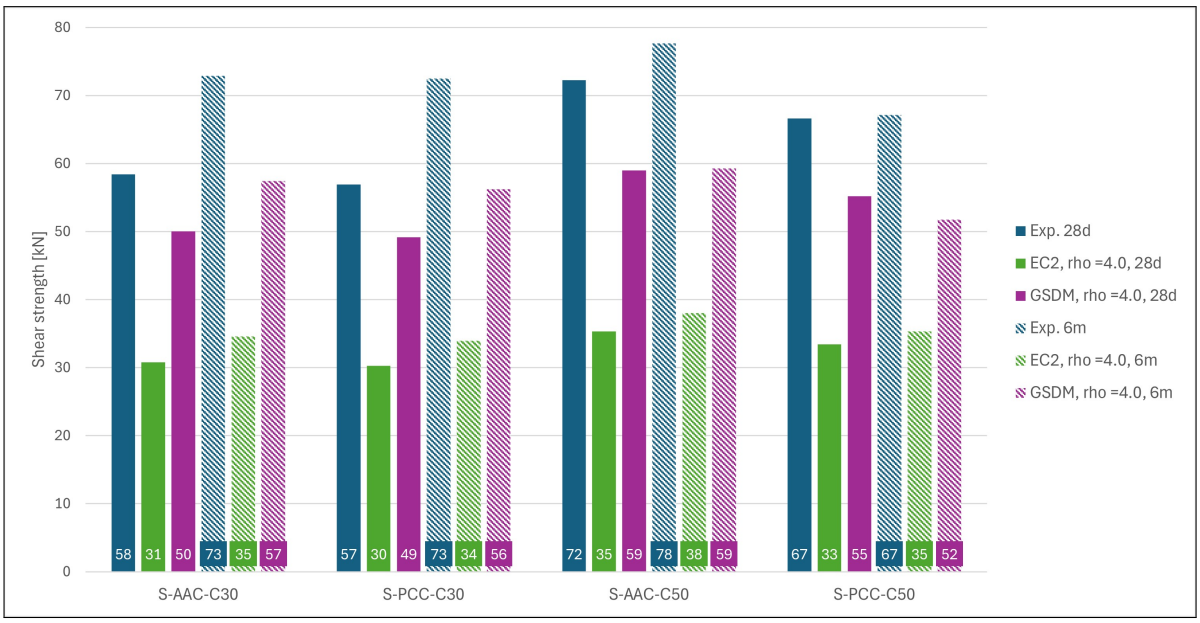

Figure D.4: Comparison of the experimental shear results without stirrups at 28 days and 6 months with the shear resistance obtained using the GSDM. The blue bars represent the experimental results, the green bars represent the calculations with NEN-EN 1992-1-1, 2015, and the purple bars represent the calculations with the GSDM. Solid bars represent the 28-day results, and striped bars represent the 6-month results.

With stirrups

For members with shear reinforcement, the design shear strength can be calculated by using equation D.17 (Cladera and Marí, 2004b).

$$V = V_c + V_s \tag{D.17}$$

Where V_c is the shear resistance of the concrete (Equation D.18) and V_s is the shear resistance of the steel stirrups (Equation D.19).

$$V_c = \left[0.17 \cdot \xi \cdot (100 \cdot \rho_l)^{\frac{1}{2}} \cdot f_c^{0.2} \cdot \tau^{\frac{1}{3}}\right] \cdot b_w \cdot d \tag{D.18}$$

Where ξ is a coefficient taking into account the size effect, ρ_l is the amount of longitudinal reinforcement, f_c is the concrete compressive strength in Mpa, τ is the shear stress in MPa, b_w is the web width in mm and d is the effective depth in mm.

$$V_s = d_v \cdot \frac{A_w}{s} \cdot f_{ywd} \cdot \cot\theta \tag{D.19}$$

Where d_v is the mechanical depth taken to be $0.9 \cdot d$ in mm, A_w is the area of the shear reinforcement, s spacing of the stirrups, f_{ywd} is the design yielding strength of the shear reinforcement and θ is the angle of the compression struts.

The size effect is calculated with equation D.20.

$$\xi = min\left[1 + \sqrt{\frac{200}{s_x}}; 2.75\right] \tag{D.20}$$

Where s_x is the minimum of the internet lever arm, $z = 0.9 \cdot d = 146.25\ [mm]$ or the centre-to-centre distance of the longitudinal compression and tension reinforcement, $127.5\ [mm]$.

The amount of longitudinal reinforcement is calculated with equation D.21.

$$\rho_l = min\left[\frac{A_l}{b_w \cdot d}; 0.02\left(1 + \frac{f_c}{100}\right)\right] \tag{D.21}$$

The shear stress is calculated with equation D.22.

$$\tau = min\left[\frac{V_d}{b_w \cdot d_v}; 3.0\right] \tag{D.22}$$

Where V_d is the designing shear strength $V_d = V_k \cdot \gamma_f$.

The angle of the compression strut is calculated with equation D.23.

$$\theta = min\left[20 + 15 \cdot \epsilon_x + 45 \cdot \frac{\tau}{f_c}; 45^o\right] \tag{D.23}$$

Where the longitudinal strain in the web (ϵ_x) is calculated with equation D.24

$$\epsilon_x = min\left[0.5 \cdot \frac{\frac{M_d}{d_v} + V_d}{E_s \cdot A_l} \cdot 1000; 1\right] \text{ only if } \frac{\tau}{f_c} \geq 0.05 \tag{D.24}$$

For S-PCC-C30-S, the calculation of V_c is:

$$\xi = min\left[1 + \sqrt{\frac{200}{127.5}}; 2.75\right] = 2.25$$

$$\rho_l = min\left[\frac{981.75}{150 \cdot 162.5}; 0.02\left(1 + \frac{36.90}{100}\right)\right] = min\left[0.04; 0.03\right] = 0.03$$

$$\tau = min\left[\frac{98.87 \cdot 10^3}{150 \cdot 146.25}; 3.0\right] = min\left[4.5; 3.0\right] = 3.0$$

Where V_d is taken as $F_u/2$. Where F_u is the ultimate load obtained by the experiments.

$$V_c = \left[0.17 \cdot 2.25 \cdot (100 \cdot 0.03)^{\frac{1}{2}} \cdot 34.51^{0.2} \cdot 3.0^{\frac{1}{3}}\right] \cdot 150 \cdot 162.5 = 44.83\ [kN]$$

For S-PCC-C30-S the calculation of V_s is:

$$\epsilon_x = min\left[0.5 \cdot \frac{\frac{49.435 \cdot 10^6}{146.25} + 98.87 \cdot 10^3}{200000 \cdot 981.75} \cdot 1000; 1\right] = min\left[1.11; 1.0\right] = 1.0$$

$$\theta = min\left[20 + 15 \cdot 1.0 + 45 \cdot \frac{3.0}{32.51}; 45^o\right] = min\left[38.91^o; 45^o\right] = 38.91^o$$

$$V_s = 146.25 \cdot \frac{100.53}{250} \cdot 1.12 \cdot 500 \cdot \cot\left(38.91^0\right) = 40.80[kN] \tag{D.25}$$

For S-PCC-C30-S the calculation of V is:

$$V = V_c + V_s = 44.83 + 40.80 = 85.63\ [kN]$$

For the mixtures S-AAC-C30, S-PCC-C30, S-AAC-C50, and S-PCC-C50, the shear resistance using the GSDM at 28 days is 87, 86, 96, and 92 kN, respectively. This corresponds to approximately 85% of the experimental results.

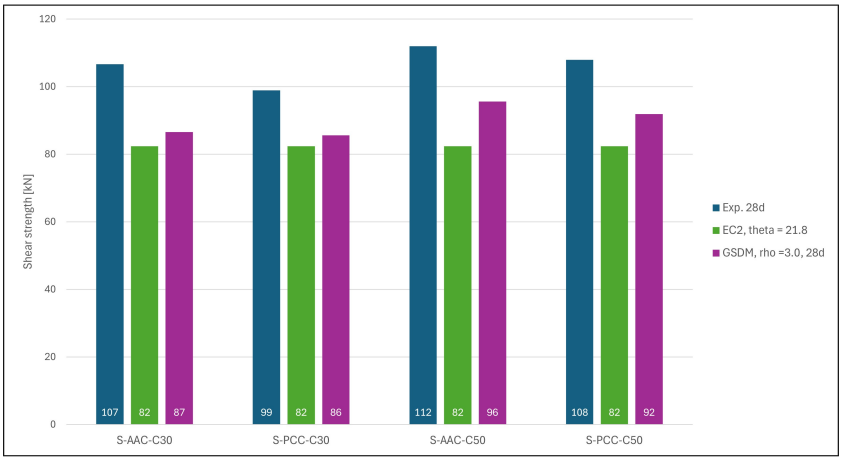

Figure D.5: Comparison of the experimental shear results with stirrups at 28 days with the shear resistance obtained using the GSDM. The blue bars represent the experimental results, the green bars represent the calculations with NEN-EN 1992-1-1, 2015, and the purple bars represent the calculations with the GSDM.

The results in Figures D.4 and D.5 indicate that the GSDM provides a closer approximation to the experimental results for beams with and without stirrups compared to the method presented in NEN-EN 1992-1-1, 2015.